

Present and Future Isochronous Mass Spectrometry at GSI-FAIR:

25 New Masses of Fission Fragments

Novel Analysis Method

Design of a New Time-of-Flight Detector System

Inauguraldissertation zur Erlangung des Doktorgrades der
Naturwissenschaftlichen Fakultät der Justus-Liebig-Universität Gießen

vorgelegt von

Marcel Diwisch
geboren in Wetzlar

Fachbereich 07 - Mathematik und Informatik, Physik, Geographie

II. Physikalisches Institut Justus-Liebig-Universität Gießen

Gießen 2015

Selbstständigkeitserklärung

Ich erkläre: Ich habe die vorgelegte Dissertation selbständig und ohne unerlaubte fremde Hilfe und nur mit den Hilfen angefertigt, die ich in der Dissertation angegeben habe. Alle Textstellen, die wörtlich oder sinngemäß aus veröffentlichten Schriften entnommen sind, und alle Angaben, die auf mündlichen Auskünften beruhen, sind als solche kenntlich gemacht. Bei den von mir durchgeführten und in der Dissertation erwähnten Untersuchungen habe ich die Grundsätze guter wissenschaftlicher Praxis, wie sie in der „Satzung der Justus-Liebig-Universität Gießen zur Sicherung guter wissenschaftlicher Praxis“ niedergelegt sind, eingehalten.

Datum

Marcel Diwisch

Erstgutachter: Prof. Dr. Dr. h.c. Hans Geissel
Zweitgutachter: Prof. Dr. Christoph Scheidenberger

Contents

| | |
|--|-----------|
| Abstract | 3 |
| 1. Introduction | 5 |
| 1.1. Mass Models | 5 |
| 1.2. Motivation for Mass Measurements | 8 |
| 2. Production and Separation of Exotic Nuclei | 13 |
| 2.1. Nuclear Reactions | 13 |
| 2.2. Separation of Exotic Nuclear Beams | 16 |
| 2.2.1. ISOL Facility | 17 |
| 2.2.2. In-Flight Facility | 18 |
| 2.3. The Fragment Separator FRS | 18 |
| 3. Methods of Mass Measurements | 23 |
| 3.1. Deflection in Magnetic and Electric Fields | 23 |
| 3.2. Q-values | 24 |
| 3.3. Penning Traps | 25 |
| 3.4. Time-of-Flight Spectrometer | 27 |
| 3.5. Storage Rings | 28 |
| 4. Isochronous Mass Spectrometry | 33 |
| 4.1. Principle of Isochronous Mass Spectrometry (IMS) | 33 |
| 4.2. The Experimental Storage Ring ESR | 40 |
| 4.3. Time-of-Flight Detector | 43 |
| 4.3.1. Secondary Electron Creation | 44 |
| 4.3.2. Motion of Charged Particles in E-Fields and B-Fields | 46 |
| 4.3.3. Timestamp Determination | 50 |
| 5. The ESR ToF Detector | 55 |
| 5.1. Modifications and Improvements | 55 |
| 5.1.1. Efficiency of the ToF Detector | 55 |
| 5.1.2. Timing properties of the ToF Detector | 55 |
| 5.2. Results of the ToF Detector Test with Uranium Ions | 60 |
| 5.3. Planned Modifications | 62 |
| 6. Data Analysis of Measurements with and without Accurate Momentum Definition in the FRS | 65 |
| 6.1. Determination of Revolution Times | 65 |
| 6.2. Identification | 71 |
| 6.3. Matrix Method | 75 |

| | | |
|------------|--|------------|
| 6.4. | Limitations of IMS | 83 |
| 6.4.1. | Contribution of ToF Detector and CFD Method | 83 |
| 6.4.2. | Contribution of the Isochronicity of the Ring | 86 |
| 7. | Results | 91 |
| 7.1. | Reference Masses | 92 |
| 7.2. | New Masses | 95 |
| 7.3. | Improved Masses | 97 |
| 7.4. | Comparison with Theory | 100 |
| 8. | Simulations for the new CR ToF detector | 103 |
| 8.1. | The Collector Ring CR at FAIR | 103 |
| 8.2. | Foil Diameter | 104 |
| 8.3. | Electron Transport | 108 |
| 8.4. | Magnetic Field | 109 |
| 9. | Design of new CR ToF detector | 113 |
| 9.1. | New Structure of Foil-Frame in the CR-ToF detector | 113 |
| 9.2. | Results of the Electric Field Simulations | 114 |
| 9.3. | Results of the Magnetic Field Simulations | 117 |
| 9.4. | Final Design | 117 |
| 10. | Outlook | 121 |
| A. | Appendix | 125 |
| A.1. | Experiments with and without Momentum Definition | 125 |
| A.2. | Analysis | 126 |
| A.3. | Additional Simulation Results | 131 |

List of Figures

| | |
|--|----|
| 1.1. Deviations of the liquid-drop model from experimental data versus neutron number N | 7 |
| 1.2. Measured abundances of the elements in the solar system | 9 |
| 1.3. Predictions of different mass models for Cd isotopes | 11 |
| 2.1. Production mechanisms shown in the chart of nuclides | 14 |
| 2.2. Principle of Fusion | 14 |
| 2.3. Principle of Projectile Fragmentation | 15 |
| 2.4. Principle of Projectile Fission | 16 |
| 2.5. Principles of ISOL and In-Flight Facilities | 17 |
| 2.6. Principle of Separation of Exotic Nuclei In-Flight | 20 |
| 2.7. Schematic layout of the high energy exotic nuclear beam facility at GSI | 21 |
| 3.1. Principle of Mass Measurements via Q-Value | 24 |
| 3.2. Principle of Mass Measurements with a Penning Trap | 26 |
| 3.3. Principle of Time-of-Flight Mass Measurements | 27 |
| 3.4. Different Types of Time-of-Flight Mass Spectrometers | 29 |
| 3.5. Principle of Schottky-Mass-Spectrometry (SMS) | 30 |
| 3.6. Principle of Isochronous-Mass-Spectrometry (IMS) | 31 |
| 4.1. Illustration of orbits for different $B\rho$ | 34 |
| 4.2. Coefficient $\left(1 - \frac{\gamma^2}{\gamma_0^2}\right)$ as a Function of the Velocity Deviation between Unknown and Reference Particle | 37 |
| 4.3. Isochronicity curves for different m/q | 38 |
| 4.4. Comparison between experiments with and without $B\rho$ -tagging | 40 |
| 4.5. Lattice and Ring Parameters of the ESR | 42 |
| 4.6. Schematic drawing of the ToF detector | 43 |
| 4.7. Secondary Electron Spectra | 46 |
| 4.8. Electron Transport from foil to MCP detector | 47 |
| 4.9. Calculated Electron Trajectories in crossed E and B Fields | 49 |
| 4.10. Walk effects for different signals | 52 |
| 4.11. Principle of the Constant Fraction Discrimination | 53 |
| 5.1. Transport Efficiency Simulation and Measurements | 56 |
| 5.2. Setup and Results of Timing Measurements in Dependence on the Start Position on the Foil | 57 |
| 5.3. Time Spread for Different Kinetic Energies of the Secondary Electrons | 58 |

| | | |
|-------|--|-----|
| 5.4. | Ion survival in the ring | 59 |
| 5.5. | Optimum CFD parameters at a sampling rate of 10GS/s | 60 |
| 5.6. | Measured Timing Uncertainties in the Online Test 2014 | 61 |
| 5.7. | Measured Uranium ToF Spectrum from the Online Test 2014 | 62 |
| 5.8. | Influence of External Magnetic Fields and Acceleration Voltages of the MCP Detector on the Signal Shapes | 63 |
| 6.1. | Time-of-Flight spectrum obtained in an IMS experiment | 66 |
| 6.2. | Algorithm to identify Patterns in the ToF Spectrum | 67 |
| 6.3. | Residuals of Fits of Different Polynomial Order for the Revolution Time Determination | 67 |
| 6.4. | Example of the Determination of the Revolution Time and its Un- certainty | 70 |
| 6.5. | Theoretical m/q values around $m/q = 2.5$ and a revolution time spectrum measured with IMS | 73 |
| 6.6. | Identification process | 74 |
| 6.7. | Principle of the Correlation Matrix Method | 77 |
| 6.8. | s-Factor of Different m/q Intervals Determined with the Correla- tion Matrix Method | 81 |
| 6.9. | Uncertainties of the Revolution Time for a Timestamp Uncertainty of 125 ps at different Turn Numbers | 84 |
| 6.10. | Uncertainties of the Revolution Time for a Timestamp Uncertainty of 50 ps at different Turn Numbers | 85 |
| 6.11. | Uncertainties of the Revolution Time for a Timestamp Uncertainty of 125 ps for 200 Turns and Different Detection Efficiencies | 86 |
| 6.12. | Influence of the Ring Isochronicity | 87 |
| 6.13. | Isochronicity Limits of the ESR | 88 |
| 6.14. | Summary of Major Contributions to IMS | 90 |
| 7.1. | Mass Deviation of Reference Masses (Systematic Error) | 94 |
| 7.2. | Mass difference between extrapolated AME12 mass values and this work for masses measured for the first time | 96 |
| 7.3. | Mass difference between AME12 and this work for masses with improved uncertainty | 97 |
| 7.4. | New Masses Covered in the Present Analysis | 98 |
| 7.5. | One-Neutron Separation Energy and Pairing-Gap Energies for the Cadmium and Tin Chain | 99 |
| 7.6. | Comparison of Iodine Isotopes with Theory | 101 |
| 7.7. | Differences between Measured S_n Values and Theoretical Predictions | 101 |
| 8.1. | Lattice and Ring Parameters of the Collector Ring | 105 |
| 8.2. | MOCADI Simulations for different Foil Diameters | 107 |
| 8.3. | Isochronicity Limits of the CR | 108 |
| 8.4. | Working phases of the SIMION simulations | 110 |
| 9.1. | Simulation results for different foil holders | 113 |
| 9.2. | Comparison between existing foil structure and newly designed one | 114 |

| | |
|--|-----|
| 9.3. Comparison of field homogeneity for geometry with and without grid | 115 |
| 9.4. Scheme of the Geometry for the Displacement of the MCP Detector. | 116 |
| 9.5. Simulation of Time Spread for different Displacements of the MCP Detector | 116 |
| 9.6. Simulation Results for the Magnet Field Homogeneity | 118 |
| 9.7. Technical Drawing of the New CR-ToF Detector (Electrodes only) | 119 |
| 9.8. Scheme of the Electrodes and Applied Voltages | 120 |
| 9.9. Technical Drawing of the New CR-ToF Detector placed inside the Vacuum Chamber and Magnet | 120 |
| 10.1. Known and Unknown Masses | 122 |
| 10.2. Gain in Transmission for Fission and Fragmentation Products of the Super-FRS compared to the FRS | 123 |
| A.1. MOCADI simulations for different foil diameters and different numbers of turns in the CR | 131 |
| A.2. Simulated ToF Spectra for a Displacement of 6 mm | 132 |
| A.3. Magnetic Field Simulations for different Pole Shoe Diameters and a Gap of 258 mm | 133 |
| A.4. Magnetic Field Simulations for different Pole Shoe Diameters and a Gap of 240 mm | 134 |

List of Tables

| | |
|--|-----|
| 1.1. Fit parameters of nuclear binding energies for all known 2149 masses in 2003 [Pea07]. | 6 |
| 5.1. Electric and magnetic field strengths for the initial and optimized detector settings. | 55 |
| 5.2. Comparison of the measured time spread for uranium ions and α -particles. | 61 |
| 7.1. Experimental field settings for different isochronous centered ions. | 91 |
| 7.2. List of used reference masses. | 93 |
| 7.3. List of masses measured for the first time. | 95 |
| 7.4. List of masses with improved uncertainty. | 97 |
| 7.5. Comparison of measured data with models. RMS deviations for I isotopes for different theoretical models are presented. In this comparison the new IMS values and the tabulated experimental values of AME12 are included. | 100 |
| 8.1. Comparison between ESR and CR ring parameters in the isochronous mode | 106 |
| 9.1. Performance and parameters of the ESR and CR ToF detectors. . | 117 |
| A.1. IMS experiments with the FRS-ESR facilities since 2002. | 125 |
| A.2. The data points used for the example given in 6.1. | 126 |
| A.3. Matrix elements in 3rd order for the isochronous mode of the ESR. | 128 |
| A.4. Matrix elements in 3rd order for the isochronous mode of the CR. | 130 |

Zusammenfassung

In dieser Arbeit wurden die grundlegenden Eigenschaften der isochronen Massenspektrometrie (IMS), wie sie an den Anlagen der GSI, sowie in zukünftigen Experimenten an FAIR durchgeführt wird, experimentell und theoretisch untersucht. Die Perspektiven und Limitierungen der IMS wurden sorgfältig mit Rechnungen und Experimenten studiert.

Die Daten von zwei unterschiedlichen, vorherigen IMS-Experimenten an GSI wurden kombiniert und mit einer neuartigen Korrelationsmatrixmethode (CMM) analysiert. Beide Experimente wurden mit dem Fragmentseparator FRS und dem Speicherring ESR durchgeführt. In beiden Experimenten wurden Spaltfragmente, die durch ^{238}U Projektile in einem Beryllium-Target am Anfang des FRS erzeugt wurden, räumlich separiert und in den isochronen ESR injiziert. Im ersten Experiment wurde die volle $B\rho$ -Akzeptanz des ESR genutzt, wohingegen im zweiten Experiment das $B\rho$ eines jeden Fragments durch Schlitze in der dispersiven, zentralen Fokalebene des FRS definiert wurde. So wurde die magnetische Steifigkeit für alle injizierten Fragmente auf $\Delta B\rho/B\rho = 1.5 \cdot 10^{-4}$ bestimmt. Die Ausbeute dieser Analyse sind 25 neue Massen in der Nähe und am $N=82$ Schalenabschluss. Der Vergleich zwischen den experimentellen Daten mit AME Extrapolationen und verschiedenen theoretischen Modellen zeigt erhebliche Abweichungen aufgrund schwacher theoretischer Vorhersagen in diesem Massenbereich. In dieser Hinsicht muss man hervorheben, dass durch die neuartige Analysemethode dieser Arbeit 25 neue Massen gewonnen werden und zusätzlich zu den bereits von uns veröffentlichten Ergebnissen hinzugefügt werden konnten. Die vorliegende Analyse hat keine Einschränkungen auf die Daten und liefert deswegen Zugang zu einem neuen Massenbereich. Es ist fast unnötig zu erwähnen, dass die neuen Massenwerte zu verbesserten r-Prozessrechnungen, welche momentan durchgeführt werden, beitragen werden.

In der vorliegenden Analyse wurde die Matrixmethode von Z. Patyk um einen variablen Skalierungsfaktor (s) erweitert. Dieser wurde für unterschiedliche Masse-zu-Ladungsverhältnisse (m/q) bestimmt und als Funktion von m/q in die Analyse implementiert. Dies erweiterte den zugänglichen m/q Bereich der Auswertung. Die Umlaufzeit wurde durch eine Polynomannpassung 3. Ordnung an die Zeitmarken bei $N_{max}/2$ bestimmt. N_{max} steht hierbei jeweils für die maximale Anzahl an Umläufen, die jedes einzelne Ion im ESR gemacht hat. Im Gegensatz zu vorherigen Analysen wurden keine Einschränkungen an die Daten gesetzt. Dies ermöglichte selbst die exotischsten Kerne, die mit naturgemäß geringer Statistik vorkommen, in dieser Arbeit zu erfassen. Die Genauigkeit der neuen Massen-

werte, welche hauptsächlich durch systematische Fehler und der Statistik bestimmt ist, liegt bei etwa 180 keV.

Die Leistungsfähigkeit des Flugzeitdetektors, die Bestimmung der Zeitmarken (constant-fraction discrimination) sowie die ionenoptischen Eigenschaften bestimmen die Genauigkeit und die Limitierung der IMS inklusive der CMM. Diese unterschiedlichen Beiträge wurden in der vorliegenden Arbeit mittels systematischer Simulationen und Testexperimenten untersucht. Ein Hauptergebnis dieser Studien ist, dass die Leistungsfähigkeit des jetzigen Flugzeitdetektors für Ionen, die mehr als 200 Umläufe im Ring machen, nur einen geringen Einfluss auf die Massengenauigkeit hat. Die Ionenoptik des Ringes hat den größeren Einfluss. MOCADI Simulationen mit erster und dritter Ordnung Transfermatrizen zeigen dies besonders deutlich für m/q Werte mit großer Abweichung zu dem m/q Wert des isochronen Ions. Diese Ergebnisse bestätigen die früheren Feststellungen [G⁺06], dass für die IMS neben der Umlaufzeit eine Messung der magnetischen Steifigkeit oder eine Messung der Geschwindigkeit notwendig ist. In zukünftigen IMS Experimenten kann diese Forderung mit einem neuen dualen Flugzeitdetektorsystem, welches ebenfalls im Rahmen dieser Dissertation entworfen wurde, erfüllt werden.

Das Timing des gegenwärtigen ESR Flugzeitdetektors wurde erheblich verbessert, indem die elektrische Feldstärke von 156 V/mm auf 300 V/mm erhöht wurde. Durch diese Änderung wurde die Zeitverbreiterung von 45 ps auf 35 ps reduziert. Die Ergebnisse wurden aus Simulationen gewonnen und mit Testexperimenten mit Alphateilchen bestätigt. Die exzellente Übereinstimmung zwischen Messungen und Simulationen war die Grundlage des Entwurfs des zukünftigen dualen Flugzeitdetektorsystems, welches im Collector Ring an FAIR installiert werden wird. Die beiden Flugzeitdetektoren werden in einem Abstand von 22 m voneinander eingebaut und erlauben eine Genauigkeit der Geschwindigkeitsmessung von besser als 10^{-4} , die für eine genaue Massenbestimmung benötigt wird. Der neue Flugzeitdetektor ist eine große Herausforderung, da der Foliendurchmesser im Inneren des Detektors im Vergleich zum jetzigen ESR Detektor verdoppelt werden muss. Eine größere Folie ist notwendig, damit der Detektor zu der viel größeren Emittanz der gespeicherten Fragmentstrahlen im CR passt. Der Durchmesser der geplanten Kohlenstoffolie beträgt 80 mm und die geometrischen Dimensionen des Detektors sind: 562 mm Breite, 180 mm Höhe und 236 mm Tiefe entlang der Strahlrichtung. Der Entwurf des neuen Detektors wurde erarbeitet und die Leistungsfähigkeit in systematischen Simulationen untersucht. Das außerordentliche Ergebnis dieser Untersuchung ist, dass sich das Timing des neuen Detektors, trotz seiner viel größeren Dimension, im Vergleich zum ESR Detektor verbessert hat. Durch Nachbildung gemessener Daten des ESR Detektors in den Simulationen wurde die Gültigkeit der Simulationsergebnisse des neuen Detektors untersucht. In diesem Sinne sind wir zuversichtlich, dass mit dem neuen dualen Flugzeitdetektorsystem IMS Experimente ein großes Entdeckungspotential besitzen. Dies gilt besonders für sehr kurzlebige exotische Kerne, die mit keiner anderen experimentellen Methode erreicht werden können.

Abstract

In this work the basic features of isochronous mass spectroscopy (IMS) for the present facilities at GSI and also for the future experiments at FAIR have been experimentally and theoretically investigated. The prospects and limitations of IMS have been carefully studied with calculations and experiments.

The data of two different previous IMS experiments at GSI have been combined and analyzed with a novel correlation-matrix method (CMM). Both experiments were performed with the fragment separator FRS and the experimental ion storage ring ESR. In both experiments fission fragments, created by ^{238}U projectiles in a beryllium target at the entrance of the FRS, were spatially separated and injected into the isochronous ESR. In the first experiment the full $B\rho$ acceptance of the ESR was used whereas in the second one the $B\rho$ of each fragment was defined by slits in the dispersive central focal plane of the FRS. In this way the magnetic rigidity was well-determined for all injected fragments to $\Delta B\rho/B\rho = 1.5 \cdot 10^{-4}$. The harvest of this analysis is 25 new masses near and at the $N=82$ shell closure. The comparison of the experimental results with the AME extrapolation and different theoretical models reveal significant differences due to the low theoretical prediction power of the calculations in this mass range. In this respect one has to emphasize that due to the novel analysis method in this work these 25 new masses could be extracted additional to our previously already published results. The present analysis has no restrictions to the data and thus gave access to a new mass region. It is almost needless to mention that the new mass values will contribute to improved r-process calculations which are in progress.

In the present analysis the matrix method of Z. Patyk was extended with a variable scaling factor (s). The scaling factor was determined for each mass-to-charge ratio (m/q) of the measured ions and implemented as a function of m/q in the analysis. This has extended the accessible m/q range. The revolution time was determined via a 3rd-order fit of the time stamps at $N_{max}/2$, where N_{max} represents the maximum number of turns an individual ion has reached circulating in the ESR. Contrary to previous analysis works no restriction was applied and thus the most exotic nuclides with naturally low statistics were included here. The accuracy for the new mass values are about 180 keV which is mainly determined by the systematic error and the statistics.

The performance of the ToF detector, the extraction of the time stamps (constant-fraction discrimination), and the ion-optical properties determine the accuracy and limitation of IMS including CMM. These different contributions were inves-

tigated in the present work by systematic simulations and test experiments. A main result of these studies is that for ions that circulate 200 turns or more the present timing performance of the ToF detector has a minor influence on the possible mass accuracy but the ion-optics of the ring. MOCADI simulations with first- and third-order matrices clearly demonstrate the latter statement, especially for m/q values far from the isochronous ion. This result confirms the previous statements [G⁺06] that for IMS one has to measure the revolution time and independently the magnetic rigidity or the velocity. In future IMS experiments this requirement can be fulfilled with the new dual ToF detector system designed in the frame work of this doctoral thesis.

The timing performance of the present ESR ToF detector has been substantially improved by increasing the electric field strength from 156 V/mm to 300 V/mm. This change has decreased the time spread from 45 ps to 35 ps. The results were obtained in simulations and verified in test experiments with alpha particles. The excellent agreement between measurements and simulations has been the basis for the design of the future dual time-of-flight detector system which will be installed in the Collector Ring of FAIR. The two ToF detectors will be installed about 22 m apart and allow a velocity determination of better than 10^{-4} which is needed for accurate mass determination. The new ToF detector is a big challenge because the foil diameter has to be doubled compared to the present ESR detector. The increase in size is needed to match the much larger emittance of the stored fragment beam circulating in the CR. The diameter of the planned carbon foil is 80 mm and the geometrical dimensions of the detector are:

562 mm width, 180 mm height, and 236 mm length in beam direction. The design of the new detector was done and the performance investigated in systematic simulations. The excellent result is that despite of the much larger dimension of the detector the timing performance has even increased compared to the ESR detector. The validity of the results from the simulation programs has been tested by reproducing the measured data of the present ESR detector. In this sense we are confident that with the new dual ToF detector system IMS experiments have a large discovery potential especially for the very short-lived exotic nuclei that cannot be accessed by other experimental methods.

1. Introduction

The origin of modern nuclear physics was the discovery of radioactivity by Henri Becquerel and experiments by Pierre and Marie Curie. Their work was honoured with the Nobel Prize in physics in 1903 [Nob14]. In the following years many important experiments were performed to establish a new and better understanding of the atomic structure. In 1909 Ernest Rutherford and his students Hans Geiger and Ernest Marsden performed the famous scattering experiment with α -particles on a gold foil that completely changed the understanding of the atoms [GM09]. Rutherford concluded from the results that almost the complete mass and the positive charge of the ions have to be concentrated in its tiny centre, the nucleus.

Further experiments with α -particles and hydrogen atoms showed, that the mass of an α -particle is less than 4 times the mass of hydrogen. Arthur Stanley Eddington connected this so called "mass defect" in 1920 [Edd20] to the popular equation by Einstein $E = mc^2$ and it was believed that it is the source of stellar energy. After the discovery of the proton by Ernest Rutherford (1920) [Rut20] and the neutron by James Chadwick (1932) [Cha32], the two nuclear constituents were known and descriptions of nuclei as we know them today, e.g. α -particles(= ${}^4_2\text{He}$) consist of 2 protons and 2 neutrons, were possible. Later investigations and theories showed that the mass difference (mass defect) between a bound nucleus and its constituents is a result of the binding energy of the nucleus. Carl Friedrich von Weizsäcker introduced a first (semi-empirical) mass model in 1935[vW35]. This model made it possible to predict the masses of nuclei with different compositions of neutrons and protons in a good approximation.

1.1. Mass Models

A nucleus can be described by its element symbol X , that is given by its charge number Z and its mass number A . It is the sum of charge number and number of neutrons $A = Z + N$. In some cases Z is stated as an additional information as well A_ZX .

The mass of an atom with a given number of neutrons N and a number of protons

Z can be written as

$$M(N, Z) = \underbrace{Z \cdot m_p + N \cdot m_n - BE_{\text{nuclear}}}_{\text{nuclear contribution}} + \underbrace{Z \cdot m_e - BE_{\text{electrons}}}_{\text{atomic contribution}}, \quad (1.1)$$

where m_p , m_n , m_e are the rest masses of a proton, a neutron and an electron respectively, BE_{nuclear} is the nuclear binding energy, and $BE_{\text{electrons}}$ is the binding energy of the electrons for a neutral atom. Since the masses of neutrons and protons are well known, the contribution of the nuclear binding energy is the value of interest. The goal of mass models is to describe and predict this binding energy.

A first approach to introduce a general formula for the binding energy of any nuclei A_ZX was given by Weizsäcker and Bethe [vW35]. The idea of this model is that a nucleus can be described as a liquid drop. This liquid-drop model includes several terms. The model includes a volume term (*vol*), a surface term (*sf*), a coulomb term, an asymmetry term (*sym*) and a pairing term. Most of them are based on a macroscopic picture:

$$BE_{\text{nuclear}}(A, Z) = a_{\text{vol}}A + a_{\text{sf}}A^{2/3} + \frac{3e^2}{5r_0}Z^2A^{-1/3} + a_{\text{sym}}AI^2 + \begin{cases} +2\delta, & \text{e-e nuclei} \\ 0, & \text{e-o or o-e nuclei} \\ -2\delta, & \text{o-o nuclei} \end{cases} \quad (1.2)$$

In this case $I = \frac{N-Z}{A}$ and all other parameters a_{vol} , a_{sf} , a_{sym} , r_0 , and δ are free fit parameters that can be fitted to all known measured masses. This can be done for example for all known 2149 masses collected in the Atomic Mass Evaluation 2003 [AWT03]. The results of the free fit parameters can be found in table 1.1.

Table 1.1.: Fit parameters of nuclear binding energies for all known 2149 masses in 2003 [Pea07].

| Parameter | Value |
|------------------|----------------|
| a_{vol} | -15.697550 MeV |
| a_{sf} | 17.662690 MeV |
| a_{sym} | 26.308165 MeV |
| a_{ss} | -17.003132 MeV |
| r_0 | 1.221897 fm |
| δ | -1.250000 MeV |

In figure 1.1 the difference between the calculated binding energy of the liquid-drop model and the experimental data for nuclides with different number of neutrons is plotted. One can recognize a pattern that leads to larger deviations of the formula for certain numbers of neutrons, namely at $N = 20, 28, 50, 82, 126$. This was a clear signature for the shell structure in nuclei. At these N values the corresponding nuclei were stronger bound than predicted.

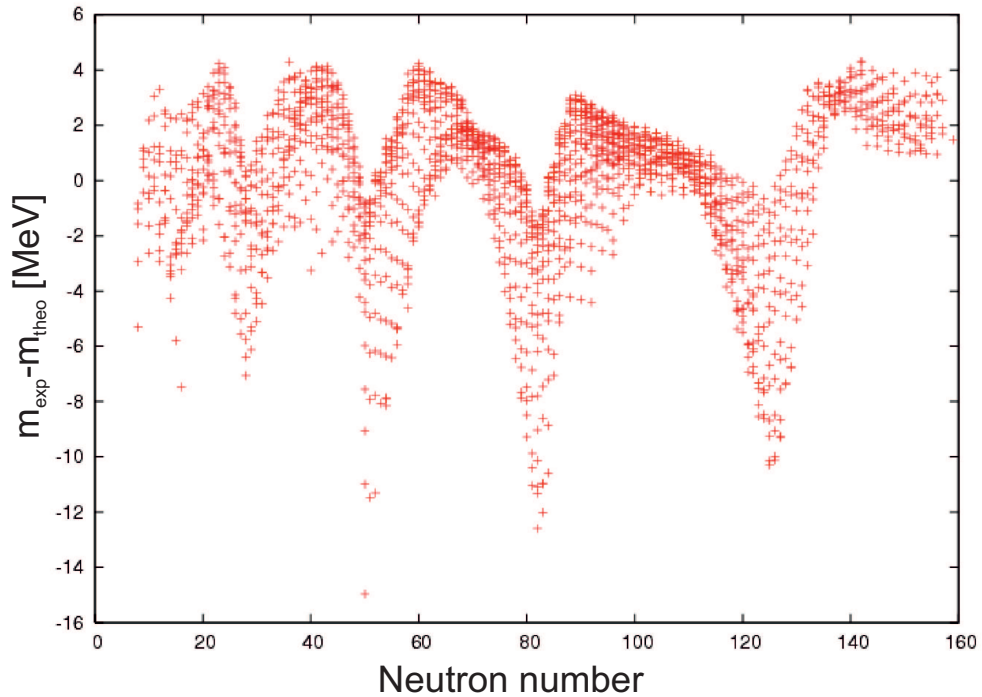


Figure 1.1.: Comparison of calculated nuclear binding energies from the liquid-drop model and the experimental data versus the neutron number N [Pea07]

The deviation is a good indication for a substructure existing in the nucleus that is not considered by the liquid drop model and has to be investigated further. As we know today this substructure can be explained by the nuclear shell model. A shell-correction term was included in the liquid drop model by Myers and Swiatecki in 1966 [MS66]. Nevertheless this macroscopic model has its limits. A more promising approach for modern mass models is the consideration of microscopic effects.

A pure microscopic theoretical solution for masses of nuclides of any composition can be formulated with the nuclear many body Hamiltonian.

$$H\Psi = E\Psi \quad (1.3)$$

with

$$H = -\frac{\hbar^2}{2M} \sum_i \nabla_i^2 + \sum_{i>j} V_{ij} + \sum_{i>j>k} V_{ijk} \quad (1.4)$$

Unfortunately, the solution of this Schrödinger equation is very difficult and no available solution fulfills the required accuracy for astrophysical applications. The approach of semi-empirical mass models (as already done by Weizsäcker) has to be used again, as it is the only way to achieve a mass model with reasonable accuracy. At this point there are two possible ways to achieve feasible and reliable mass models.

One way is to go back to the Weizsäcker formula and refine it with a lot of additional parameters. This approach leads to the so called macroscopic-microscopic models ,e.g. Finite-Range-Droplet Model (FRDM) and Finite-Range-Liquid-Drop Model (FRLDM) [MNMS95].

The other possibility is the so called Hartree-Fock model which simplifies the many body problem from equation 1.3 and uses an effective shell model Hamiltonian

$$H^{\text{eff}} = -\frac{\hbar^2}{2M} \sum_i \nabla_i^2 + \sum_{i>j} v_{ij}^{\text{eff}}. \quad (1.5)$$

With this Hamiltonian, it is possible to construct a force v_{ij} and fit its parameters to known mass values. A force that was found in this way and that is used in many mass models is the 10 parameter Skyrme force [Pea07][SGP04]. Since this model still lacks the possibility to handle pairing correlations the Hartree-Fock-Bogoluibov (HFB) method is introduced into the theory by adding an additional pairing force.

Over the past years, a lot of additional contributions and physical phenomena have been included in the development of HFB models, which led to new versions, e.g. from HFB14 in 2007 [GSP07] to HFB27 in 2013 [GCP13].

1.2. Motivation for Mass Measurements

The application of macroscopic-microscopic or pure microscopic (HFB) approaches and the information from new measurements led to the development of numerous different theoretical mass models. The predictive power in a new mass region is a crucial criterion for the validity of a model or semi-empirical formula. New mass measurements of known masses with higher accuracy and the extension in unknown regions are both crucial tests for theoretical descriptions. However, a good mass model must in principle also be able to predict other basic nuclear properties, like lifetimes and radii, if the strong interaction is well included.

The knowledge of the nuclear binding and structure is the base to understand also the creation of matter in the universe. The nucleosynthesis of the chemical elements is closely connected to the nuclear properties. Figure 1.2 shows the measured abundances of chemical elements in the solar system compared to theoretical predictions based on different mass models.

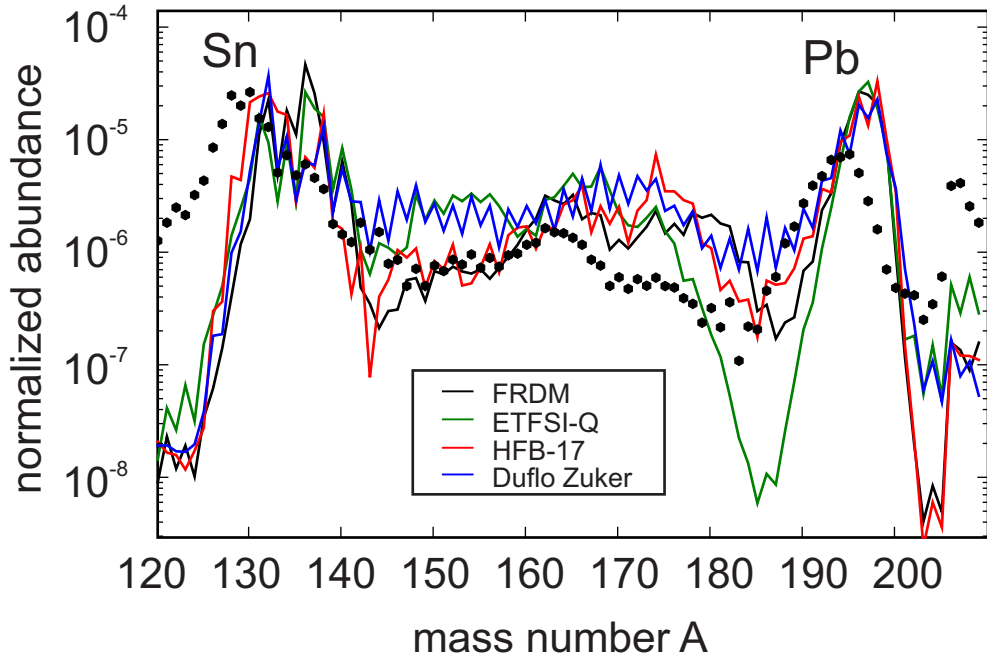


Figure 1.2.: Measured abundances of the elements in the solar system (filled circles) compared with theoretical predictions based on different mass models [Arc10].

The creation of elements started with the big bang and the formation of hydrogen. After the clustering of matter, the formation of stars, hydrogen fusion was ignited due to the gravitational pressure and the correlated temperature rise. Fusion processes in stars can energetically produce only elements up to iron (exothermic reaction).

The origin of trans-iron elements is believed to be in supernovae explosions. In those explosions neutron capture creates the heaviest known elements in the universe. Whilst the pretty well known p-process (proton capture) and other processes on the proton rich side of the nuclear chart explain some of the observed solar system abundances, they do not explain everything which means other processes have to be involved. On the neutron-rich side of the nuclear chart the so called r-process (rapid neutron capture) add neutrons to a seed nuclei on different timescales and leads to the formation of heavier nuclei from β^- -decay. The synthesis along the so called r-process path is crucial for the explanation of the abundances of those elements not producible by proton capture processes, but it is still not completely understood. The investigation of very neutron rich elements is not easy, since the production rate in the most modern accelerator facilities is fairly small. Presently the r-process path is mainly based on theoretical predictions with large uncertainties and has to be verified experimentally by measuring the masses of those very neutron rich nuclei. Since the binding energy of a nucleus is approximately only 1% of its total mass it is necessary to measure the mass very precisely.

Depending on the physical problem, the needed accuracy to yield new information should be between $\Delta m/m \approx 10^{-6} - 10^{-7}$ for nuclear structure and nuclear astrophysics down to a requirement of $\Delta m/m \approx 10^{-8}$ for fundamental questions

like weak interactions [LPT03][Bla06][FGM08].

One of the above mentioned accelerator facilities that enables experiments with exotic nuclei is the "GSI Helmholtzzentrum für Schwerionenforschung" in Darmstadt, Germany. After producing the nuclei they can be separated by the Fragment Separator (FRS) and stored in the Experimental Storage Ring (ESR) where Isochronous Mass Spectrometry (IMS) is used to measure very precisely and accurately the masses of nuclei with half-lives down to a few tens of μs [S⁺10].

The work presented in this thesis can be divided into two parts. The first part describes the recently performed improvements on the existing IMS performance at the FRS-ESR facility and presents mass measurements of 25 newly measured masses gained with a new data evaluation approach from experiments performed in 2002 and 2006. The second part concentrates on the development of a new dual time-of-flight (TOF) detector system, which will be employed in the future Collector Ring (CR) at the FAIR facility, and which allows the investigation of even more exotic nuclei as well as measure them with a higher accuracy.

As stated above, there are many different mass models. In general, most models reproduce well all masses in the range of experimentally known nuclei, but show large deviation for new regions. This is shown in figure 1.3. For known masses all models are in good agreement but for new regions, the prediction power is poor, especially for models with a large number of fit parameters.

This means, it is absolutely necessary to perform new accurate mass measurements of nuclei in unknown regions of the chart of nuclides. Mass and lifetime measurements are the most important properties of any discovered nuclide. These measured new values yield valuable tests of the prediction power of theoretical models.

On the next pages, the superheavy elements production and the experiments to measure their masses will be explained. The focus of this thesis will be the presentation of masses measured for the first time with the Isochronous Mass Spectrometry (IMS), as well as a discussion of the limits and future perspectives of the method.

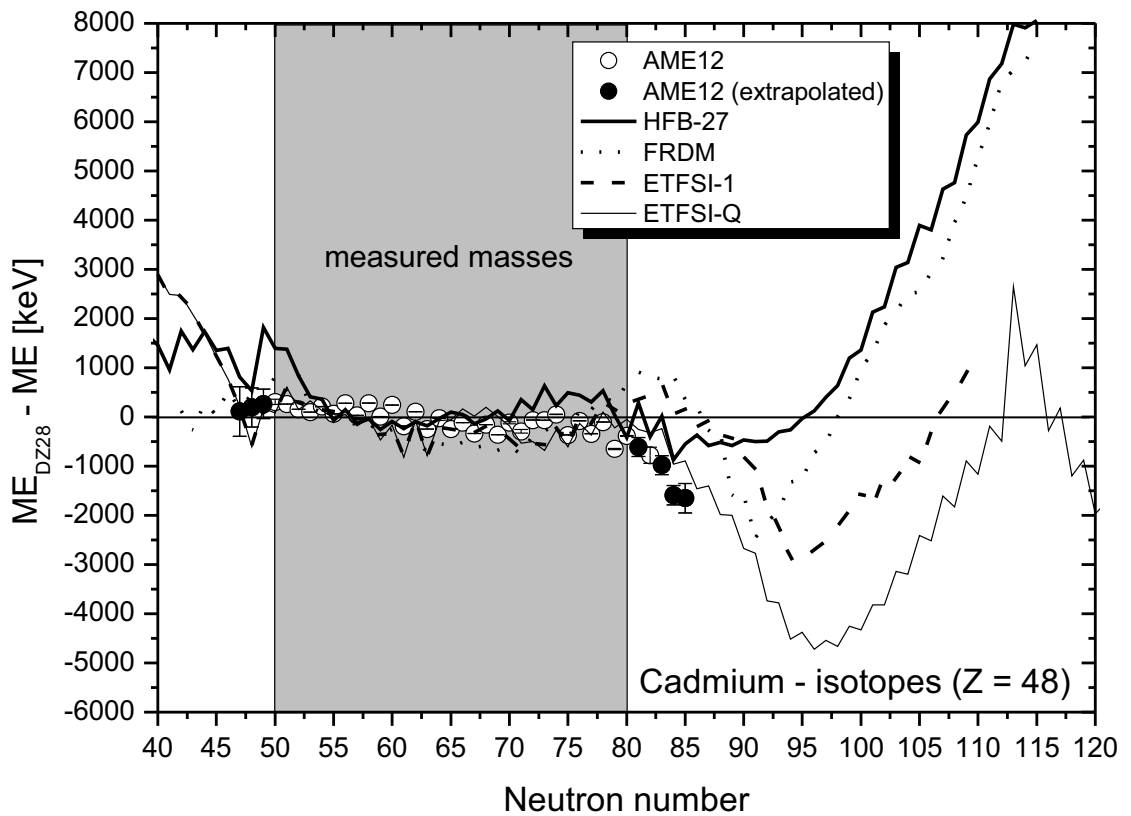


Figure 1.3.: Experimental [WAW12] and calculated [D⁺96, MNMS95, A⁺95, P⁺96, DZ99] mass values for cadmium isotopes. The region of experimental mass values is indicated by the grey area. The extrapolated values from AME2012 [WAW12] is included by full circles

2. Production and Separation of Exotic Nuclei

The most interesting species for nuclear research are radioactive short-lived nuclei far away from beta stability, because they reveal new basic properties, like novel matter distribution, excitation and decay modes. Those nuclei do not exist on Earth but in stellar environments they are still produced. Therefore, exotic nuclei have to be produced in nuclear reactions in the laboratory to investigate their unusual properties. However, exotic nuclei represent a great experimental challenge, because in general their production cross sections are very small and their lifetimes short. The consequence is that one needs powerful accelerators with large primary beam intensities and fast and efficient separators in combination with spectrometers and detectors.

2.1. Nuclear Reactions

The first man-made nuclear reaction was performed by Ernest Rutherford in 1917 and published in 1919 [Rut19]. He shot α -particles onto nitrogen-14 which transformed into oxygen-17 ($^{14}\text{N}(^4\alpha,^1\text{H})^{17}\text{O}$). Following his example many other experiments have been performed to artificially produce new isotopes or even new elements. By varying the experimental parameters (projectile energy, projectile particle, target material, etc.), different reactions can be chosen for the production of the nuclei of interest. One distinguishes between three reaction mechanisms:

- i) Fusion
- ii) Fission
- iii) Fragmentation

Figure 2.1 demonstrates which nuclei can be best produced via fusion, fission and fragmentation. While fusion processes mainly create proton-rich nuclei it is not feasible to use fusion to create neutron-rich particles with stable projectile-target combinations. To access very neutron rich areas one has to use fragmentation. Fission products can reach medium mass nuclei and their distribution depends mainly on the excitation energy of the impinging projectile.

Which one of the above mentioned scenarios will take place depends mainly on the chosen energy of the projectile and the target material.

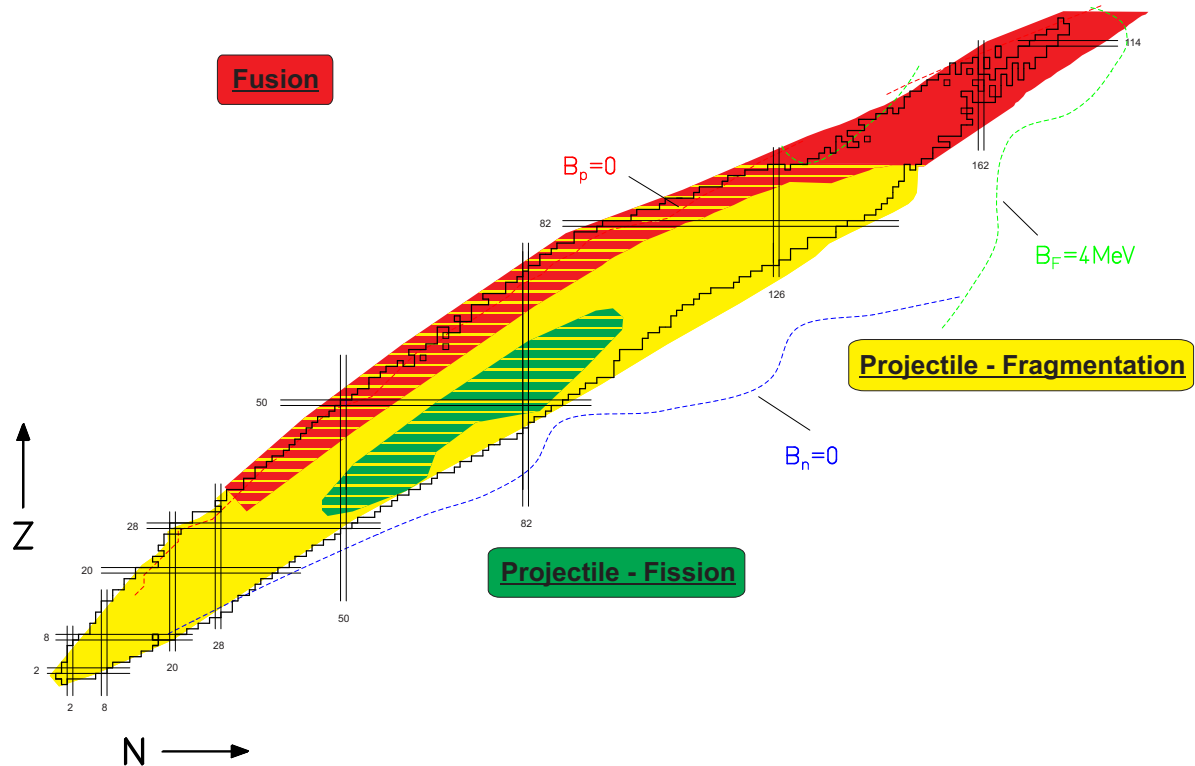


Figure 2.1.: The different areas of exotic nuclides together with their established production mechanisms are shown in the chart of nuclides with the magic numbers in N and Z , the proton drip line B_p , the neutron drip line B_n and the fission barrier B_F at 4 MeV [GHMD14].

Projectile energies close to the Coulomb barrier allow the projectile to fuse with the target nuclei and form a heavier compound nucleus in an excited state (see figure 2.2).

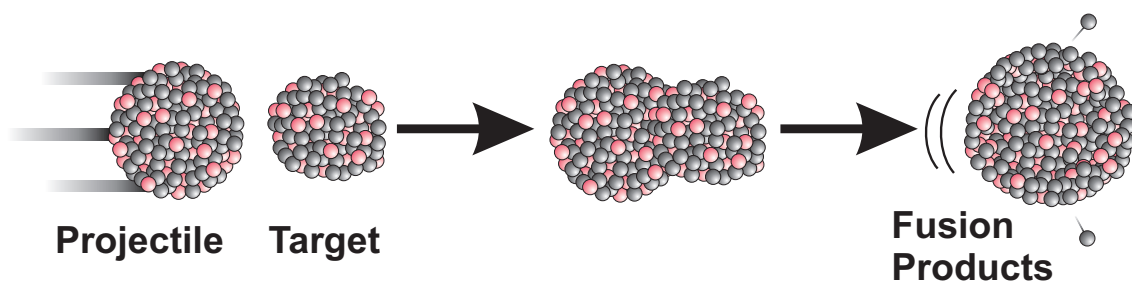


Figure 2.2.: Scheme of Fusion. In the fusion process two nuclei overcome the Coulomb barrier in central collisions and fuse into a heavier excited compound nucleus which de-excites by emission of γ -rays and nucleons.

The compound nucleus de-excites by emitting γ -rays and evaporation of nucleons. The formed compound nucleus only survives if the de-excitation happens via γ

emission. Because of momentum conservation the compound nucleus carries the total momentum of the projectile:

$$\vec{v}_{\text{fusion}} = \frac{A_{\text{proj}}}{A_{\text{proj}} + A_{\text{targ}}} \cdot \vec{v}_{\text{proj}}, \quad (2.1)$$

where A_{proj} is the mass number of the projectile, A_{targ} is the mass number of the target nucleus, and \vec{v}_{fusion} and \vec{v}_{proj} are the velocities of the fused nucleus and the target, respectively.

By increasing the energy of mostly heavy nuclei (such as, e.g. uranium) up to relativistic energies and using light target materials (such as, e.g. beryllium) fragmentation of the projectile nucleus occurs, see figure 2.3.

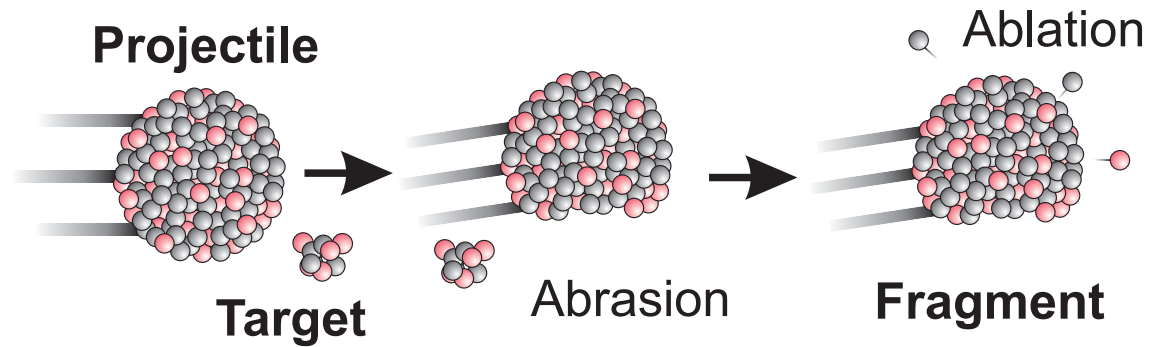


Figure 2.3.: Scheme of projectile fragmentation. Fast heavy projectiles interact with target nuclei in peripheral collisions. In the abrasion stage nucleons are removed and a pre-fragment is formed. The de-excitation process ablates nucleons and clusters.

In the collision nucleons are removed from the projectile via abrasion and a pre-fragment is formed in an excited state. The pre-fragment de-excites via ablation, which leads to the final fragment that then can be transported to different experimental areas. Since the energy deposition is small, the velocity of the fragment is approximately the same as the velocity of the projectile.

$$\vec{v}_{\text{frag}} \approx \vec{v}_{\text{proj}}, \quad (2.2)$$

with \vec{v}_{frag} and \vec{v}_{proj} being the velocity of the fragment and the projectile, respectively.

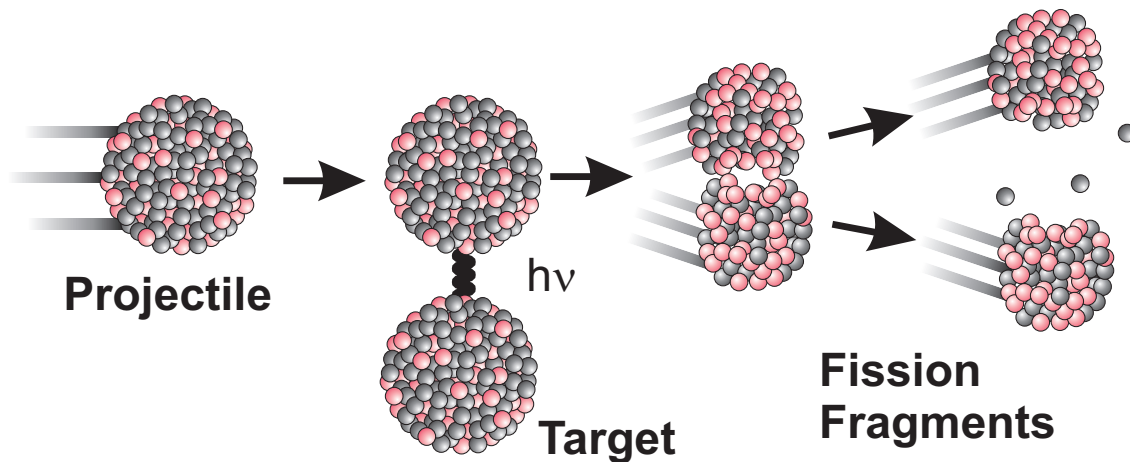


Figure 2.4.: Scheme of electromagnetic projectile fission. Electromagnetic excitation occurs in distant collisions with impact parameters larger than the strong interaction zone. The interaction of their Coulomb fields excites the nucleus which then may de-excite by evaporation of nucleons and fission. Projectile fission can also be induced by abrasion (Abrasion-Fission) in the first collision process. A nucleon removal reaction creates a residual nucleus with an excitation of about 30 MeV.

By passing a heavy nucleus with another heavy nucleus the Coulomb interaction between both nuclei can excite the projectile which then de-excites by evaporating single nucleons or fission. The impact parameter of the impinging projectile is an important parameter that determines the distribution of the fission products. Large impact parameters (i.e. peripheral reactions) lead to asymmetric product distributions with a light and heavy group [HS39][Wag91][Ich12]. The velocity distribution of the fission products \vec{v}_{prod} is rather large due to the velocity of the projectile \vec{v}_{proj} and the additional velocity \vec{v}_{fiss} added by the fission process itself.

2.2. Separation of Exotic Nuclear Beams

Exotic nuclei can be produced by the reactions described in the previous section. Unfortunately, the most interesting and most exotic nuclei have very small production cross section down to the pico-barn domain. Therefore, these species can only be studied if the non-reacted primary beam and all the abundant less interesting nuclides have been removed.

Over the last 50 years, mainly two different separations have been established. One is the so called Isotope Separator OnLine (ISOL) method and the other one is the in-flight method. Recently, a combined separation scenario has been established in addition. The in-flight separated exotic nuclei are energy bunched and stopped in a helium filled gas cell. The reviews by Geissel et al. [GHMD14]

and Blumenfeld et al. [BND13] give a detailed overview of the modern developments of separation techniques for exotic nuclei. A "flow chart" of the different techniques can be found in figure 2.5.

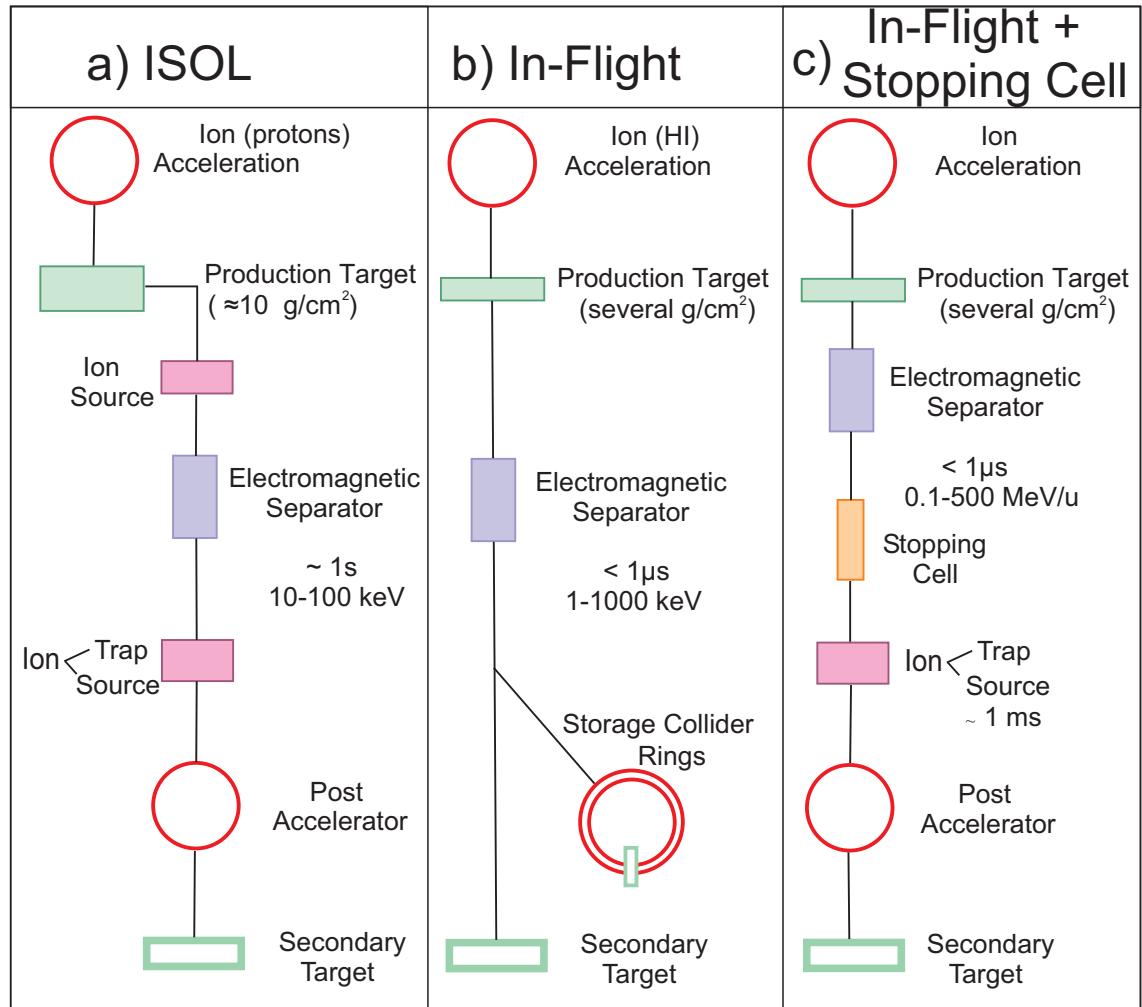


Figure 2.5.: Principles of ISOL and in-flight facilities and their combination. The ISOL (panel a)) and in-flight (panel b)) methods are powerful and complementary for the production and separation of exotic nuclides. The combination of an in-flight facility with a gas-filled stopping cell presents the advantages of both methods (panel c)) [GMR95, GHMD14].

2.2.1. ISOL Facility

The first beams separated with the ISOL method were reported in 1951 by O. Kofoed-Hansen and K.O. Nielsen [KHN51]. The idea is to produce the ions of interest with a high current ion beam (achievable with light elements) impinging on a thick and heated target. The nuclei of interest are produced in the target, thermalized and diffuse toward the target surface. From the target surface they are transported into an ion source for ionization and are accelerated to energies

typically between 10-100 keV. These accelerated ions can then be separated according to their mass-to-charge (m/q) ratio by electrical and magnetic fields and transported to designated experimental areas.

While the very intense ion beams allow for a high production rate in the target itself, the extraction efficiency and the diffusion process out of the target are limiting factors for the yield of the extracted ions since it depends strongly on the chemical properties of the selected elements. Another disadvantage of this method is the relatively long time that the elements need to diffuse to the surface, which makes it impossible to extract secondary ion beams consisting of very exotic (hence short lived) nuclei. The minimum half-life of nuclei in the beam achievable is in the order of a few tens of ms [B⁺99].

2.2.2. In-Flight Facility

An in-flight separator uses relatively thin production targets and takes advantage of the high kinetic energy of the reaction products. The separation time is only limited by the time-of-flight through the separator elements and is usually less than 1 μ s, at relativistic energies several hundred nanoseconds. Depending on the energy domain of the primary beam different spatial separation scenarios can be applied. At low energies near the Coulomb barrier electric and magnetic fields can be applied, whereas at relativistic energies the electric fields are replaced by the separation properties of atomic energy loss in shaped solid materials. Electric sector fields reach at high rigidities a technical limit for realisation. Gas-filled separators are applied for fusion products and are besides velocity filters the most successful facilities for the research with superheavy elements.

The main advantages of the separation in-flight is the universal access of very short-lived exotic nuclei, the spatial separation without any influence of the chemical properties of the fragments, and finally the high kinematic energies which directly allow the investigation of exotic nuclides via secondary nuclear reactions. The combination of the in-flight production and separation techniques with stopping in a gas-filled cell opens up new experimental fields for low-energy high precision experiments with traps [P⁺13]. This separation principle is illustrated in the right panel of figure 2.5.

2.3. The Fragment Separator FRS

The heavy-ion results presented in this thesis have been obtained in experiments performed with the FRS-ESR facilities at GSI. Detector tests have been made with α -particles in the laboratory or in the ESR test chamber.

Projectile fragments and fission products have been produced with primary beams

delivered by the UNiversal Linear ACcelerator (UNILAC) and the heavy-ion synchrotron SIS18 with a maximum magnetic rigidity of up to 18 Tm. The UNILAC is capable of pre-accelerating any stable element ranging from hydrogen up to uranium to an energy of 11.4 MeV/u [AS69]. These accelerated beams are injected into SIS18 and post-accelerated up to 90% of the speed of light depending on the ionic charge state [BF92].

The primary beams from SIS18 are focused on the production targets placed at the entrance of the FRagment Separator (FRS) [G⁺92b]. The production targets are most often beryllium targets but can also be made of heavier elements depending on the experimental goals. The targets are relatively thin, of the order of 10% of the atomic range of the projectiles. The kinetic energies of the fragments emerging from the target are in the range of 70-90 % of the velocity of light. Most ions are fully ionized at these high velocities thus the charge-state population is no problem for the in-flight-separation.

The FRS has 4 magnetic dipole stages with quadrupole and hexapole magnets. The maximum magnetic rigidity of the FRS is 18 Tm. The FRS has 3 branches which are used in combination with different experimental setups. One branch injects the spatially separated beams into the storage ring ESR for accurate mass measurements. The spatial separation is based on two-fold magnetic rigidity analysis in front and behind the shaped energy degrader ($B\rho-\Delta E-B\rho$ separation method)[G⁺92b, SG98].

The ion-optical system of the FRS is achromatic at the final focal plane. The energy degrader is relatively thick, of the order of half of the atomic range of the selected fragments. The degrader is shaped such that the achromatism is preserved at the final focal plane. An achromatic system has the best performance for spatial separation of mono-isotopic beams. The principle of the $B\rho-\Delta E-B\rho$ separation with the FRS is shown in figure 2.6.

The FRS is primarily a powerful separator but represents simultaneously also a high-resolution spectrometer. This property is used in a pilot experiment combined with the isochronous ESR analysed in this thesis. The $B\rho$ resolution in the central focal plane of FRS can be used to determine the velocity spread of each fragment beam before it is injected in the ESR. In experiments with the ESR fast-extracted beams from SIS18 have to be used thus that only with mechanical slits one can realize such a momentum definition. In experiments with slow-extraction from SIS18 of course, one can use position-sensitive detectors in coincidence. Note that the isochronous operation of the ESR with uncooled beams has only a moderate transverse resolving power. However, the ESR has always a high longitudinal $B\rho$ resolving power, which can be used in frequency measurements for accurate mass and lifetime experiments.

In experiments with the goal of mass measurements in the ESR the degrader at the FRS is usually thin or even omitted to measure simultaneously a broad

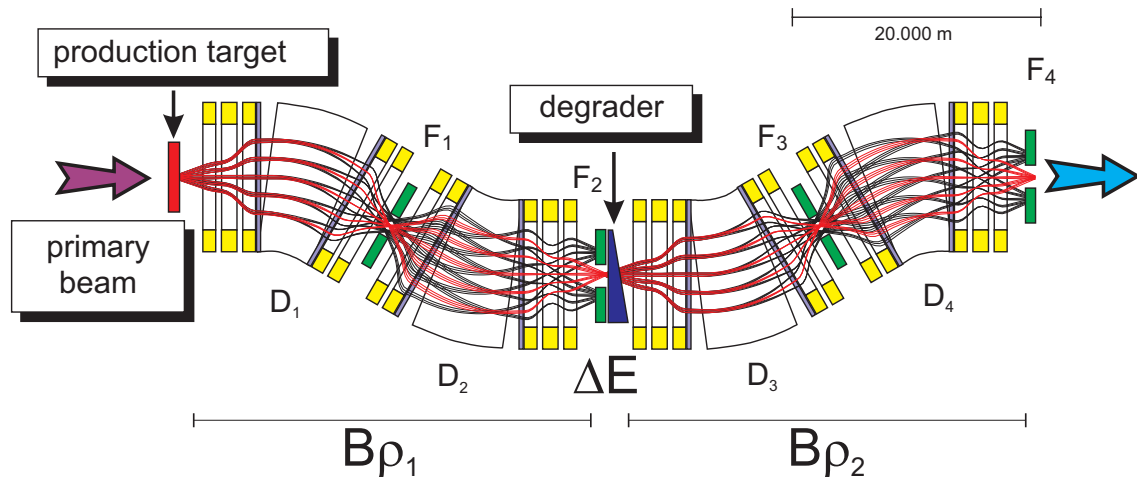


Figure 2.6.: Principle of the in-flight separation of exotic nuclei with the FRS applying the $B\rho$ - ΔE - $B\rho$ technique. The 4 dipole stages (D_1 - D_4) including the quadrupole and hexapole lenses are shown together with calculated envelopes in the dispersive plane. The shaped energy degrader is placed in the symmetric midplane of the ion-optical system. The overall system is achromatic as it is demonstrated with the calculated ion-optical trajectories.

spectrum with known and unknown masses. A schematic layout of the complete SIS-FRS-ESR system is given in figure 2.7.

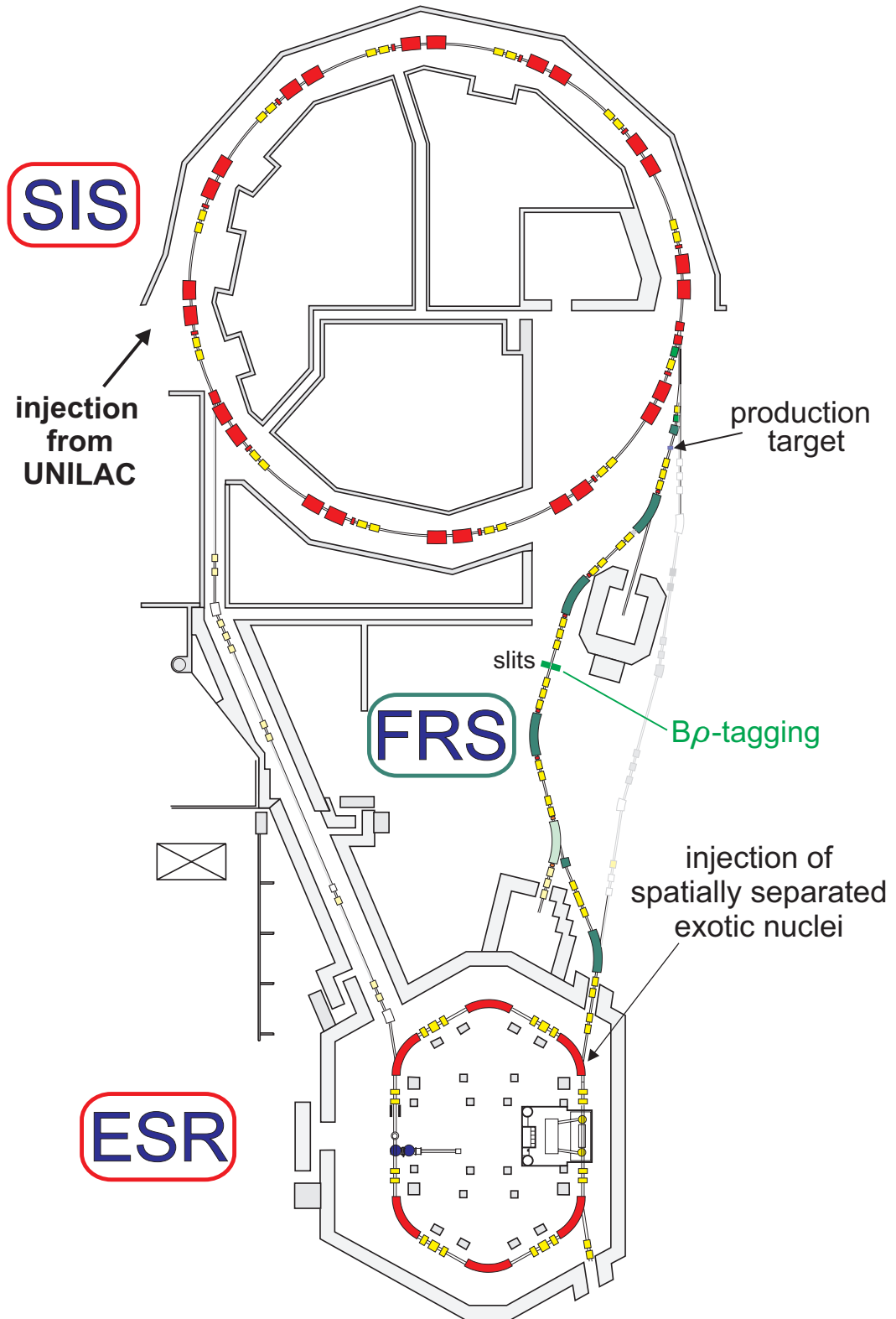


Figure 2.7.: Schematic layout of the high energy exotic nuclear beam facility at GSI. It consists of the synchrotron SIS18, the fragment separator FRS and the experimental storage ring ESR. The third branch of the FRS with the experimental setups in the other caves are not shown in this picture.

3. Methods of Mass Measurements

The determination of atomic masses can be performed with many different experimental methods. Often special beam preparations are necessary to perform mass measurements. For example, they can include the stopping of relativistic ion beams in a gas-filled cell or the storage of a pulsed beam in an ion storage ring.

Historically, one has distinguished between indirect (e.g. Q-value) and direct (e.g. Isochronous Mass Spectrometry) mass measurements. Both methods have advantages and are characterized by different systematic errors.

3.1. Deflection in Magnetic and Electric Fields

The first mass-spectrometry experiments were performed in 1912 by Joseph John Thomson [Tho12] and 1919 by Francis William Aston [Ast19]. They used a simple spectrometer that deflected different ion species according to their mass-to-charge ratio and velocity. With the known magnetic field strength (B), known charge state (q) and knowledge of their velocity (v), it was possible to measure their masses (m) directly by the determination of the bending radius ρ . They obtained accurate mass values by reference measurements with known masses in the same spectrum. This experimental method is still applied in modern experiments nowadays.

$$\rho = \frac{m v}{q B} \iff \frac{m}{q} = \frac{B\rho}{v} \iff v = \frac{B\rho}{m/q} \quad (3.1)$$

Although the mass resolving power ($(m/\Delta m) \approx (130-600)$) of these pioneer experiments were not high, yet the nature of isotopes was discovered. F.W. Aston has 207 isotopes discovered by his mass measurements! The setups of the pioneers have been steadily improved. In a double focusing mass spectrometer (Mattauch-Herzog geometry and Nier-Johnson geometry) an ion beam with different kinetic energies is firstly separated according to its kinetic energies in the electrostatic sector field and secondly deflected by the magnetic sector field according to its momentum, hence its mass-to-charge ratio is the final result. The ions were singly charged thus the mass values were directly extracted.

The kinetic energy in an electrostatic field with potential U is given by

$$E_{\text{kin}} = \frac{1}{2}mv^2 = Uq \quad (3.2)$$

This means that by combining magnetic and electrostatic fields (combining equation 3.1 and 3.2) one can determine the mass-to-charge ratio by

$$\frac{m}{q} = \frac{B^2\rho^2}{2U} \quad (3.3)$$

With this formula the mass resolving power R of a double focusing sector field with constant magnetic field B and constant electrical potential U is

$$R = \frac{m}{\Delta m} = \frac{\rho}{2\Delta\rho} \quad (3.4)$$

These double focusing sector field mass spectrometers are the classical mass analyzers. Advantages are the high reproducibility of the measurements, the high resolving power (up to 100,000), and the large dynamic range. The limitations of the method are the large geometrical setups and the high cost.

3.2. Q-values

Another approach is to measure the mass of an unknown nucleus via determination of the Q-value of a nuclear reaction, see principle in figure 3.1.

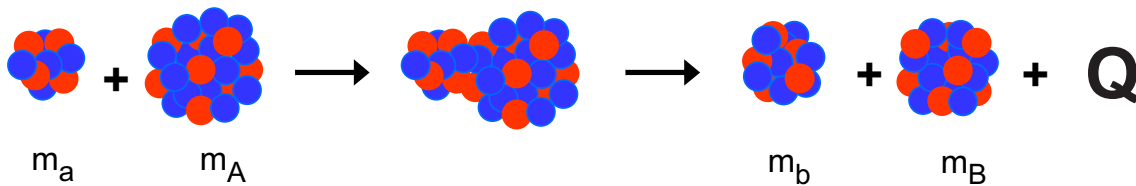


Figure 3.1.: Principle of mass measurements via Q-value measurements. The incident projectile with mass m_a interacts with target m_A . In the reaction m_b and ejectile m_B are created and the binding energy Q is released.

For a nuclear reaction



with a, A, b, B being different nuclei involved in the reaction, the Q-value is defined as

$$Q = [(m_a + m_A) - (m_b + m_B)] c^2 \quad (3.6)$$

or via the total initial and final kinetic energies $E_{\text{kin}}^{\text{initial}}$ and $E_{\text{kin}}^{\text{final}}$, respectively

$$Q = \sum E_{\text{kin}}^{\text{initial}} - \sum E_{\text{kin}}^{\text{final}}. \quad (3.7)$$

If three masses are known the unknown mass can be determined. The Q-value is also completely determined if all kinetic energies are measured.

Similar to the Q-value measurements, one can measure radioactive decays in order to access new masses. In these kind of measurements all decay products and their energy have to be measured and identified [H⁺79]. In most applications (especially for superheavy elements) the nuclei of interest are implanted into a silicon detector where the decay products are recorded. The task is simple for pure alpha-decay into the ground state of the daughter. This method is successfully used for example in experiments at the Separator for Heavy Ion reaction Products (SHIP) [MFH⁺79] [H⁺12b]. In this way the reaction products have been unambiguously identified by A and Z.

A disadvantage of mass measurements via the Q-value method is that all decay products and possible excited states have to be known.

3.3. Penning Traps

Penning traps are used for direct mass measurements at low beam energies. At most ISOL facilities the masses of the created ions are measured with one or more Penning traps. The condition that the kinetic energy of the secondary beams from an ISOL system is about 10 - 100 keV it is ideal to inject the exotic nuclides in traps.

However, it is also possible to use secondary beams from in-flight separators. This is done, for example, with the SHIP velocity filter [MFH⁺79]. The fusion products are stopped after in-flight separation in a gas-filled stopping cell and from there extracted for the Penning-trap measurement.

In a Penning trap ions are injected via tiny holes in the end caps and confined by quadrupolar electrical fields in axial direction and by a magnetic field parallel to the beam axis in radial direction. The trajectories in the trap are dependent on the applied magnetic field strength and the mass-to-charge ratio of the injected ion. The motion is a superposition of three independent motions namely the modified cyclotron motion ω_{cyclo^+} , the magnetron motion ω_{magn} and the axial motion ω_{axial} .

The mass information of the ion in the trap is given by the cyclotron frequency:

$$\omega_{\text{cyclo}} = \frac{q}{m}B = \omega_{\text{cyclo}^+} + \omega_{\text{magn}} \quad (3.8)$$

The axial motion can be neglected in the cyclotron frequency, which is induced by the magnetic field, because the axial contribution of the magnetic field is 0. A schematic view of a Penning trap and the three super positioned frequencies can be found in figure 3.2.

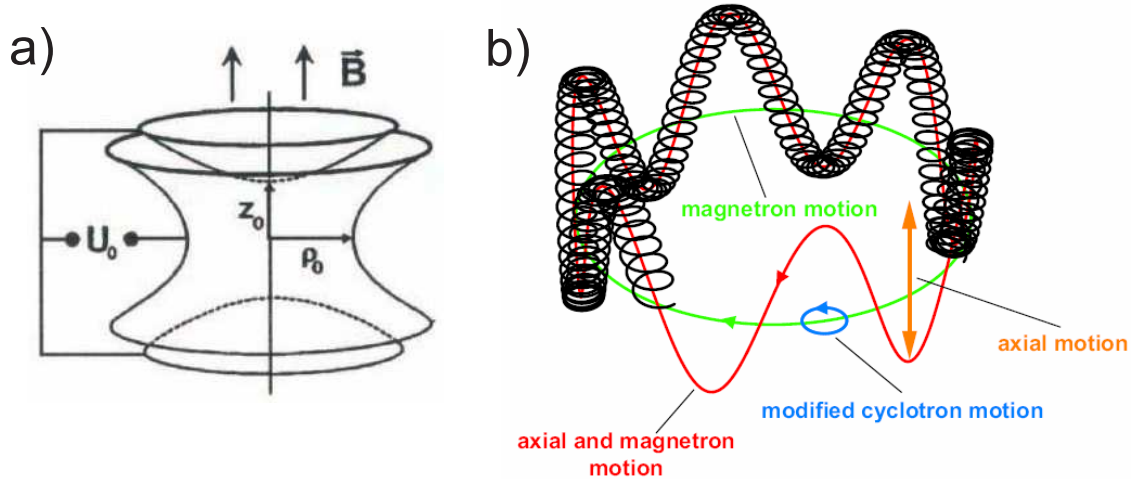


Figure 3.2.: Panel a): Principle setup of a toroidal penning trap. The electrode shapes, the applied electrical potential, and the magnetic field are shown. Panel b): Shown are the magnetron, modified cyclotron and axial motion, which are the basic motions inside a penning trap. [Hei12]

The measurement of the cyclotron frequency can be done in three different ways: the Fourier transform of the ion cyclotron resonance (FT-ICR) [MHJ98], the time-of-flight ion cyclotron resonance (ToF-ICR) [K⁺95], and the phase imaging ion cyclotron resonance method (PI-ICR) [Gon14]. In the FT-ICR the cyclotron frequency is measured by a pair of electrode plates picking up mirror charges that can then be analysed via Fourier transformation.

In the ToF-ICR a time-of-flight resonance curve is measured that yields the cyclotron frequency. An additional electric radio-frequency is applied to excite the ion in the trap. If the applied radio frequency is close to the cyclotron frequency, the radial motion increases. The variation of the radial motion leads to the corresponding variation in the time-of-flight for the ion ejected from the trap onto a ToF detector.

The new PI-ICR method measures the phases of the magnetron and modified cyclotron ion motion, accumulated after a given period of the excitation-free phase evolution which increases the accuracy [Gon14] but also relies on measuring the ToF as in the ToF-ICR method.

The mass resolving power R of the ToF-ICR method for a measurement time t is

$$R = \frac{m}{\Delta m} = \frac{\omega_{\text{cyclo}} t}{2\pi} \quad (3.9)$$

The advantage of Penning traps are high accuracy and resolving power. However, they cannot access the most exotic nuclei with half-lives of sub ms. A measurement time in the order of seconds is required to achieve a very high accuracy.

3.4. Time-of-Flight Spectrometer

The Time-of-Flight (ToF) mass measurements use the relation between the flight time t and the covered distance L determined by a given kinetic energy K . The kinetic energy is determined by an acceleration voltage U .

$$t = \frac{L}{v} = L\sqrt{\frac{m}{2K}} = L\sqrt{\frac{m}{2Uq}} \quad (3.10)$$

Ions with the same kinetic energy K but different mass-to-charge ratios have different velocities v , which causes a separation in time. With known calibrants in a ToF mass spectrometer a calibration curve with the simple correlation $m/q = a_1 \cdot t^2 + a_2$ can be fitted that allows to measure masses for unknown ions and molecules. Figure 3.3 shows the three main parts of a ToF-mass spectrometer. The ions are created and stored in the ion source. A starting pulse opens the ion source and allows the ions to leave into a field free drift space (the analyzer). Here the separation of the different masses happens and in the last stage the time signals are detected by detectors that yield the ToF spectrum for all measured ions.

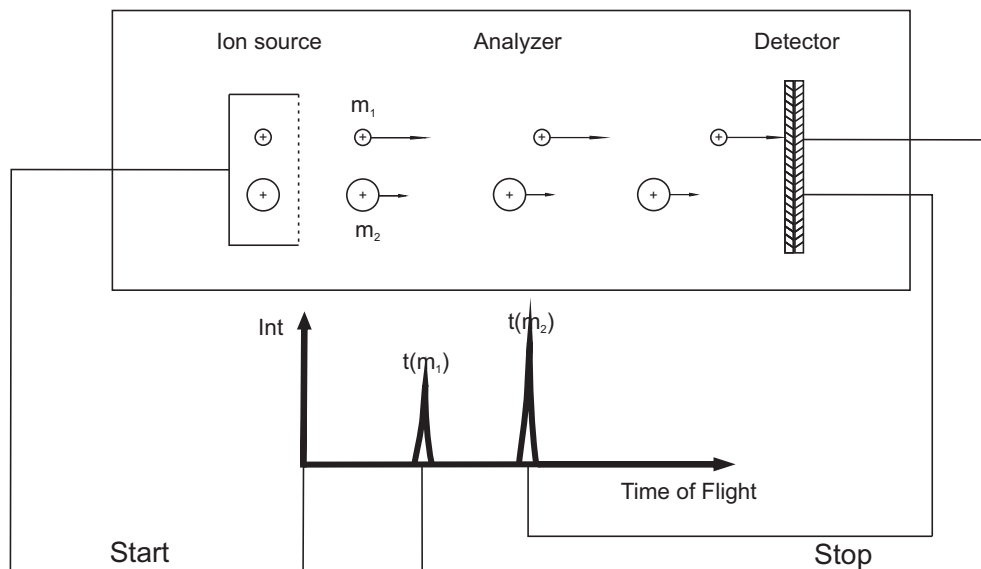


Figure 3.3.: Principle of time-of-flight mass measurements. Ions are produced in an ion source and released with the same kinetic energy into an analyzer where they are separated in time according to their m/q ratio. A detector system records the time of arrival of each ion which leads to a ToF spectrum from which the masses of the ions can be determined.

In measurements the ions can differ in their start position as well as in their start velocity. This leads to a broadening of the measured ToF spectrum for one species and decreases the mass resolving power $R = m/\Delta m$. These influences can be partly compensated by using ion optics that shift the so called time and energy focus onto the detector plane. A simple example of how to compensate is an electrostatic reflector as shown in panel (b) in figure 3.4 that deflects the incoming ions by 180° . Ions with larger kinetic energy penetrate deeper into the reflector, whilst slower ions are reflected faster and leave the reflector earlier. Beside the possibility to shift the time focus of the ions toward the detector, the reflector allows to measure the absolute ToF more precisely as the total flight path also increases. Pushing this principle even further yields the possibility to build a multiple reflection time of flight mass spectrometer (MR-ToF-MS) (panel (c) of figure 3.4) that can prolong the total flight path [Dic06] [Dic10]. With the MR-ToF-MS a mass resolving power of 500,000 (FWHM) can be achieved. Other types of time-of-flight mass spectrometer can also be found in figure 3.4. The mass resolving power R is for a constant flight length L and a constant electrical potential U according to equation 3.10

$$R = \frac{m}{\Delta m} = \frac{t}{2\Delta t} \quad (3.11)$$

A disadvantage of the ToF mass spectrometry is that only pulsed beams can be used.

3.5. Storage Rings

Another method to measure the masses of nuclei by their ToF over a certain distance can also be accomplished in storage rings. Those mass measurements in rings were proposed in 1987 [Wol87c] [WWV87] [FGM87] and later demonstrated in the Experimental Storage Ring (ESR) at GSI [G⁺92a] [R⁺97] [W⁺97]. Two complementary methods to deduce the masses of nuclei by measuring their revolution time in the ring are established. These methods are the Schottky-Mass-Spectrometry (SMS) and the Isochronous Mass Spectrometry (IMS). Whilst different kinetic energies of ions lead to uncertainties in mass measurements via the already presented ToF method in section 3.4 the same holds for different kinetic energies of ions injected into a storage ring.

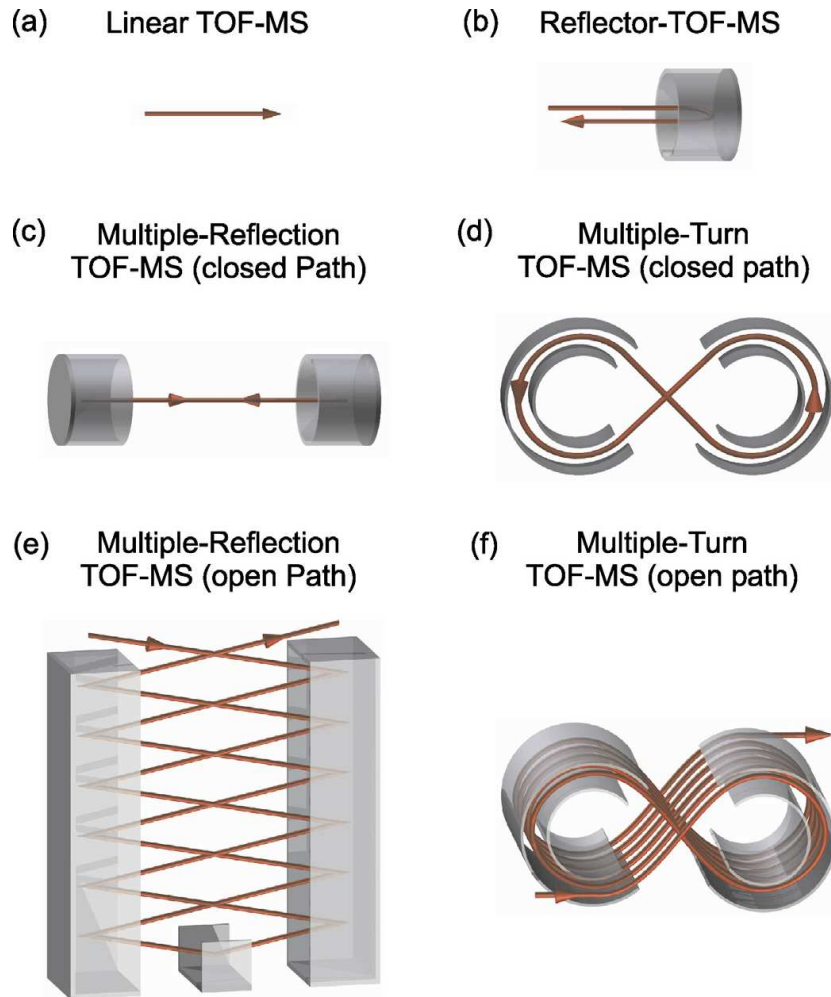


Figure 3.4.: An overview of different time-of-flight mass spectrometers is given in panels (a)-(f). (a) represents the linear, (b) the single reflection, (c) the multiple-reflection with closed path, (d) the multiple-turn with closed path, (e) the multiple-reflection with open path and (f) the multiple-turn with open path types. [P⁺13]

The difference of both methods is the compensation of the velocity spread which adds an additional term to the simple dependence between revolution frequency and mass-to-charge ratio. The SMS method uses stochastic cooling and electron cooling to decrease the velocity contribution of the beam to a relative velocity distribution $\Delta v/v \approx 10^{-7}$. The revolution frequency is measured by non-destructive Schottky-noise pickups [Lit03].

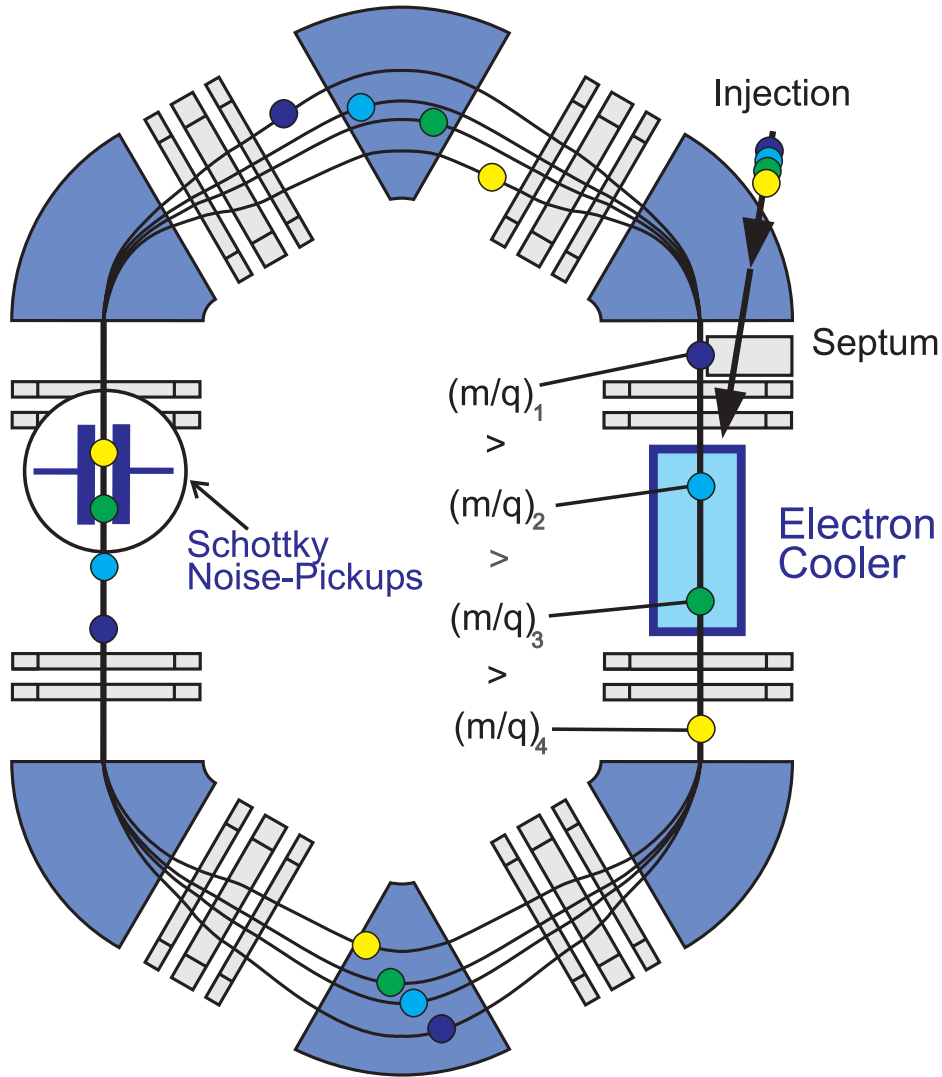


Figure 3.5.: SMS uses stochastic and electron cooling to reduce the relative velocity spread of ions injected into the ESR to $\approx 10^{-7}$. In this way the revolution time of the ions stored in the ring depends only on the m/q ratio and can be used to determine the masses. The revolution frequency is recorded with Schottky-Noise pickups.

Due to the needed beam cooling -which presently lasts a few seconds- the method is limited to nuclei with half-lives of a few seconds as well.

In order to access exotic nuclei with half-lives down to a few tens of μs the IMS method can be used [S⁺10]. In IMS the ring is operated in an ion optical mode that different velocities of ions of the same species are compensated by different path lengths in the ring. This means that faster particles travel longer trajectories and slower particles travel shorter trajectories in such a way that all particles of the same species but different velocities have the same revolution time at one position (time focus). A ToF detector system is placed at that very position to measure the revolution time T of single ions [T⁺92] [Trö93].

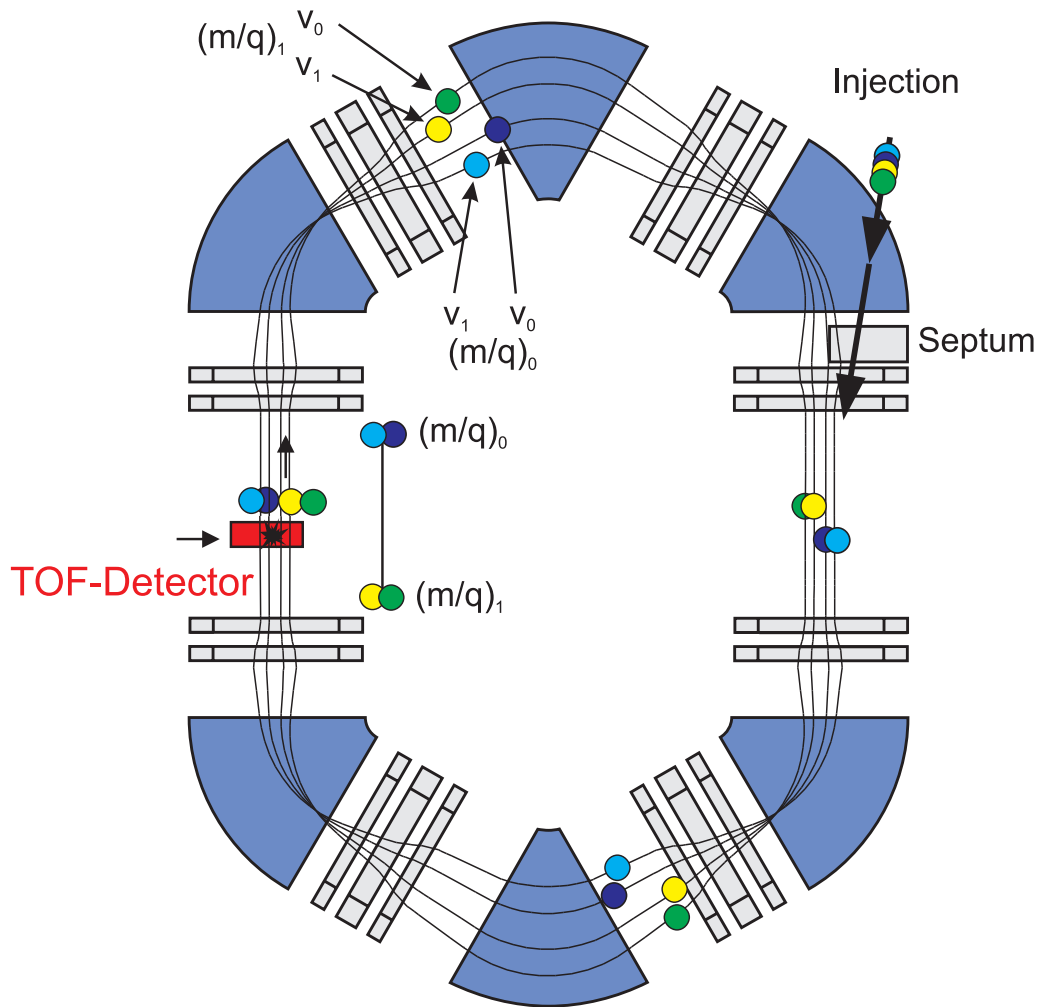


Figure 3.6.: Principle of Isochronous-Mass-Spectrometry (IMS). In IMS the different velocities of the injected ion species are compensated by different trajectories to yield the same revolution time for each m/q . Calculated ion trajectories for two different velocities and two different species are shown. The revolution time is recorded with a Time-of-Flight (ToF) detector.

The mass resolving power of IMS with transition point γ_t (an explanation follows in the next chapter) is

$$R = \frac{m}{\Delta m} = \frac{1}{\gamma_t^2} \frac{T}{\Delta T} \quad (3.12)$$

A more detailed consideration of the motions in storage rings will be given in chapter 4.

4. Isochronous Mass Spectrometry

4.1. Principle of Isochronous Mass Spectrometry (IMS)

The revolution time T of an ion with velocity v in a ring with circumference C is given as

$$T = \frac{C}{v} \quad (4.1)$$

the total differential then is

$$dT = \frac{\delta T}{\delta C}dC + \frac{\delta T}{\delta v}dv = \frac{1}{v}dC - \frac{C}{v^2}dv \quad (4.2)$$

Using equation 4.1 the relative change in revolution time dT/T can be written as

$$\frac{dT}{T} = \frac{1}{vT}dC - \frac{C}{v^2T}dv = \frac{dC}{C} - \frac{dv}{v} \quad (4.3)$$

With this relation one can already see that the revolution time depends on the relative change in circumference (hence the orbit in the ring) as well as on the relative change in velocity. The differences between the flight paths of the reference particle and the non-reference particle will be considered. In terms of accelerator physics the relative change of the orbit in a circular accelerator or storage ring is described with the so called momentum compaction factor α_p [BJ93]. α_p is defined as

$$\alpha_p = \frac{1}{C} \oint \frac{D(s)}{\rho} ds \quad (4.4)$$

with $D(C')$ being the dispersion from the central orbit at position C' and ρ the deflection radius. The dispersion describes the dependency between a shift from the central orbit ρ' relative to its momentum p . Since the momentum of a confined particle in a ring depends on the magnetic rigidity of the central orbit $B\rho$ and its change according to the shift from the orbit, the dispersion can be written as

$$D(s) = \frac{\rho'(s)}{d(B\rho)/(B\rho)} \quad (4.5)$$

Figure 4.1 illustrates that particles with central orbit (ρ) move along the trajectory ds whilst particles with an orbit $\rho + \rho'$ move along a different trajectory $ds + dC'$. The trajectory $ds + dC'$ belongs to the particle with magnetic rigidity of $B\rho + B\rho' = B\rho + d(B\rho)$.

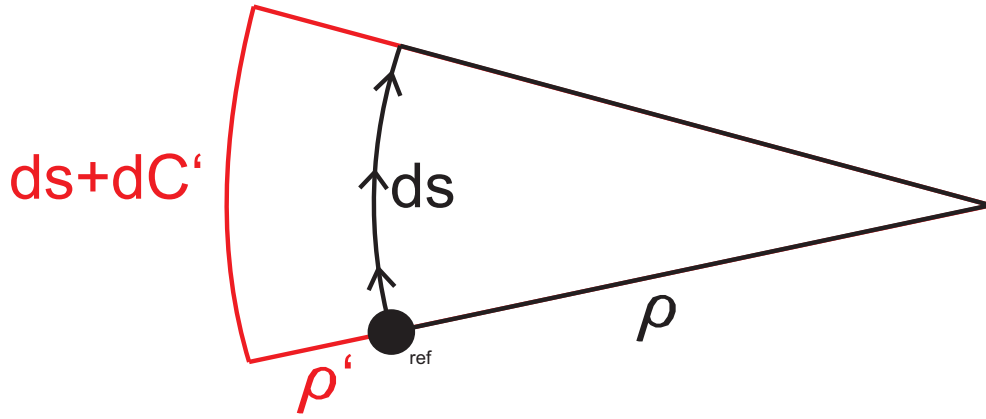


Figure 4.1.: Reference particles with central orbit (ρ) move along the trajectory ds . Particles with orbit $\rho + \rho'$ move along a different trajectory $ds + dC'$. The trajectory $ds + dC'$ corresponds to the particle with a magnetic rigidity of $B\rho + B\rho' = B\rho + d(B\rho)$.

This also means that

$$\frac{\rho}{\rho + \rho'} = \frac{ds}{ds + dC'} \quad \text{and} \quad \frac{\rho}{\rho'} = \frac{ds}{dC'} = \frac{1}{\gamma^2} \quad (4.6)$$

With these relations and knowing that $dC = \oint dL$ is the difference in the full revolution circumference, we can rewrite equation 4.4 into

$$\alpha_p = \frac{1}{C} \oint \frac{\rho'(s)}{d(B\rho)/(B\rho)} \frac{ds}{\rho} = \oint \frac{dC'}{d(B\rho)/(B\rho)} = \frac{dC}{C} \frac{B\rho}{d(B\rho)} = \frac{1}{\gamma^2} \quad (4.7)$$

Going back to equation 4.3 and using equation 4.7 we get

$$\frac{dT}{T} = \alpha_p \frac{d(B\rho)}{B\rho} - \frac{dv}{v} \quad (4.8)$$

In mass measurements the magnetic rigidity is a measure for the mass-to-charge ratio and can be written for a magnetic dipole field in the relativistic case with momentum $p = \gamma mv$ as

$$B\rho = \frac{p}{q} = \frac{\gamma mv}{q} = \frac{m}{q} \gamma \beta c \quad (4.9)$$

With c the speed of light in vacuum, $\beta = v/c$, the relativistic Lorentz factor $\gamma = (1 - \beta^2)^{-1/2}$ and $\gamma\beta = \beta(1 - \beta^2)^{-1/2}$. The total differential of equation 4.9 is

$$d(B\rho) = \frac{\delta(B\rho)}{\delta\left(\frac{m}{q}\right)} d\left(\frac{m}{q}\right) + \frac{\delta(B\rho)}{\delta(\gamma\beta)} d(\gamma\beta) = \gamma\beta c \cdot d\left(\frac{m}{q}\right) + \frac{m}{q} c \cdot d(\gamma\beta) \quad (4.10)$$

Taking again the relative differential and using equation 4.9 yields

$$\frac{d(B\rho)}{B\rho} = \frac{d\left(\frac{m}{q}\right)}{\frac{m}{q}} + \frac{d(\gamma\beta)}{\gamma\beta} \quad (4.11)$$

In a final step the last term $\frac{d(\gamma\beta)}{\gamma\beta}$ will be evaluated.

Taking the total differential

$$d(\gamma\beta) = \frac{\delta(\gamma\beta)}{\delta\beta} d\beta = \left(\frac{1}{\sqrt{1-\beta^2}} + \frac{\beta^2}{(1-\beta^2)^{3/2}} \right) d\beta = (\gamma + \beta^2\gamma^3) d\beta = \gamma(1 + (\gamma\beta)^2) d\beta \quad (4.12)$$

and then using the relative differential

$$\begin{aligned} \frac{d(\gamma\beta)}{(\gamma\beta)} &= (1 + (\gamma\beta)^2) \frac{d\beta}{\beta} = \left(1 + \frac{\beta^2}{1-\beta^2} \right) \frac{d\beta}{\beta} = \left(\frac{1-\beta^2 + \beta^2}{1-\beta^2} \right) \frac{d\beta}{\beta} = \\ &= \left(\frac{1}{1-\beta^2} \right) \frac{d\beta}{\beta} = \gamma^2 \frac{d\beta}{\beta} \end{aligned} \quad (4.13)$$

Combining equation 4.11 with 4.13 one gets

$$\frac{d(B\rho)}{B\rho} = \frac{d\left(\frac{m}{q}\right)}{\frac{m}{q}} + \gamma^2 \frac{d\beta}{\beta} \quad (4.14)$$

Substitution of equation 4.14 in equation 4.8 with $d\beta/\beta = dv/v$ finally yields the dependency between revolution time T and the mass-to-charge ratio m/q

$$\frac{dT}{T} = \alpha_p \left(\frac{d\left(\frac{m}{q}\right)}{\frac{m}{q}} + \gamma^2 \frac{dv}{v} \right) - \frac{dv}{v} = \alpha_p \frac{d\left(\frac{m}{q}\right)}{\frac{m}{q}} + (\alpha_p \gamma^2 - 1) \frac{dv}{v} \quad (4.15)$$

Using the so called transition point $\gamma_t = \frac{1}{\sqrt{\alpha_p}}$ from equation 4.6, equation 4.15 can be written for revolution time T or revolution frequency f as

$$\frac{dT}{T} = -\frac{df}{f} = \frac{1}{\gamma_t^2} \frac{d\left(\frac{m}{q}\right)}{\left(\frac{m}{q}\right)} + \left(\frac{\gamma^2}{\gamma_t^2} - 1 \right) \frac{dv}{v} \quad (4.16)$$

This equation allows it to connect the revolution times of known (reference) and unknown nuclei with their mass-to-charge ratio if the second term in equation 4.16 vanishes. For the Schottky Mass Spectrometry the statistic and electron cooling leads to $dv/v \approx 10^{-7}$, which makes the second term negligible in a first order approximation. For the Isochronous Mass Spectrometry the second term also cancels, however this is not done with cooling but by tuning the ion optical parameter γ_t to be equal to the Lorentz factor γ of one selectable m/q . During the experiments it is more practicable to set the ring to a fixed γ_t and change the energy (and with it their Lorentz factor) of the particles injected into the ring until $\gamma = \gamma_t$ is reached. Together with formula 4.16 the mass resolving power R is given by

$$R = \frac{m}{dm} = \frac{1}{\gamma_t^2} \frac{T}{dT}. \quad (4.17)$$

The isochronous condition is only valid for one single m/q value. Particles with different mass-to-charge ratios are not isochronous and their revolution time is not independent from their velocity therefore the distribution gets broader which decreases the mass accuracy of the method.

This fact is discussed in the publications of Y. Yamaguchi [Y⁺08] and A. Ozawa [O⁺12] and emphasized by the introduction of a velocity dependent factor k . The assumption of a perfect cyclotron with circumference $C = 2\pi\rho$ together with the relativistic ion velocity $v = q/mB\rho/\gamma$ (equation 4.9) yields the revolution time T being:

$$T = \frac{C}{v} = 2\pi \frac{m}{q} \frac{\gamma}{B} \quad (4.18)$$

In case of the isochronous reference particle T_0 , m_0 , q_0 and $\gamma_0 = \gamma_t$ are fixed and known. In order to determine the mass-to-charge ratio of an unknown non isochronous particle (m_1/q_1), it is assumed that the reference particle and the unknown particle have the same $B\rho$, hence the same path length in the ring. With this assumption the ratio between reference revolution time T_0 and measured revolution time T_1 can be written as

$$\frac{T_0}{T_1} = \frac{m_0\gamma_0}{q_0} \frac{q_1}{m_1\gamma_1} \quad (4.19)$$

which can be solved for m_1/q_1 and yields

$$\frac{m_1}{q_1} = \frac{m_0}{q_0} \frac{T_1}{T_0} \frac{\gamma_0}{\gamma_1} \quad (4.20)$$

Because both particles circulate on the same orbit ($B\rho$ is identical for both) one can use

$$\beta_1 T_1 = \beta_0 T_0. \quad (4.21)$$

To evaluate the influence of each single variable on the final measurement of m_1/q_1 the relative differential $\frac{d(m_1/q_1)}{m_1/q_1}$ is derived and is

$$\frac{d(m_1/q_1)}{m_1/q_1} = \frac{d(m_0/q_0)}{m_0/q_0} + \gamma_0^2 \frac{d(T_1/T_0)}{T_1/T_0} + k \frac{d\beta_1}{\beta_1}. \quad (4.22)$$

As stated in [Y⁺08] and [O⁺12] the additional factor k is

$$k = \left(\frac{T_1}{T_0}\right)^2 \frac{\beta_1^2}{1 - (T_1/T_0)^2 \beta_1^2} - \frac{\beta_1^2}{1 - \beta_1^2}. \quad (4.23)$$

It is important to note at that this complicated expression can be further simplified and reduces to

$$k = \left(\frac{T_1}{T_0}\right)^2 \beta_1^2 \gamma_0^2 - \beta_1^2 \gamma_1^2 = \gamma_0^2 + \frac{1}{\beta_1^2 - 1} = \gamma_0^2 - \gamma_1^2, \quad (4.24)$$

which is exactly the expression as in equation 4.16 solved for $d(m/q)/(m/q)$:

$$\frac{d\left(\frac{m}{q}\right)}{\left(\frac{m}{q}\right)} = \gamma_0^2 \frac{dT}{T} + (\gamma_0^2 - \gamma_1^2) \frac{dv}{v} \quad (4.25)$$

Alternatively to the velocity the magnetic rigidity $B\rho$ can be measured as well. Using equation 4.14 equation 4.16 can be written in terms of $B\rho$:

$$\frac{d\left(\frac{m}{q}\right)}{\left(\frac{m}{q}\right)} = \gamma_1^2 \frac{dT}{T} + \left(1 - \frac{\gamma_1^2}{\gamma_0^2}\right) \frac{d(B\rho)}{B\rho} \quad (4.26)$$

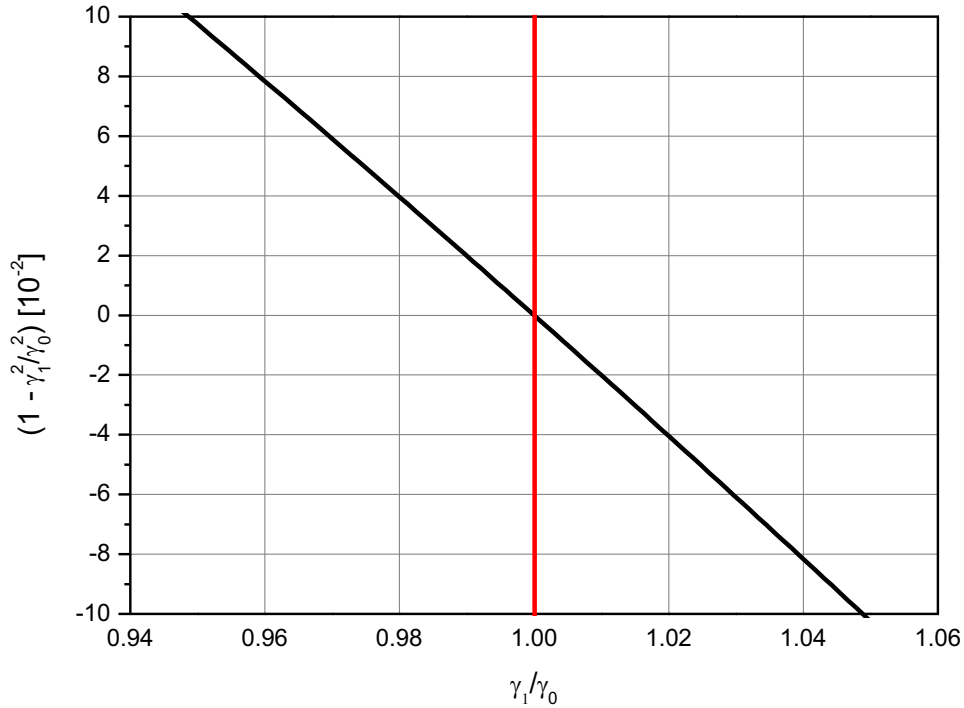


Figure 4.2.: Coefficient $\left(1 - \frac{\gamma_1^2}{\gamma_0^2}\right)$ as a function of the velocity deviation of particles with unknown mass (index 1) and reference particle (index 0).

Both equations (in terms of velocity and in terms of magnetic rigidity) show that for non isochronous particles an additional factor has to be considered. To achieve a mass accuracy of $d(m/q)/(m/q)$ in the order of 10^{-6} , all terms have to be known with the same accuracy or better. The required $B\rho$ accuracy is determined by the term $\left(1 - \frac{\gamma_1^2}{\gamma_0^2}\right)$. As can be seen in figure 4.2, this coefficient is in the order of 10^{-2} for velocity deviations between the unknown particle and the reference particle of $\pm 2\%$. This means that a relative velocity and magnetic rigidity determination in the order of 10^{-4} is needed to correct for this additional term in order to maintain an overall accuracy of 10^{-6} . In experiments without additional velocity and magnetic rigidity determination the mass accuracy will

decrease progressively for m/q ratios different to the m/q value of the reference particle.

To check the isochronicity of the ring in the beginning of an experiment the so called isochronicity curves can be measured by using an electron cooler. By varying the cooler voltage of the electron beam the injected beam in the ring can be varied in energy hence its nominal magnetic rigidity. Scanning the magnetic rigidity and measuring the revolution time for each rigidity results in a isochronicity curve.

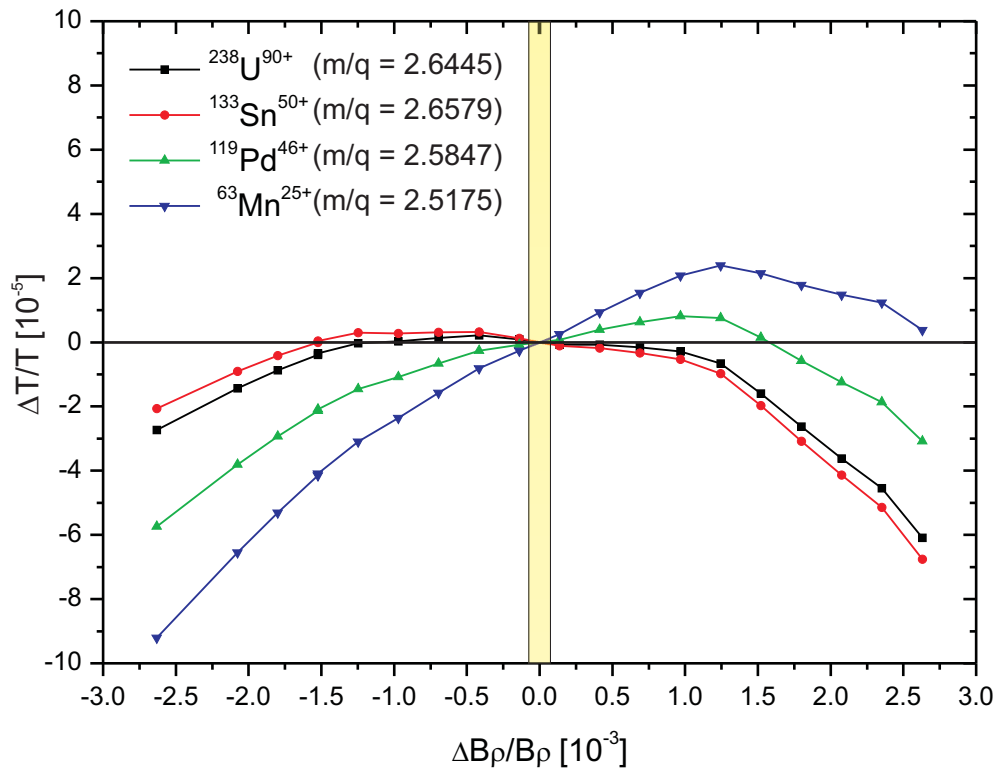


Figure 4.3.: Measured relative deviation in revolution time $\Delta T/T$ versus the relative change in $B\rho$ is shown for different m/q ratios. This isochronicity curve illustrates that the isochronous condition is only well fulfilled for one specific m/q . The same accuracy for very different m/q values can only be achieved by knowing the $B\rho$ for every ion or accepting only a $B\rho$ deviation of $\pm 1.5 \cdot 10^{-4}$ (indicated by the yellow area) into the ring. [G⁺06]

Figure 4.3 shows a measured isochronicity curve for the primary beam $^{238}\text{U}^{90+}$ and transformed isochronicity curves for other mass-to-charge ratios. The transformation is done by assuming again that $B\rho$ is identical for all particles. With this assumption the measured revolution frequency f is directly proportional to the velocity v of the particle. The velocity can also be written in terms of $B\rho$ and m/q :

$$\begin{aligned} \frac{1}{v^2} &= \frac{1 - v^2/c^2 + v^2/c^2}{v^2} = \frac{1 - v^2/c^2}{v^2} + \frac{1}{c^2} = \frac{1}{\gamma^2 v^2} + \frac{1}{c^2} = \\ &= \frac{m^2/q^2}{m^2/q^2} \frac{1}{\gamma^2 v^2} + \frac{1}{c^2} = \frac{m^2/q^2}{B^2 \rho^2} + \frac{1}{c^2} \end{aligned} \quad (4.27)$$

Using $f \propto v$ the transformed frequency can be calculated with

$$\frac{f_{\text{trans}}}{f_{\text{exp}}} = \frac{v_{\text{trans}}}{v_{\text{exp}}} \quad (4.28)$$

The relation between measured frequency f_{exp} and the transformed frequency f_{trans} is then

$$f_{\text{trans}} = f_{\text{exp}} \frac{\sqrt{\left(\frac{(m/q)_{\text{exp}}}{B\rho}\right)^2 + \frac{1}{c^2}}}{\sqrt{\left(\frac{(m/q)_{\text{trans}}}{B\rho}\right)^2 + \frac{1}{c^2}}} \quad (4.29)$$

The ion optical setting can compensate for different magnetic rigidities for one specific m/q ratio and results in a constant time of flight. For nuclei with different mass-to-charge ratios the time of flight deviations start to increase for larger $B\rho$ deviations (hence larger velocity deviations) as predicted in 4.26.

The broadening of the revolution time spectrum for non reference mass-to-charge ratios limits the mass accuracy reachable with the IMS method as shown in equation 4.26. In order to overcome this problem additional $B\rho$ determinations are necessary. One approach to do so was performed for the first time in 2005 by using the so called $B\rho$ -tagging. This tagging method uses geometrical slits at the central high-resolution focal plane in the FRS in order to determine the relative magnetic rigidity of $\Delta B\rho/B\rho \approx 1.5 \cdot 10^{-4}$ [G⁺06]. The improvement gained by this technique is visualized in figure 4.4.

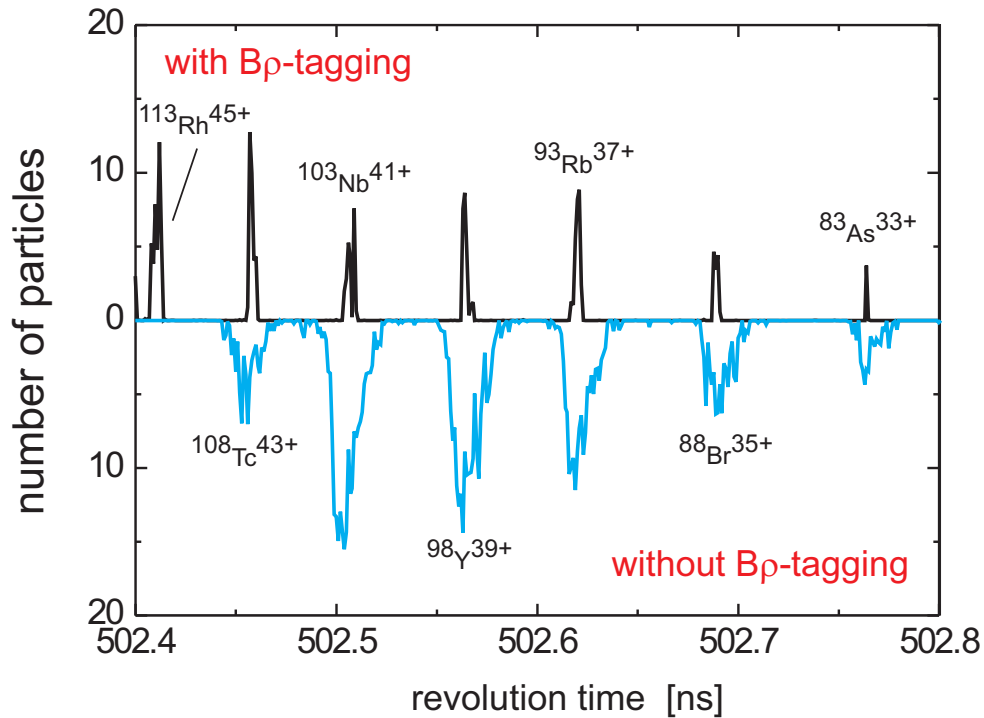


Figure 4.4.: Shown are two measured revolution time spectra for identical isotopes. The upper spectrum (black line) shows the measurements from an experiment performed in 2005 with additional $B\rho$ definition of $\pm 1.5 \cdot 10^{-4}$ ($B\rho$ -tagging). The lower spectrum (blue line) shows the revolution time measurements from an experiment performed in 2002 without any additional $B\rho$ definition. [G⁺06]

A drawback of this technique is the loss of any particle with $\Delta B\rho/B\rho > 1.5 \cdot 10^{-4}$ at the slits which leads to a reduced statistic of the overall experiment.

The second and more elegant way to define the $B\rho$ of each particle would be a dedicated velocity measurement of each particle in addition to its revolution time. This can be done by implementation of a second ToF-detector. Future experiments performed at the Collector Ring (CR) at FAIR aim to implement this and will be discussed in chapter 8.

4.2. The Experimental Storage Ring ESR

The experimental data of this work have been measured at the Experimental Storage Ring (ESR) at GSI. The ring has a circumference of 108.36 m, six large dipole magnets with a maximum magnetic field of 1.6 T, four quadrupole triplets and doublets, and eight sextupole magnets. The ring can be used for different kinds of experiments (e.g. laser spectroscopy or mass measurements in different modes). An electron cooler, which is installed in one of the straight sections of the

ring, allows to match (cool) the velocity of revolving ions via coulomb interactions with electrons with well defined velocities.

In order to apply the IMS the ring has to be set into the isochronous mode which differs from the standard one. In the standard storage mode of the ring the transition point γ_t equals 2.5, which is changed to 1.4 for the isochronous mode by changing the quadrupoles. The ring itself is evacuated to a pressure of approximately 10^{-11} mbar which can only be reached by baking the whole system with temperatures of about $300\text{ }^\circ\text{C}$. The layout of the ESR and the measurement position for IMS is shown in figure 4.5.

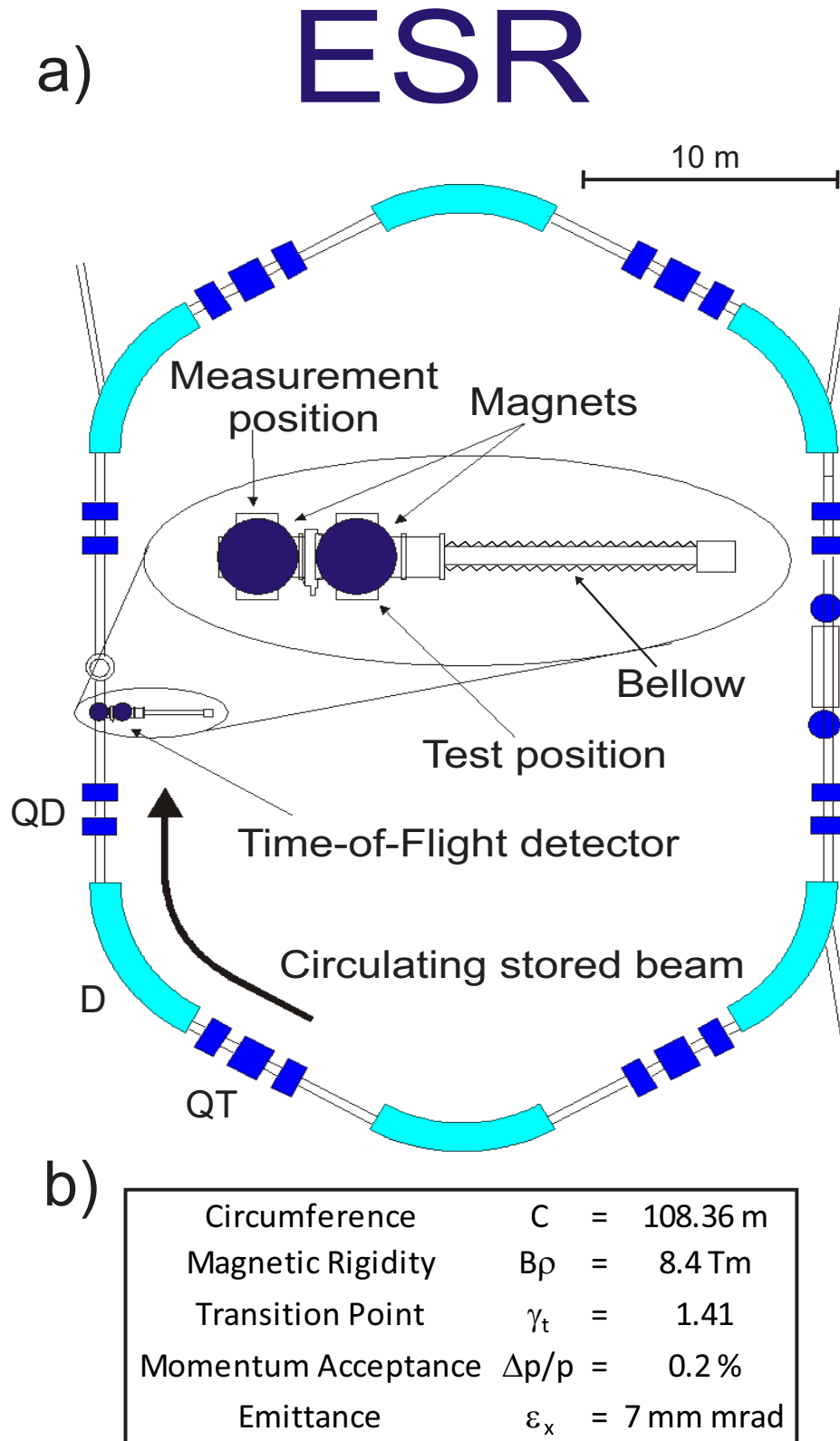


Figure 4.5.: Panel a): The lattice of the ESR including the ToF detector. The dipole magnets (D) are colored in cyan and the quadrupole magnets (duplets QD and triplets QT) are colored in dark blue. The magnets surrounding the ToF detector are Helmholtz magnets. Panel b): The main ring parameters of the ESR.

4.3. Time-of-Flight Detector

With revolution times of about 500 ns in the ring a very fast detection system in the order of tens of picoseconds is needed to measure the revolution time of the particles in the ring. A Time-of-Flight (ToF) detector capable of this requirement was built at the University Gießen in 1993 and continuously improved over the last two decades [Fab08] [Diw09] [Diw11] [Kuz11]. The principle of this detector is similar to the detector designed by J. Bowman and R. Heffner [BH78] and is based on a thin foil inside the beamline surrounded by an arrangement of electric and magnetic fields. When heavy relativistic ions (as stored in the ESR) pass through the foil, they create secondary electrons (SEs) which are detected. For one turn the energy loss for ^{238}U is approximately 250 keV. However, after a few hundred turns (depending on the foil thickness) the total energy loss of the ions is too large; they can no longer be stored and are lost. The position of the detector in the ring is placed at the time focus at which the ions are isochronous. In case of the ESR this is at the straight section opposite to the injection section.

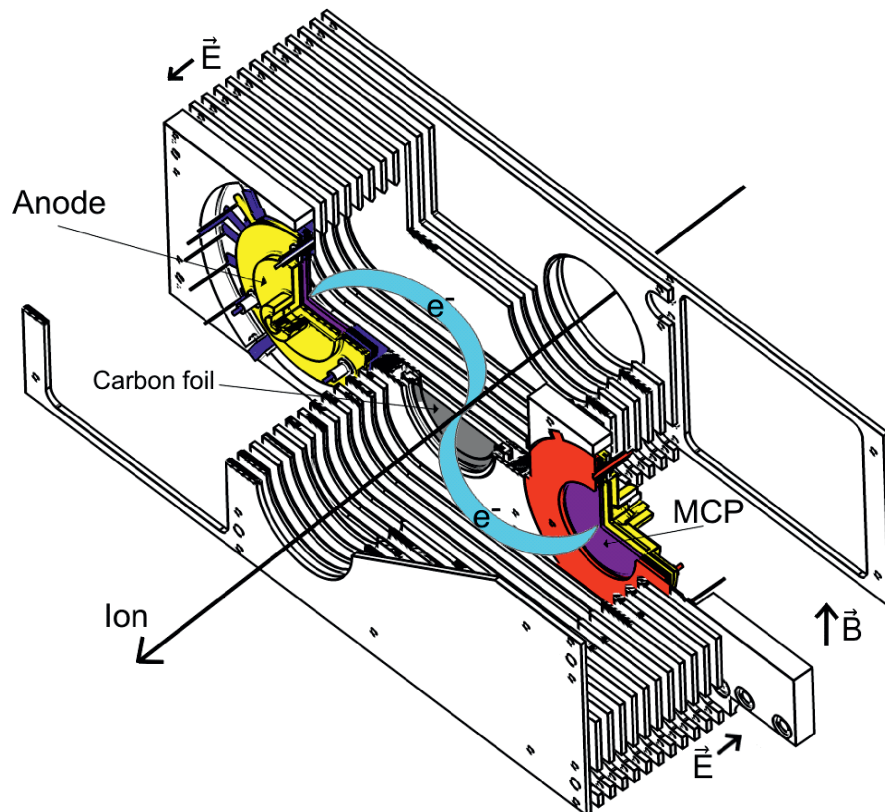


Figure 4.6.: Schematic drawing of the ESR-ToF-detector. A thin foil in the center of the detector is used to provide secondary electrons each time an ion passes through. The electrons are then guided by electrical and magnetic fields in forward and backward direction to the Micro-Channel-Plate (MCP) detectors.

In order to detect the created secondary electrons electrical fields along the beam

axis and magnetic fields perpendicular to the beam axis transport the electrons isochronously to Micro-Channel-Plate (MCP) detectors positioned in forward and backward beam direction parallel to the foil. Figure 4.6 illustrates the principle of the ToF detector and its electrodes to shape the fields as it is used at GSI. A duplicated detector at University Gießen allows faster and easier tests and improvements on the detector that are then implemented at the detector at GSI.

4.3.1. Secondary Electron Creation

The ToF detector used in the IMS experiments, is capable to detect the ions in the ring because of secondary electrons (SEs) that are emitted from a thin carbon foil placed in the center of the detector. Creating those SEs is not a trivial issue and has been investigated for a long time. The theory of ion induced secondary electron emission can be separated into two processes:

When ions penetrate through matter, they create via inelastic collisions fast δ -electrons and slow "real" secondary electrons along their way [HGK98]. The interaction of relativistic ions with charge number Z , energy E and velocity v with matter can be described by the Bethe formula [Bet32]

$$-\frac{dE}{dx} = \frac{4\pi N z Z^2}{m_e c^2 \beta} \cdot \left(\frac{e^2}{4\pi\epsilon_0} \right) \cdot \left[\ln \left(\frac{2m_e c^2 \beta^2}{I \cdot (1 - \beta^2)} \right) - \beta^2 \right] \quad (4.30)$$

dE/dx is the energy loss per path length (stopping power), N is the number of atoms in the material with charge number z , m_e is the electron mass, c the velocity of light, $\beta = v/c$, ϵ_0 the vacuum permittivity and I the mean excitation potential of the matter. Equation 4.30 is only a first-order Born approximation and systematically deviates for relativistic ions from the measured energy loss [S+94]. One has to correct for these systematic deviations by using additional correction terms in order to describe the experimental observations. Formula 4.30 can be rewritten

$$-\frac{dE}{dx} = \frac{4\pi N z Z^2}{m_e c^2 \beta} \cdot \left(\frac{e^2}{4\pi\epsilon_0} \right) \cdot L \quad (4.31)$$

where $L = \left[\ln \left(\frac{2m_e c^2 \beta^2}{I \cdot (1 - \beta^2)} \right) - \beta^2 \right]$ for the Bethe-Formula. The Bethe-Formula is only valid in first Born approximation which is not applicable for heavy ions. To account for relativistic effects, L becomes a superposition of multiple correction terms:

$$L = L_{\text{Bethe}} + \delta L_{\text{shell}} + \delta L_{\text{density}} + \delta L_{\text{Barkas}} + \delta L_{\text{LS}} + \delta L_{\text{screen}} \quad (4.32)$$

The correction terms δL_{shell} , $\delta L_{\text{density}}$, δL_{Barkas} , δL_{LS} , and δL_{screen} are correct for involved shell effects, for the Fermi-density effect [Fer40], for the Barkas-effect [B+63], for the Lindhard and Sørensen expansion and for the screening effect respectively. A more detailed explanation of each correction term can be found in [SG98].

Released SEs diffuse through the material to the surface and (if they are energetic enough) overcome the surface barrier into the vacuum [Ste57].

True SEs are those with a kinetic energy between 0 and 50 eV [DD96] and represent the majority in the overall SE spectrum. Because of their low kinetic energies and low mass, SE's are ideal detection particles in the ToF detector since moderate electrical (few kV/cm) and magnetic fields (few tens of mT) are sufficient to guide them from their creation point to the MCP detectors without disturbing the trajectories of the heavy and high energetic ions in the ring. The shape of the secondary electron spectra depends on the target material, the projectile species and projectile energy [H⁺86]. A lot of measurements of secondary electron yields after interaction of ions or protons with thin foils have been performed [H⁺86] [R⁺90] [DD96].

A total electron spectrum is presented in figure 4.7. It shows besides the true SE's also the other contributions to the spectrum that are not considered and used in the IMS experiments. Electrons with larger energies cannot be detected by the ToF detector.

Simulations of the ToF detector consider this spectrum and use a homogenous Maxwellian velocity distribution with a most probable knockout energy of 1.8 eV. A more detailed description on how the amount of created secondary electrons depends on the foil material can be found in [R⁺95] and is discussed in terms of IMS in [Fab08] and [Kuz11].

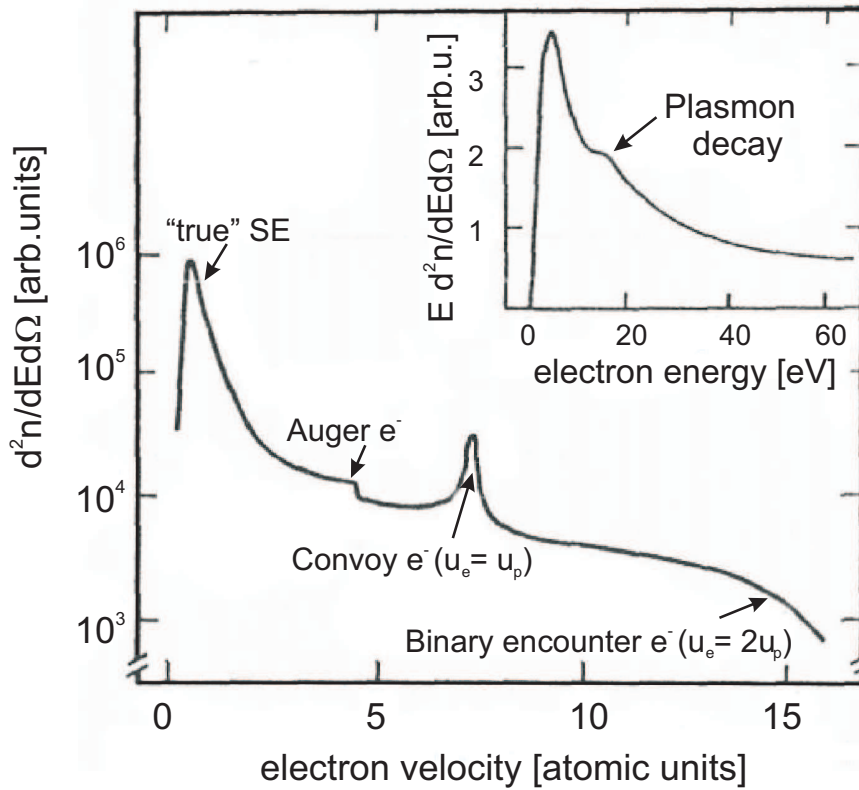


Figure 4.7.: Secondary electron yields produced with 1.2 MeV protons in carbon target with a thickness of 1500 Å under 0° emission angle versus the electron velocity are shown in the large graph. The secondary electron yield versus the electron energy is shown in the graph in the upper right corner. The slow secondary electrons ("true" SE's) are detected by the ToF detector.[HGK98]

4.3.2. Motion of Charged Particles in E-Fields and B-Fields

The transport of the created SE from the foil surface to the MCPs is achieved by electrical and magnetic fields aligned perpendicular to each other. Figure 4.8 illustrates the geometry of the detector used as well as the orientation of the fields. The force created by an electric field \vec{E} and a magnetic field \vec{B} on a charged particle with charge q is given as

$$m\vec{a} = q \left(\vec{E} + \vec{v} \times \vec{B} \right), \quad (4.33)$$

which can also be written as

$$m \frac{d^2 \vec{r}}{dt^2} = q \left(\vec{E} + \frac{d\vec{r}}{dt} \times \vec{B} \right) \quad (4.34)$$

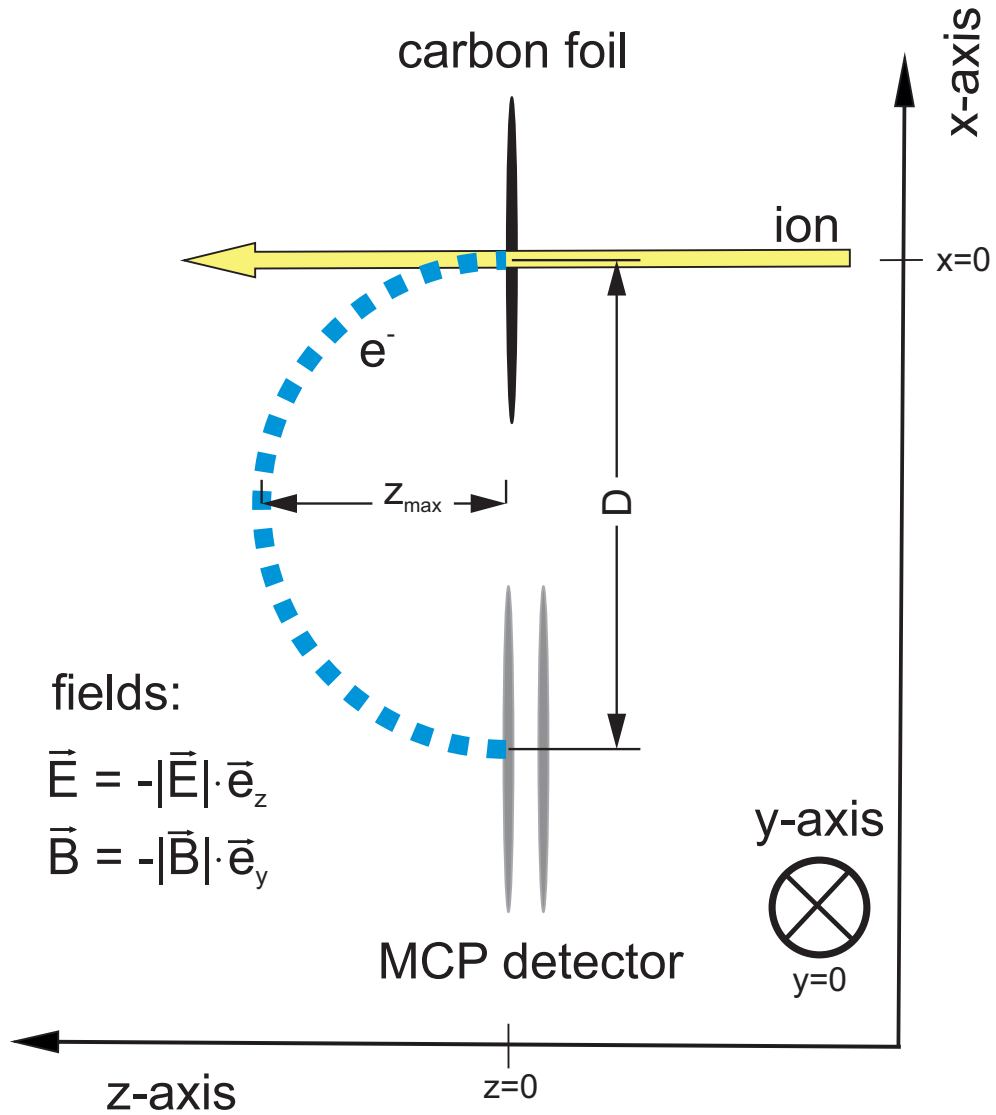


Figure 4.8.: The electron transport from the foil ($\vec{r}(0) = (0, 0, 0)$) to the MCP detectors ($\vec{r}(T) = (D, 0, 0)$) is shown. The electrical field \vec{E} and the magnetic field \vec{B} force the electron on a cycloidal path with cycle duration $T = 2\pi m/(qB)$.

Transforming this into Cartesian coordinates yields the general equation system

$$m \frac{d^2 x}{dt^2} = q \left(E_x + \frac{dy}{dt} B_z - \frac{dz}{dt} B_y \right) \quad (4.35)$$

$$m \frac{d^2 y}{dt^2} = q \left(E_y + \frac{dz}{dt} B_x - \frac{dx}{dt} B_z \right) \quad (4.36)$$

$$m \frac{d^2 z}{dt^2} = q \left(E_z + \frac{dx}{dt} B_y - \frac{dy}{dt} B_x \right) \quad (4.37)$$

Taking the direction of the electrical field $\vec{E} = -|\vec{E}| \cdot \vec{e}_z$ and magnetic field $\vec{B} = -|\vec{B}| \cdot \vec{e}_y$ simplifies this to

$$m \frac{d^2x}{dt^2} = q \frac{dz}{dt} B \quad (4.38)$$

$$m \frac{d^2y}{dt^2} = 0 \quad (4.39)$$

$$m \frac{d^2z}{dt^2} = -q \left(\frac{dx}{dt} B + E \right) \quad (4.40)$$

The solution of this coupled differential equations of second order is [BH78]

$$x(t) = \frac{v_x(0) + E/B}{\omega} \sin(\omega t) - \frac{E}{B} t + \frac{v_z(0)}{\omega} (\cos(\omega t) - 1) + x(0) \quad (4.41)$$

$$y(t) = v_y(0)t + y(0) \quad (4.42)$$

$$z(t) = \frac{v_x(0) + E/B}{\omega} (\cos(\omega t) - 1) - \frac{v_z(0)}{\omega} \sin(\omega t) + z(0) \quad (4.43)$$

with the starting position $\vec{r}_0 = (x(0), y(0), z(0))$ and

velocity $\vec{v}_0 = (v_x(0), v_y(0), v_z(0))$ of the electrons starting from the foil, and the cyclotron frequency $\omega = qB/m$.

The total motion of the electrons is a cycloidal path with a cycle duration of $T = 2\pi/\omega$. This means the time needed for one full cycle is T ($z(0)=z(T)$) and the lateral (x-direction) distance D covered is

$$D = x(T) - x(0) = x(0) - \frac{2\pi E}{\omega B} - x(0) = \frac{2\pi E m_e}{B^2 q} = \frac{2\pi E m_e}{B^2 e} \quad (4.44)$$

The maximum distance covered in z direction z_{\max} is then given by

$$z_{\max} = z(T/2) - z(0) = z(0) - \frac{2(v_x(0) + E/B)}{\omega} - z(0) = \frac{(v_x(0) + E/B)2m_e}{Be} \quad (4.45)$$

For a distance of 79 mm between the center of the carbon foil and the center of MCP a ratio E/B of $1.85 \cdot 10^7$ m/s is needed to detect the electrons. The transport time T for a given magnetic field of typically 8.41 mT (as used in the ESR) is approximately 4.248 ns with a maximum distance in z-direction $z_{\max} = 26$ mm. The timing fluctuations dT can be approximated with the relative differential and using $v = D\omega$

$$\frac{dT}{T} = \frac{dv}{v} = \frac{v(0)}{D\omega} = \frac{v(0)}{2\pi E/B}$$

which yields after multiplication with $T = 2\pi/\omega$

$$dT = \frac{1}{\omega} \frac{v(0)}{(E/B)} = \frac{m v(0)}{q E} = 2\pi \left(\frac{m}{q} \right)^2 \frac{v(0)}{B^2 \cdot D} \quad (4.46)$$

Together with the needed electric field E of 156 V/mm and a most probable electron starting kinetic energy of 1.8 eV the timing fluctuation is approximately $dT = 29$ ps. The calculated trajectories for electrons ($q = -e$) with start velocity 1.8 eV and 0 eV are plotted in figure 4.9.

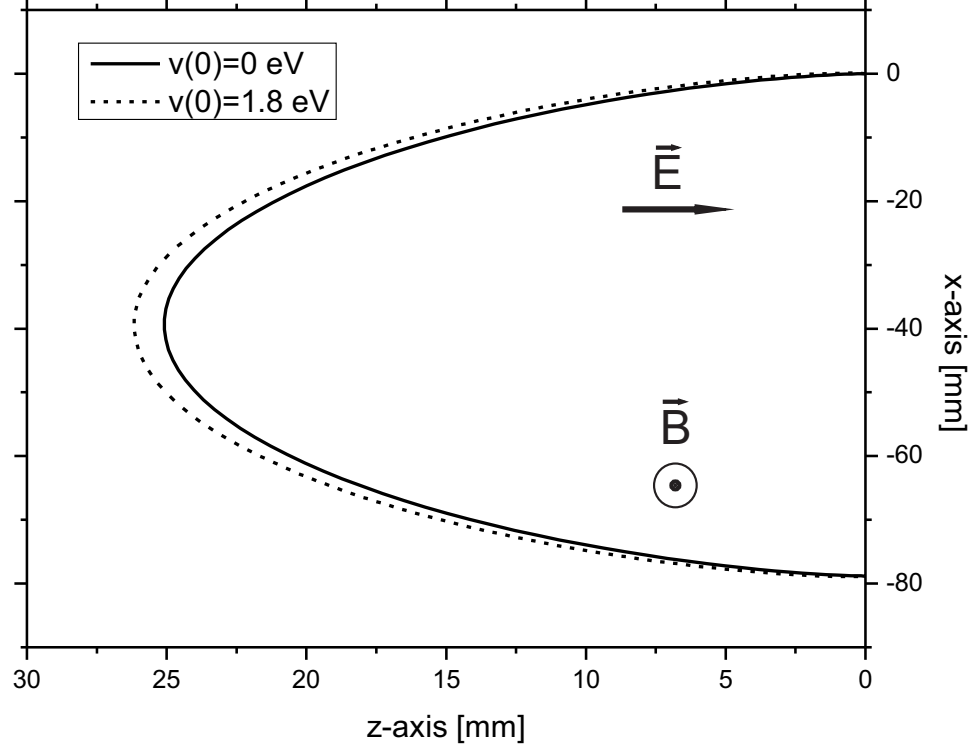


Figure 4.9.: Calculated trajectories of electrons in the x-z plane for two different starting velocities $v(0)$. $E = 156$ V/mm and $B = 8.41$ mT were used for the calculation.

At this point the influence of changing the geometry of such a detector, which will be necessary for the future ToF detector at FAIR (see also chapter 8), will be discussed. Assuming the whole geometry is scaled by a factor S , this also scales the distance D from foil to MCP. Besides the lateral distance D the distance d between the electrodes will change, too. This means that for the same applied voltages the electric field strength $E = U/d$ changes with $1/S$. Increasing the applied potentials is not a trivial issue but would be necessary to compensate for larger geometries. In case one has to use the same potentials for all geometries, the scaled magnetic field can then be calculated using 4.44:

$$B_{\text{scaled}} = \sqrt{\frac{2\pi m_e E_{\text{scaled}}}{q D_{\text{scaled}}}} = \sqrt{\frac{2\pi m_e E_{\text{original}}}{q S^2 D_{\text{original}}}} = \frac{1}{S} B_{\text{original}} \quad (4.47)$$

Equation 4.46 then becomes

$$dT_{\text{scaled}} = 2\pi \left(\frac{m}{q}\right)^2 \frac{v(0)}{B_{\text{scaled}}^2 D_{\text{scaled}}} = 2\pi \left(\frac{m}{q}\right)^2 \frac{Sv(0)}{B_{\text{original}}^2 D_{\text{original}}} = SdT_{\text{original}} \quad (4.48)$$

which shows that the detector uncertainty is directly proportional to the scaling factor S . To be able to keep the timing fluctuations of the original geometry, one has to guarantee that the electrical field strength after scaling is the same as in the original geometry.

The last step of the detection in the ToF detector is the micro-channel-plate detector which amplifies the incoming secondary electrons by a factor up to 10^6 the total ToF spectrum is then recorded with a digital oscilloscope. In order to achieve a maximum detection efficiency of the MCP detectors for single electrons the kinetic energy of the electron has to be at least 300 eV and saturates between 300 eV and 1000 eV [Wiz79] [BC79].

For the above mentioned principle the impact energy of the electrons at the MCPs is $v_z(0)$, which is only in the order of 1-2 eV. Two options can be used to still be able to detect the electrons. The first option is a slight displacement of the MCP detector towards the electron trajectory (in our example in positive z-direction), but this leads to a non isochronous impact for different start positions. The second option is to apply a more negative voltage to the foil than to the MCP detector. The average kinetic energy with which the electrons hit the MCPs is then given by the potential difference between foil and MCP detector. These both options can be used together and are realized in the ToF detector.

4.3.3. Timestamp Determination

The determination of a time stamp for each ion circulating in the ring is the result of the detection of the secondary electrons hitting the MCP detectors. An electron that hits the inside of a MCP tube with at least 300 eV causes an avalanche of many electrons throughout the tube like a many-dynode system does in a photomultiplier tube (PMT). The difference is that MCP channels are continuous dynodes with an outer gradient field that allows the MCP to be very thin in comparison to a normal PMT. One plate is capable of amplifying by a factor of $10^3 - 10^4$. By adding a second MCP after the first this factor can be increased up to 10^6 . To ensure that no electron can pass both MCPs without hitting the walls the channels have a skew angle of about 10° and both plates are turned 180° in respect to each other. This configuration is called Chevron-configuration and represents a standard configuration for MCP detectors.

The fast MCP signals are recorded with a digital oscilloscope. The MCP signals and parameters of the digital oscilloscope are crucial for the quality of the timestamp determination. Important parameters for the oscilloscope are the bandwidth, which should be at least 1 GHz for the fast MCP signals of approximately 1 ns signal width, the sampling rate, which should be as large as possible to

sample the signals with enough points, the vertical resolution (8-bit is standard) and a large and fast memory to record spectra over several μs .

Besides these technical parameters of the oscilloscope other uncertainties in determining the time out of signals arise from the signal itself. One can distinguish between three main contributions that add up in uncertainties for the time determination (see also figure 4.10):

- signal noise
- rise-time walk
- amplitude walk

The signal noise cause different time stamps for two identical signals due to signal noise fluctuations. These fluctuations mainly originate from thermal instabilities (thermal noise) that can only be reduced by cooling the whole system. Compared to the two other effects the signal noise can be neglected.

Two signals with the same trigger level, the same amplitude and the same starting time, but different rise times result in different time stamps because of the so called rise time walk effect. This effect can be minimized by very fast rise times in general or by ensuring that all signals have the same rise time.

The last and in our case main effect is the so called amplitude walk effect that leads to different time stamps for signals with the same rise time but different amplitudes.

Using a simple threshold determination of signals with varying rise times and fluctuating amplitudes result in different timestamps, even if the signals start at the same time. A more sophisticated way to determine the timestamps of such signals is the constant fraction discrimination (CFD). The principle is shown in figure 4.11. In the CFD method the measured signal is split into two signals. One of the two signals is delayed by a certain time whilst the second signal is attenuated and inverted. Summing up the two signals results in a new signal which (in case the delay and attenuation was done properly) crosses the baseline (zero crossing). The time at which the resulting signal crosses the baseline is then the determined timestamp. This method can be applied directly to the measured signals or after recording the signals via software and is capable of canceling the rise-time walk as well as the amplitude walk.

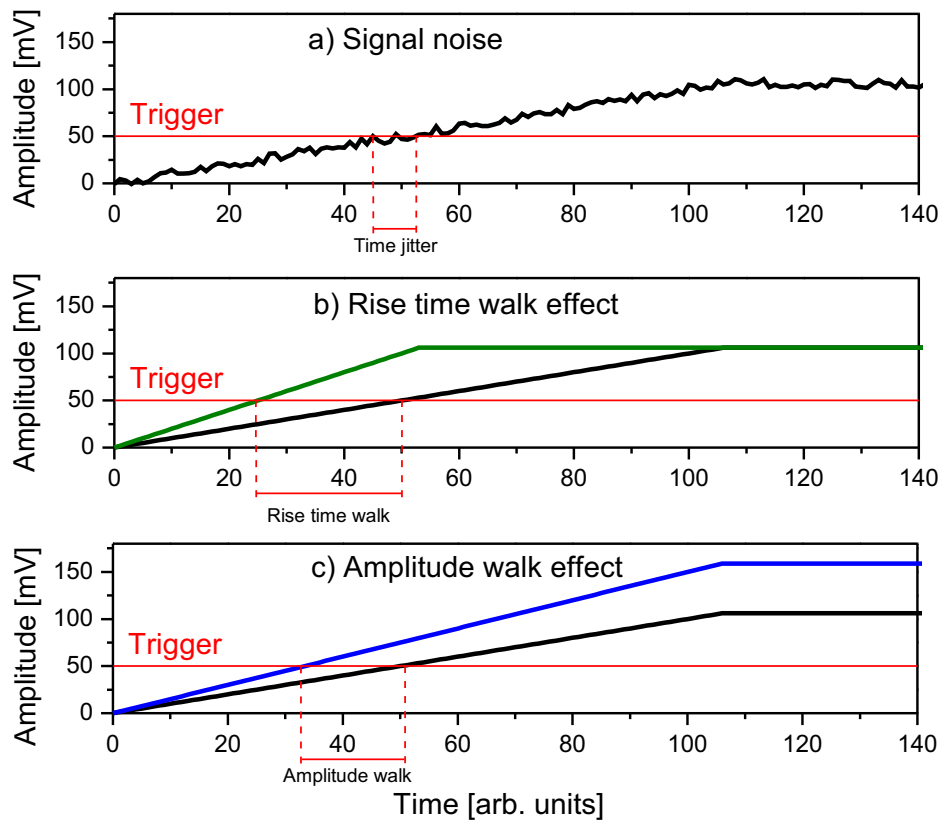


Figure 4.10.: Panel a): The fluctuations of the signal noise induce a time jitter that adds an uncertainty to the determination of the timestamp. Panel b): Two signals with the same trigger level, same amplitude and same starting time but different rise times yield different time stamps due to the so called rise time walk effect. Panel c): Two signals with the same trigger level, same rise time and same starting time but different amplitudes result in different time stamps because of the amplitude walk effect.

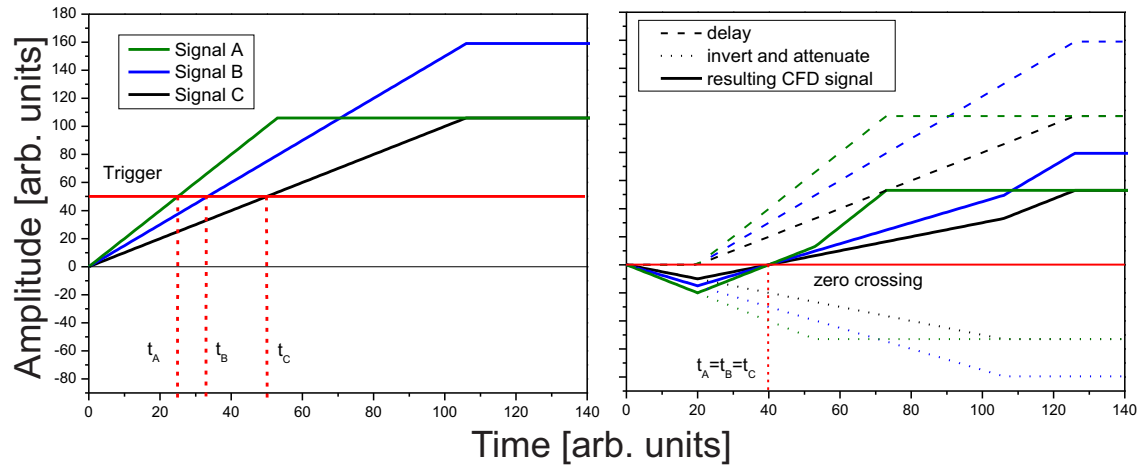


Figure 4.11.: Left hand side: The amplitudes of three Signals (A-C) with the same starting time but different rise times and different amplitudes against the time. The trigger level (red horizontal line) indicates the timestamps determined by the given threshold. Right hand side: The amplitudes of the delayed (dashed lines), inverted and attenuated (dotted lines) and the resulting CFD signal (solid lines) for three different signals against the time. The zero crossing (red horizontal line) determines the timestamp in the CFD method. One can see that with this CFD method the time walk can be canceled for different rise-times and amplitudes.

5. The ESR ToF Detector

5.1. Modifications and Improvements

5.1.1. Efficiency of the ToF Detector

Many modifications and improvements of the ESR-ToF detector were performed and achieved since the first installation and use of a ToF detector in the isochronous mode in the ESR in 1993 [T⁺92] [Trö93]. Ion or electron trajectories in electromagnetic fields can be simulated using 3D simulation programs like COMSOL [COM08] or SIMION [MD07]. In order to optimize the transport efficiency of the ToF detector simulations for the existing geometry of the ToF detector have been performed and a new combination of electric and magnetic fields was found to increase the transport efficiency from 38% to 83% [Fab08]. The non-optimized and optimized voltage settings are shown in table 5.1. A laser was used to measure the transport efficiency in dependence of the start position on the foil to verify the simulations [Kuz11]. The results are shown in figure 5.1.

Table 5.1.: Electric and magnetic field strengths for the initial and optimized detector settings.

| | initial | optimized |
|--|----------|-----------|
| MCP potential | -2,700 V | -2,700 V |
| Foil potential | -3,400 V | -3,400 V |
| Largest negative electrode potential U^- | -2,000 V | -2,700 V |
| Largest positive electrode potential U^+ | 5,200 V | 5,000 V |
| E-field | 144 V/mm | 154 V/mm |
| B-field | 7.9 mT | 8.4 mT |

5.1.2. Timing properties of the ToF Detector

Besides the transport efficiency, the timing performance for different start positions on the foil were measured too [Lip11]. For the time measurements alpha particles were used to release SE from the foil. The MCP signals of the detector

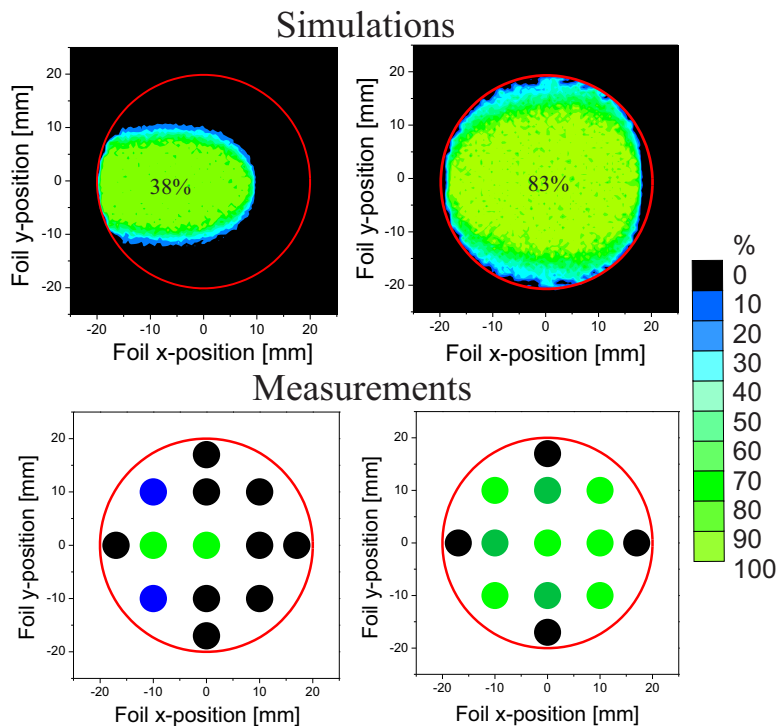


Figure 5.1.: Simulations (top) and measurements (bottom) of the transport efficiency of the secondary electrons (SE) for different start position on the foil for initial (left) and optimized voltage settings (right). [Fab08] [Kuz11]

in forward and backward direction were analyzed in coincidence with the alpha particles hitting a Si-detector. A movable aperture was placed in front of the Si-detector and varied for different positions to achieve a position resolved measurement. The measurements showed that ions hitting the outer area of the foil have a slightly larger timing spread (rms) than ions hitting the center of the foil (figure 5.2). However, this is in line with new and more detailed simulations for the support structure of the foil. This observation is caused by electric field inhomogeneities at the edge of the foil.

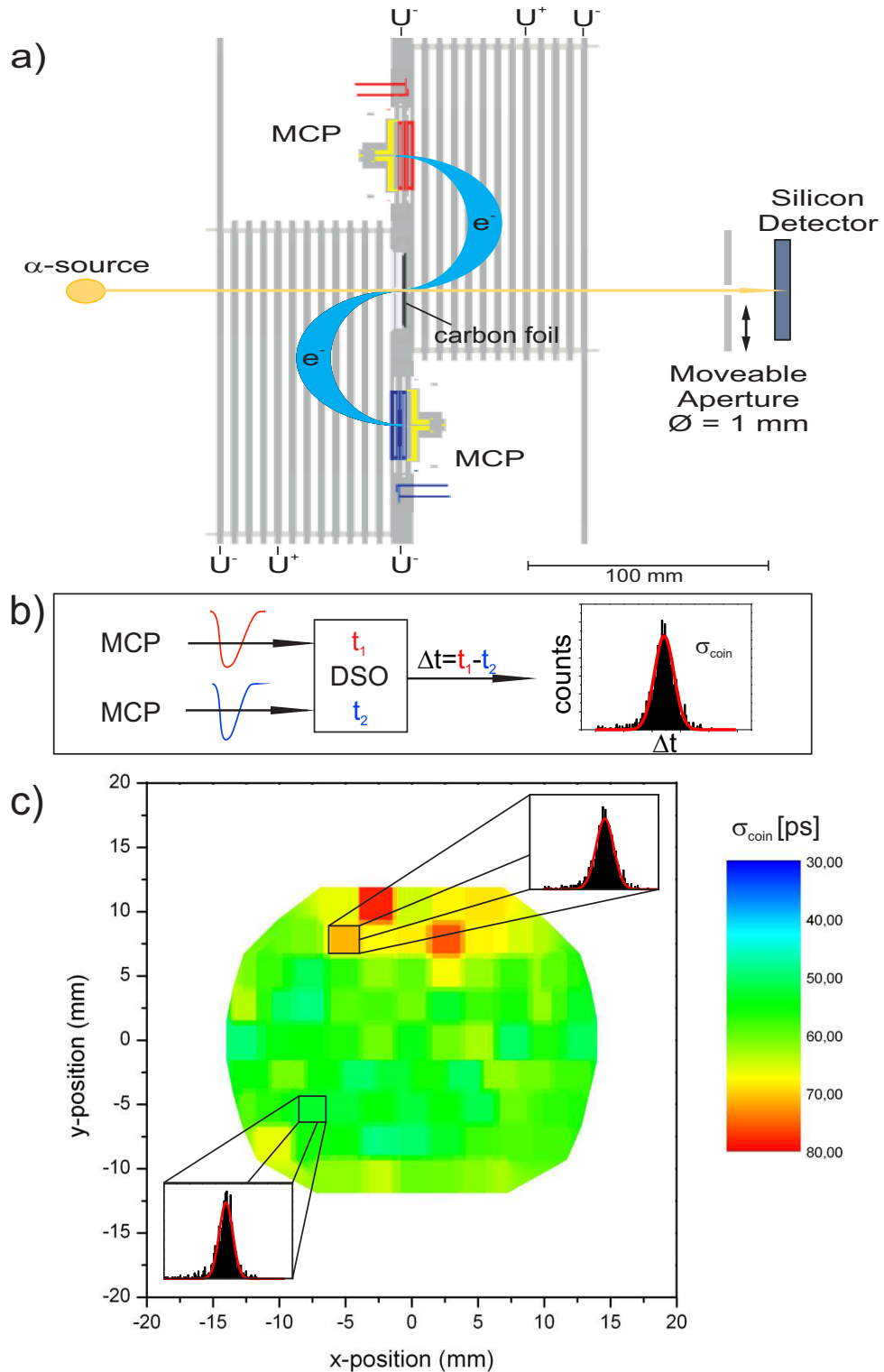


Figure 5.2.: Panel a): Setup used for position-resolved time measurements. 5.5 MeV alpha particles release SE from the foil and are detected by a silicon detector. A moveable aperture in front of the silicon detector yields the position information where the alpha particle passed the foil. Time measurements of the ToF detector in coincidence with the alpha particle allowed a distinction between different start positions on the foil. Panel b): Schematic illustration of the determination of σ_{coin} from the time difference between two MCP signals. Panel c): Results of the position-resolved time measurements. For each measured position the determined standard deviation of the time spectrum σ_{coin} is plotted.

Larger field strengths, to reduce the time spread, have been applied to the detector to increase the kinetic transport energy of the SE from foil to MCP detector. Simulations of the electron transport showed already an improvement of the time spread with increasing transport energies. The duplicate of the detector, operated in Gießen, was upgraded to be able to be used up to 20 kV. The measurements confirmed the simulations. Since the simulations could not account for all contributions that are present in experiments a constant offset of 25 ps (sigma) for additional contributions (e.g. transit time spread of the MCPs or the uncertainty of the event time determination) was experimentally determined and added independently to the simulation. The measured time distribution is in very good agreement with the simulations [Diw11]. The results are presented in figure 5.3.

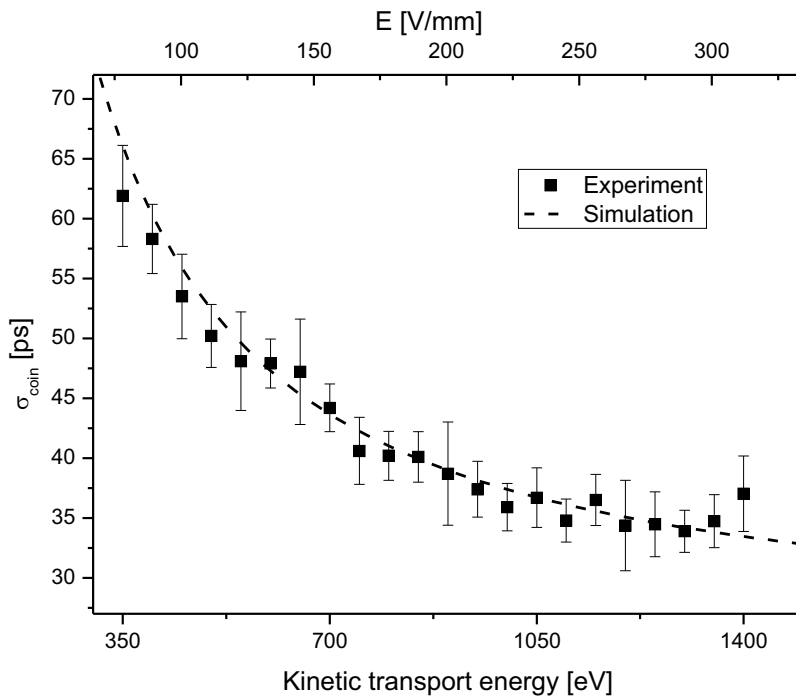


Figure 5.3.: Measured and simulated time spread σ_{coin} as a function of the kinetic energy of the secondary electrons (lower axis) versus and the corresponding electrical field strength (upper axis) [Diw11].

The capability to measure many ions over a large number of turns in the ring is also essential for accurate mass measurements. Two changes from the original design have been made in order to achieve this. Firstly, the foil thickness was changed from $17 \mu\text{g}/\text{cm}^2$ carbon foils coated on both sides with $10 \mu\text{g}/\text{cm}^2$ CsI down to $10 \mu\text{g}/\text{cm}^2$ carbon foils without any coating. The reduction in foil thickness and omitting the additional coating decreases the amount of emitted SE per ion but decreases also the energy loss per turn for each ion [Kuz11]. The latter influence is superior for accurate measurements.

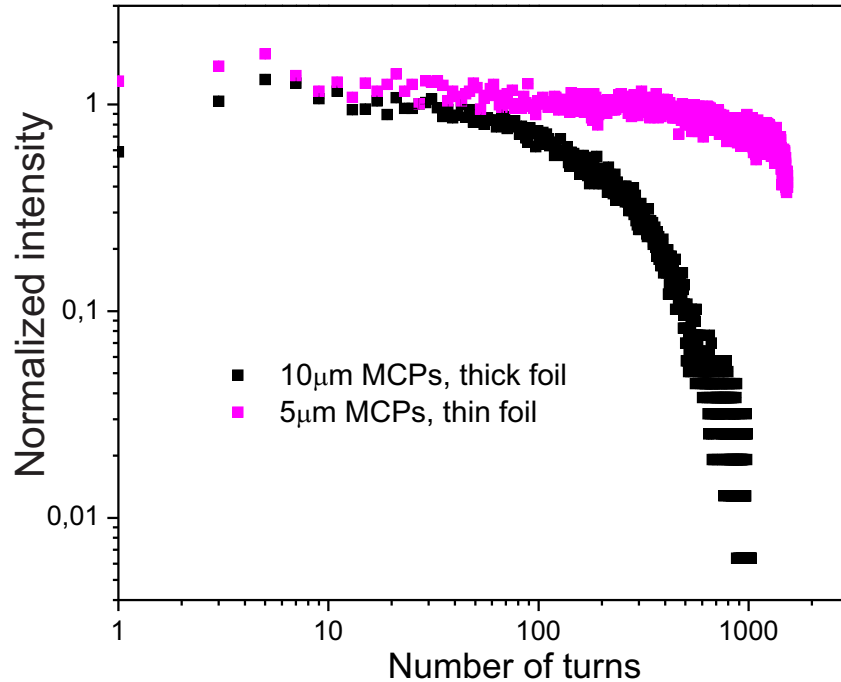


Figure 5.4.: Comparison of different experiments with uranium fission fragments at energies at the transition point $\gamma_t = 1.41$. Shown is the normalized intensity versus the achieved number of turns in the ring. The colors indicate the different foil thicknesses (thick: [10CsI:17C:10CsI] $\mu\text{g}/\text{cm}^2$, and thin: (10 $\mu\text{g}/\text{cm}^2$) carbon foil) and pore sizes of the used MCPs.[Kuz11]

Secondly, the MCP pore diameter was changed from 10 μm to 5 μm , which allows the operation of a 4 times higher rate [Diw09]. These two changes led to a total increase of the detection efficiency over many turns in the ring [Kuz11], see also figure 5.4.

As already described in 4.3.3 the determination of the timestamps uses a software CFD method. The software implementation of the method needs inputs on how to treat the experimental data. The main two parameters are the so called bin shift parameter b (delay of the signal) and the fraction parameter f (attenuation of the signal). Because the quality of the determination of the timestamp varies for a fixed set of b and f for different sampling rates of the oscilloscope, optimum parameters have to be found.

Therefore, a detailed investigation was performed and a program was written to scan the parameters to find the optimum value for different sampling rates of the scope, different mean amplitudes, and rise times of the signals [Ber14].

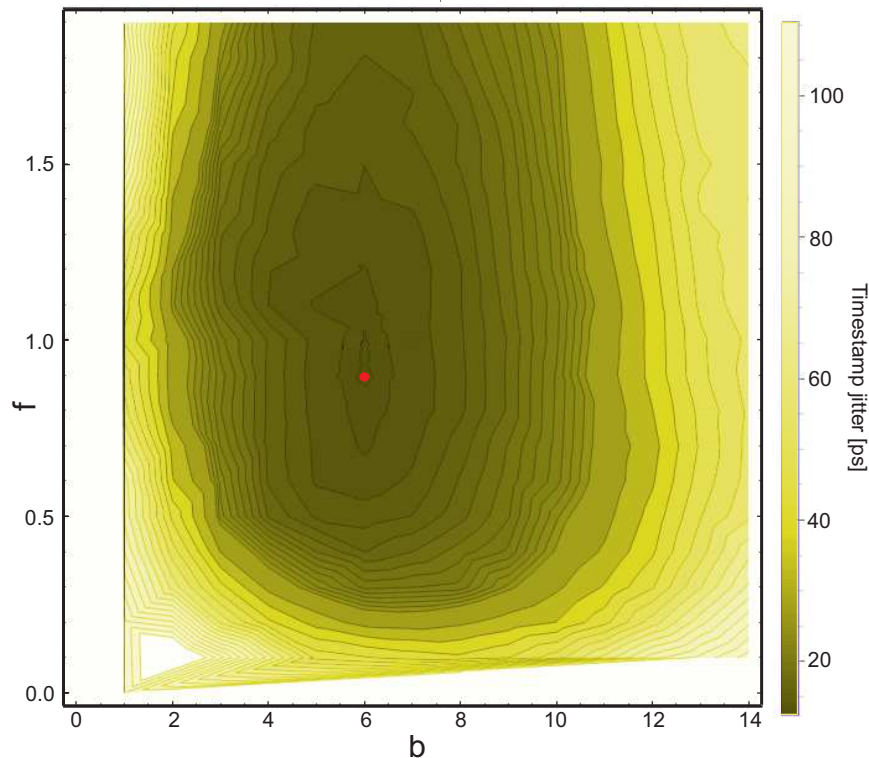


Figure 5.5.: Measured time spreads are shown for the different CFD input parameters (fraction f and bin shift b). The optimum parameters for 10 GS/s were $f = 0.89$ and $b = 6$ (0.6 ns) with a time spread of about 20 ps [Ber14]. The optimum parameter combination is indicated by a red dot.

5.2. Results of the ToF Detector Test with Uranium Ions

The ESR-ToF detector was modified to be able to test the full performance offline as well. This was achieved by installing an α -source and two Si-detectors. The α -source is mounted on a rotary feed-through to perform measurements with and without. Both Si-detectors are placed on a rotatable disc behind the detector to measure the transport efficiency in the center as well for the outer areas of the foil. Due to the geometrical path of the α -particles the spatial resolution of the measurement is approximately 3 mm. This new offline test setup will be routinely used in preparation to mass-measurement runs in the ring.

In a short experiment in October 2014, it was possible to test the ToF detector with uranium ions circulating in the ESR and thus compare the results to the measurements with the α -particles. The intrinsic time spread between forward and backward MCP detectors was measured. As already explained in 5.1.2 the

time spread of the detector depends on the applied electrical field strength. The goal of the uranium experiment was to verify the results obtained from the α -measurements. Two electric field strength of 68 V/mm and 156 V/mm were used in these measurements. The corresponding time distributions are shown in figure 5.6. The standard deviations of the distributions are presented in the figures and are listed in table 5.2. The results from the online tests are in excellent agreement with the offline measurements and thus verify the role of higher field strengths in time measurements.

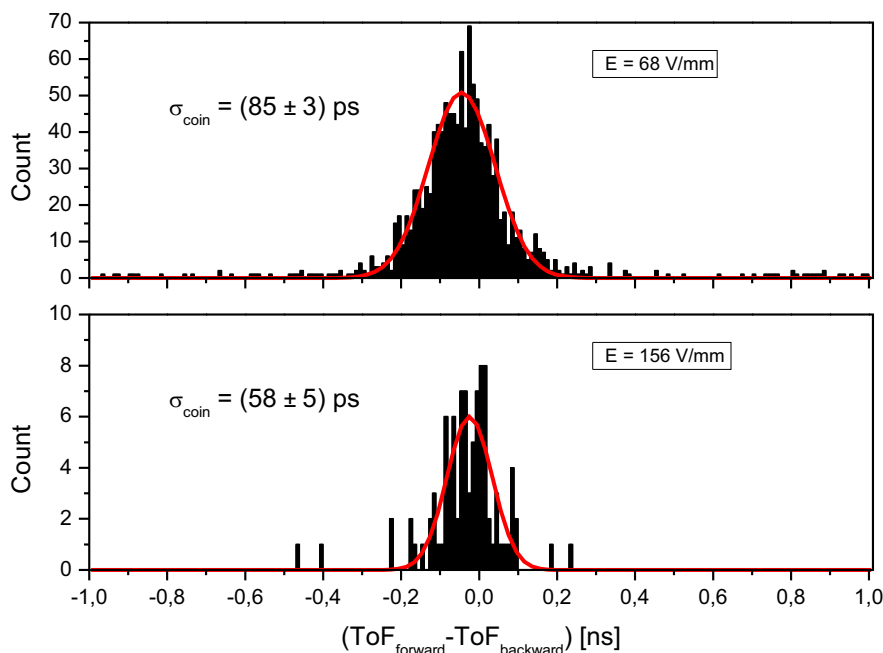


Figure 5.6.: The measured time distributions and their standard deviations σ_{coin} are shown. The measurements have been performed with a coincidence of forward and backward MCPs. The upper spectrum was measured with a 68 V/mm electrical field strength. For the lower spectrum an electrical field strength of 156 V/mm was used.

Table 5.2.: Comparison of the measured time spread for uranium ions and α -particles.

| Ions | $E = 67$ V/mm | $E = 156$ V/mm |
|--|-----------------|-----------------|
| ${}^4\text{He}^{2+}$ (1.4 MeV/u) | (91 ± 3) ps | (55 ± 3) ps |
| ${}^{238}\text{U}^{90+}$ (193.7 MeV/u) | (85 ± 3) ps | (58 ± 5) ps |

Another goal of the experiment was the determination of the detection efficiency for uranium ions. Heavy ions such as uranium release a large number of electrons in the carbon foil which are easily detected by the MCPs. This leads to a detection efficiency of almost 100% even if the transport efficiency of single electrons is less

than 70%. A measured spectrum for both detector branches is depicted in figure 5.7.

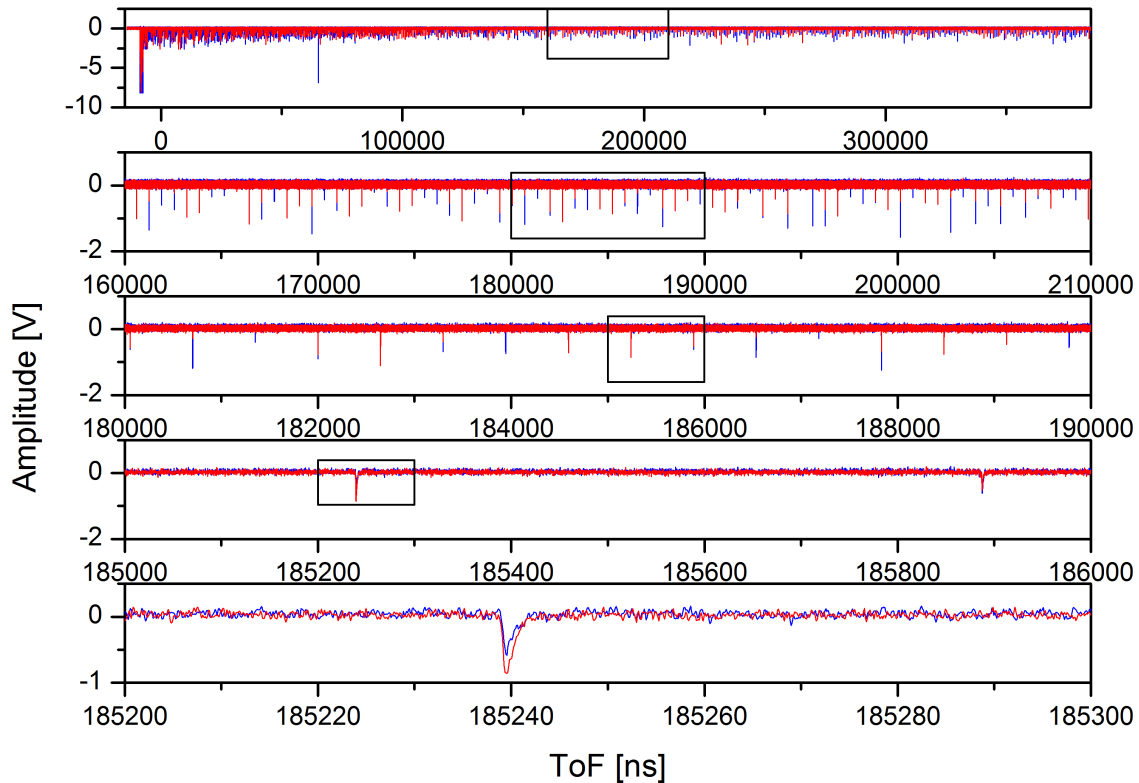


Figure 5.7.: A complete signal trace of an uranium primary beam is shown on the top. The spectra below are successive zooms of the marked areas. The revolution time of the shown particle is approximately 647.954 ns.

5.3. Planned Modifications

As mentioned in the previous sections, it is possible to decrease the time spread of the ToF detector by increasing the electric field strength. This requires higher electrode potentials. For the present electric field strength of the ESR-ToF detector of 156 V/mm a maximum voltage of 7,800 V has to be applied. Increasing the voltage up to 20,000 V the maximum field strength applicable will be 400 V/mm. This goal has been reached with the duplicated detector in the laboratory. The implementation for the ESR detector is planned.

The signal shape of the MCP detectors was also subject of investigations and could be improved by designing a new anode geometry that has less parasitic capacity and transmits higher bandwidths. In total, the new anode is capable of decreasing the signal width from approximately 1100 ps down to 650 ps for dark counts without the magnetic field [Kuz11]. However, in real ToF measurements a magnetic field is present. Its influence was investigated in the following mea-

measurements. The schematic setup of the measurement is similar to the one shown in figure 5.2.

The results of the measurements with α -particles and varied magnetic fields are summarized in figure 5.8. In general, the signal widths (FWHM) are improved by the new geometrical anode design [Kuz11] as demonstrated in figure 5.8 by the measured range of acceleration voltages above 600 V for all applied magnetic fields [Hor13].

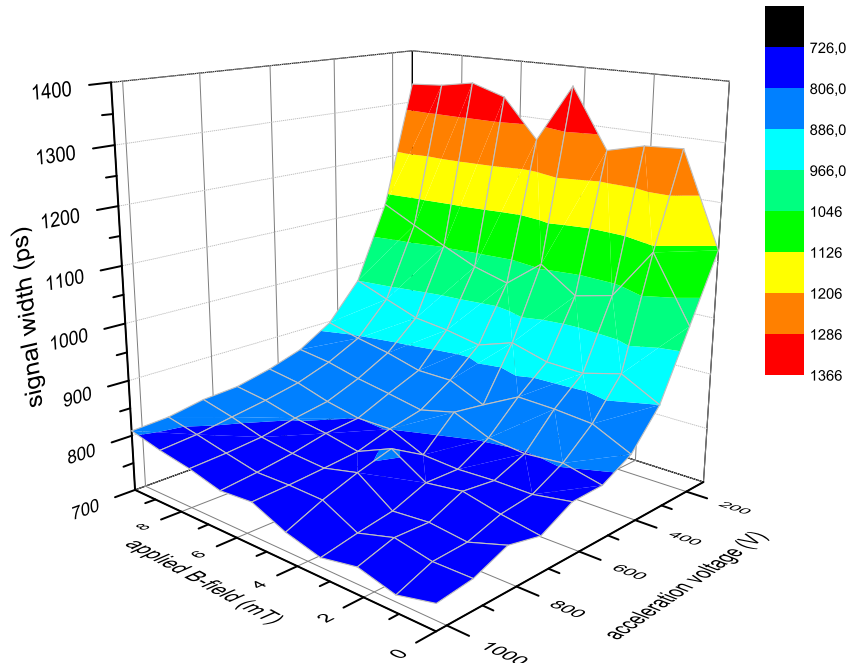


Figure 5.8.: The plot shows measured signal widths (FWHM) for different applied magnetic fields and different acceleration voltages.[Hor13]

In addition to the geometrical optimization of the anode, it is planned to implement a position sensitive anode that would allow tracking the ion motion perpendicular to the beam axis. This would help to track the ion motion between two ToF detectors and yield the correlation of time resolution and position on the foil (see section 5.1.2). Depending on the local dispersion at the detector position it might be possible to deduce information on the energy loss and magnetic rigidity.

Another desirable concept for future IMS experiments is the introduction of a pilot ion-beam during the experiment. This reference pilot beam could be a primary beam in a selected charge states. It could be used for additional calibration and monitoring of any drift during the measurement. The injection of a pilot beam every 5 minutes would be ideal to avoid or correct for drifts.

6. Data Analysis of Measurements with and without Accurate Momentum Definition in the FRS

In this work a novel data analysis is used for IMS mass measurements. Compared to previous IMS analyses this work uses a new insight into the IMS method improved analysis process and helps with the understanding of how future experiments should be performed in order to achieve the maximum accuracy possible. The new approach allowed the combination of data from two different experiments and different conditions (with and without momentum definition) in one analysis. This combination leads to an increase in statistics and enhances the quality of the data without momentum definition by correlation to the experiment with momentum definition.

The following sections explain how the measured raw data yield to the final mass determination. The basic method and tools used for the determination of the revolution time are already well established and can be found, for instance, in [Hau99] [Sta02] [Mat04] [Knö08].

6.1. Determination of Revolution Times

The revolution times of the ions in the storage ring are determined with the ToF detector and recorded with a Digital Sampling Oscilloscope (DSO). An example of an obtained ToF spectrum can be seen in figure 6.1. Depending on the used DSO (high sampling rates needed) smoothing of the signal is an option to reduce the noise. In case of high sampling rates of the DSO one is more sensitive to noise that might overlap signals with small amplitudes. Smoothing the signal reduced the effect of the noise on the signal and improves the timestamp determination. In the experiment performed in 2006 the data were recorded using a DSO with a sampling rate of 40 GS/s. The exact description of smoothing the data can be found in [Knö08]. Signals of experiments recorded with smaller sampling rates have not been smoothed.

As already explained in section 4.3.3 a CFD method is used to determine the times recorded with the DSO. Each timestamp has an uncertainty. The total

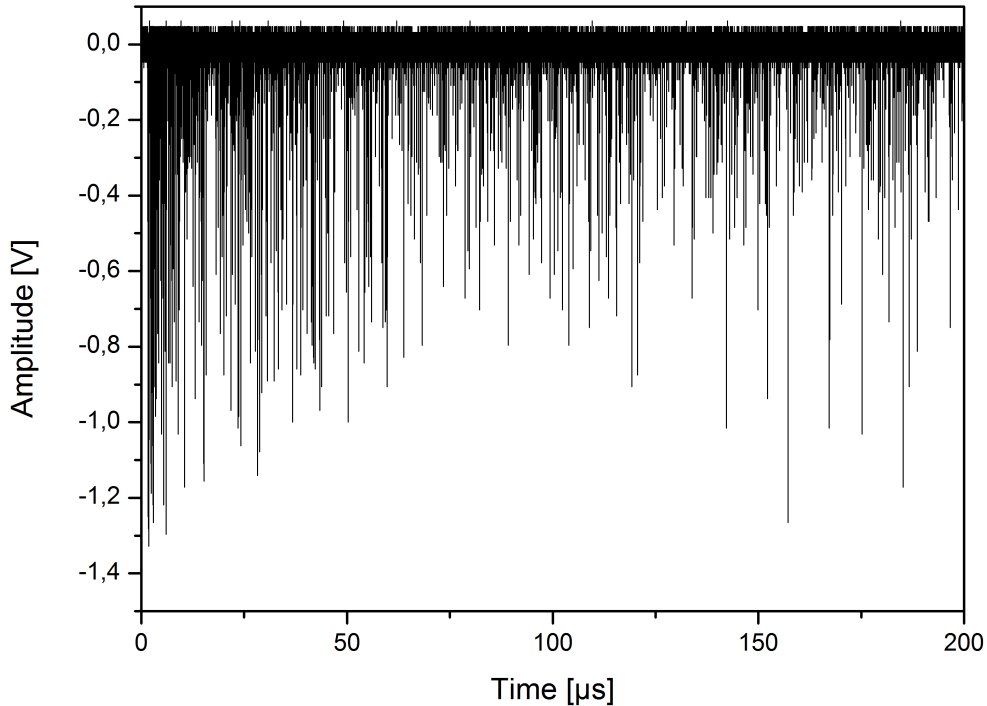


Figure 6.1.: Recorded signals of the ToF detector for uranium fission fragments at energies corresponding to $\gamma_t = 1.41$ within the first 200 μs after injection.

timestamp uncertainty consists of the uncertainty of the CFD method and the timing uncertainty due to the SE transport in the ToF detector.

$$\sigma_{\text{timestamp}} = \sqrt{\sigma_{\text{CFD}}^2 + \sigma_{\text{detector}}^2} \quad (6.1)$$

With a list of timestamps found in a spectrum a pattern algorithm [Hau99] is used to assign the timestamps to the corresponding particle within a given time window. In our case, this time window was chosen to be between 450 and 550 ns, which corresponds to $\pm 10\%$ of the reference ToF of approximately 500 ns. The program "mtrace" [Hau99] [Sta02] uses the last timestamp in the list and calculates its difference to the second last one. After this, the list is searched for another timestamp that corresponds to an integer multiple of this difference in a window of 0.6 ns. This procedure is repeated for all entries in the list starting from the last one and proceeds with new starting points down to the second one. In some cases this leads to an ambiguous assignment of timestamps and particles. In this case the routine crosschecks the number of total events per particle. In case of ambiguous timestamps the given timestamp is assigned to the particle with more timestamps. The routine offers also the possibility to combine chains in the spectrum that seem to be 2 separate particles but are the result of low detection efficiency. Another condition that can be set for different experiments is the amount of timestamps needed (usually 7) to define a particle. In previous works the settings have been optimized and are taken for this analysis as well. An illustration of the tracing procedure is shown in figure 6.2.

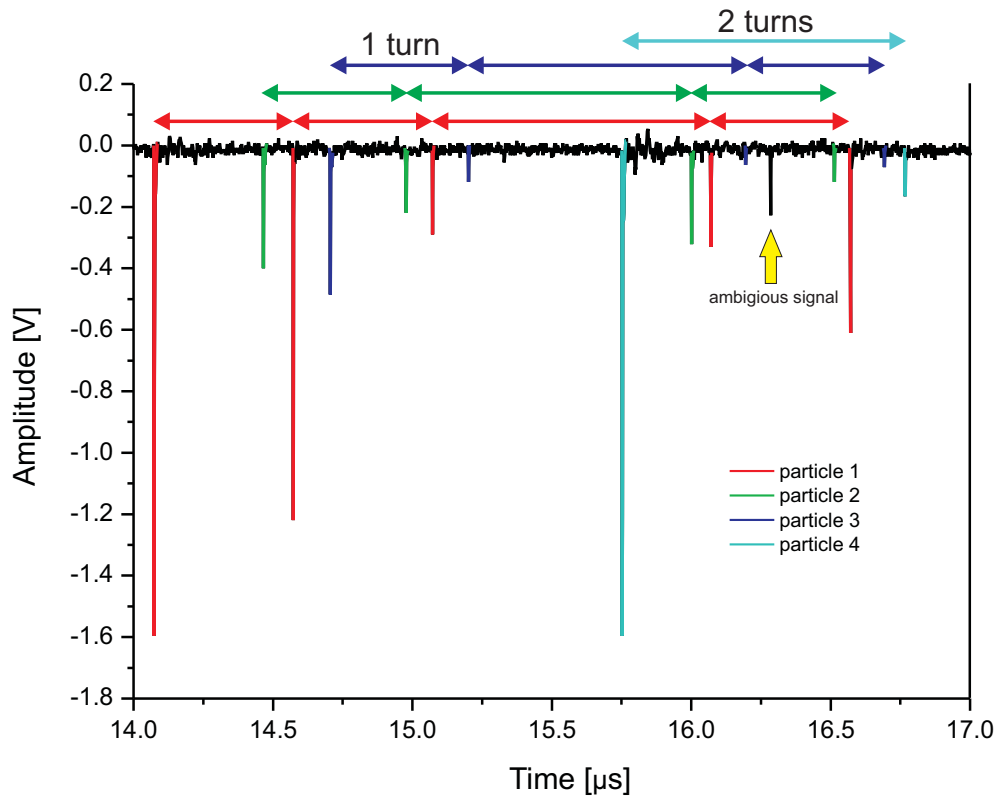


Figure 6.2.: Illustration of the pattern algorithm used to assign the timestamps to single particles. Events with the same multiple of its event time are assigned to the same particle.[Knö08]

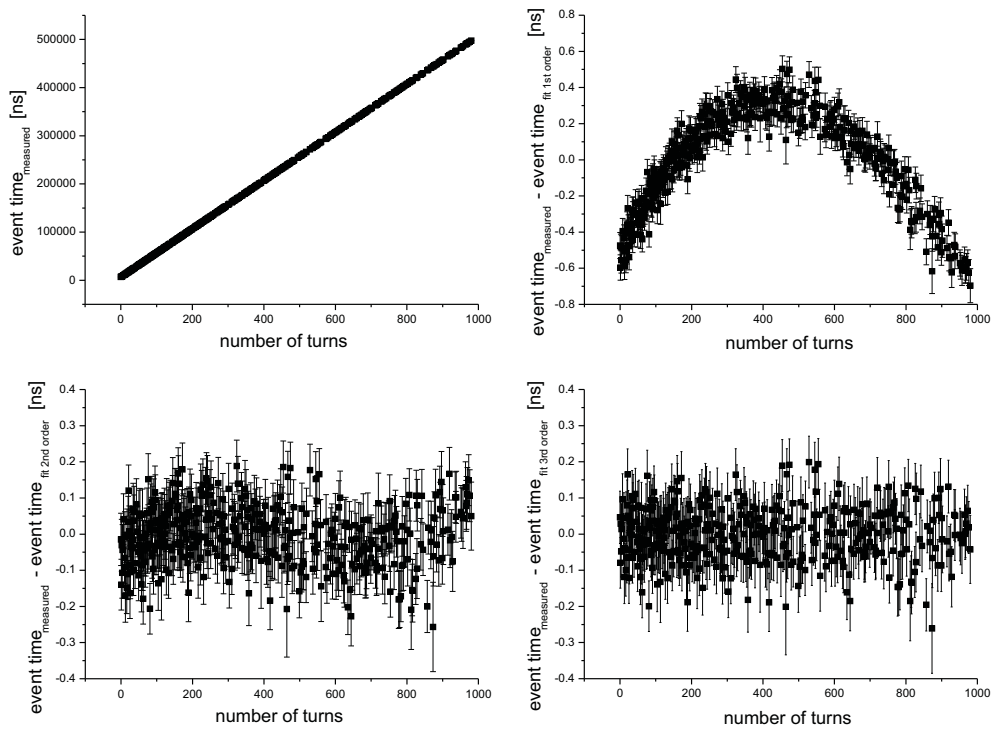


Figure 6.3.: Measured ToF against the turn number (upper left). The residuals for a linear fit (top right), a polynomial fit of 2nd order (bottom left) and a polynomial fit of 3rd order (bottom right) are shown. [Knö08]

With the time stamps assigned to the corresponding particle the revolution time of each particle is determined. To do so the event that occurs first is assumed to be the starting point. For each following event a turn number is assigned according to the integer multiple of the difference between two neighboring events. With the functional correlation between event time and turn number a function can be fitted. The fit function is a 3rd order polynomial. The 3rd order is necessary since fit functions of smaller order show that the correlation between event time and turn number is not described well (see figure 6.3). A linear function does not describe the dependency between ToF and turn number because of the energy loss in the foil in case for non isochronous particles. In case of perfectly isochronous particles an exact linear dependence can be observed.

The least square method (as for example described in [BR02]) can be used to fit data with a polynomial of any order.

The fit function is defined as

$$y(x_i) = \sum_{k=0}^m a_k f_k(x_i) \quad (6.2)$$

with $f_k(x_i) = x_i^k$. Here k defines the order of the polynomial fit function, m is the number of data points and a_k are the free fit parameters that are determined by the method.

The least square method investigates the χ^2 function and minimizes it with a set of coupled linear equations.

$$\chi^2 = \sum_{i=0}^m \frac{1}{\sigma_{y_i}^2} [y_i - y(x_i)]^2 \quad (6.3)$$

A fit function can be found that fulfills

$$\sum \frac{1}{\sigma_{y_i}^2} y_i f_l(x_i) = \sum_{k=0}^{m-1} \left\{ a_k \sum \left[\frac{1}{\sigma_{y_i}^2} f_l(x_i) f_k(x_i) \right] \right\} \quad (6.4)$$

This linear equation system can be written in form of matrices:

$$\boldsymbol{\beta} = \mathbf{a}\boldsymbol{\alpha} \quad (6.5)$$

with the matrix elements

$$\beta_k = \sum \left[\frac{1}{\sigma_{y_i}^2} y_i f_k(x_i) \right] \quad , \quad \alpha_{lk} = \sum \left[\frac{1}{\sigma_{y_i}^2} f_l(x_i) f_k(x_i) \right] \quad (6.6)$$

Inverting $\boldsymbol{\alpha}$ yields the fit parameters a_k . In case of a polynomial fit of 3rd order ($k = 3$) the matrices have the following structures

$$\boldsymbol{\beta} = [\beta_0, \beta_1, \beta_2, \beta_3] \quad \mathbf{a} = [a_0, a_1, a_2, a_3] \quad (6.7)$$

$$\boldsymbol{\alpha} = \begin{pmatrix} \alpha_{00} & \alpha_{01} & \alpha_{02} & \alpha_{03} \\ \alpha_{10} & \alpha_{11} & \alpha_{12} & \alpha_{13} \\ \alpha_{20} & \alpha_{21} & \alpha_{22} & \alpha_{23} \\ \alpha_{30} & \alpha_{31} & \alpha_{32} & \alpha_{33} \end{pmatrix} \quad (6.8)$$

The inverse of $\boldsymbol{\alpha}$ is the so called covariance matrix $\boldsymbol{\epsilon}$

$$\boldsymbol{\epsilon} = \boldsymbol{\alpha}^{-1} \quad (6.9)$$

$$\boldsymbol{\epsilon} = \begin{pmatrix} \epsilon_{00} & \epsilon_{01} & \epsilon_{02} & \epsilon_{03} \\ \epsilon_{10} & \epsilon_{11} & \epsilon_{12} & \epsilon_{13} \\ \epsilon_{20} & \epsilon_{21} & \epsilon_{22} & \epsilon_{23} \\ \epsilon_{30} & \epsilon_{31} & \epsilon_{32} & \epsilon_{33} \end{pmatrix} \quad (6.10)$$

The fit parameters $\mathbf{a} = [a_0, a_1, a_2, a_3]$ are the result of

$$\mathbf{a} = \boldsymbol{\beta} \cdot \boldsymbol{\epsilon} \quad (6.11)$$

Errors for the determined fit parameters can be calculated using the covariances (errors can be interdependent) as

$$\sigma_i^2 = \sum_{k,l} \left(\frac{\delta f}{\delta a_k} \right) \left(\frac{\delta f}{\delta a_l} \right) \Delta a_{k,l}^2 \quad (6.12)$$

Taking the covariance matrix this expression can be written for a 3rd order polynomial fit.

$$\begin{aligned} \sigma_i^2 = & \epsilon_{00} + x_i^2 \epsilon_{11} + x_i^4 \epsilon_{22} + x_i^6 \epsilon_{33} + \\ & + 2(x_i \epsilon_{10} + x_i^2 \epsilon_{20} + x_i^3 \epsilon_{30} + x_i^3 \epsilon_{21} + x_i^4 \epsilon_{31} + x_i^5 \epsilon_{32}) \end{aligned} \quad (6.13)$$

The revolution time is determined from the slope at a given turn number. In previous experiments and publications the turn number at which the revolution time was extracted was defined to be 0th turn in 2002 [Mat04] and the 50th turn in 2006 [Knö08] [Sun08]. In this work the given turn number of 50 is not applicable anymore since also particles with a maximum turn number of less than 50 turns are analyzed. An evaluation at the 50th turn of a particle with less than 50 turns in the ring would lead to an extrapolation of the fit function and thereby to a large error.

The combined experiments have a large difference in maximum turn numbers and therefore a variable choice of turn number (specific for each particle) has been implemented.

The final fit function is

$$f(x) = a_0 + a_1 x + a_2 x^2 + a_3 x^3, \quad (6.14)$$

where the revolution time T is given by:

$$T = f'(x) = a_1 + 2a_2x + 3a_3x^2 \quad (6.15)$$

The first derivative of the error σ_{ToF} is

$$\sigma_{\text{ToF}}^2 = \epsilon_{11} + 4x^2\epsilon_{22} + 9x^4\epsilon_{33} + 4x\epsilon_{12} + 6x^3\epsilon_{13} + 12x^3\epsilon_{23} \quad (6.16)$$

As an example the function of the revolution time of a particle that was measured with 22 events circulating 33 turns in the ring is shown in figure 6.4. The data points and fit parameters for this example are attached in the appendix.

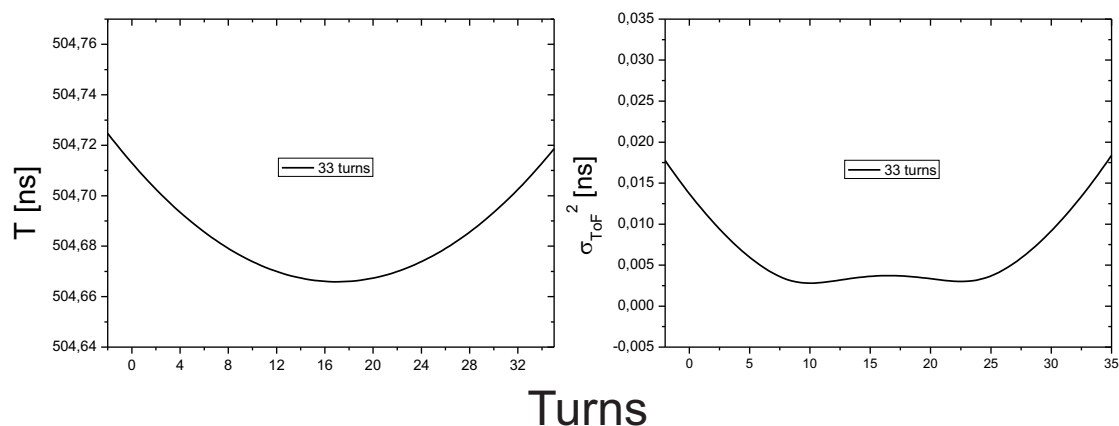


Figure 6.4.: Left hand side: Example of a first derivative of a polynomial fit of 3rd order against the turn number. Right hand side: Function to determine the ToF uncertainty σ_{ToF} against the turn number. In the example the particle revolved for 33 turns in the ring.

To be able to compare the revolution times of particles with different turn numbers, each particle has to be analyzed under the same physical conditions. In order to do so the turn number of choice is variable and dependent on the number of maximum turns circulated in the ring. According to the fit functions the minimum of the fit function for each particle j in terms of revolution time and its error is found at turn number $N_{max}^j/2$. For each particle $N_{max}^j/2$ was then chosen to be the turn number at which the revolution time was determined.

A last step of the fitting process introduces another χ^2 test to measure the quality of the fit function according to the slope of each point. An additional factor is introduced that is multiplied to the assumed error of the revolution time. A factor < 1 indicates that no large scattering of the data points used was observed and that the fit function describes the data points very well. Factors above 1 indicate that the assumed error does not perfectly account for larger scattering of the data points. In general, particles with only few detected events have a larger scattering and therefore a large factor. Revolution time errors (including the factor) larger than 6 ps are declared as non reliable determinations. The

factor is defined as

$$\text{factor} = \sqrt{\frac{\chi^2}{(N - (m - 1))}} = \sum_i \left[\frac{t - \left(\frac{y_{i+1} - y_i}{x_{i+1} - x_i} \right)^2}{\Delta t_i^2} \right] \quad (6.17)$$

with

$$\Delta t_i = \frac{(\sigma_{y_{i+1}}^2 + \sigma_{y_i}^2)}{(x_{i+1} - x_i)} \quad (6.18)$$

6.2. Identification

With the revolution time determined for all measured particles the next step of the analysis is the identification of each particle. To do so MOCADI [MOC15] simulations of the ESR in the isochronous mode as used in the experiments as well as simple calculations with LISE++ [LIS15] were performed to get the theoretical revolution time of nuclei expected to be measured in the experiment.

The revolution times are binned (1 ps) into a revolution time spectrum. From this spectrum a start point for the identification has to be found to be able to identify all the other nuclei according to formula 4.16. If one particle is identified, particles close to the reference identification can be identified as well. The formula including a reference identification can be written for ideal isochronous conditions ($\gamma = \gamma_t$) as

$$\frac{dT}{T} = \frac{1}{\gamma_t^2} \frac{d(m/q)}{(m/q)} \iff \frac{T_{\text{theory}} - T_{\text{ref}}}{T_{\text{ref}}} = \frac{1}{\gamma_t^2} \frac{(m/q)_{\text{theory}} - (m/q)_{\text{ref}}}{(m/q)_{\text{ref}}} \quad (6.19)$$

Here T_{ref} and $(m/q)_{\text{ref}}$ are the revolution time and mass-to-charge ratio of the reference identification respectively. For theory values of the mass-to-charge ratio $(m/q)_{\text{theory}}$ the corresponding theoretical revolution time T_{theory} can be found by solving equation 6.19 for T_{theory} :

$$T_{\text{theory}} = \frac{1}{\gamma_t^2} \frac{(m/q)_{\text{theory}} - (m/q)_{\text{ref}}}{(m/q)_{\text{ref}}} T_{\text{ref}} + T_{\text{ref}} \quad (6.20)$$

To find a reference identification in the revolution time spectrum, a mass to charge ratio distribution around 2.5 can be used. Looking into all known masses of the atomic mass evaluation 2012 [WAW12] a gap of nuclei below and above $m/q = 2.5$ can be found. This same gap of nuclei can be found in the revolution time spectra of the IMS experiments.

This gives a first glance on the m/q values for the revolution times obtained in this very region. A closer look into this region allows us to find characteristic

peaks with given relative differences in their revolution times that can only correspond to unambiguous identifications found for nuclei close to $m/q = 2.5$.

Having one unambiguous reference identification equation 6.20 allows identifying all other peaks in the revolution time spectra. Figure 6.6 illustrates how the identification process works for a reference identification (in this case $^{25}\text{Ne}^{10+}$). By choosing one peak to be the reference mass the theoretical revolution time for all surrounding peaks can be calculated and compared to the measured ones. In case the chosen reference was correct, the measured revolution times fit to the calculated ones. If this is not the case another reference identification for the same peak has to be taken and the theoretical revolution times have to be recalculated. This is done until the pattern fits to the theoretical values. An additional aspect which, helps to be certain about the identification, is the occurrence of characteristic patterns along the identification. For example, it is expected to find chains of identifications that differ in $A = \pm 5$ and $Z = \pm 2$. This pattern can also be seen in figure 6.6.

Note: Equation 6.20 is only valid for revolution times close to the reference revolution time. Taking this into account one has to change the reference identification towards larger (or smaller) m/q values by declaring a newly identified peak to be the new reference identification. The final identification list contains the measured revolution time T (including its uncertainty σ_{ToF}) connected to a mass number A , an atomic number Z , a charge state q , the theoretical m/q value and the information whether it is an isomeric state or not.

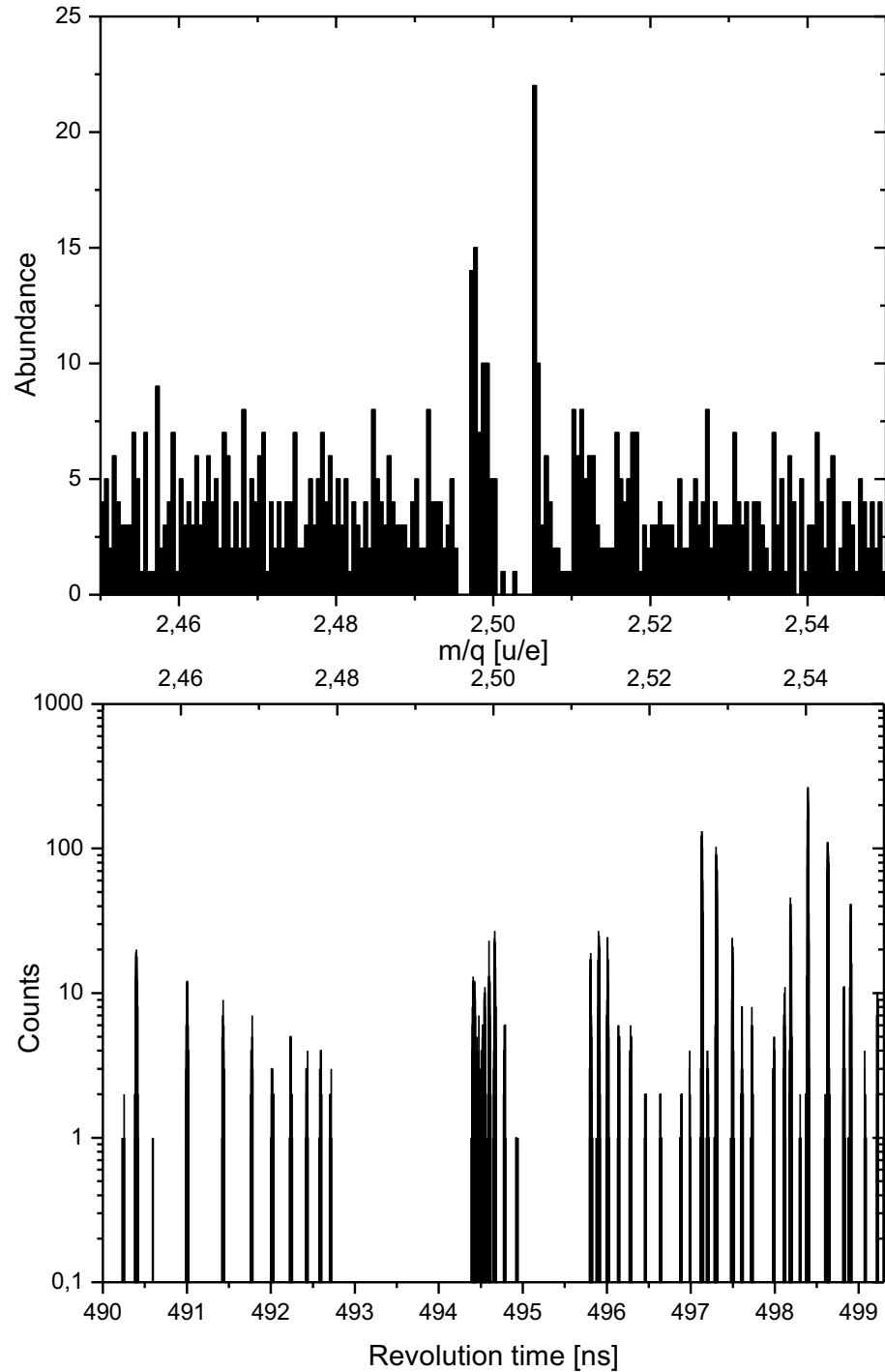
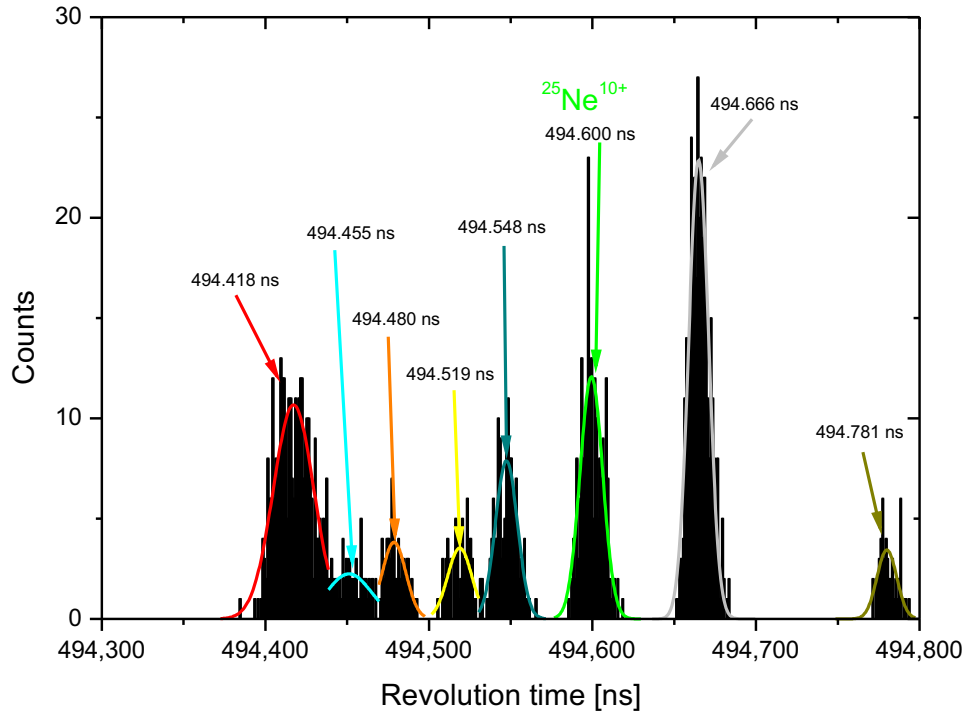


Figure 6.5.: The upper panel shows all possible m/q values around $m/q = 2.5$ as known in the AME 12 [WAW12]. A revolution time spectrum measured with IMS is shown in the lower panel and shows the characteristic gap at $m/q = 2.5$ as well.



| T theory [ns] | m/q [Th] | A | Z | Q |
|---------------|------------|-----|----|----|
| 494,414913 | 2,497218 | 90 | 36 | 36 |
| 494,425082 | 2,497328 | 50 | 20 | 20 |
| 494,425393 | 2,497332 | 95 | 38 | 38 |
| 494,427262 | 2,497352 | 65 | 26 | 26 |
| 494,429170 | 2,497373 | 60 | 24 | 24 |
| 494,431521 | 2,497398 | 100 | 40 | 40 |
| 494,433452 | 2,497419 | 55 | 22 | 22 |
| 494,438819 | 2,497477 | 105 | 42 | 42 |
| 494,441182 | 2,497503 | 110 | 44 | 44 |
| 494,447974 | 2,497577 | 120 | 48 | 48 |
| 494,448117 | 2,497578 | 115 | 46 | 46 |
| 494,451109 | 2,497611 | 125 | 50 | 50 |
| 494,454902 | 2,497652 | 130 | 52 | 52 |
| 494,457193 | 2,497677 | 45 | 18 | 18 |
| 494,462790 | 2,497737 | 135 | 54 | 54 |
| 494,479403 | 2,497918 | 40 | 16 | 16 |
| 494,519342 | 2,498351 | 35 | 14 | 14 |
| 494,547354 | 2,498655 | 30 | 12 | 12 |
| 494,599983 | 2,49922549 | 25 | 10 | 10 |
| 494,667837 | 2,499961 | 20 | 8 | 8 |
| 494,783765 | 2,501218 | 15 | 6 | 6 |
| 494,932945 | 2,502835 | 10 | 4 | 4 |

Figure 6.6.: Illustration of the performed identification process with $^{25}\text{Ne}^{10+}$ chosen to be the reference identification for revolution time 494.600 ns. Calculating the theoretical revolution times for possible identifications from literature shows that the other measured revolution times fit perfectly to the literature values and verifies the identification.

6.3. Matrix Method

The correlation-matrix method used to extract the mass values from the measured data is similar to the one used in several previous analyses. The first analysis using the correlation matrix method was done for Schottky mass measurements [R⁺00]. Since both IMS and SMS experiments measure the revolution time (frequency) calibrated with literature values, the matrix can also be applied to IMS data.

The mathematical description below follows the description of these works [R⁺00].

The basic idea of the matrix method is to use a maximum likelihood method to find a maximum in a joint probability density function that describes all interconnections and correlations between measured masses and reference masses. For each revolution time T_j^μ in a spectrum j and nucleus μ the m/q value can be described by a polynomial function with coefficients a_j^k and order k

$$m/q = \sum_{k=0} a_j^k (T_j^\mu)^k \quad (6.21)$$

The difference l_j^μ between the real m/q value and the fit function is expected to be Gaussian distributed around 0 and can be written as

$$\frac{m_j^\mu}{q_j^\mu} - \sum_{k=0} a_j^k (T_j^\mu)^k = l_j^\mu \pm \Delta_j^\mu \quad (6.22)$$

with Δ_j^μ being the standard deviation of the Gaussian distribution, which is also directly connected by a scaling factor s to the standard deviation $\sigma_{T_j^\mu}$ of measured revolution time T_j^μ

$$\Delta_j^\mu = s\sigma_{T_j^\mu} \quad (6.23)$$

The scaling factor is necessary because the input data are revolution times and revolution time uncertainties. s scales and translates the revolution time uncertainty into a mass uncertainty. It is important to note that for IMS this scaling factor is not constant for all m/q regions. Because of the isochronicity of the ring, particles with m/q ratios different to the isochronous nuclide have a larger revolution time distribution that has to be accounted for by the scaling factor. This on the other hand means that s is a function of m/q . In the first step of the analysis only small m/q intervals are analyzed and a constant s factor in this interval is assumed. For the full analysis a variable scaling factor $s(m/q)$ is used in a second iteration.

With a Gaussian distribution defined as

$$G(l, \sigma) = \frac{1}{\sqrt{2\pi}\sigma} e^{-\frac{l^2}{2\sigma^2}} \quad (6.24)$$

the equation system 6.22 can be written as a probability density function consisting of Gaussian distributions for each nucleus μ and spectrum j :

$$L_{\text{exp}} = \prod_{j,\mu} G(l_j^\mu, \Delta_j^\mu), \quad j = 1, 2, \dots, N_s \quad \text{and} \quad \mu = 1, 2, \dots, N_n \quad (6.25)$$

This correlates all measured revolution times of bare (fully ionized) nuclei. More correlations should be added to increase the strength of the matrix method. In the IMS experiments not only bare nuclides but also different charge states are measured. By adding the masses and binding energies of the extra electrons for measured charge states, additional correlations can be tied in.

This can be implemented into equation 6.22 by defining the measured mass m_j^μ in general to be

$$m_j^\mu = m_\mu^b + E_j^\mu \quad (6.26)$$

Here m_μ^b is the mass of the bare nucleus μ and E_j^μ the total electron binding energy including the electron rest masses for the corresponding charge state. For bare nuclides measured E_j^μ is simply 0. The values of the rest mass and binding energies of the electrons have been extracted from atomic data tables [H⁺78], [JS85] and [PJS94].

Besides unknown nuclides also very well known nuclides are measured in the experiments. For those nuclides another correlation to literature values of the atomic mass evaluation (AME) 2012 [WAW12] can be added. For the measured reference masses a similar dependency, as assumed in equation 6.22, can be written:

$$m_\eta - m_\eta^{\text{ref}} = l_\eta \pm \Delta m_\eta \quad (6.27)$$

The difference l_η between the estimated mass value in the data analysis m_η and the corresponding literature value m_η^{ref} is also expected to be a Gaussian distribution around 0 with a standard deviation Δm_η , which is given by the uncertainty of the literature value m_η^{ref} . The probability density function for the reference correlations (here N_r is the number of total reference masses) is

$$L_{\text{ref}} = \prod_{\eta} G(l_\eta, \Delta m_\eta), \quad \eta = 1, 2, \dots, N_r \quad (6.28)$$

Ultimately joining the probability density function of the correlated experimental masses L_{exp} together with the probability density function of the correlated reference masses L_{ref} yields the likelihood function

$$L = L_{\text{exp}} \cdot L_{\text{ref}} = \prod_{j,\mu} G(l_j^\mu, \Delta_j^\mu) \cdot \prod_{\eta} G(l_\eta, \Delta m_\eta) \quad (6.29)$$

Figure 6.7 illustrates the correlation between every measured revolution time, the input data for reference masses (AME2012) and the joining of the two probability density functions L_{exp} and L_{ref} .

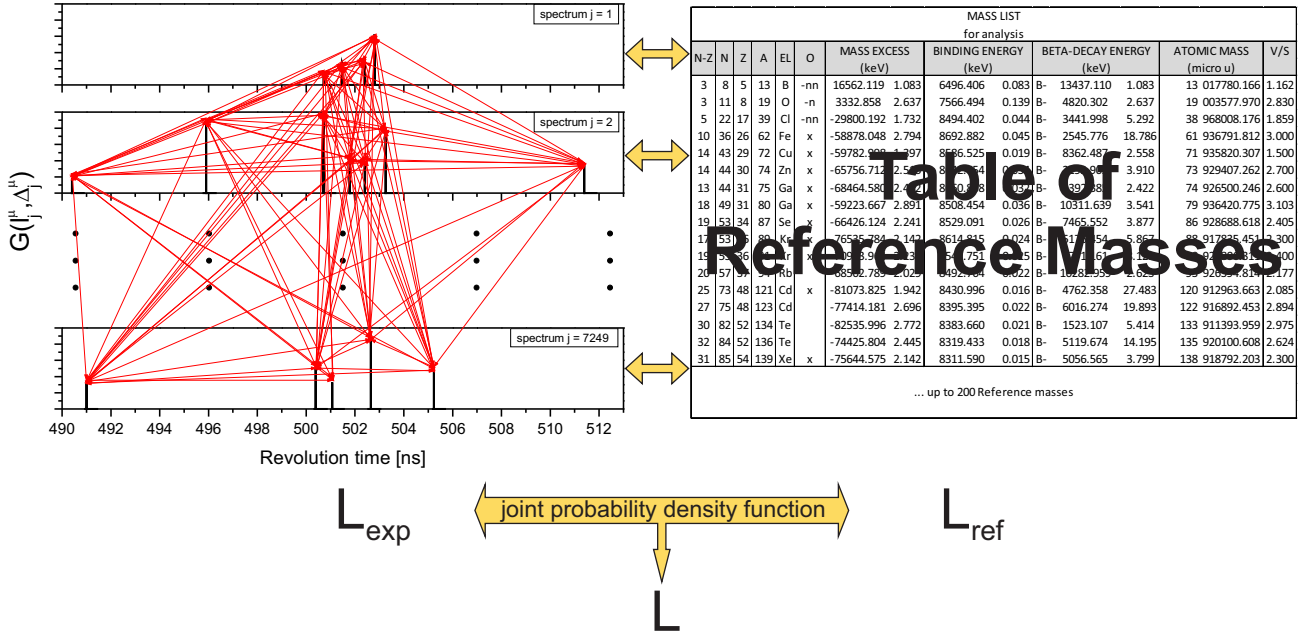


Figure 6.7.: Principle of the correlation matrix method. Each measured revolution time in every spectrum (black bars in left graph) is correlated to all other measured revolution times (demonstrated by the red arrows). This is included in the probability density function L_{exp} . Reference masses (right tabular) are represented by the probability density function L_{ref} . Combining the measured revolution times with the reference masses (yellow arrows) leads to the joint probability density function L that is then minimized in the maximum likelihood method.

To find the maximum of this joint probability density function as a function of the calibration curve the coefficients a_j^k , the mass of a bare nucleus m_μ^b and (in small m/q intervalls) the scaling factor s , have to be found with the three likelihood conditions. In order to simplify the expressions of the Gaussian functions the natural logarithm is commonly applied to L . The values that maximize the normal probability density function L are the same that maximize the logarithmic form $\ln L$, because the logarithm is a strictly monotonically increasing function. The three likelihood conditions are:

$$\frac{\delta \ln L}{\delta a_j^k} = 0 \quad (6.30)$$

$$\frac{\delta \ln L}{\delta m_\mu^b} = 0 \quad (6.31)$$

$$\frac{\delta \ln L}{\delta s} = 0 \quad (6.32)$$

The solution for equation 6.30 includes for each spectrum j unknown coefficients. It can be written as

$$\hat{\mathbf{A}}_j \begin{pmatrix} a_j^0 \\ a_j^1 \\ \vdots \\ a_j^k \end{pmatrix} = \sum_{\mu} w_j^{\mu} \frac{m_j^{\mu}}{q_j^{\mu}} \begin{pmatrix} 1 \\ T_j^{\mu} \\ \vdots \\ (T_j^{\mu})^k \end{pmatrix} \quad (6.33)$$

w_j^{μ} are the weights

$$w_j^{\mu} = \frac{1}{(\Delta_j^{\mu})^2} = \frac{1}{s^2(\sigma_{T_j^{\mu}})^2} \quad (6.34)$$

and $\hat{\mathbf{A}}_j$ is a $k \times k$ matrix of the form:

$$\hat{\mathbf{A}}_j = \begin{pmatrix} \sum_{\mu} w_j^{\mu} & \sum_{\mu} w_j^{\mu} T_j^{\mu} & \dots & \sum_{\mu} w_j^{\mu} (T_j^{\mu})^k \\ \sum_{\mu} w_j^{\mu} T_j^{\mu} & \sum_{\mu} w_j^{\mu} (T_j^{\mu})^2 & \dots & \sum_{\mu} w_j^{\mu} (T_j^{\mu})^{k+1} \\ \vdots & \vdots & \ddots & \vdots \\ \sum_{\mu} w_j^{\mu} (T_j^{\mu})^k & \sum_{\mu} w_j^{\mu} (T_j^{\mu})^{k+1} & \dots & \sum_{\mu} w_j^{\mu} (T_j^{\mu})^{2k} \end{pmatrix} \quad (6.35)$$

By inverting $\hat{\mathbf{A}}_j$ the coefficients a_j^k can be calculated from

$$\begin{pmatrix} a_j^0 \\ a_j^1 \\ \vdots \\ a_j^k \end{pmatrix} = \hat{\mathbf{A}}_j^{-1} \sum_{\mu} w_j^{\mu} \frac{m_j^{\mu}}{q_j^{\mu}} \begin{pmatrix} 1 \\ T_j^{\mu} \\ \vdots \\ (T_j^{\mu})^k \end{pmatrix} \quad (6.36)$$

Dependent on the choice of the polynomial order k the analytical solution for the $k \times k$ matrix $\hat{\mathbf{A}}_j^{-1}$ can get pretty complex (starting from $k = 3$). To still be able to use polynomial fits with orders larger than 3, the inversion of the matrix $\hat{\mathbf{A}}_j$ has to be performed numerically.

The second equation 6.31 can be solved for each mass by using the relation

$$\sum_j w_j^{\mu} \frac{m_j^{\mu}}{(q_j^{\mu})^2} - \sum_j w_j^{\mu} \frac{\hat{T}_j(T_j^{\mu})}{q_j^{\mu}} - \frac{\delta \ln L_{\text{ref}}}{\delta m_{\mu}^b} = 0 \quad (6.37)$$

The function \hat{T}_j can be rewritten in a matrix notation:

$$\hat{T}_j(T_j^\mu) = \sum_k a_j^k (T_j^\mu)^k = (1, T_j^\mu, \dots, (T_j^\mu)^k) \begin{pmatrix} a_j^0 \\ a_j^1 \\ \vdots \\ a_j^k \end{pmatrix} \quad (6.38)$$

Equation 6.38 now allows us to substitute equation 6.36 into equation 6.37 which yields

$$\sum_j w_j^\mu \frac{m_j^\mu}{(q_j^\mu)^2} - \sum_j \frac{w_j^\mu}{q_j^\mu} \left[(1, T_j^\mu, \dots, (T_j^\mu)^k) \hat{\mathbf{A}}_j^{-1} \begin{pmatrix} 1 \\ T_j^\mu \\ \vdots \\ (T_j^\mu)^k \end{pmatrix} \frac{w_j^\beta m_j^\beta}{q_j^\beta} \right] - \frac{\delta \ln L_{\text{ref}}}{\delta m_\mu^b} = 0 \quad (6.39)$$

Index β runs over all nuclei that appear in spectrum j . This is the final equation to determine the masses m_μ^b . A shorter way to write this equation can be done symbolically by introducing a $N_m \times N_m$ (N_m is the number of different nuclei) matrix \mathbf{W} :

$$\mathbf{W} \vec{M} = \vec{w} \quad (6.40)$$

The diagonal elements of the matrix \mathbf{W} are given as

$$W_{\mu\mu} = \sum_j \frac{w_j^\mu}{(q_j^\mu)^2} \left[1 - w_j^\mu (1, T_j^\mu, \dots, (T_j^\mu)^k) \hat{\mathbf{A}}_j^{-1} \begin{pmatrix} 1 \\ T_j^\mu \\ \vdots \\ (T_j^\mu)^k \end{pmatrix} \right] + \frac{1}{(\Delta m_\mu)^2} \quad (6.41)$$

and the non diagonal elements are given as

$$W_{\mu\nu} = - \sum_j \left[\frac{w_j^\mu w_j^\nu}{q_j^\mu q_j^\nu} (1, T_j^\mu, \dots, (T_j^\mu)^k) \hat{\mathbf{A}}_j^{-1} \begin{pmatrix} 1 \\ T_j^\mu \\ \vdots \\ (T_j^\mu)^k \end{pmatrix} \right] \quad \text{for } \mu \neq \nu \quad (6.42)$$

The vector \vec{w} differs for reference nuclei and non reference nuclei. For reference nuclei \vec{w} is

$$w_\mu = \sum_{j,\beta} \frac{w_j^\mu w_j^\beta}{q_j^\mu q_j^\beta} (1, T_j^\mu, \dots, (T_j^\mu)^k) \hat{\mathbf{A}}_j^{-1} \begin{pmatrix} 1 \\ T_j^\mu \\ \vdots \\ (T_j^\mu)^k \end{pmatrix} E_j^\beta - \sum_j \frac{w_j^\mu E_j^\mu}{(q_j^\mu)^2} + \frac{m_\mu}{(\Delta m_\mu)^2} \quad (6.43)$$

and in case of non reference nuclei the last term $m_\mu/(\Delta m_\mu)^2$ is not added.

The final mass values m_μ^b for bare nuclei can be obtained by solving equation 6.40 for \vec{M} . To do so \mathbf{W} has to be inverted and multiplied with \vec{w} :

$$\vec{M} = \mathbf{W}^{-1}\vec{w} \quad (6.44)$$

The last equation from the maximum likelihood ansatz 6.32 allows us to determine the scaling parameter s

$$s^2 = \frac{1}{N_n} \sum_{j,\mu} \frac{(l_j^\mu)^2}{(\sigma_{T_j^\mu})^2} \quad (6.45)$$

As already mentioned above, an analytical solution for these matrices is not possible. The solutions for equation 6.44 and 6.45 were achieved by numerical iteration.

With this first iteration of the analysis only mass values and a scaling factor s for a investigated m/q interval are valid. In a second and final iteration the found scaling factors can be used to determine the variable scaling factor as a function of m/q . This function is then implemented into the matrix and a final analysis of all measured m/q regions is possible in one correlation. This also means that in the second and final evaluation the third likelihood condition 6.32 is not needed anymore. Figure 6.8 shows the determined scaling factors after the first analysis step and the fit function implemented for the final evaluation.

The determination of the statistical error in this method uses the diagonal elements of the inverse matrix \mathbf{W}^{-1} and is defined as

$$(\sigma_{m_\mu}^{\text{stat}})^2 = \mathbf{W}_{\mu\mu}^{-1} \quad (6.46)$$

In the application of the matrix to measured data one has to assure that enough connections between measured and reference masses are possible. This can be done by summing up a minimum of 100 particles for each spectrum j . Increasing the number of particles inside a spectrum makes the connections stronger and decreases the statistical error for exotic nuclei, because with increasing particle number it gets more likely that exotic nuclei are in the same spectrum as the reference mass closest to it. A drawback of adding too many particles into one spectrum is the time needed to measure the amount of particles. If the measurement time to accumulate the desired amount of particles per spectrum in the experiment is too long, additional errors due to drifts (e.g. magnet drifts) decrease the measurement accuracy. In order to minimize the influence of time-dependent effects the number of accumulated particles per spectrum must

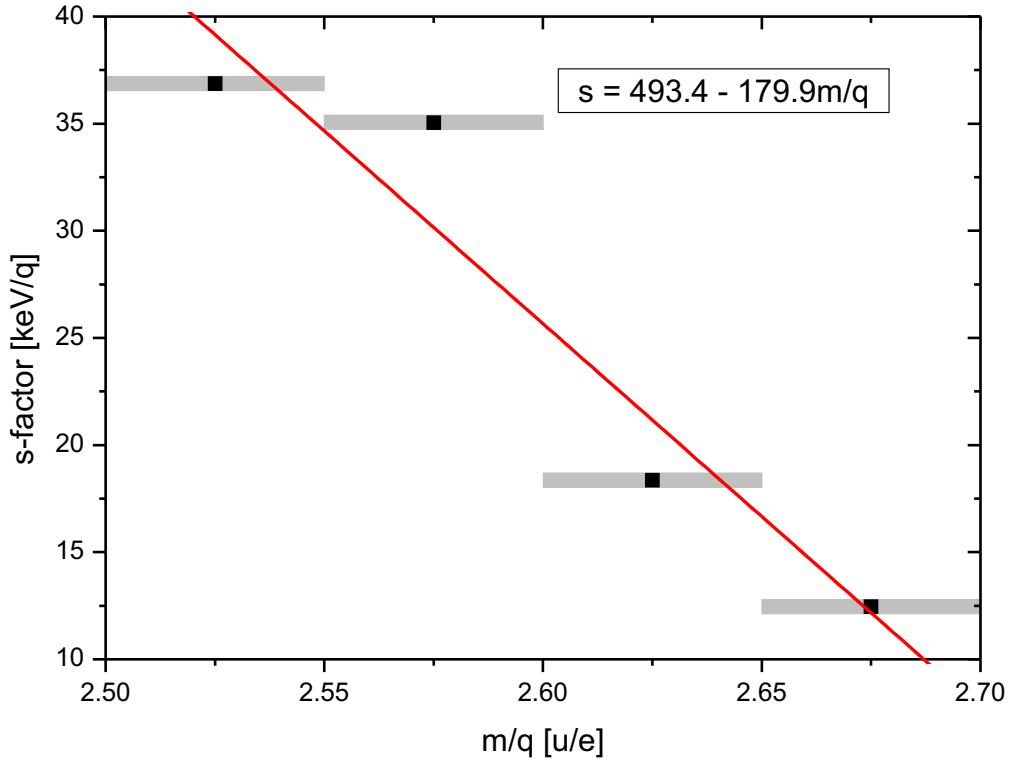


Figure 6.8.: The scaling factor s for different m/q intervals. A 2nd order polynomial fit is shown in red. The observed dependence reflects the fact that the mass uncertainty is indeed dependent on m/q . For the isochronous m/q value a minimum s -factor is reached.

be chosen appropriately.

The estimation of the systematical error σ^{syst} of the experiment was done using the relation

$$\sum_{\eta} \frac{(m_{\eta}^b - \tilde{m}_{\eta}^b)^2}{(\Delta\tilde{m}_{\eta}^b)^2 + (\sigma^{\text{syst}})^2 + (\sigma^{\text{stat}})^2} = N_r \quad (6.47)$$

where \tilde{m}_{η}^b are the mass values and $\Delta\tilde{m}_{\eta}^b$ the uncertainties of the reference nuclides. σ^{stat} are the statistical errors of the measured masses m_{η}^b . N_r is the number of reference masses and σ^{syst} the systematic error.

For the described procedure a Gaussian statistical distribution is assumed. However, for very rare nuclides characterized with a few recorded events in the whole experiment, a Gaussian description is very likely to underestimate the uncertainty. Therefore, it was looked for additional correlations. Indeed, a strong correlation between the measured uncertainty of the revolution time σ_T and the number of turns recorded in the ring could be observed. An average error for nuclides with low statistics has been calculated by taking into account this additional uncertainty as a function of the turn number. The additional error σ^{lstat} is quadratically added for nuclides with less than 15 recorded ions.

The reason for this observed correlation is probably the influence of the initial

phase-space coordinates, e.g., the position and angular coordinates of the injected ions before they reached a close orbit in the ring. The transformation from the time uncertainty to the corresponding mass uncertainty was done using the relation:

$$\delta m = \delta T/T \cdot \gamma_t^2 \cdot m \quad (6.48)$$

This relation yields, for example, 480 keV/ps for an ion with a mass of 130 u and an ionic charge of 50. Hence overall uncertainty of the measured mass is

$$\Delta m = \sqrt{(\sigma^{\text{stat}})^2 + (\sigma^{\text{syst}})^2} \quad (6.49)$$

and for nuclides with less than 15 counts

$$\Delta m = \sqrt{(\sigma^{\text{stat}})^2 + (\sigma^{\text{lstat}})^2 + (\sigma^{\text{syst}})^2}. \quad (6.50)$$

6.4. Limitations of IMS

The introduced variable s-factor in the matrix method is necessary because one has to account for the different isochronicity quality for different m/q values. A discussion of the basic limitations of the IMS method follows. Altogether the final uncertainty of the mass determination is a combination of many different error contributions starting from the revolution time uncertainty for non isochronous nuclei, adding uncertainties from the detector for each turn and its timestamp determination.

The sources of possible uncertainties to the final mass determination can be separated into three fields:

- ToF Detector
- Analysis Method
- Storage Ring

6.4.1. Contribution of ToF Detector and CFD Method

The observable that determines the final mass value is the revolution time T . The uncertainty of the revolution time is dependent on the uncertainty of each timestamp and the number of turns in the ring. The uncertainty of the timestamp was assumed to be: $\sigma_{\text{timestamp}} = \sqrt{\sigma_{\text{detector}}^2 + \sigma_{\text{CFD}}^2}$. This uncertainty is determined by the CFD method. For a typical revolution time of 500 ns a list of timestamps according to a selectable turn number was generated for 100 particles assuming the time uncertainties to be Gaussian distributed. The timestamps were analyzed with the program "mtrace" [Hau99] [Sta02] as explained in section 6.1. The distribution of the revolution time T and the corresponding standard deviations $\sigma_T(\text{det})$ are presented in the figures. The figures 6.9 and 6.10 show the results for different turn numbers.

Stored ions measured for only 30 turns in the ring with a timestamp uncertainty of 125 ps yield a broad revolution time distribution of approximately 2.7 ps standard deviation. This time spread will cause even for perfectly isochronous ions a severe limit in the resolving power. 1 ps uncertainty of the revolution time corresponds to 480 keV in the mass resolving power for an ion mass of 133 u. For a 125 ps timestamp uncertainty this means only particles with more than 120 turns must be selected to achieve an accuracy of 240 keV.

By improving the timing performance from 125 ps to 50 ps only 70 turns are required to reach the same accuracy. Presently the best measured timing performance of the detector reached is 35 ps (see figure 5.3). Combined with the best CFD method accuracy of 20 ps (high sampling rates needed) the best timestamp accuracy achieved until now is 40 ps.

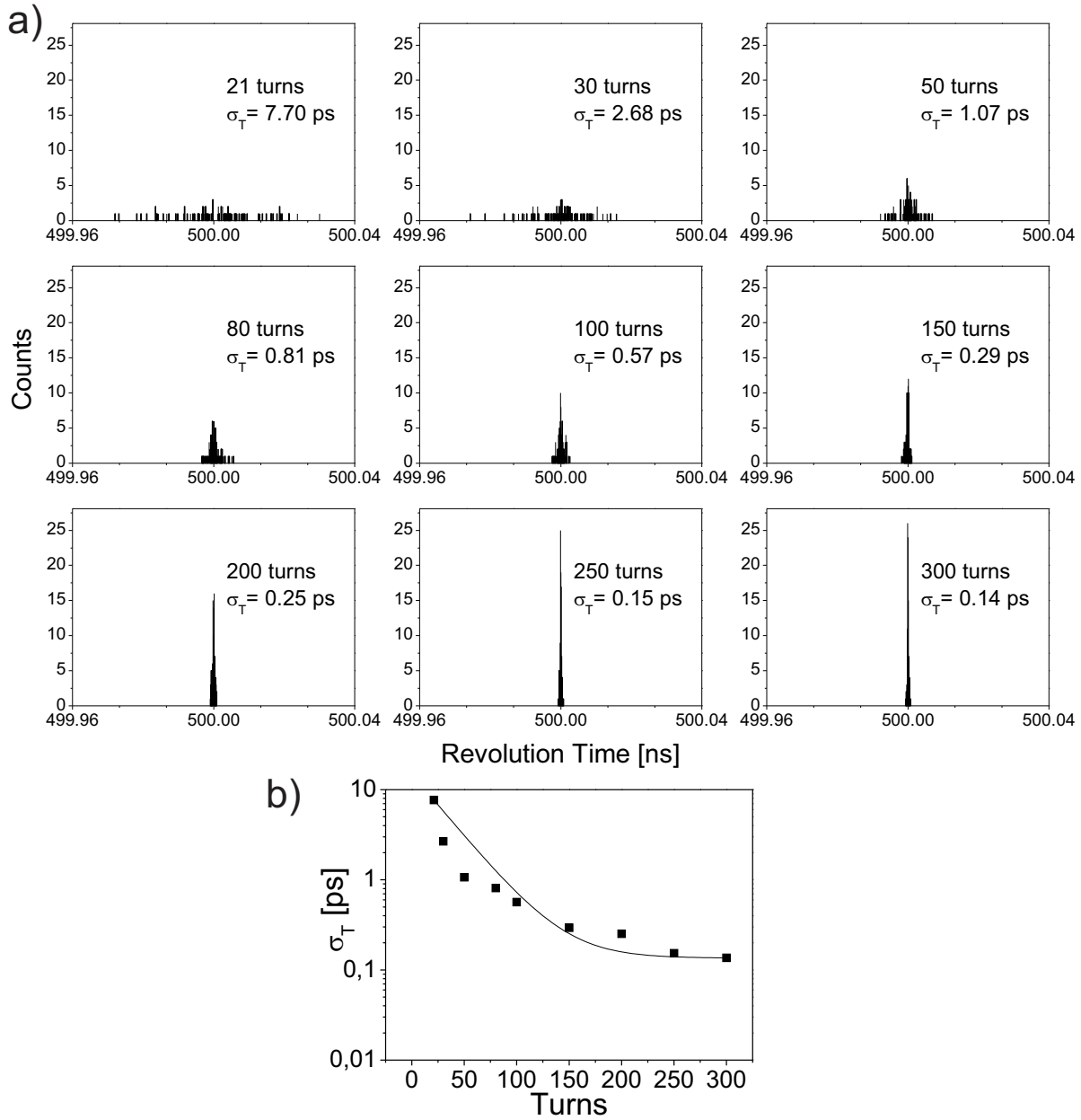


Figure 6.9.: Panel a): Calculated distributions of the revolution time and the corresponding standard deviations for a 125 ps time spread of the timestamps for different turns. Panel b): Standard deviations for 125 ps time spread of the timestamps as a function of the turn number.

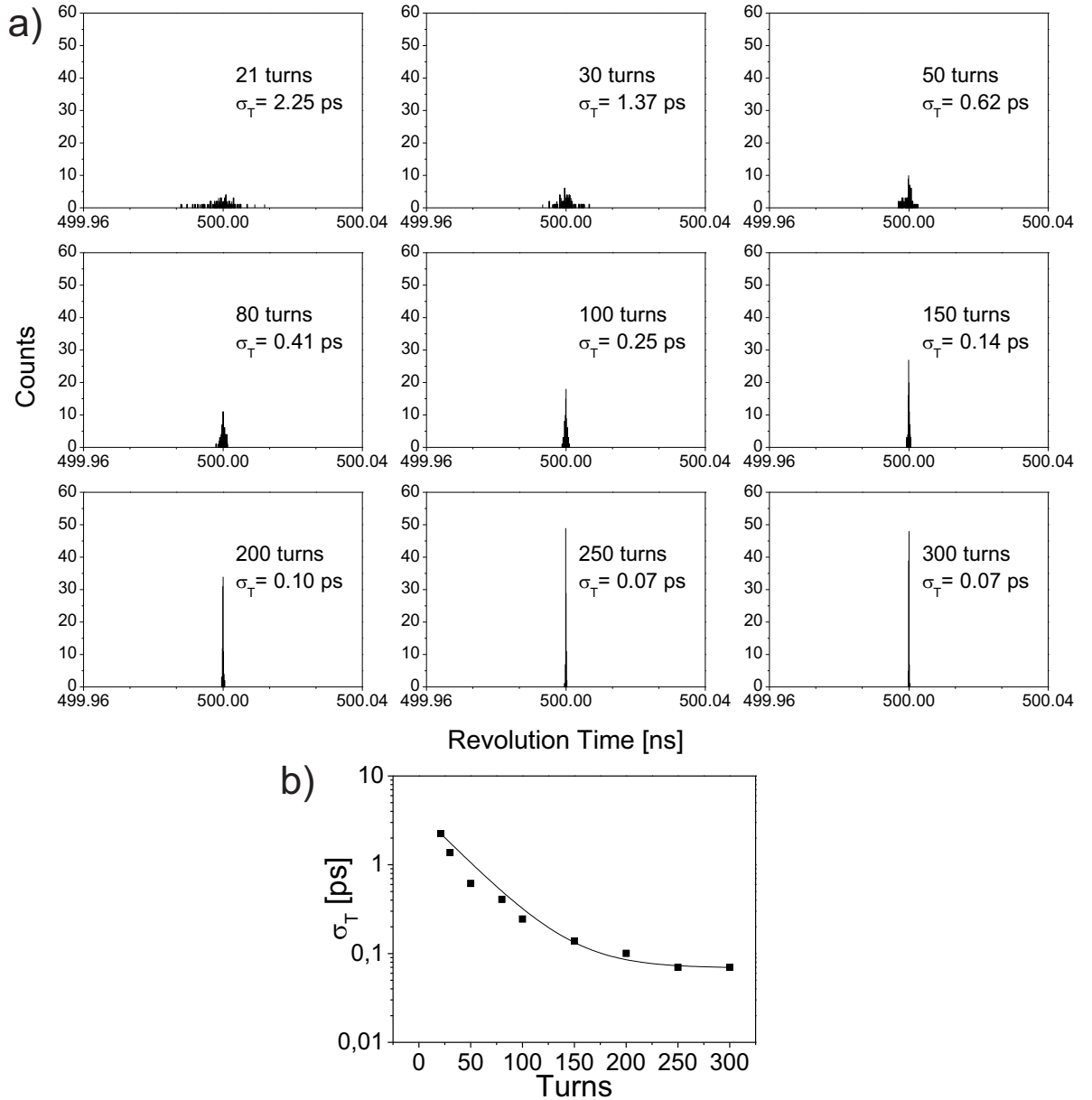


Figure 6.10.: Panel a): Calculated distributions of the revolution time and the corresponding standard deviations for a 50 ps time spread of the timestamps for different turns. Panel b): Standard deviations for 50 ps time spread of the timestamps as a function of the turn number.

For the investigations shown above a detection efficiency of 100% was assumed. However, in the experiment the detection efficiencies can be lower especially for light elements. To investigate the impact of the detection efficiency, a revolution time of 500 ns was used to generate a Gaussian distributed timestamps for 200 turns. The missing timestamps due to the limited efficiency were randomly selected between the 1st and 200th turn. The results for a timestamp uncertainty of 125 ps after 200 turns with detection efficiencies of 25%, 50%, 75% and 100% can be found in figure 6.11. For low detection efficiencies less timestamps are avail-

able for the fitting algorithm to obtain the mean revolution time for each particle (see procedure illustrated in figure 6.3). This causes broader distributions of the revolution time.

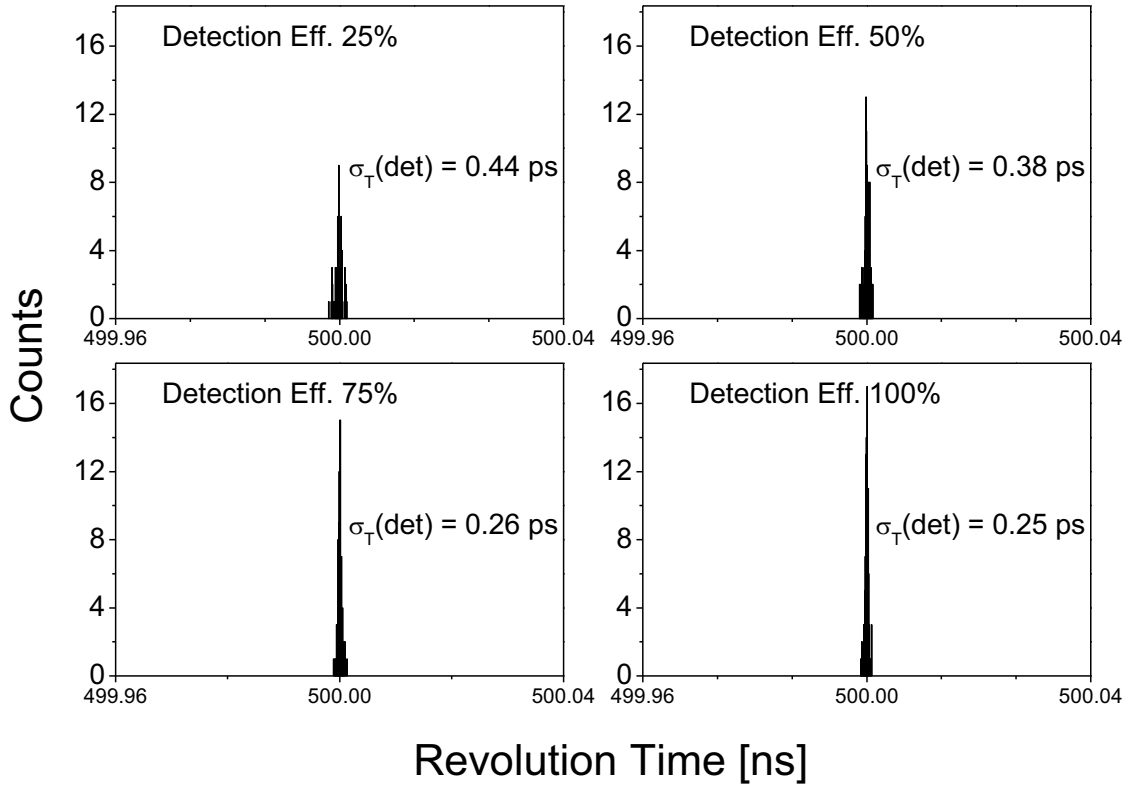


Figure 6.11.: Calculated distributions of the revolution time and the corresponding standard deviations for a 125 ps time spread of the timestamps and 200 turns assuming 25%, 50%, 75% and 100% detection efficiency.

6.4.2. Contribution of the Isochronicity of the Ring

The calculated results from the previous section have demonstrated that stored ions with at least 200 turns and less than 125 ps timestamp uncertainty yield an error of the revolution time of 0.5 ps. As stated above, in the experiments the isochronicity quality of the ring contributes in addition to the revolution time distribution.

Two different experiments have been performed with the FRS-ESR. In the first experiment the full $B\rho$ -acceptance ($\approx 1.2 \cdot 10^{-3}$) of the ring was used. In the second experiment the $B\rho$ -resolving power of the ion optical system of the FRS was used to define the $B\rho$ window of the injected fragments. The selected $B\rho$ window ($\approx 1.4 \cdot 10^{-4}$) was realized with slits (± 0.5 mm) at the central focal plane of the FRS. Taking into account the results from the contribution of the ToF detector and CFD method we analyzed particles with at least 200 turns. The results of both experiments are shown in the upper panel of figure 6.12. The observation

is that even for the most isochronous ions σ_T is larger than 0.5 ps demonstrating that for the different mass-to-charge ratios of the stored ions the overall measured σ_T values could have only a minor contribution from the ToF detector and CFD method. Note that for $m/q = 2.66$, corresponding to $^{133}\text{Sn}^{50+}$, the isochronicity ($\gamma_t = 1.41594$) of the ESR was tuned. The latter hypothesis is in the following verified with MOCADI simulations including the ion-optical properties of the ESR. The ring optics was included in the simulations with a transfer matrix of 3rd order [Wei15], see table in appendix A.3.

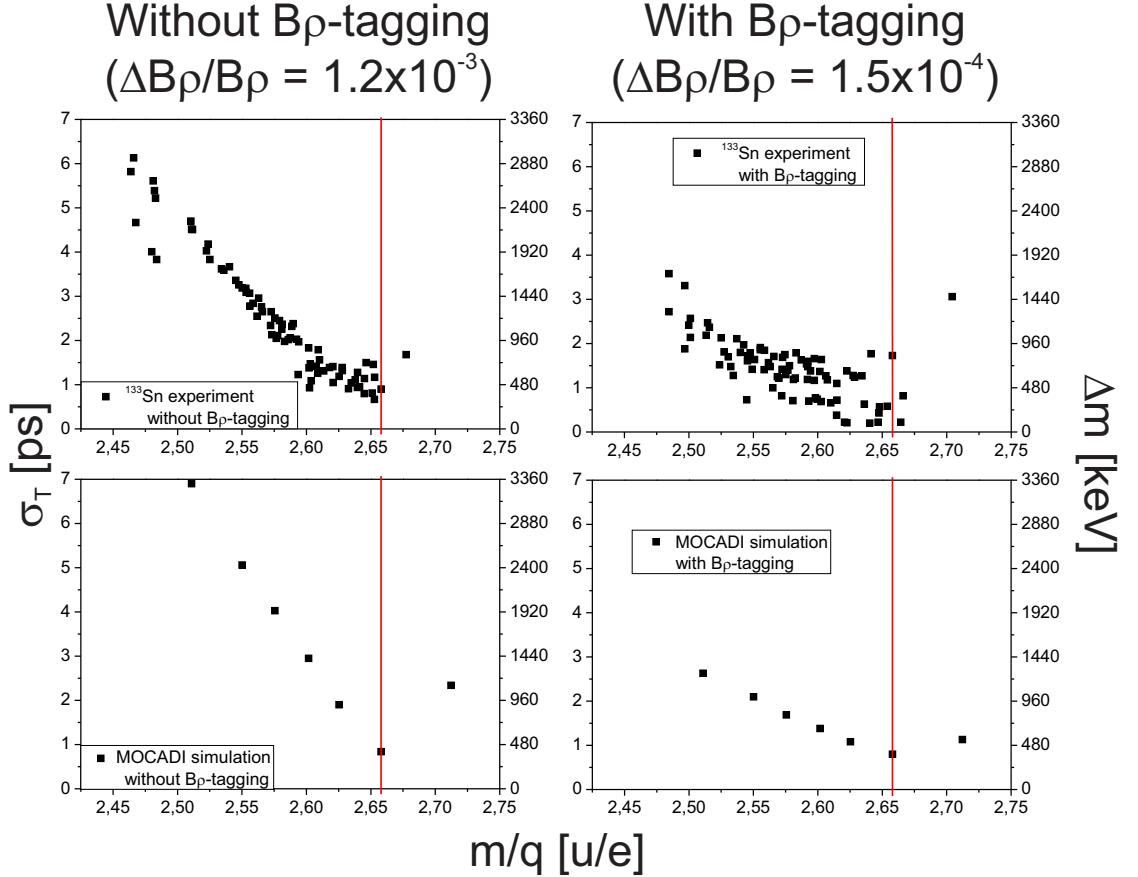


Figure 6.12.: Measured revolution time uncertainties versus m/q for experimental data (upper row) and calculated MOCADI results (lower row). The results without $B\rho$ -tagging are shown in the left hand columns, the results with $B\rho$ -tagging are shown in the right hand columns. The m/q value of the reference nuclei ^{133}Sn is indicated with the red vertical line.

We have used 10,000 particles in the MOCADI simulation (see chapter 8 for a discription of MOCADI) with a mean $B\rho = 8.28039$ Tm. The $B\rho$ window in the simulation was set to the experimental slit conditions for the ions injected in the ESR. The m/q of the simulated ions was varied from 2.5 to 2.8 and the recorded time of flights for different turns were analyzed with the "mtrace" program in the same way as the experimental data.

The results of the simulation are presented in the lower panel of figure 6.12 and demonstrate excellent quantitative agreement with the measurements. This means our hypothesis is verified.

The previous investigation gives us confidence that the simulation reflects the experimental conditions and limitations well. An interesting question in this respect is, which value of the $B\rho$ -tagging is necessary to obtain $\sigma_T = 1$ ps for the complete m/q range. This would guide the future goal of velocity measurements with the dual ToF system. The result is illustrated in figure 6.13 and shows that $\Delta B\rho/B\rho = 5 \cdot 10^{-5}$ would be needed. This condition corresponds to a velocity accuracy of $2.5 \cdot 10^{-5}$. The geometry and performance of the dual ToF detector system will fulfill this requirement.

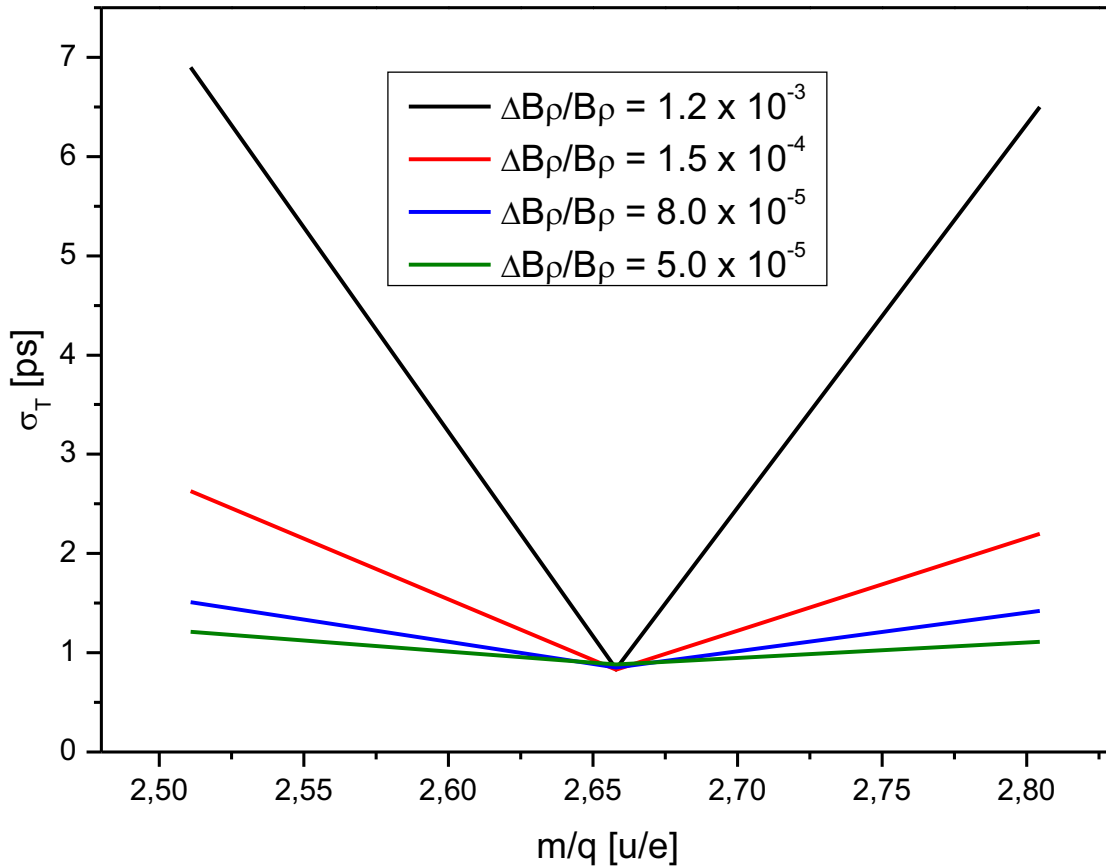


Figure 6.13.: Simulated uncertainties of the revolution time versus m/q for different $B\rho$ -definitions. The calculated σ_T values are only determined by the non-isochronicity of the ring and additional detector effects are excluded.

In total this means that for particles with more than 200 turns the uncertainty of the determination of the revolution time is mainly determined by the non-isochronicity of the ring. The uncertainty of the revolution time yields the mass resolving power (equation 4.17), which is given, for example, for the reference nuclide ^{133}Sn with $T = 511$ ns, $\gamma_t = 1.41$, $\sigma_T(\text{det}) = 0.5$ ps and $\sigma_T(\text{iso}) = 0.8$ ps

to be

$$R = \frac{m}{\Delta m} = \frac{1}{\gamma_t^2} \frac{T}{\Delta T} = \frac{1}{\gamma_t^2} \frac{T}{\sqrt{\sigma_T(det)^2 + \sigma_T(iso)^2}} = 270,000 \quad (6.51)$$

After unambiguous identification the final mass is evaluated by the correlation-matrix method that yields presently a systematic error of ≈ 180 keV (see chapter 7). A summary of all major contributions to the achieved mass resolving power from the experimental components and analysis procedure is illustrated in figure 6.14.

6. Data Analysis of Measurements with and without Accurate Momentum Definition in the FRS

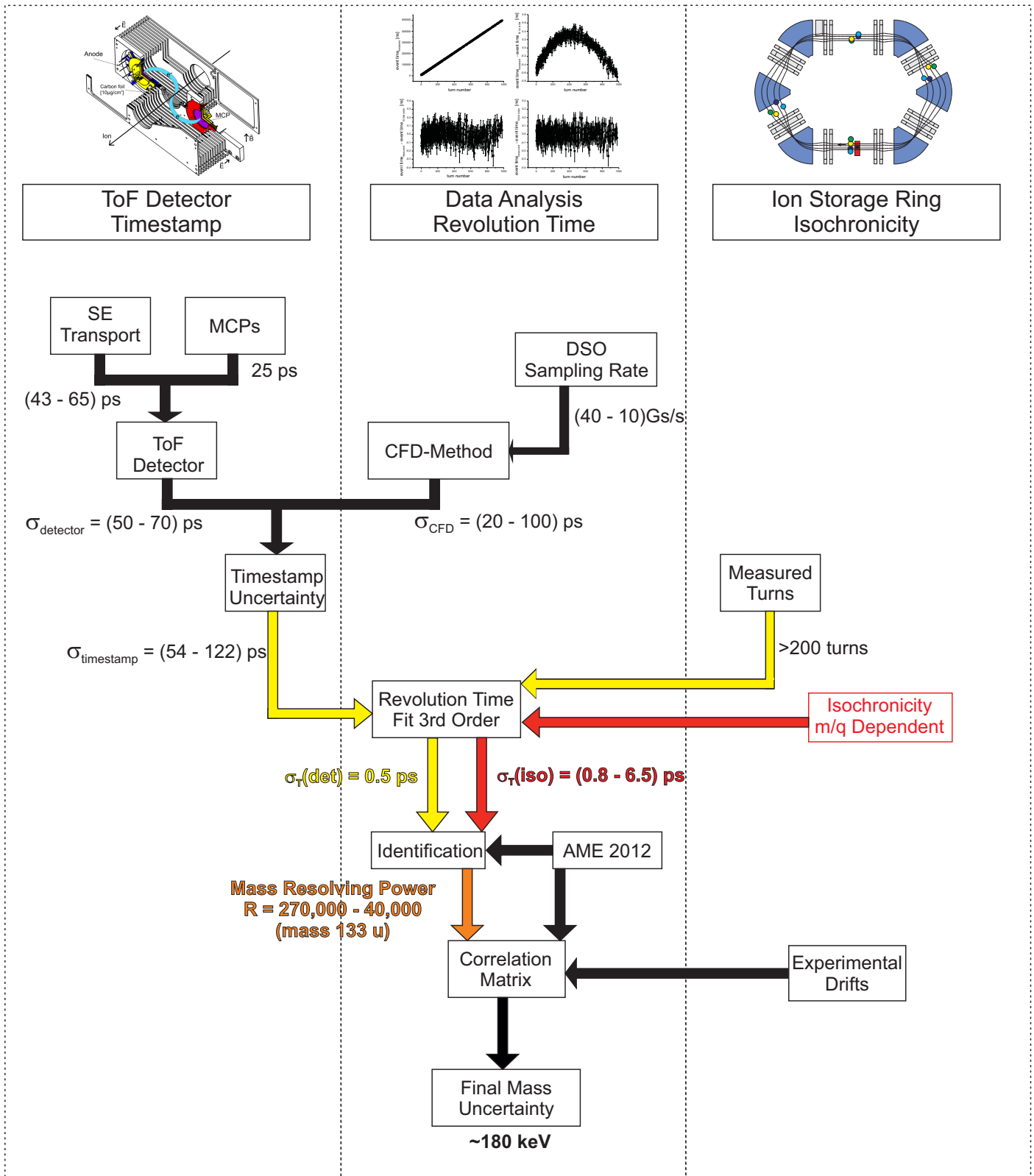


Figure 6.14.: Contributions to the achieved mass resolving power of IMS in the ESR from the experimental components and analysis procedure.

7. Results

A 410 MeV/u ^{238}U projectile beam was extracted from the synchrotron SIS-18 with an average intensity of $1 \cdot 10^9/\text{spill}$ and impinged on a 1032 mg/cm^2 beryllium target at the entrance of the fragment separator FRS. Neutron-rich fission fragments created via abrasion-fission were separated in flight with the FRS applying pure magnetic rigidity ($B\rho$) separation with the standard ion-optical operation mode. The separation mode, without degraders, was enabled by the large mean velocity difference of the projectile fragments and fission products and the restricted angular acceptance of the FRS. Practically this means, a suitable $B\rho$ -selection with the FRS can provide fission fragment beams without significant contributions of projectile fragments. The ions of interest were injected into the Experimental Storage Ring ESR for IMS at a mean velocity corresponding to the transition energy of $\gamma_t = 1.41$. The magnetic fields of the FRS and ESR were set for $^{133,135,136}\text{Sn}$ ions in different runs, i.e., these isotopes were subsequently centered at the optical axis. The ESR was operated in the isochronous mode [HAB+00] without application of any cooling.

IMS measurements have been performed with and without $B\rho$ -tagging for the same 2 settings of the magnetic fields of the FRS and ESR. The signals of the ToF detector were recorded with commercial digital oscilloscopes (Tektronix TDS 6154C, 40 GS/s, 15 GHz; LeCroy LC584AM, 4 GS/s, 1 GHz). The data sets of the two different experiments, with and without $B\rho$ -tagging, were combined and analysed with the new correlation-matrix method [Pat15] as described in chapter 6. The advantage of this new analysis is that it is possible to include ions with very low statistics down to a few events of a single isotope. An overview of each experimental setting can be found in table 7.1.

Table 7.1.: Experimental field settings for different isochronous centered ions.

| Centered Isochronous Ion | $B\rho$ | Energy [MeV/u] | $B\rho$ -tagging |
|--------------------------|---------|----------------|------------------|
| $^{130}\text{Sn}^{50+}$ | 7.505 | 340.326 | without |
| $^{131}\text{Sn}^{50+}$ | 7.969 | 372.425 | without |
| $^{133}\text{Sn}^{50+}$ | 8.189 | 380.169 | without |
| $^{135}\text{Sn}^{50+}$ | 8.314 | 380.256 | without |
| $^{133}\text{Sn}^{50+}$ | 8.222 | 382.792 | with |
| $^{136}\text{Sn}^{50+}$ | 8.404 | 382.437 | with and without |

Previously, the experiments were analyzed separately and only for the experi-

ments with $B\rho$ -tagging the correlation-matrix method was applied. For the analysis of the experiment performed without $B\rho$ -tagging strong restrictions were applied to the analyzed m/q and isochronicity range in the past. The restrictions were [Mat04]:

- at least 50 identified ions of the same isotope
- a maximum standard deviation of the time-of-flight distribution of 2 ps
- restricted m/q range $2.56 \leq m/q \leq 2.65$

For the experiment with $B\rho$ tagging the following restrictions were applied [Knö08] [Sun08] [S⁺08]:

- the stored ions must at least circulate for 100 turns
- restricted m/q range $2.56 \leq m/q \leq 2.65$
- restriction on the fit of the revolution time: coefficient of 2nd order must be $< 2 \cdot 10^{-5}$
- ions excluded with an error of the revolution time larger than 0.5 ps

Additional condition for the minimum accepted number of particles per peak was 10 for the results presented in [Sun08] and [S⁺08] and a minimum of 5 particles per peak for the results presented in [Knö08].

In the present work there are no restrictions applied in the data analysis of both experiments with and without $B\rho$ tagging. A main goal of the present analysis is to include the most exotic nuclei with naturally low statistics that were excluded by the restrictions in past.

7.1. Reference Masses

The masses in the presented experiments have been determined by accurate revolution-time measurements of reference nuclides with well-known masses combined with the ions for which the mass values were measured for the first time. Therefore, it is valuable not only to present the new experimental data but also the reference masses used. A list of all reference masses used can be found in table 7.2. The used reference masses were measured at JYFLTRAP [JYF12]. Usually the mass value of an atom is presented in tables as mass excess (ME) defined as:

$$ME = m - A \quad , \quad (7.1)$$

where m is the mass of the atom and A is the corresponding mass number in atomic units u . The conversion from atomic units to energy the following relation $1u = 931.494061\text{MeV}/c^2$ was used [WAW12]. This mass-excess value ME , the corresponding accuracies ΔME and their literature references are tabulated. The information is also given in atomic mass units (m and Δm). Furthermore, the total number of ions for each isotope recorded in the ESR are stated.

Table 7.2.: List of used reference masses.

| Isotope | ME [keV] | ΔME [keV] | m [μu] | Δm [μu] | counts | Reference |
|-------------------|-------------|----------------------|------------------|---------------------------|--------|----------------------|
| ⁷⁹ Ga | -62547 | 1 | 78932853 | 1 | 706 | [H ⁺ 08] |
| ⁸⁰ Ga | -59223 | 2 | 79936421 | 2 | 358 | [H ⁺ 08] |
| ⁸¹ Ga | -57628 | 3 | 80938134 | 3 | 138 | [H ⁺ 08] |
| ⁸² Ga | -52930 | 2 | 81943177 | 2 | 47 | [H ⁺ 08] |
| ⁸² Ge | -65415 | 2 | 81929774 | 2 | 1181 | [H ⁺ 08] |
| ⁸³ Ge | -60976 | 2 | 82934540 | 2 | 452 | [H ⁺ 08] |
| ⁸⁵ Ge | -53123 | 3 | 84942970 | 3 | 55 | [H ⁺ 08] |
| ⁸⁵ As | -63189 | 3 | 84932164 | 3 | 1204 | [H ⁺ 08] |
| ⁸⁶ As | -58962 | 3 | 85936702 | 3 | 568 | [H ⁺ 08] |
| ⁸⁷ As | -55617 | 3 | 86940293 | 3 | 116 | [H ⁺ 08] |
| ⁸⁶ Se | -70503 | 2 | 85924312 | 2 | 4381 | [H ⁺ 08] |
| ⁸⁷ Se | -66426 | 2 | 86928689 | 2 | 4174 | [H ⁺ 08] |
| ⁸⁹ Se | -58992 | 3 | 88936669 | 3 | 455 | [H ⁺ 08] |
| ⁸⁹ Br | -68275 | 4 | 88926704 | 4 | 8130 | [R ⁺ 07] |
| ⁹⁰ Br | -64001 | 4 | 89931292 | 4 | 3350 | [R ⁺ 07] |
| ⁹² Br | -56233 | 7 | 91939631 | 8 | 164 | [R ⁺ 07] |
| ⁹⁵ Rb | -65935 | 4 | 94929216 | 4 | 7529 | [R ⁺ 07] |
| ⁹⁷ Rb | -58519 | 6 | 96937177 | 6 | 828 | [R ⁺ 07] |
| ⁹⁶ Sr | -72926 | 10 | 95921711 | 11 | 8976 | [H ⁺ 06] |
| ⁹⁷ Sr | -68587 | 10 | 96926369 | 11 | 7906 | [H ⁺ 06] |
| ¹⁰¹ Y | -65065 | 8 | 100930150 | 9 | 4049 | [H ⁺ 07b] |
| ¹⁰³ Y | -58457 | 11 | 102937244 | 12 | 59 | [H ⁺ 11] |
| ¹⁰¹ Zr | -73164 | 10 | 100921455 | 11 | 7689 | [H ⁺ 06] |
| ¹⁰³ Zr | -67819 | 10 | 102927193 | 11 | 4079 | [H ⁺ 06] |
| ¹⁰⁵ Nb | -69907 | 5 | 104924952 | 5 | 405 | [H ⁺ 07b] |
| ¹⁰⁷ Nb | -63715 | 9 | 106931599 | 10 | 1231 | [H ⁺ 07b] |
| ¹⁰⁸ Nb | -59545 | 9 | 107936076 | 10 | 390 | [H ⁺ 11] |
| ¹⁰⁹ Mo | -66670 | 12 | 108928427 | 13 | 1390 | [H ⁺ 06] |
| ¹¹⁰ Mo | -64547 | 24 | 109930706 | 26 | 172 | [H ⁺ 06] |
| ¹¹¹ Mo | -59933 | 13 | 110935659 | 14 | 95 | [H ⁺ 11] |
| ¹¹¹ Tc | -69018 | 11 | 110925906 | 12 | 156 | [H ⁺ 07a] |
| ¹¹² Tc | -65250 | 6 | 111929951 | 6 | 886 | [H ⁺ 07a] |
| ¹¹³ Tc | -62812 | 4 | 112932569 | 4 | 368 | [H ⁺ 11] |
| ¹¹² Ru | -75624 | 10 | 111918814 | 11 | 1284 | [H ⁺ 07a] |
| ¹¹⁴ Ru | -70221 | 4 | 113924615 | 4 | 36 | [H ⁺ 11] |
| ¹¹⁵ Ru | -66071 | 8 | 114929070 | 9 | 580 | [H ⁺ 07a] |
| ¹¹⁶ Ru | -64069 | 4 | 115931219 | 4 | 158 | [H ⁺ 11] |

| Isotope | ME [keV] | Δ ME [keV] | m [μ u] | Δ m [μ u] | counts | Reference |
|-------------------|-------------|----------------------|-----------------|--------------------------|--------|----------------------|
| ^{118}Rh | -64894 | 24 | 117930333 | 26 | 331 | [H ⁺ 07a] |
| ^{119}Rh | -62823 | 10 | 118932557 | 11 | 118 | [H ⁺ 11] |
| ^{119}Pd | -71415 | 9 | 118923333 | 10 | 55 | [H ⁺ 07a] |
| ^{122}Pd | -64616 | 19 | 121930632 | 20 | 43 | [H ⁺ 11] |
| ^{131}In | -68025 | 2 | 130926972 | 2 | 19 | [H ⁺ 12a] |
| ^{133}Sn | -70874 | 2 | 132923914 | 2 | 184 | [H ⁺ 12a] |
| ^{133}Sb | -78921 | 4 | 132915275 | 4 | 128 | [H ⁺ 12a] |
| ^{135}Sb | -69689 | 2 | 134925186 | 2 | 1892 | [H ⁺ 12a] |
| ^{135}Te | -77727 | 2 | 134916557 | 2 | 2606 | [H ⁺ 12a] |
| ^{136}Te | -74425 | 2 | 135920101 | 2 | 14 | [H ⁺ 12a] |

Our systematic error, as stated in equation 6.47, was determined in the following way. The masses of N reference isotopes (table 7.2) were separately evaluated by excluding always the one to be determined but using all other N-1 reference masses for the calculation of the systematic error. The mass difference between the reference masses and the corresponding mass value of this work is shown in figure 7.1. The result of this analysis was a systematical error of 172 keV.

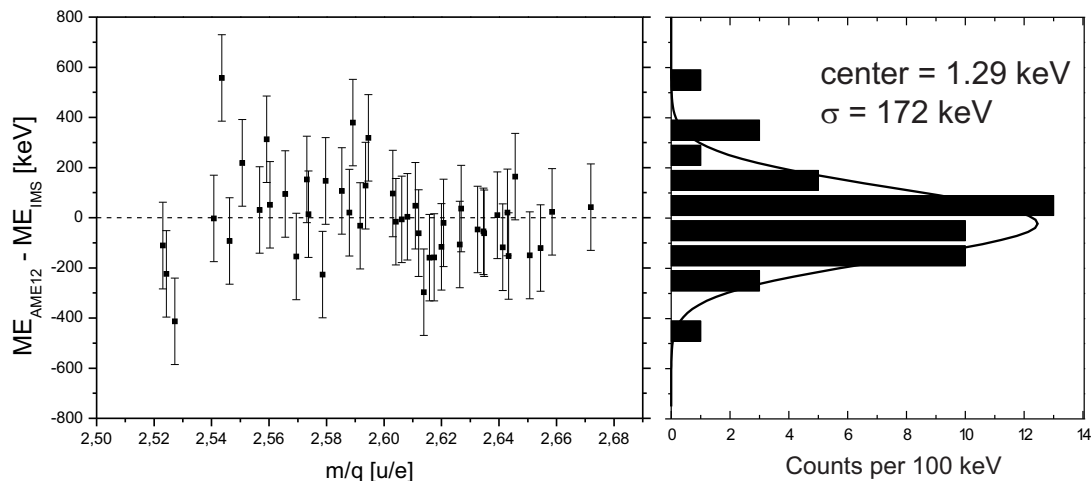


Figure 7.1.: The mass difference between reference mass [JYF12] and this work is shown on the left hand side. On the right side the projection of the deviation to the reference is plotted. From this analysis the systematic error of the new mass measurements was deduced.

7.2. New Masses

For neutron-rich isotopes ($Z = 30$ to 60) 25 masses were measured for the first time. The masses are shown in table 7.3. The columns have the same meaning as defined in table 7.2. The errors ΔME and Δm represent the total uncertainties with the contributions discussed in detail in the previous chapter. A comparison to the extrapolated mass values of the AME12 [WAW12] is shown in figure 7.2.

Table 7.3.: List of masses measured for the first time.

| Isotope | ME [keV] | ΔME [keV] | m [μu] | Δm [μu] | counts |
|-------------------|-------------|----------------------|------------------|---------------------------|--------|
| ⁸⁶ Ge | -49406 | 175 | 85946960 | 188 | 30 |
| ⁹¹ Se | -50577 | 173 | 90945703 | 185 | 16 |
| ⁹⁴ Br | -46812 | 398 | 93949745 | 428 | 9 |
| ¹⁰⁵ Y | -51280 | 528 | 104944949 | 567 | 5 |
| ¹⁰⁶ Zr | -58547 | 173 | 105937147 | 185 | 120 |
| ¹⁰⁷ Zr | -54382 | 491 | 106941619 | 528 | 11 |
| ¹¹⁰ Nb | -52315 | 336 | 109943838 | 361 | 3 |
| ¹¹³ Mo | -53402 | 323 | 112942671 | 347 | 3 |
| ¹¹⁴ Tc | -58595 | 173 | 113937096 | 185 | 61 |
| ¹¹⁵ Tc | -56323 | 330 | 114939535 | 354 | 9 |
| ¹¹⁸ Ru | -57633 | 204 | 117938128 | 219 | 2 |
| ¹²¹ Rh | -56265 | 271 | 120939597 | 290 | 2 |
| ¹²³ Pd | -60428 | 331 | 122935128 | 355 | 10 |
| ¹²⁴ Pd | -60200 | 387 | 123935373 | 415 | 4 |
| ¹²⁶ Ag | -61411 | 328 | 125934073 | 353 | 14 |
| ¹²⁹ Cd | -63145 | 173 | 128932211 | 186 | 18 |
| ¹³¹ Cd | -55583 | 961 | 130940329 | 1032 | 2 |
| ¹³⁸ Sb | -54253 | 439 | 137941757 | 471 | 9 |
| ¹⁴¹ I | -60023 | 173 | 140935563 | 185 | 177 |
| ¹⁴³ I | -50178 | 486 | 142946132 | 522 | 6 |
| ¹⁴⁹ Ba | -53124 | 175 | 148942969 | 188 | 29 |
| ¹⁵⁰ Ba | -51482 | 377 | 149944732 | 405 | 3 |
| ¹⁵⁰ La | -56135 | 174 | 149939737 | 187 | 26 |
| ¹⁵¹ La | -53308 | 174 | 150942772 | 187 | 47 |
| ¹⁵⁴ Ce | -52543 | 590 | 153943593 | 633 | 6 |

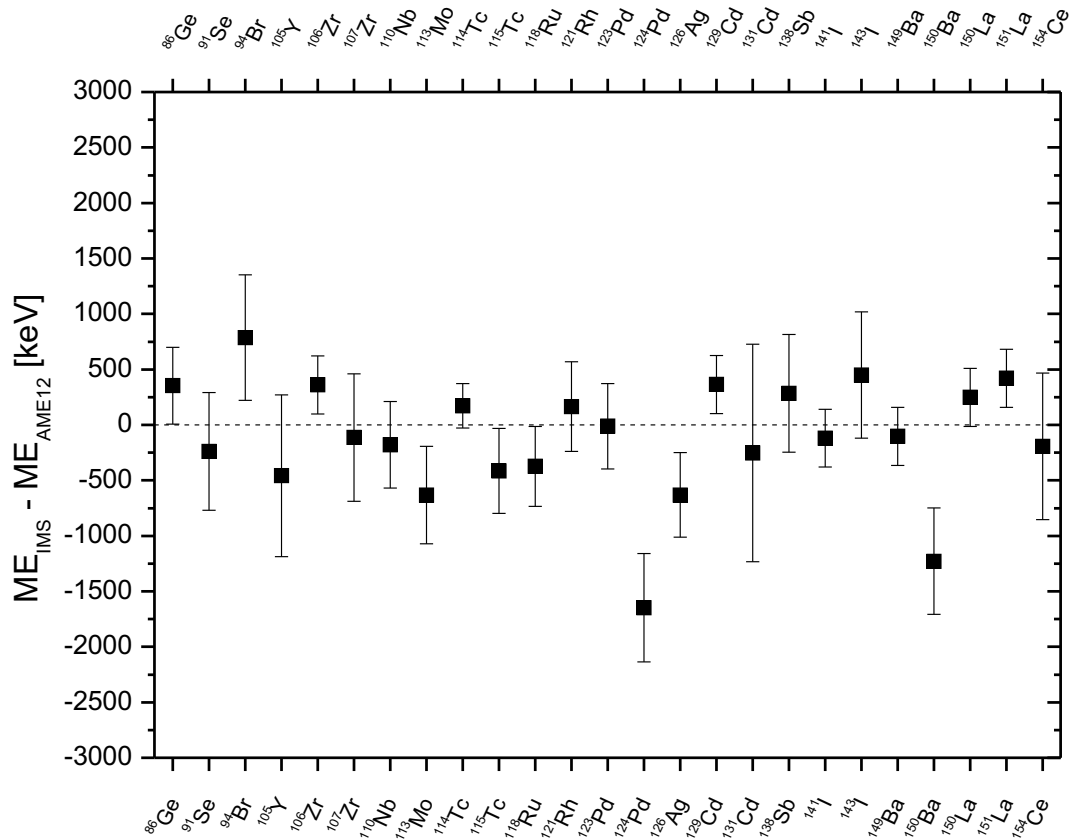


Figure 7.2.: The mass difference between extrapolated mass values stated in the AME12 and this work against the mass number A is shown for nuclides measured for the first time.

In comparison to the extrapolated mass values of the AME12 the masses obtained in this work are within ± 500 keV for almost all measured nuclides and therefore in good agreement. The largest deviation to the AME12 was observed for ^{124}Pd and is 1.6 MeV. In general, there is a slight tendency observed that the extrapolated mass values have lower mass-excess values. The mean value of the projection is about -120 keV.

7.3. Improved Masses

Besides newly measured masses also known masses could be remeasured and the uncertainty of the mass value could be improved. The mass value of ^{130}Cd could be measured directly for the first time and is listed together with the improved masses in table 7.4 and shown in figure 7.3.

Table 7.4.: List of masses with improved uncertainty.

| Isotope | ME [keV] | ΔME [keV] | m [μu] | Δm [μu] | counts |
|---------------------|-------------|----------------------------|------------------|---------------------------|--------|
| ^{93}Br | -52884 | 172 | 92943227 | 185 | 79 |
| ^{109}Nb | -56690 | 172 | 108939141 | 185 | 76 |
| ^{117}Ru | -59493 | 173 | 116936132 | 185 | 33 |
| ^{125}Ag | -64514 | 173 | 124930741 | 185 | 66 |
| $^{130}\text{Cd}^1$ | -62131 | 438 | 129933300 | 471 | 5 |
| ^{137}Sb | -60620 | 173 | 136934922 | 186 | 94 |
| ^{140}I | -63529 | 173 | 139931799 | 185 | 750 |

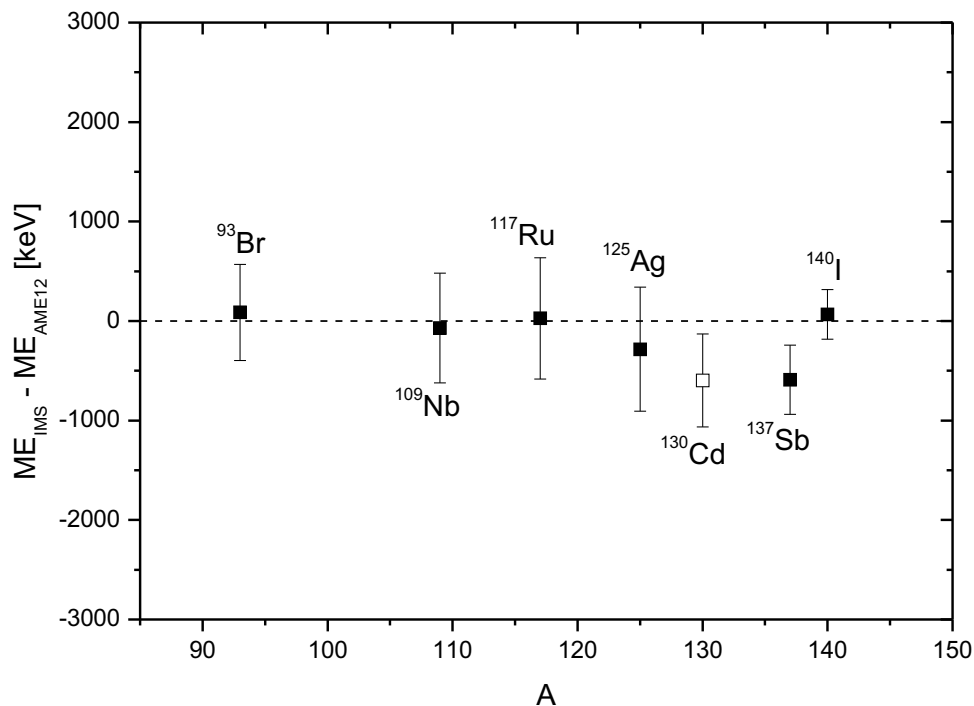


Figure 7.3.: The mass difference between mass values stated in the AME12 and this work against the mass number A is shown. The identification of the nuclide is labeled for each data point.

¹measured directly for the first time

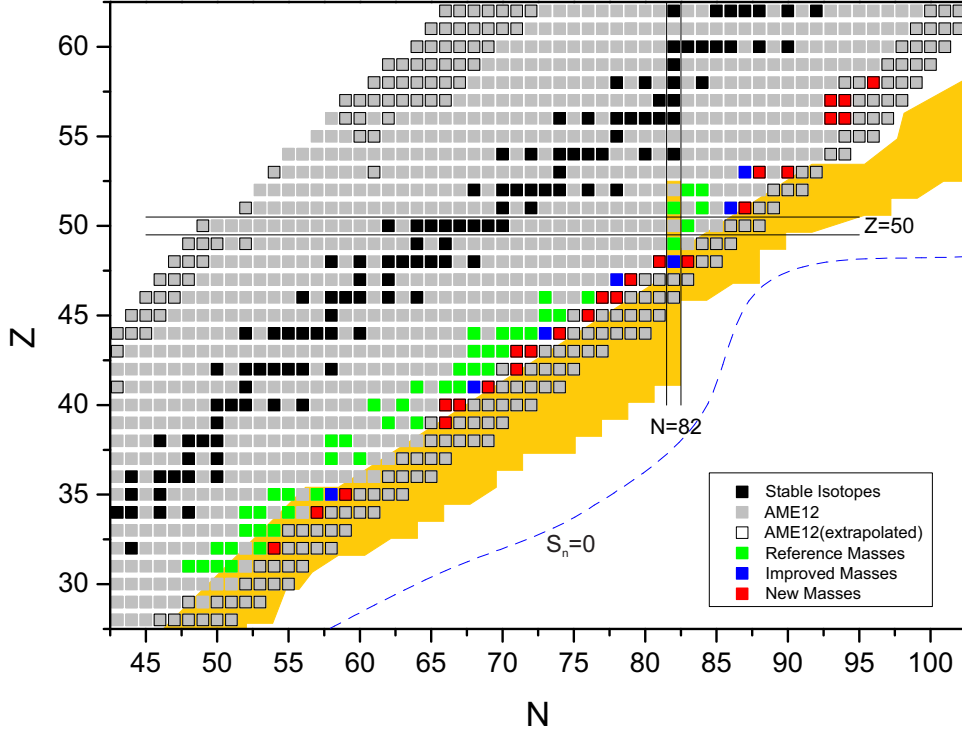


Figure 7.4.: The 25 new masses covered in the present analysis (red squares), the improved masses (blue squares), and reference masses (green squares) are presented in the chart of nuclides.

Other established results from mass measurements to discuss the evolution of nuclear structure and shells are the nucleon separation energies and their derivatives. The one-neutron separation energy S_n and the pairing gap energy $\Delta_n^{(3)}$ is defined by:

$$S_n = -M(Z, N) + M(Z, N - 1) + M(0, 1) \quad (7.2)$$

$$\Delta_n^{(3)} = (-1)^N \frac{1}{2} [S_n(Z, N) - S_n(Z, N + 1)] \quad (7.3)$$

$M(Z, N)$ is the mass of the nucleus with proton number Z and neutron number N , and m_n is the neutron mass.

According to [B⁺12] and [A⁺14] the isotopes $^{130,131}\text{Cd}$ are candidates with high impact on the astrophysical r-process. The masses of those two isotopes were measured for the first time directly in this work. The corresponding one-neutron separation energy S_n for cadmium isotopes including the new masses together with tin isotopes from the AME12 are shown in figure 7.5. The peak in the $\Delta_n^{(3)}(Z, N)$ values is evidence of a shell closure for cadmium at $N=82$.

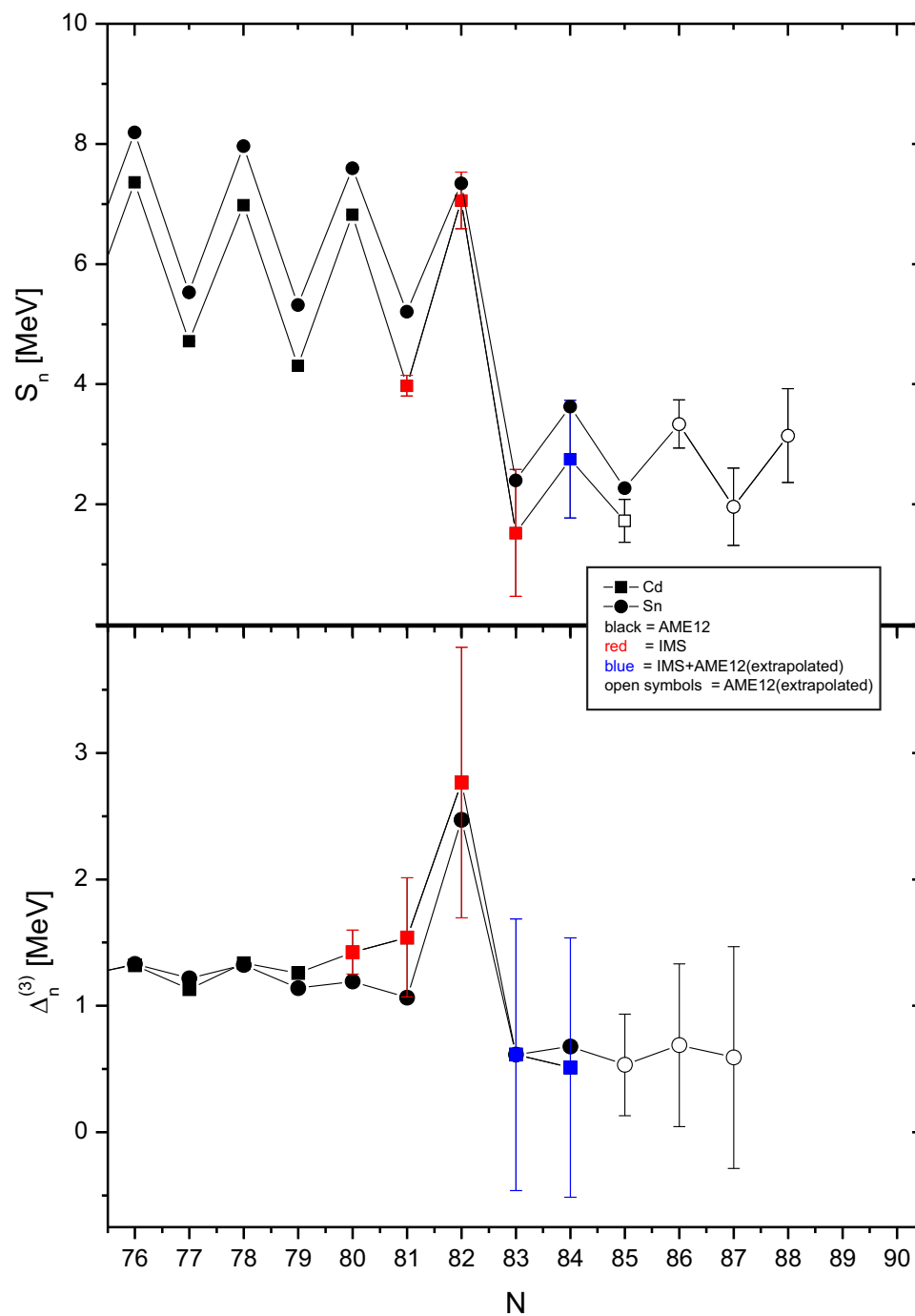


Figure 7.5.: In the upper panel experimental one-neutron separation energies (S_n) are shown for Cd and Sn isotopes. In the lower panel the corresponding pairing-gap energies are presented.

7.4. Comparison with Theory

Results of new mass measurements are an important benchmark test of the predictive power of theoretical models. In figure 7.6 a representative comparison of our new and improved mass values for iodine isotopes with different mass models. The models are based on microscopic-macroscopic descriptions [A⁺95] [P⁺96] [MNMS95] [W⁺13b], the Hartree-Fock-Bogoliubov (HFB) theory [D⁺96] and the shell-model inspired model of Duflo-Zuker [DZ99]. It is clearly seen that the deviation becomes largest for the most neutron-rich ions, i.e. the previously experimentally unknown masses. The predictive power of the different models can be quantitatively characterized by the σ_{rms} values. They are listed in table 7.5 for iodine isotopes.

Table 7.5.: Comparison of measured data with models. RMS deviations for I isotopes for different theoretical models are presented. In this comparison the new IMS values and the tabulated experimental values of AME12 are included.

| | $\sigma_{\text{rms},1}$ [keV] | $\sigma_{\text{rms},2}$ [keV] |
|-----------------------------|----------------------------------|----------------------------------|
| FRDM [MNMS95] | 450 | 491 |
| HFB-27 [D ⁺ 96] | 317 | 413 |
| DZ28 [DZ99] | 355 | 443 |
| ETFSI-1 [A ⁺ 95] | 376 | 310 |
| ETFSI-Q [P ⁺ 96] | 363 | 349 |
| WS3 [W ⁺ 13b] | 360 | 391 |

It is interesting also to compare the one-neutron separation energies (S_n) for the new masses with the same theoretical models used for the comparison of the mass excess values. In some regions of the mass surface the difference of the experimental and theoretical S_n values are normally systematically smaller than the corresponding comparison with the direct mass or ME values, because deficiencies of models can cancel in differences. Looking to the comparison in figure 7.7, one observes that the differences of experimental and theoretical S_n values reach similar large discrepancy as observed with the ME-value comparison.

Further investigations on the impact on the nuclear structure of the new masses are currently in progress and will be presented in a future publication.

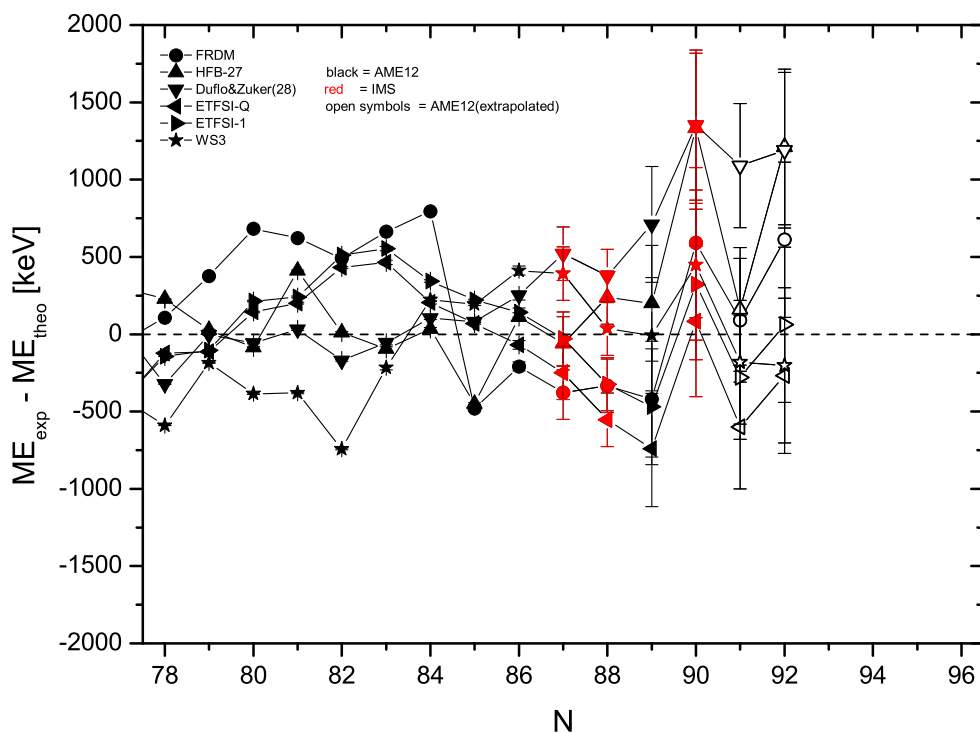


Figure 7.6.: The mass predictions of different theories and experimental results are shown for iodine isotopes.

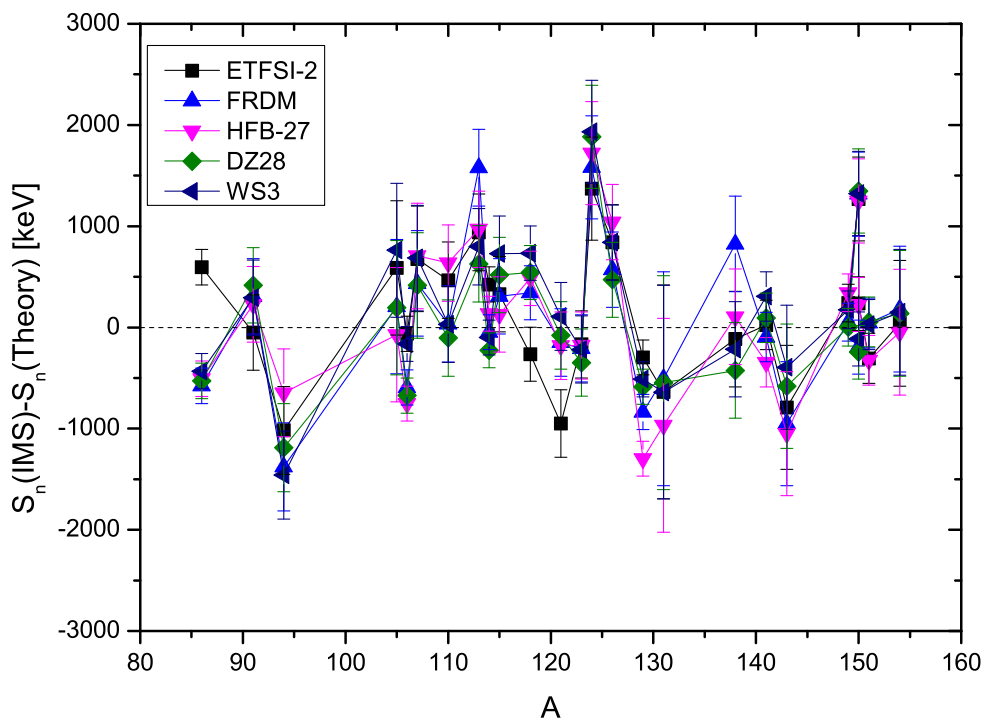


Figure 7.7.: Differences between measured S_n values and theoretical predictions.

8. Simulations for the new CR ToF detector

The second main part of this work concentrates on the simulations and design of a new dual ToF detector system that will be installed at the future facility FAIR for advanced isochronous mass spectrometry in the new collector ring CR within the ILIMA collaboration [W⁺13a]. For the design of the new detector certain requirements have to be considered:

- the detector acceptance has to match the large emittance of the CR (see next section)
- the timing performance of the detector should be equal or better than the one of the present ESR-ToF detector
- the secondary electron transport efficiency should reach more than 75%
- a compact geometry

8.1. The Collector Ring CR at FAIR

The Collector Ring CR is a part of the planned new Facility for Antiproton and Ion Research (FAIR) in Darmstadt [GSI15]. The FAIR facility will provide access to new short-lived nuclides. The nuclides will be produced by projectile fission and fragmentation reactions and will be separated with the Super-FRS [Dra08b] [G⁺03] and injected in the CR [Dra08a]. The CR will include sextupole and octupole magnets. Besides storing and accumulating antiprotons and rare isotope beams the CR can also be used for IMS experiments. As already shown in section 6.4 the limits of the IMS are the isochronicity conditions of the ring and the velocity spread of non-isochronous ions. A lot of investigations and simulations have already been performed in order to achieve the best possible isochronicity condition of the new CR for future IMS experiments [D⁺07] [D⁺11] [L⁺13].

One of the most important changes for IMS will be the implementation of the new dual ToF detector system, which will be placed in the straight section with a distance of approximately 22 m. The dual ToF detector system allows the measurement of the revolution time and the velocity of the circulating particles.

The additional velocity measurement will be a functional substitution of the $B\rho$ -tagging. $B\rho$ -tagging with a position measurement of the ions with the FRS after fast extracted beams is not possible presently due to technical limitations. Figure 8.1 shows the layout of the future CR including the new dual ToF detector system. The mass resolving power of IMS experiments is mainly determined by the isochronicity of the ring and the timing performance of the ToF detector as outlined in the previous chapters.

8.2. Foil Diameter

The new ToF detector will be installed in the new collector ring (CR). Simulations of the isochronous mode in the planned CR have been performed with the Monte Carlo program MOCADI. Excerpt from the MOCADI documentation [MOC15]:

”MOCADI is a Monte Carlo simulation program to calculate the transport of primary beams, projectile fragments, and fission fragments or fusion products [M⁺07] through ion optical systems described by third or fifth order transfer matrices and through layers of matter. The ion optical matrices can be calculated with the program GICOSY. Currently, input data describing the FRS with all branches, other fragment separators and storage rings are available for different ion optical settings. Atomic interactions [S⁺94] [S⁺96] and nuclear interactions of relativistic heavy ions with matter are calculated according to [I⁺97].”

The following ion optical coordinates are defined [Wol87c] [Wol87b] and also used in the simulations:

$$X \tag{8.1}$$

$$A = \frac{p_x}{p_0} \tag{8.2}$$

$$Y \tag{8.3}$$

$$B = \frac{p_y}{p_0} \tag{8.4}$$

$$E = E_0(1 + \delta) \tag{8.5}$$

$$T = T_0(1 + t) \tag{8.6}$$

where X is the horizontal and Y the transversal position of the particle relative to the optical axis, A and B the corresponding angles, p_x the horizontal component of the momentum, p_y the transversal component of the momentum, p_0 the momentum of the reference particle, E and T the corresponding energy and time deviations compared to a reference particle (index 0) respectively. Using this nomenclature the behavior of particles in electromagnetic fields can be described with transfer matrices. For each ion-optical element a transfer matrix has to be calculated. The final transfer matrix for a complex system with many ion-optical elements is the result of the multiplication of every single transfer matrix along

the path.

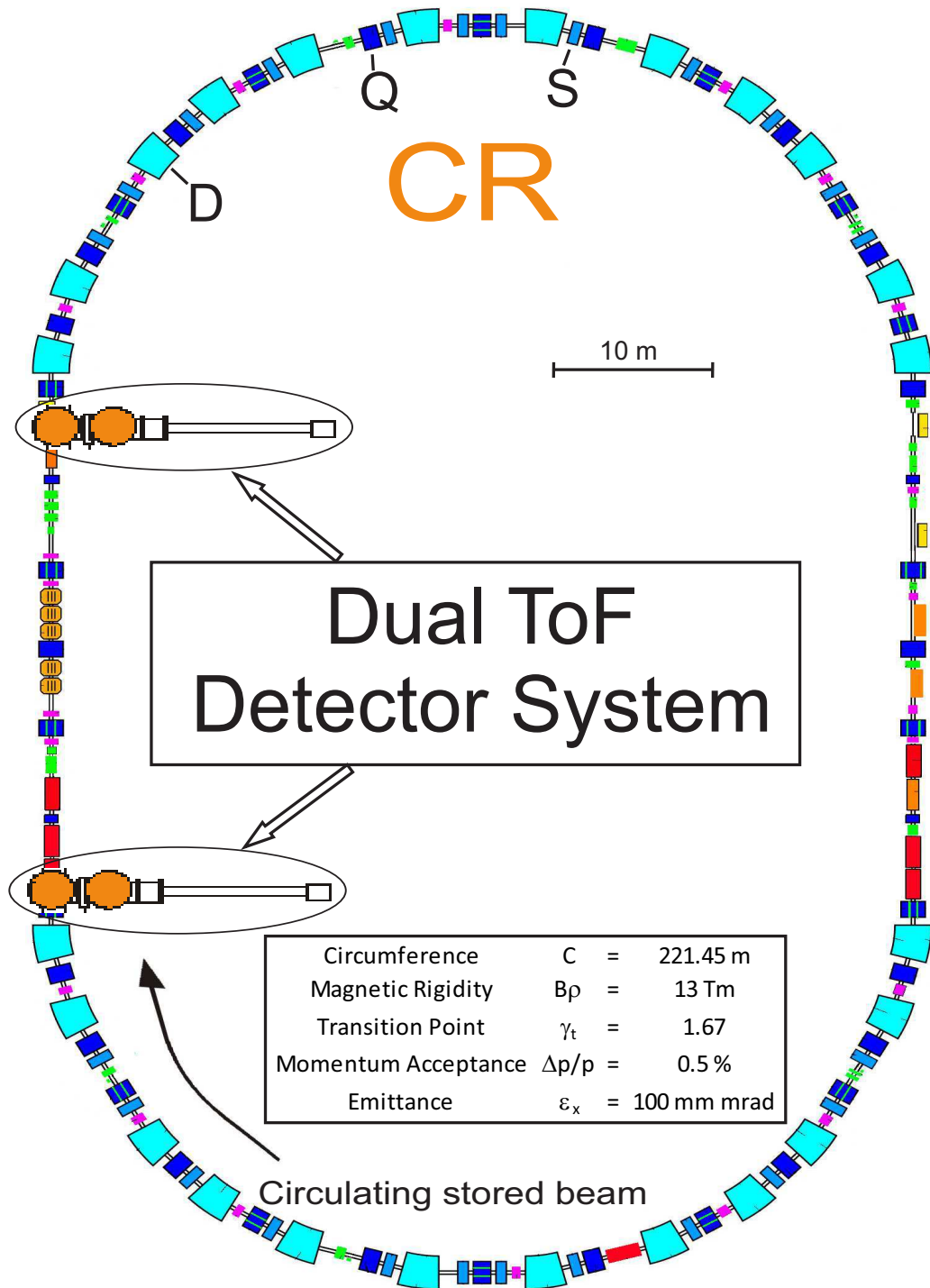


Figure 8.1.: The lattice of the Collector Ring (CR) with the new dual ToF detector system is shown. The dipole (D), quadrupole (Q) and sextupole (S) magnets are used to store the ions in the ring. For IMS the new dual ToF detector system will be placed in the straight section. The distance between the two detectors is approximately 22 m. The main ring parameters for the isochronous mode are listed in the insert.

Based on the transfer matrices calculated for the isochronous setting (CR68-iso) by S. Litvinov [Lit08] simulations for the ToF detector system have been performed with MOCADI. In general, the existing ToF detector design cannot efficiently be used in the new ring because the emittance of the CR is approximately 14 times larger than the one of the ESR, which means the geometrical aperture (i.e. the foil diameter) of the existing detector is simply too small and causes a significant beam loss after a few turns. An overall comparison between the ring parameters of the existing ESR and the future CR can be found in table 8.1.

Table 8.1.: Comparison between ESR and CR ring parameters in the isochronous mode

| | ESR | CR |
|-----------------------------------|-----------|-------------|
| Circumference | 108.36 m | 221.45 m |
| Maximum magnetic rigidity $B\rho$ | 6.4 Tm | 13 Tm |
| Transition point γ_t | 1.41 | 1.67 |
| Momentum acceptance $\Delta p/p$ | 0.2% | 0.5% |
| Emittance | 7 mm mrad | 100 mm mrad |

In the MOCADI simulations 10000 $^{157}\text{Sn}^{+50}$ ($m/q=3.14$) were uniformly distributed in the center of the straight section opposite to the two TOF detectors. The distribution was chosen according to the emittance ($\epsilon_x = \epsilon_y = 100$ mm mrad) of the CR in isochronous mode $\gamma_t = 1.67$:

Number of particles : 10000

Initial energy E_0 [MeV/u] : 620.5191 ± 0.625 (uniformly distributed)

Mass of particle [u] : 157.0639

Phase space distribution XA : $(X/3.22)^2 + (A/3.11)^2 \leq 1$ (elliptically distributed)

Phase space distribution YB : $(Y/2.71)^2 + (B/3.69)^2 \leq 1$ (elliptically distributed)

The results of the simulations for different foil diameter are shown in figure 8.2. It can be seen that the much larger emittance of the CR requires a new detector with a much larger foil diameter. A foil diameter of 80 mm was chosen even though larger foil diameters would yield a higher transmission. Nevertheless, there are several reasons to not exceed a 80 mm diameter:

First of all the practical feasibility of self supporting thin foils ($10\mu\text{g}/\text{cm}^2$) with diameters > 80 mm is doubtful and the production is not possible with existing devices [Sei13]. Increasing the thickness of the foils to improve the mechanic stability reduces the number of turns ions survive in the ring, which excludes this option since the number of turns in the ring is one of the most important criteria

for a high resolving mass measurement. (see chapter 6)

Secondly only MCPs with a maximum diameter of 80 mm and pore sizes of 10 μm are available [PHO14]. By increasing the foil and not increasing the MCPs or focussing one gains a higher transmission but loses in detection efficiency. Thirdly and most importantly the increase of the foil diameter also requires the increase of the total detector geometry. With only limited space available in the CR this limits the maximum size of the total detector and is already at the limit for foils with 80 mm diameter.

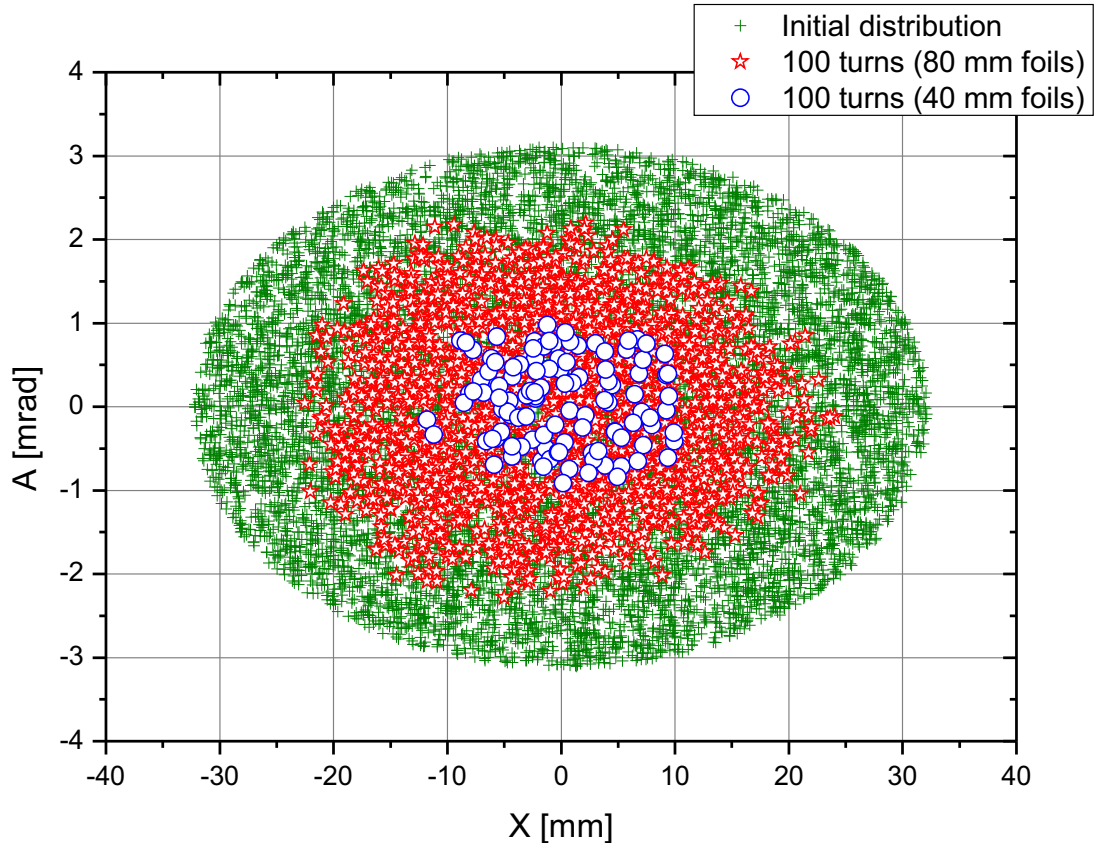


Figure 8.2.: Simulations of ions circulated in the CR with an initial distribution of 100 mm mrad (green crosses) after 100 turns. At each turn the ions penetrate two detectors with each 40 mm foil diameter (blue circles) and 80 mm foil diameter (red stars). The foil thicknesses in the simulation were $20 \mu\text{g}/\text{cm}^2$ [KF⁺13].

Simulations analog to the ones shown for the ESR (figure 6.13) were also performed and the results can be found in figure 8.3. The performance of the CR for ideal isochronous ions is better than in the ESR ($\sigma_T < 0.3$ ps in the CR compared to $\sigma_T = 0.8$ in the ESR). However, this does not hold for non-isochronous particles. For a change in m/q of 5.5% relative to the isochronous m/q σ_T increases drastically for $\Delta B\rho/B\rho > 1 \cdot 10^{-4}$. This result shows that the additional velocity measurement in the CR is mandatory. Without the additional velocity measurement accurate mass measurements for non-isochronous ions are not

possible.

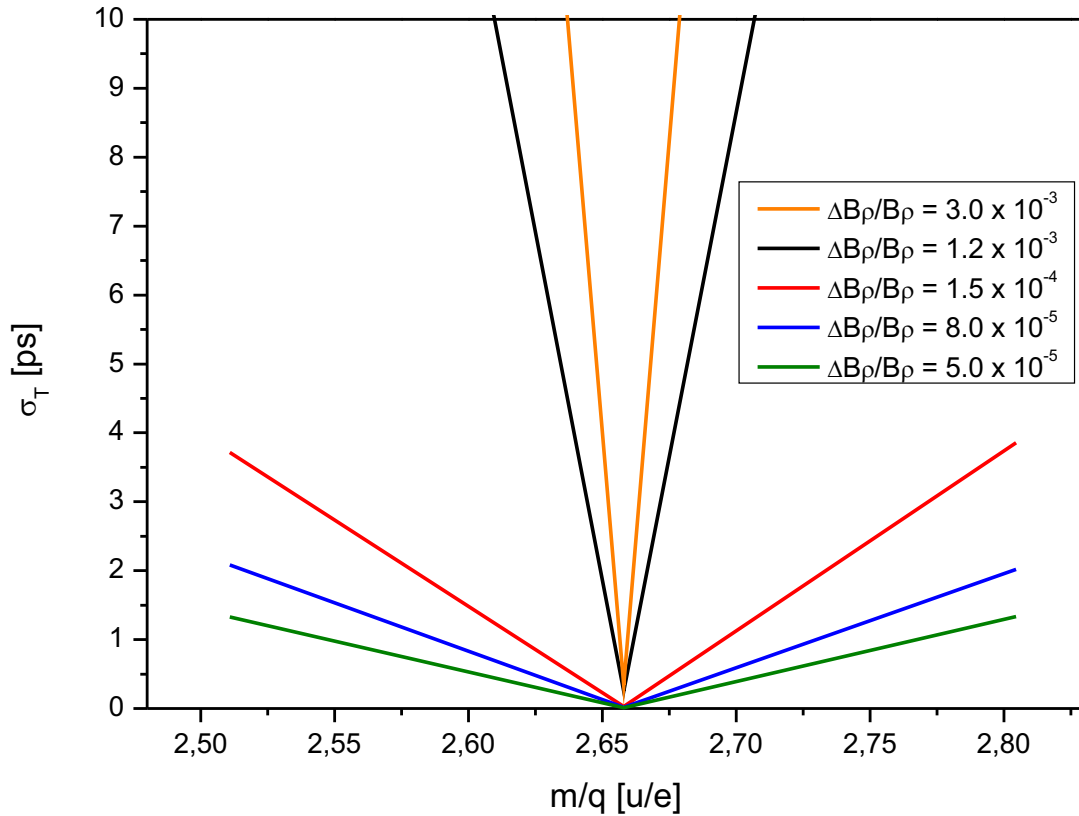


Figure 8.3.: Simulated revolution time uncertainties against m/q for different $B\rho$ -definitions.

8.3. Electron Transport

Three dimensional simulations for a new geometry of the new detector were performed and investigated in terms of electron transport efficiency and timing uncertainty σ_{detector} taking the new foil diameter of 80 mm as the starting point of the design. The simulations were performed with SIMION [MD07], which numerically solves the equations for the given physical problem. We are interested in the electron trajectories generated by electrostatic and magnetic fields. The description of the electrostatic (\vec{E}) and magnetic (\vec{B}) fields is realized by the Laplace equation for electrostatic or magnetic field potentials \vec{V} (defined as Volts or Mags in SIMION):

$$\Delta \vec{V} = \nabla^2 \vec{V} = \nabla \cdot \nabla \vec{V} = 0 \quad (8.7)$$

$$\nabla \vec{V} = (\delta \vec{V} / \delta x) i + (\delta \vec{V} / \delta y) j + (\delta \vec{V} / \delta z) k = \vec{E} \quad (8.8)$$

$$\nabla^2 \vec{V} = \nabla \cdot \vec{E} = \delta E_x / \delta x + \delta E_y / \delta y + \delta E_z / \delta z = 0 \quad (8.9)$$

The boundary conditions for the solution of the Laplace equation are given by the user as a 3 dimensional geometrical input of the electrodes or poles. In all per-

formed simulations 1000 electrons have been started uniformly distributed over the whole foil area. The kinetic energy distribution used in the simulations is a Maxwellian velocity distribution with a most likely kinetic energy of 1.8 eV as theoretically proposed [DD96]. Contrary to the first 3D simulations of the ToF detector performed by B. Fabian [Fab08] in this work both branches of the detector have been simultaneously simulated. This allows to investigate the time uncertainty for coincidences between forward and backward branch of the detector.

Furthermore, to verify the simulations, calculations for the existing ESR ToF detector were performed and the results were compared to measurements. They **agree** very well to the experimental results (figure 5.3 [Diw11]) and thus give confidence for the prediction of the performance of the new design.

The relative transport efficiencies are determined by taking the ratio of electrons hitting the MCPs and the amount of initial electrons starting from the foil. The statistical uncertainty of all stated transport efficiencies is 3%. The determination of the timing uncertainties σ_{fw} (forward) and σ_{bw} (backward) was done by simulating the ToF of the SEs from foil to the MCPs for each branch. An example of the time distribution is shown in the appendix in figure A.2. These ToF distributions were fitted with a Gaussian function

$$y = \frac{A}{w\sqrt{\pi/2}} e^{-2\frac{(x-x_c)^2}{w^2}} \quad (8.10)$$

The free fit parameters are the amplitude A of the distribution, the center of the distribution x_c and the width of the distribution w . The correlation between the width and the standard deviation σ of this distribution is simply $\sigma = w/2$. The determination of the coincidence timing uncertainty σ_{coin} was also determined by fitting the same Gaussian to the coincidence ToF distribution.

The fields and electron trajectories for the different geometries were created with the programs SIMION [MD07] and ITSIM [W⁺06] and were plotted with Origin Labs version 8.5. Geometries for SIMION simulations can be imported from computer-aided design (CAD) drawings of the realistic detector. An overview of the steps that have to be performed for each new geometry is shown in figure 8.4. The accuracy for all geometries **calculated** with SIMION was 0.5 mm. A homogeneous magnetic field of $\Delta B/B = 10^{-5}$ was used in all simulations. The results of the electron transport simulations can be found in section 9.2.

8.4. Magnetic Field

Besides the importance of the geometry of the ToF detector electrodes the ToF detector needs a homogenous magnetic field perpendicular to the electrical field in the order of 10 mT to transport the SE from the foil to the MCPs. The magnet design for the existing ESR-ToF detector is a Helmholtz-magnet and was designed

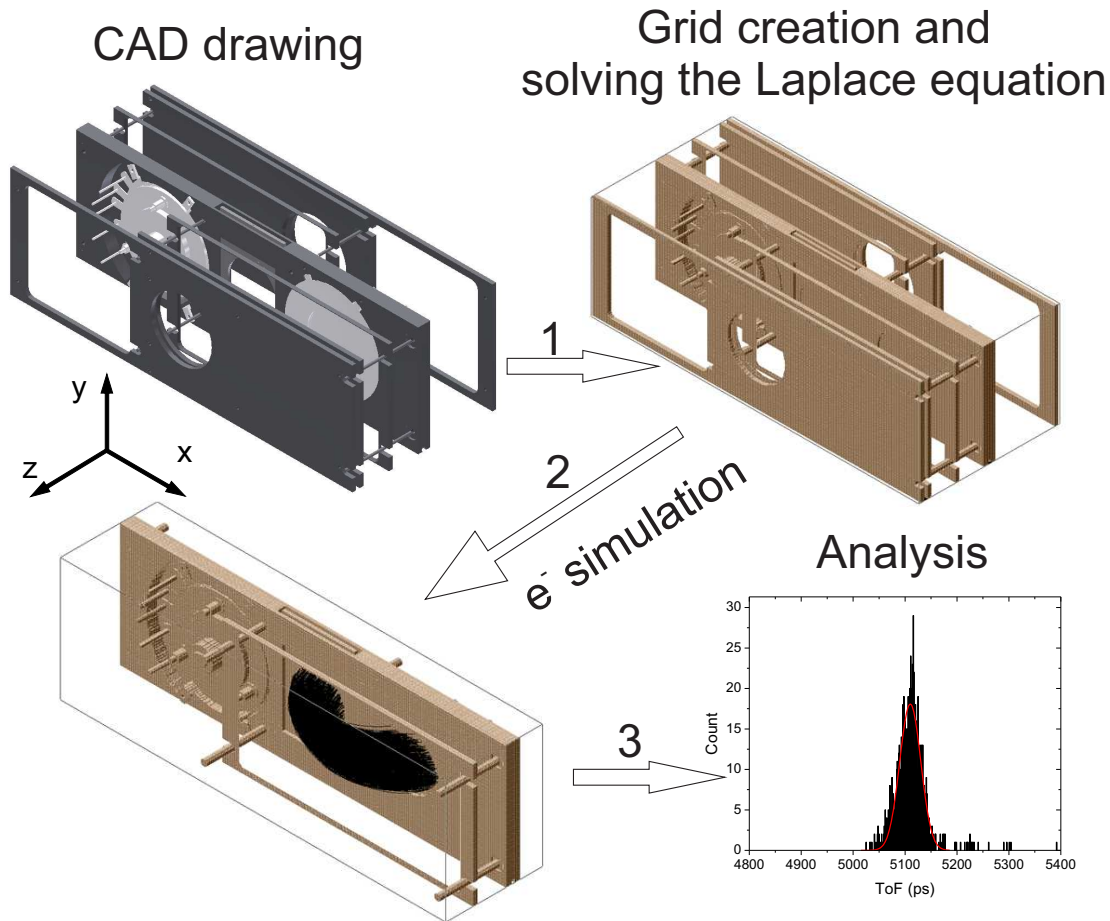


Figure 8.4.: Sequence of each step necessary to simulate the electron transport. Starting with a construction CAD drawing the geometry can be imported into a geometry grid that can be used by SIMION as boundary conditions (2). After solving the Laplace equation for the given geometry, potentials can be applied to the electrodes and electron trajectories from foil to MCPs can be simulated. The simulated flight times are then analyzed (3).

by M. Sendor in 1992 [Sen92]. To be able to place the new vacuum chamber (wall thickness 25 mm) and the new detector electrodes (y -direction = 180 mm) of the ToF detector in between the two pole shoes a gap (G_0) of at least 258 mm is necessary. With the Helmholtz-condition for the dimensions of the magnet ($G_0 = r_{\text{coil}}$) a pole-shoe radius r_{coil} of 258 mm fulfills the condition. However, this condition does not reflect the homogeneity of the magnet. The homogeneity $\Delta B/B$ can roughly be estimated with the following empirical formula found in previous simulations [Sen92] [Trö93]:

$$\frac{\Delta B}{B} = \exp(-2.77(x + 0.91)) \quad (8.11)$$

with

$$x = \frac{2(r_{\text{pole}} - r_{\text{homo}})}{G_0} \quad (8.12)$$

x can be calculated for any needed relative homogeneity and yields with formula 8.11 the needed pole-shoe radius r_{pole} for a required homogeneity radii r_{homo} and gap widths G_0 .

In case for $r_{\text{homo}} = 180$ mm and $G_0 = 258$ mm the calculated minimum pole-shoe diameter for $\Delta B/B = 0.001$ is 769 mm.

With this minimum dimension a larger magnet was designed following the example of the existing magnet of the ESR-ToF detector. The technical drawing of the calculated magnet was then imported into COMSOL [COM08]. COMSOL allows the simulation of static magnetic fields in Helmholtz-Coils for given geometries and materials. The support documentation of COMSOL gives an example on how the magnetic field of a Helmholtz-coil can be solved using the program [COM15]. The general physical equation that is solved numerically with the finite-element method (for explanation see [CS80]) is

$$\nabla \times \left(\frac{1}{\mu} \nabla \times \vec{A} \right) = \vec{J}^e \quad (8.13)$$

where $\mu = 4\pi \cdot 10^{-7}$ H/m is the permeability of vacuum, \vec{A} the magnetic vector potential and \vec{J}^e the externally applied current density. Since we state the magnetic flux density \vec{B} in Tesla the corresponding correlations between the magnetic vector potential, the magnetic flux density and the magnetic field strength \vec{H} have to be considered:

$$\vec{B} = \nabla \times \vec{A} \quad (8.14)$$

$$\vec{B} = \mu \vec{H} \quad (8.15)$$

The externally applied current density is determined by the static current I_0 flowing through the two parallel coils with N turns of wires. With $J_0 = (N \cdot I_0)/A$ (A being the cross section area of each wire) the current density in two circular coils in the x-z plane can be written as

$$\vec{J}^e = \begin{pmatrix} -J_0 z / (\sqrt{x^2 + z^2}) \\ 0 \\ J_0 x / (\sqrt{x^2 + z^2}) \end{pmatrix} \quad (8.16)$$

In the COMSOL simulation the user has to define the geometry of the magnet, the applied current I_0 and the number of windings N of the coil. In addition, the user has to define the used materials. In this case the material of the magnet was assumed to be iron with a relative permeability of $\mu_r = 4000$ and the coil consists of copper. The material in between the poles was defined as air. The results of the magnetic field homogeneity simulations are presented in section 9.3.

9. Design of new CR ToF detector

The new CR ToF detector is based on the knowledge and operation experience of the present ESR ToF detector. The main challenge compared to the existing ESR detector is the size of the used carbon foil (four times larger active area) to take into account the larger emittance of the CR.

9.1. New Structure of Foil-Frame in the CR-ToF detector

Simulations of the existing foil-frame structure with SIMION revealed that both detector branches behave slightly different in terms of timing and efficiency. The existing foil frames for a 40 mm foil diameter are shaped on one side, which results in an asymmetric field in forward and backward direction. As a result the design of the new foil holder is symmetric and uses a structure that avoids edges to allow for homogenous electrical fields in the foil area. The comparison between asymmetric and symmetric frames can be found in figure 9.1.

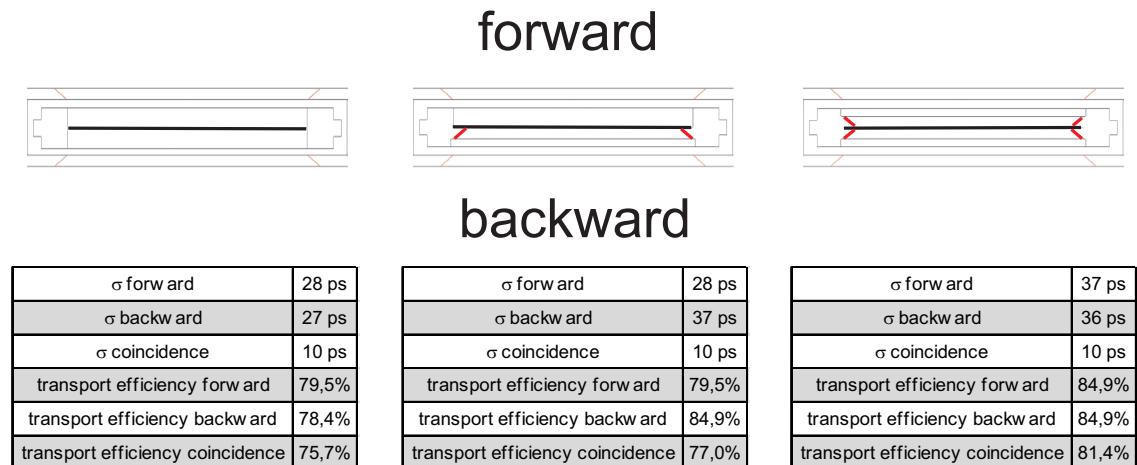


Figure 9.1.: Simulation results for different foil holders and the corresponding cross sections of the geometries are shown. Slopes (red lines) in the foil frame negatively influence the timing performance of the detector. By removing the slopes a better timing could be obtained.

This result led to the decision to remove the slopes in the foil area for the final

design of the new detector. The electric fields in the foil area are more homogeneous for larger the distances between foil and edges of the detector electrodes. A comparison between the existing and the newly designed foil area is shown in figure 9.2.

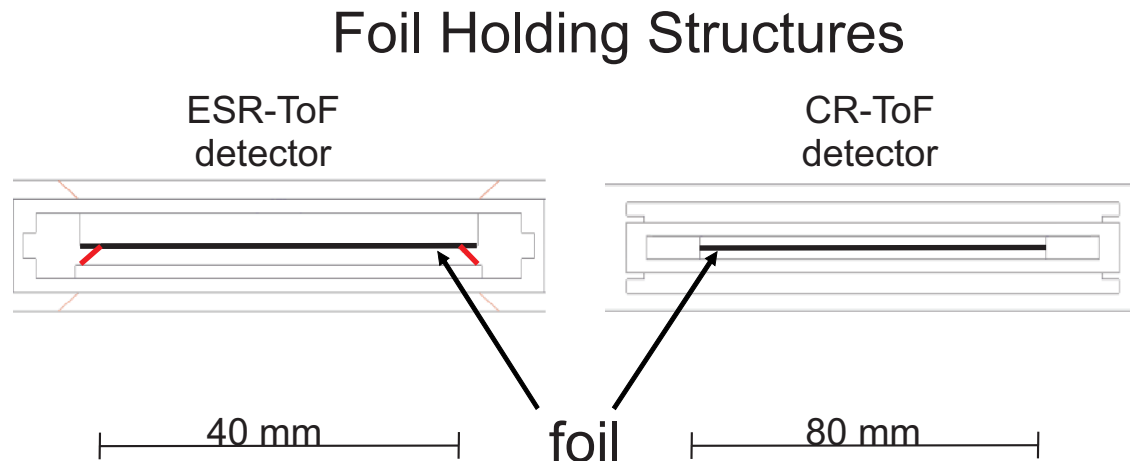


Figure 9.2.: On the left hand side is the existing foil structure as it is used in the ESR-ToF detector shown. On the right hand side the new design structure for the CR detector is shown. The new design does not have any additional sloped geometries and is completely symmetric.

9.2. Results of the Electric Field Simulations

A relative homogeneity of the involved electric and magnetic fields of 10^{-3} is needed for flight times of the secondary electrons of approximately 5 ns in the detector in order to measure with an accuracy of a few ps.

$$\frac{\Delta T}{T} = \frac{5 \text{ ps}}{5 \text{ ns}} = \frac{\Delta B}{B} + \frac{\Delta E}{E} = 10^{-3} \quad (9.1)$$

The arrangement, shape, and number of electrodes of the ToF detector had to be redesigned. A simple scaling of the existing ESR-ToF detector by the factor of 2 ($=80 \text{ mm foil diameter}/40 \text{ mm foil diameter}$) increases the time uncertainty by the same factor as already shown in chapter 4.3.2. A compact geometry with an improved transport efficiency and less electrodes was found. Nevertheless, the relative homogeneity of 10^{-3} for the electric field cannot be reached for the total flight volume of the SE. Use of grids at critical positions (see figure 9.3) would improve the homogeneity. Unfortunately, the use of grids has a significant drawback because they reduce the number of turns in the ring, which has to be avoided.

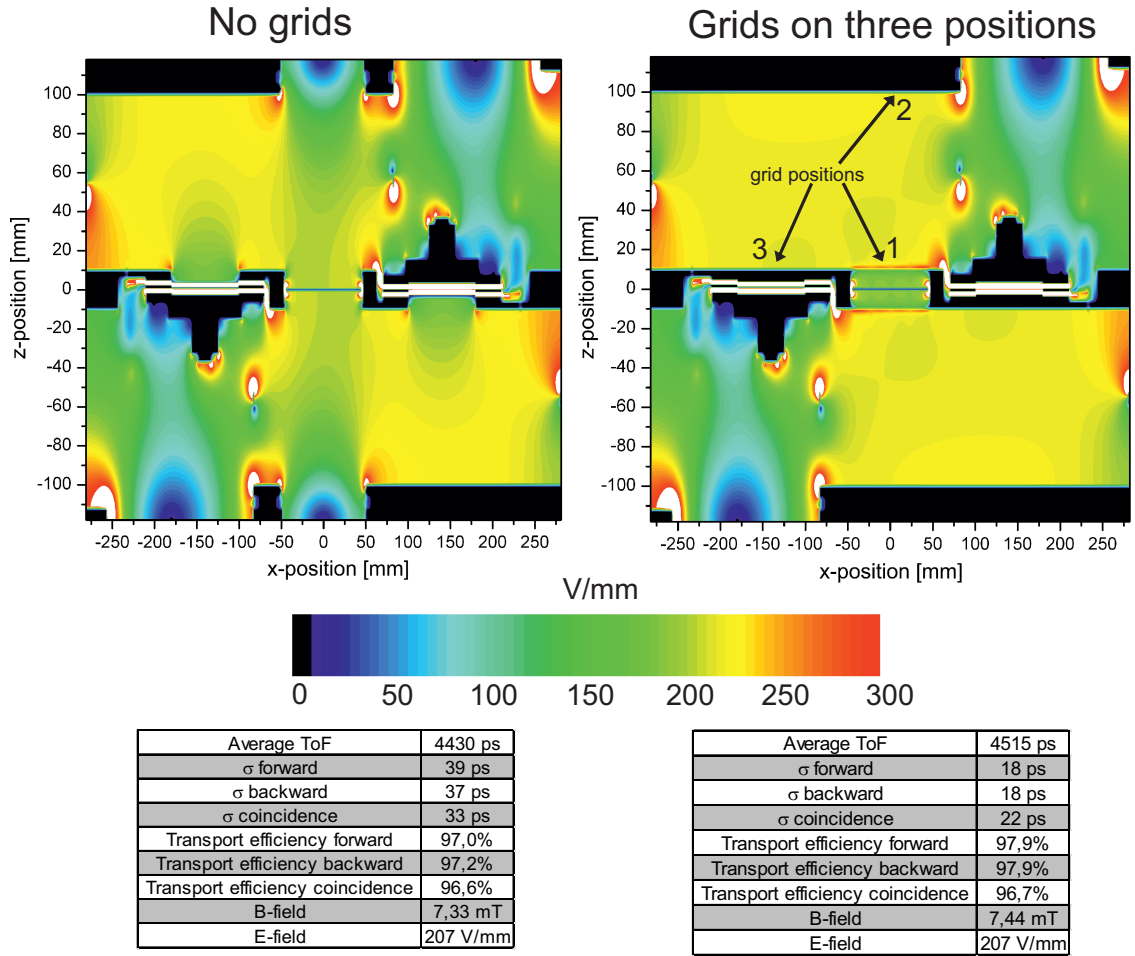


Figure 9.3.: Simulated electrical field strengths in the xz -plane ($y=0$ mm) without grids (left) and with grids (right). The simulated average ToF of the electrons, the timing uncertainties, the transport efficiencies and the simulated electrical and magnetic field are listed in the tables below the according geometry.

The displacement of the MCP detector relative to the foil position along the beam axis is major improvement. As mentioned in section 4.3.2 the displacement towards the impinging electrons increases the kinetic energy of the electrons, but also decreases on the other hand the isochronous imaging. Only for 180° deflection in the electromagnetic field the electron transport is isochronous. This means, in an ideal setup without field inhomogeneities the position for isochronous transport would be at $z = 0$. For different displacements (see figure 9.4) of the MCP detector upstream of the SE the influence for non-homogeneous fields, were simulated. The behavior for different displacements can be found in 9.5. In the simulations a displacement between 6 and 7 mm is the optimum to compensate for non-perfect fields for both operating modes (single branch and coincidence). This allows us to build the large CR-ToF detector with an even better timing performance than the existing ESR-ToF detector.

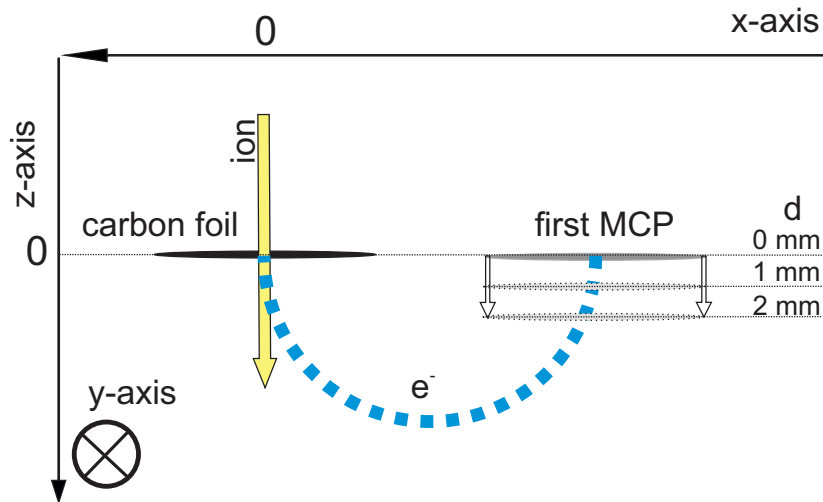


Figure 9.4.: Scheme of the geometry for the displacement (d) of the MCP detector along the z -axis. The displacement is an important parameter for optimization of the timing.

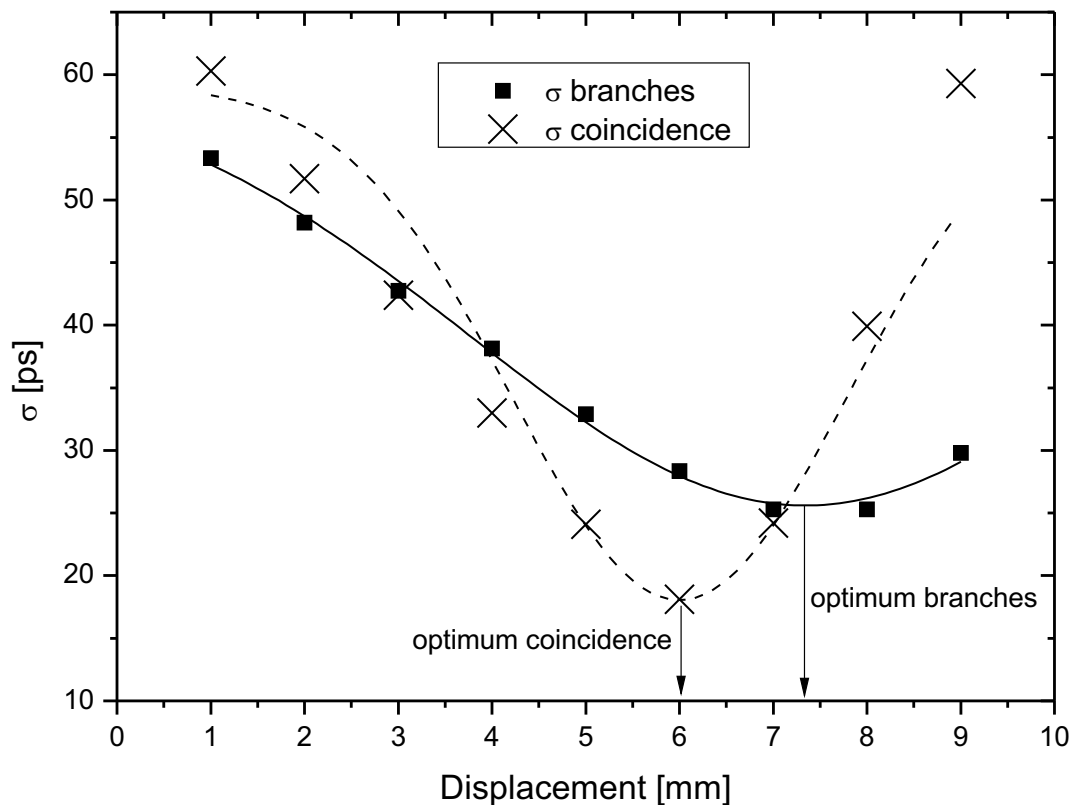


Figure 9.5.: The simulated time spread of the electron transport between foil and detector for single branches and in coincidence as a function of the displacement parameter.

9.3. Results of the Magnetic Field Simulations

A large Helmholtz-Coil magnet is necessary to ensure the requirement of 10^{-3} for the relative magnetic field deviation. In the best detector design the volume in which the SE travel from foil to MCP has as radius of 180 mm. COMSOL simulations for different pole-shoe diameters were performed for a needed gap between the magnet-pole shoes of 258 mm . The gap of 258 mm is needed and was determined by 180 mm height of the detector electrodes, 10 mm space between electrodes and vacuum chamber, 25 mm wall thickness of the vacuum chamber, and 4 mm space between chamber and magnet pole shoe. A start value of the diameter for these simulations was calculated according to equation 8.11, but it was found to be way too small. To reach the necessary homogeneity in a 180 mm radius a pole shoe diameter of at least 900 mm was found to be the minimum acceptable one. This also shows that equation 8.11 only gives a rough estimate and is not sufficient to define the magnet geometries alone. The results of COMSOL simulations for a Helmholtz-Coil with a pole-shoe diameter of 900 mm can be found in figure 9.6.

9.4. Final Design

Using **the practical** experience about the existing ESR-ToF detector **combined** with the presented results from the numerical simulations for the new CR-ToF detector a final technical design **can be made**.

Assuming that the simulations performed are as proven as for the ESR-ToF detector, the main parameters can be specified as:

Table 9.1.: Performance and parameters of the ESR and CR ToF detectors.

| | ESR-ToF detector (experiment) | CR-ToF detector (simulations) |
|--|----------------------------------|----------------------------------|
| Foil diameter | 40 mm | 80 mm |
| x (width) dimension | 300 mm | 562 mm |
| y (height) dimension | 90 mm | 180 mm |
| z (depth) dimension | 154 mm | 236 mm |
| Time spread σ_{detector} | 45 ps | 35 ps |
| Electron transport efficiency | 78% | 97% |
| Magnet pole-shoe diameter | 500 mm | ≥ 900 mm |
| Electric field (E) | 156 V/mm | 207 V/mm |
| Magnetic flux density (B) | 8.41 mT | 7.44 mT |

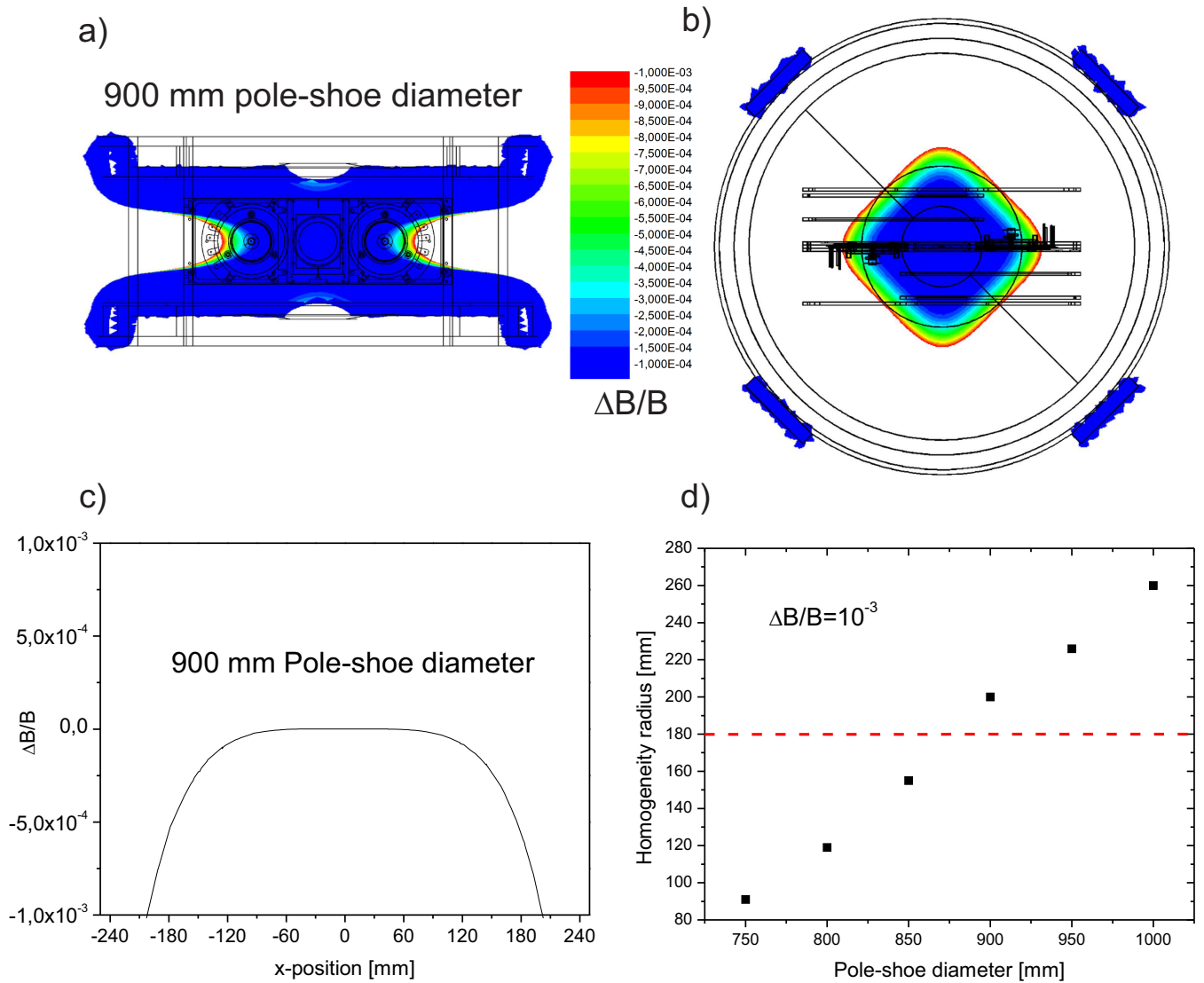


Figure 9.6.: Calculated homogeneity of the magnet field in the xy-plane (front view) (panel a)) and in the xz-plane (panel b)). The color codes represent the homogeneity for the setup in panel a) and b). Areas in white color do not fulfill the requirement of $\Delta B/B < 10^{-3}$. The position of the magnet yokes and the ToF detector are indicated by the black lines. Panel c): Relative magnetic flux density as a function of the x-position in the magnet. Panel d): The relation of the achievable homogeneity radius as a function of pole-shoe diameter for magnets with a gap of 258 mm.

Note that for the timing uncertainty σ_{forward} an additional contribution of 25 ps as described in [Diw11] was added to the simulated uncertainties. A technical drawing of the electrode arrangement for the new CR-ToF detector can be found in figure 9.7.

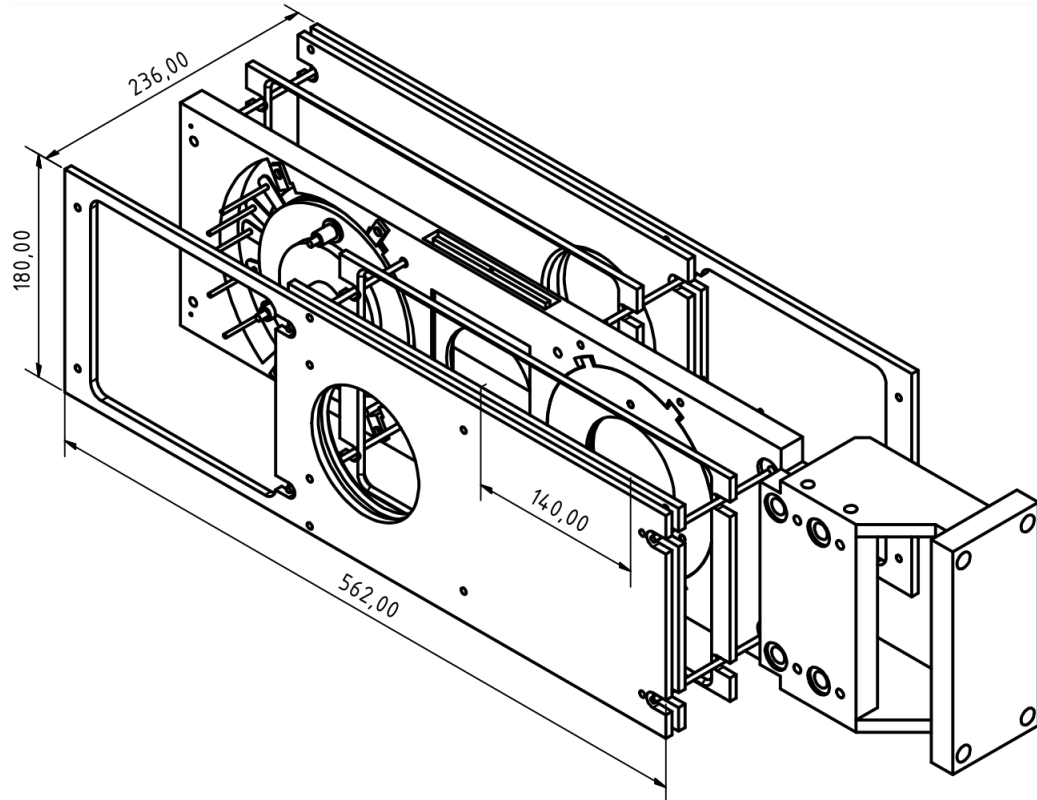


Figure 9.7.: The technical drawing of the electrode arrangement for the new CR-ToF detector. The dimensions in x-, y- and z-direction are annotated in mm.

A main difference compared to the ESR-ToF detector is the usage of only 3 electrode plates that provide the necessary electrical potentials. This results in less cabling complications inside the vacuum chamber. 4 voltages are needed to operate the detector:

- Foil (-4,500 V)
- Holder plate (-2,700 V)
- Electrode plate (17,400 V)
- MCP (chevron) (-2,700 V)

A scheme of the electrodes and the applied voltages can be found in figure 9.8

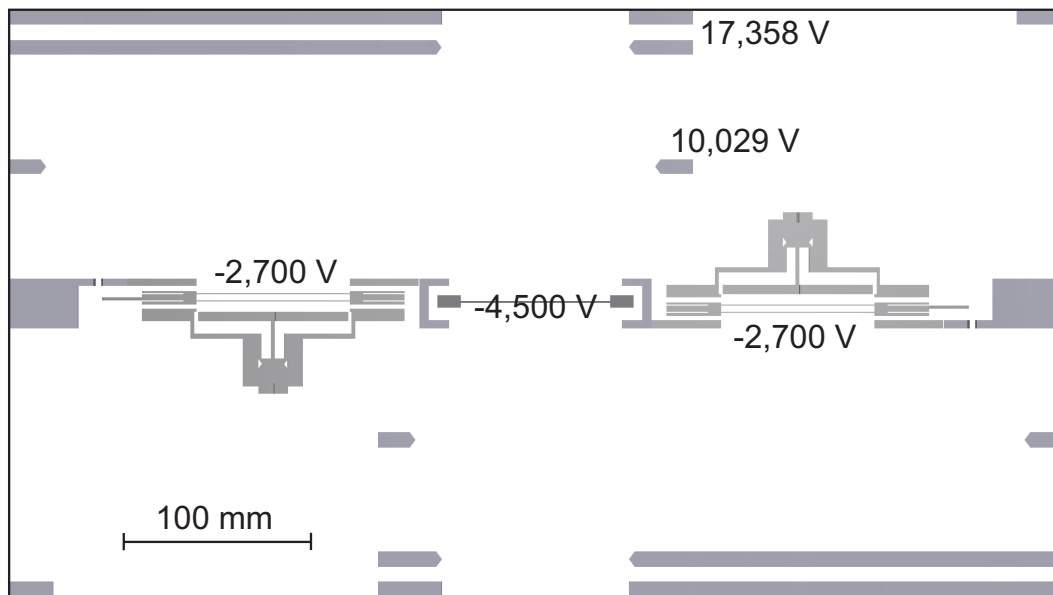


Figure 9.8.: Scheme of CR-ToF detector in xz -plane ($y=0$). Illustrated are the MCPs, electrodes and the foil including the corresponding voltages.

The corresponding vacuum chamber has to be flat on top and bottom to fit in between the parallel pole shoes of the surrounding Helmholtz-magnet. The large vacuum chamber adds a significant distance to the magnet pole shoe gap with a wall thickness of 25 mm. A thinner chamber wall however would not be stable enough for the needed sizes [VAC]. With a realistic estimation for a magnet with 1000 mm pole shoe diameter the final assembly of the ToF detector can be seen in figure 9.9.

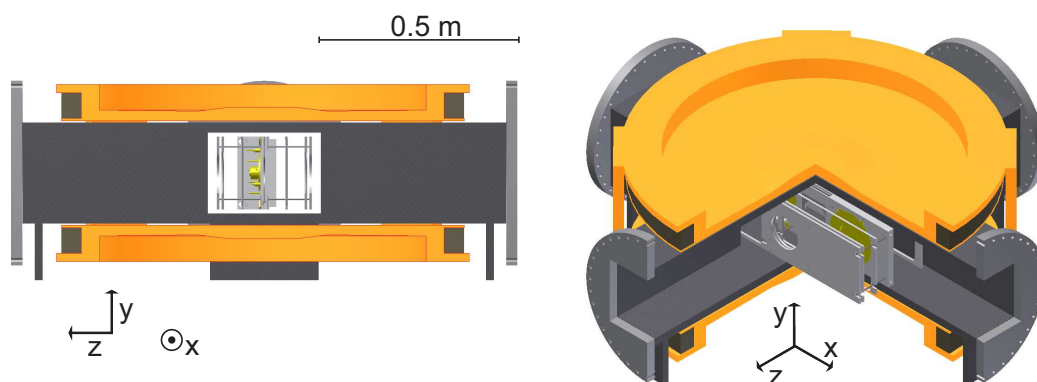


Figure 9.9.: Left panel: Section view in the yz - plane of the ToF detector surrounded by the vacuum chamber and the magnet. Right panel: Isometric view of the ToF detector with a section drawing the magnet and vacuum chamber.

10. Outlook

Atomic masses of exotic nuclei in ground and isomeric states are cornerstones for the understanding of nuclear structure and the creation of the elements in the Universe. The most interesting nuclei are short-lived and close to the driplines, such species with quite unusual neutron-to-proton ratios have demonstrated new matter distributions, new excitation energies, and new decay and reaction modes. Therefore, IMS experiments can also in future contribute to basic nuclear physics. Systematic accurate mass measurements will provide novel information on the development of shell closures and changes of the neutron-proton interactions (pairing). The strength of IMS is to map large areas of the unknown mass surface, especially of very short-lived nuclei because no cooling time is needed as it is the case for SMS. Special regions of interest are [ILI05]:

- near and at the proton- and neutron driplines
- shell closures, new shells and quenching
- near $N=Z$, the role of the neutron-proton interaction
- astrophysical pathways (r-, i- and rp-process)

IMS can contribute to all of these physics goals as clearly demonstrated with hitherto not measured short-lived masses of nuclei at the outskirts of the chart of nuclides in figure 10.1

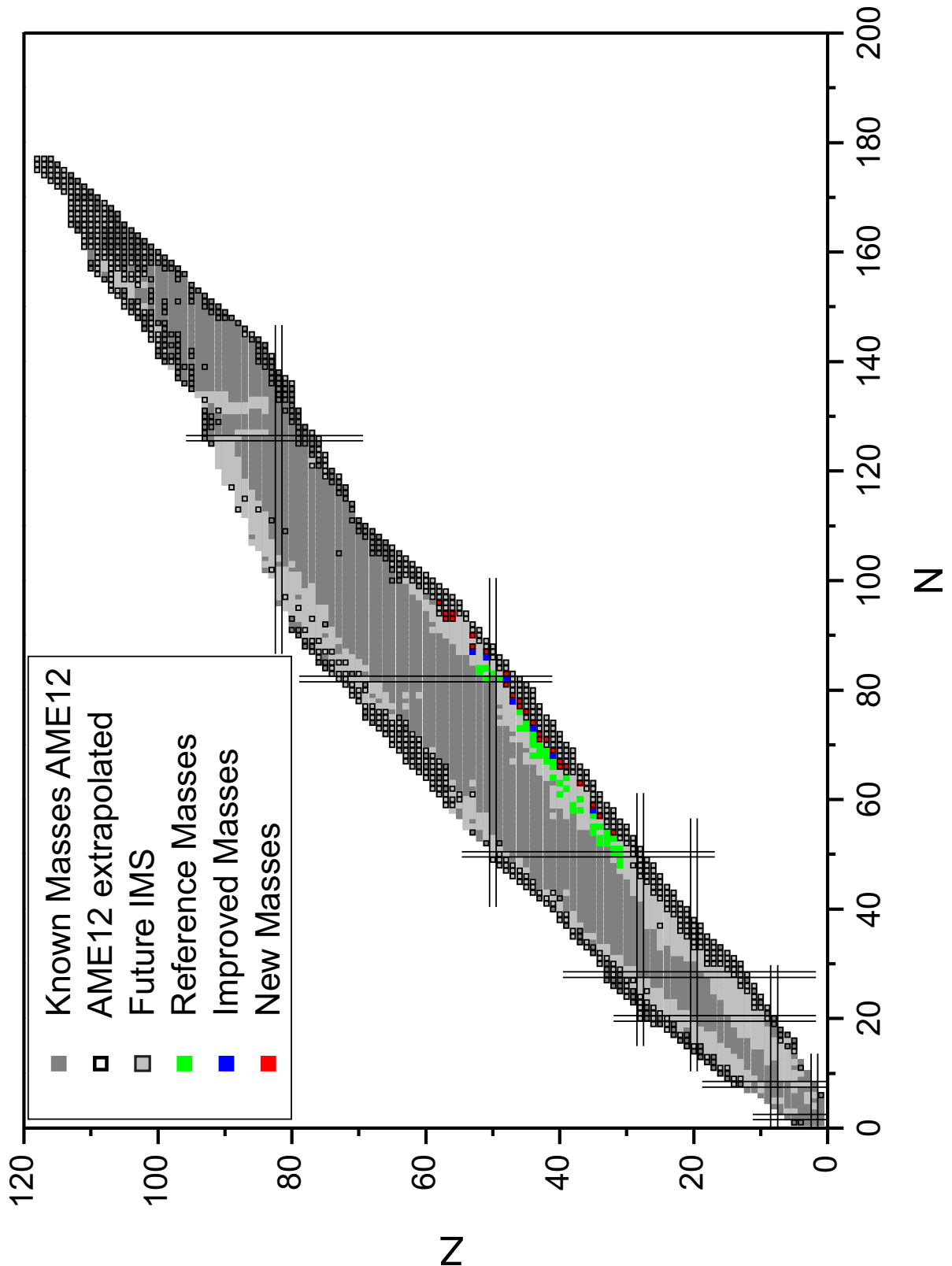


Figure 10.1.: Known and unknown masses [WAW12]. The short-lived nuclides in the life-time region of 0.5 ms to 10 s are well suited for future IMS experiments and are indicated by framed light gray squares. The presently known magic numbers are drawn in the figure.

New IMS experiments can be continued with the present FRS-ESR facilities under improved conditions as investigated in this work. The improved conditions are:

- better timing performance with the modified ESR-ToF detector
- independent velocity or $B\rho$ measurements, in addition to the revolution time with a dual ToF detector system
- position sensitive ToF detector
- improved ion-optical performance of the ring (e.g., isochronicity, phase-space matching of FRS and ESR)
- stable beams in different charge states for calibration and drift corrections

A new generation of IMS experiments will be realized with the FAIR facility, the combination of the Super-FRS and the CR in the Modularized Start Version [GSI15]. The FAIR facilities will provide many orders of magnitude larger intensities for stored exotic nuclei. This means we can reach the most exotic nuclei at the borders of the present chart of nuclides. We will be able to discover new isotopes and measure their masses for the first time. Gain factors at FAIR:

- factor 10 higher transmission of exotic nuclei with the Super-FRS (see figure 10.2)
- factor 100 higher primary beam intensities for the heaviest stable projectiles from SIS100
- factor 20 higher acceptance for the combination of the CR and the new ToF-detector (see chapter 9)

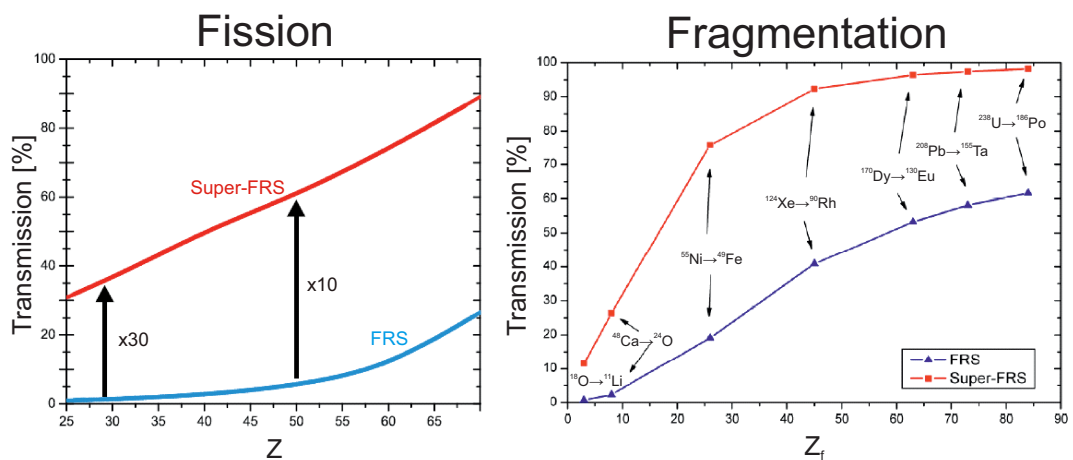


Figure 10.2.: Gain in transmission for projectile and fission fragments of the Super-FRS compared to the present FRS.[Gei12]

New IMS experiments with high intensity exotic nuclear beams can also be performed with the new RI-Ring at the RIBF facilities in Japan [Y⁺08]. The present experience with $B\rho$ -tagging of this work can be directly implemented in the RI-Ring experiments. The BigRIPS [K⁺03] in-flight separator is combined with the RI-Ring using DC-beams of exotic nuclei. The $B\rho$ -tagging can be advantageously done in this case with position sensitive particle detectors without any intensity losses. In these experiments the exotic nuclei are fully identified in-flight with particle detectors at the BigRIPS and only the ions of interest are injected in the RI-Ring via a triggered kicker system. The present design of the new ToF detector would be well suited for implementation in the RI-Ring to get experience before the CR is commissioned.

A. Appendix

A.1. Experiments with and without Momentum Definition

An overview of the performance parameters of the ToF detector in the performed IMS experiments with the FRS-ESR facilities since 2002 is listed in the table below.

Table A.1.: IMS experiments with the FRS-ESR facilities since 2002.

| SE Transport Eff. | $B\rho$ -tagging | MCP ch. \varnothing | Foil thickness [$\mu\text{g}/\text{cm}^2$] | Oscilloscope | Reference |
|-------------------|------------------|-----------------------|--|-----------------|---------------------|
| 40% | No | 10 μm | [10:17:10] CsI:C:CsI | 4 GHz; 10 GS/s | [Mat04] |
| 40% | Yes | 10 μm | [10:17:10] CsI:C:CsI | 1 GHz; 8 GS/s | [G ⁺ 06] |
| 40% | Yes | 10 μm | [10:17:10] CsI:C:CsI | 15 GHz; 40 GS/s | [Knö08], [Sun08] |
| 85% | Test | 10 μm | 10 C | 1 GHz; 2.5 GS/s | [Fab08] |
| 85% | Test | 5 μm | 10 C | 1 GHz; 2.5 GS/s | [Kuz11] |
| 85% | Test | 5 μm | 10 C | 1 GHz; 10 GS/s | this work |

A.2. Analysis

Data points for the example given in section 6.1:

Table A.2.: The data points used for the example given in 6.1.

| i | turn | timestamp [ns] | $\sigma_{\text{timestamp}}$ [ns] |
|----|------|----------------|----------------------------------|
| 0 | 0 | 0.000 | 0.127 |
| 1 | 2 | 1009.625 | 0.099 |
| 2 | 3 | 1514.287 | 0.103 |
| 3 | 4 | 2018.745 | 0.115 |
| 4 | 7 | 3532.992 | 0.137 |
| 5 | 8 | 4037.703 | 0.104 |
| 6 | 9 | 4542.354 | 0.099 |
| 7 | 11 | 5551.688 | 0.099 |
| 8 | 12 | 6056.349 | 0.099 |
| 9 | 14 | 7065.728 | 0.106 |
| 10 | 15 | 7570.232 | 0.133 |
| 11 | 17 | 8579.515 | 0.269 |
| 12 | 18 | 9084.392 | 0.100 |
| 13 | 20 | 10093.734 | 0.133 |
| 14 | 21 | 10598.311 | 0.269 |
| 15 | 22 | 11103.043 | 0.103 |
| 16 | 23 | 11607.740 | 0.106 |
| 17 | 25 | 12616.981 | 0.124 |
| 18 | 27 | 13626.409 | 0.110 |
| 19 | 28 | 14131.130 | 0.100 |
| 20 | 30 | 15140.485 | 0.157 |
| 21 | 33 | 16654.520 | 0.105 |

The fit parameters are

$$a_1 = 504.713 \quad a_2 = -0.00277 \quad a_3 = 0.0000543$$

and the covariance matrix

$$\epsilon = \begin{pmatrix} 0.00018854 & -0.0000129818 & 0.000000244305 \\ -0.0000129818 & 0.000000961618 & -0.0000000189502 \\ 0.000000244305 & -0.0000000189502 & 0.000000000385745 \end{pmatrix}$$

The matrix elements used in the MOCADI [MOC15] simulations were calculated with the program GICOSY [GIC]. The matrix elements for one turn in the ESR in 3rd order [Wei15] as used for the simulations presented in section 6.4 are shown below.

| | | X [m] | A [rad] | Y [m] | B [rad] | L [m] |
|----|-----|------------|------------|------------|------------|------------|
| 0 | | 0.000E+00 | 0.000E+00 | 0.000E+00 | 0.000E+00 | 1.084E+02 |
| 1 | X | 7.802E-02 | -1.420E-01 | 0.000E+00 | 0.000E+00 | -1.180E+00 |
| 2 | A | 6.999E+00 | 7.802E-02 | 0.000E+00 | 0.000E+00 | -7.660E+00 |
| 3 | Y | 0.000E+00 | 0.000E+00 | -2.368E-01 | 3.653E-02 | 0.000E+00 |
| 4 | B | 0.000E+00 | 0.000E+00 | -2.584E+01 | -2.368E-01 | 0.000E+00 |
| 5 | G | -6.980E-09 | -1.075E-09 | 0.000E+00 | 0.000E+00 | 4.040E-08 |
| 6 | P | -7.660E+00 | -1.180E+00 | 0.000E+00 | 0.000E+00 | 4.433E+01 |
| 7 | XX | 4.862E-01 | 4.913E-02 | 0.000E+00 | 0.000E+00 | 1.256E-01 |
| 8 | XA | 3.958E+00 | 6.380E-01 | 0.000E+00 | 0.000E+00 | -1.701E+00 |
| 9 | XY | 0.000E+00 | 0.000E+00 | 4.153E+00 | -3.768E-02 | 0.000E+00 |
| 10 | XB | 0.000E+00 | 0.000E+00 | -7.198E+01 | 2.836E+00 | 0.000E+00 |
| 11 | XG | 4.256E-09 | -2.023E-10 | 0.000E+00 | 0.000E+00 | 3.538E-09 |
| 12 | XP | 4.670E+00 | -7.998E-02 | 0.000E+00 | 0.000E+00 | 3.882E+00 |
| 13 | AA | 1.285E+01 | 3.249E+00 | 0.000E+00 | 0.000E+00 | 1.691E+01 |
| 14 | AY | 0.000E+00 | 0.000E+00 | 1.769E+01 | -2.447E-01 | 0.000E+00 |
| 15 | AB | 0.000E+00 | 0.000E+00 | -4.673E+02 | 2.769E+01 | 0.000E+00 |
| 16 | AG | -1.326E-08 | 1.723E-09 | 0.000E+00 | 0.000E+00 | 2.297E-08 |
| 17 | AP | -7.547E+00 | 1.891E+00 | 0.000E+00 | 0.000E+00 | 1.754E+01 |
| 18 | YY | -4.768E-01 | -4.733E-02 | 0.000E+00 | 0.000E+00 | 1.167E+00 |
| 19 | YB | 1.288E+01 | 1.645E+00 | 0.000E+00 | 0.000E+00 | -3.372E+01 |
| 20 | YG | 0.000E+00 | 0.000E+00 | -5.228E-08 | 6.185E-10 | 0.000E+00 |
| 21 | YP | 0.000E+00 | 0.000E+00 | -5.737E+01 | 6.422E-01 | 0.000E+00 |
| 22 | BB | -2.839E+02 | -6.219E+01 | 0.000E+00 | 0.000E+00 | 8.946E+02 |
| 23 | BG | 0.000E+00 | 0.000E+00 | 1.180E-06 | -6.226E-08 | 0.000E+00 |
| 24 | BP | 0.000E+00 | 0.000E+00 | 1.269E+03 | -6.831E+01 | 0.000E+00 |
| 25 | GG | 6.669E-09 | 1.027E-09 | 0.000E+00 | 0.000E+00 | -3.860E-08 |
| 26 | GP | 5.786E-08 | -1.024E-09 | 0.000E+00 | 0.000E+00 | 4.182E-08 |
| 27 | PP | 3.907E+01 | 1.155E+00 | 0.000E+00 | 0.000E+00 | -1.941E+01 |
| 28 | XXX | -7.632E-01 | -1.800E-02 | 0.000E+00 | 0.000E+00 | 4.091E-01 |
| 29 | XXA | -2.633E+00 | -3.419E-01 | 0.000E+00 | 0.000E+00 | 5.989E-01 |
| 30 | XXY | 0.000E+00 | 0.000E+00 | 6.916E+00 | -3.588E-01 | 0.000E+00 |
| 31 | XXB | 0.000E+00 | 0.000E+00 | -9.680E+01 | 7.109E+00 | 0.000E+00 |
| 32 | XXG | -2.952E-09 | 4.537E-10 | 0.000E+00 | 0.000E+00 | -6.818E-09 |
| 33 | XXP | -3.239E+00 | 4.488E-01 | 0.000E+00 | 0.000E+00 | -7.481E+00 |
| 34 | XAA | -2.730E+01 | -2.888E+00 | 0.000E+00 | 0.000E+00 | 1.523E+01 |
| 35 | XAY | 0.000E+00 | 0.000E+00 | 8.140E+01 | -4.892E+00 | 0.000E+00 |
| 36 | XAB | 0.000E+00 | 0.000E+00 | -9.987E+02 | 8.761E+01 | 0.000E+00 |
| 37 | XAG | 3.315E-09 | 3.923E-09 | 0.000E+00 | 0.000E+00 | -8.998E-08 |
| 38 | XAP | 7.596E+00 | 4.305E+00 | 0.000E+00 | 0.000E+00 | -1.004E+02 |
| 39 | YYY | -1.085E+00 | -1.835E-01 | 0.000E+00 | 0.000E+00 | 2.609E+00 |
| 40 | XYB | 7.808E+01 | 1.728E+01 | 0.000E+00 | 0.000E+00 | -2.333E+02 |

| | | X [m] | A [rad] | Y [m] | B [rad] | L [m] |
|----|------|------------|------------|------------|------------|------------|
| 41 | XYG | 0.000E+00 | 0.000E+00 | -1.792E-07 | 1.165E-08 | 0.000E+00 |
| 42 | XYP | 0.000E+00 | 0.000E+00 | -1.967E+02 | 1.282E+01 | 0.000E+00 |
| 43 | XBB | -1.100E+03 | -2.293E+02 | 0.000E+00 | 0.000E+00 | 2.967E+03 |
| 44 | XBG | 0.000E+00 | 0.000E+00 | 1.718E-06 | -1.571E-07 | 0.000E+00 |
| 45 | XBP | 0.000E+00 | 0.000E+00 | 1.814E+03 | -1.724E+02 | 0.000E+00 |
| 46 | XGG | -4.066E-09 | 1.933E-10 | 0.000E+00 | 0.000E+00 | -3.380E-09 |
| 47 | XGP | -1.338E-07 | -1.161E-08 | 0.000E+00 | 0.000E+00 | 2.637E-07 |
| 48 | XPP | -7.790E+01 | -6.191E+00 | 0.000E+00 | 0.000E+00 | 1.410E+02 |
| 49 | AAA | -4.771E+01 | -3.665E+01 | 0.000E+00 | 0.000E+00 | -1.422E+01 |
| 50 | AA Y | 0.000E+00 | 0.000E+00 | 2.488E+02 | -1.470E+01 | 0.000E+00 |
| 51 | AAB | 0.000E+00 | 0.000E+00 | -3.613E+03 | 2.919E+02 | 0.000E+00 |
| 52 | AAG | -1.088E-07 | 6.225E-08 | 0.000E+00 | 0.000E+00 | -3.160E-07 |
| 53 | AAP | -9.367E+01 | 7.156E+01 | 0.000E+00 | 0.000E+00 | -3.129E+02 |
| 54 | AYY | -5.361E+00 | -1.129E+00 | 0.000E+00 | 0.000E+00 | 7.786E+00 |
| 55 | AYB | 3.075E+02 | 8.109E+01 | 0.000E+00 | 0.000E+00 | -8.310E+02 |
| 56 | AYG | 0.000E+00 | 0.000E+00 | -1.119E-06 | 7.470E-08 | 0.000E+00 |
| 57 | AYP | 0.000E+00 | 0.000E+00 | -1.210E+03 | 8.197E+01 | 0.000E+00 |
| 58 | ABB | -5.288E+03 | -1.294E+03 | 0.000E+00 | 0.000E+00 | 1.344E+04 |
| 59 | ABG | 0.000E+00 | 0.000E+00 | 1.465E-05 | -1.313E-06 | 0.000E+00 |
| 60 | ABP | 0.000E+00 | 0.000E+00 | 1.514E+04 | -1.413E+03 | 0.000E+00 |
| 61 | AGG | 1.267E-08 | -1.646E-09 | 0.000E+00 | 0.000E+00 | -2.195E-08 |
| 62 | AGP | -4.584E-07 | -1.980E-07 | 0.000E+00 | 0.000E+00 | 1.640E-06 |
| 63 | APP | -2.449E+02 | -1.105E+02 | 0.000E+00 | 0.000E+00 | 8.885E+02 |
| 64 | YYY | 0.000E+00 | 0.000E+00 | 8.189E+00 | -4.536E-02 | 0.000E+00 |
| 65 | YYB | 0.000E+00 | 0.000E+00 | -2.874E+02 | 3.431E+00 | 0.000E+00 |
| 66 | YYG | 1.238E-08 | 1.718E-09 | 0.000E+00 | 0.000E+00 | -2.763E-08 |
| 67 | YYP | 1.359E+01 | 1.933E+00 | 0.000E+00 | 0.000E+00 | -3.032E+01 |
| 68 | YBB | 0.000E+00 | 0.000E+00 | 6.123E+03 | -1.456E+02 | 0.000E+00 |
| 69 | YBG | -8.680E-07 | -2.010E-07 | 0.000E+00 | 0.000E+00 | 2.477E-06 |
| 70 | YBP | -9.396E+02 | -2.205E+02 | 0.000E+00 | 0.000E+00 | 2.684E+03 |
| 71 | YGG | 0.000E+00 | 0.000E+00 | 4.995E-08 | -5.910E-10 | 0.000E+00 |
| 72 | YGP | 0.000E+00 | 0.000E+00 | 2.822E-06 | -2.002E-07 | 0.000E+00 |
| 73 | YPP | 0.000E+00 | 0.000E+00 | 1.603E+03 | -1.108E+02 | 0.000E+00 |
| 74 | BBB | 0.000E+00 | 0.000E+00 | -9.729E+04 | 6.730E+03 | 0.000E+00 |
| 75 | BBG | 1.242E-05 | 2.879E-06 | 0.000E+00 | 0.000E+00 | -3.516E-05 |
| 76 | BBP | 1.306E+04 | 3.097E+03 | 0.000E+00 | 0.000E+00 | -3.679E+04 |
| 77 | BGG | 0.000E+00 | 0.000E+00 | -1.128E-06 | 5.948E-08 | 0.000E+00 |
| 78 | BGP | 0.000E+00 | 0.000E+00 | -2.759E-05 | 3.234E-06 | 0.000E+00 |
| 79 | BPP | 0.000E+00 | 0.000E+00 | -1.573E+04 | 1.840E+03 | 0.000E+00 |
| 80 | GGG | -5.065E-09 | -7.801E-10 | 0.000E+00 | 0.000E+00 | 2.932E-08 |
| 81 | GGP | -5.950E-08 | 3.283E-10 | 0.000E+00 | 0.000E+00 | -1.555E-08 |
| 82 | GPP | 5.173E-07 | 2.092E-07 | 0.000E+00 | 0.000E+00 | -1.680E-06 |
| 83 | PPP | 1.401E+02 | 7.511E+01 | 0.000E+00 | 0.000E+00 | -5.937E+02 |

Table A.3.: Matrix elements in 3rd order for the isochronous mode of the ESR.

The matrix elements of the CR in 3rd order [Wei15] are listed in table A.4

| | | X [m] | A [rad] | Y [m] | B [rad] | L [m] |
|----|-----|------------|------------|------------|------------|------------|
| 0 | | 2.240E-21 | 4.211E-22 | 0.000E+00 | 0.000E+00 | 2.215E+02 |
| 1 | X | 5.828E-01 | -7.842E-02 | 0.000E+00 | 0.000E+00 | -3.034E-06 |
| 2 | A | 8.421E+00 | 5.828E-01 | 0.000E+00 | 0.000E+00 | -1.614E-05 |
| 3 | Y | 0.000E+00 | 0.000E+00 | 3.370E-01 | -1.279E-01 | 0.000E+00 |
| 4 | B | 0.000E+00 | 0.000E+00 | 6.931E+00 | 3.370E-01 | 0.000E+00 |
| 5 | G | -1.221E-14 | -3.229E-15 | 0.000E+00 | 0.000E+00 | 8.963E-08 |
| 6 | P | -1.614E-05 | -3.034E-06 | 0.000E+00 | 0.000E+00 | 7.977E+01 |
| 7 | XX | -4.577E+00 | -6.637E-02 | 0.000E+00 | 0.000E+00 | -1.444E-01 |
| 8 | XA | 5.903E+01 | -7.062E-01 | 0.000E+00 | 0.000E+00 | -4.173E+00 |
| 9 | XY | 0.000E+00 | 0.000E+00 | -1.703E-01 | 4.027E-02 | 0.000E+00 |
| 10 | XB | 0.000E+00 | 0.000E+00 | -1.155E+00 | 1.437E+00 | 0.000E+00 |
| 11 | XG | -3.547E-14 | -5.568E-10 | 0.000E+00 | 0.000E+00 | 8.624E-09 |
| 12 | XP | -5.424E-05 | -4.172E-01 | 0.000E+00 | 0.000E+00 | 7.676E+00 |
| 13 | AA | 1.570E+02 | -5.574E+01 | 0.000E+00 | 0.000E+00 | 1.551E+01 |
| 14 | AY | 0.000E+00 | 0.000E+00 | 1.959E+01 | 2.143E-01 | 0.000E+00 |
| 15 | AB | 0.000E+00 | 0.000E+00 | -6.145E+00 | -1.285E+01 | 0.000E+00 |
| 16 | AG | -5.979E-08 | 2.731E-13 | 0.000E+00 | 0.000E+00 | 4.588E-08 |
| 17 | AP | -4.480E+01 | 2.727E-04 | 0.000E+00 | 0.000E+00 | 4.083E+01 |
| 18 | YY | -7.858E-01 | 9.868E-02 | 0.000E+00 | 0.000E+00 | -1.555E-01 |
| 19 | YB | 5.816E+00 | -2.051E-01 | 0.000E+00 | 0.000E+00 | -6.396E+00 |
| 20 | YG | 0.000E+00 | 0.000E+00 | 3.070E-14 | -1.037E-09 | 0.000E+00 |
| 21 | YP | 0.000E+00 | 0.000E+00 | 2.773E-05 | -7.949E-01 | 0.000E+00 |
| 22 | BB | 6.893E+01 | -3.956E-01 | 0.000E+00 | 0.000E+00 | 8.426E+00 |
| 23 | BG | 0.000E+00 | 0.000E+00 | -5.618E-08 | 9.048E-14 | 0.000E+00 |
| 24 | BP | 0.000E+00 | 0.000E+00 | -4.308E+01 | 8.994E-05 | 0.000E+00 |
| 25 | GG | 2.678E-14 | -3.472E-15 | 0.000E+00 | 0.000E+00 | -6.994E-08 |
| 26 | GP | 4.588E-08 | 8.624E-09 | 0.000E+00 | 0.000E+00 | -3.215E-08 |
| 27 | PP | 2.042E+01 | 3.838E+00 | 0.000E+00 | 0.000E+00 | -7.655E+01 |
| 28 | XXX | -1.164E+01 | -4.703E-01 | 0.000E+00 | 0.000E+00 | -2.857E-01 |
| 29 | XXA | -7.509E+01 | 1.125E-01 | 0.000E+00 | 0.000E+00 | -6.392E+00 |
| 30 | XXY | 0.000E+00 | 0.000E+00 | -1.236E+01 | -2.923E-01 | 0.000E+00 |
| 31 | XXB | 0.000E+00 | 0.000E+00 | 2.893E+01 | -4.034E+00 | 0.000E+00 |
| 32 | XXG | -6.600E-08 | -1.518E-09 | 0.000E+00 | 0.000E+00 | -7.324E-09 |
| 33 | XXP | -5.874E+01 | -1.284E+00 | 0.000E+00 | 0.000E+00 | -6.518E+00 |
| 34 | XAA | -4.388E+03 | -2.443E+02 | 0.000E+00 | 0.000E+00 | -2.472E+02 |
| 35 | XAY | 0.000E+00 | 0.000E+00 | 7.544E+01 | 2.925E-01 | 0.000E+00 |
| 36 | XAB | 0.000E+00 | 0.000E+00 | -3.885E+02 | -1.362E+01 | 0.000E+00 |
| 37 | XAG | 4.200E-07 | -1.113E-08 | 0.000E+00 | 0.000E+00 | 4.393E-07 |
| 38 | XAP | 4.328E+02 | -9.908E+00 | 0.000E+00 | 0.000E+00 | 3.868E+02 |
| 39 | XYX | -5.181E+00 | -4.555E-01 | 0.000E+00 | 0.000E+00 | 1.354E+00 |
| 40 | XYB | 4.097E+01 | -2.366E+00 | 0.000E+00 | 0.000E+00 | -6.092E+00 |
| 41 | XYG | 0.000E+00 | 0.000E+00 | 1.542E-08 | 5.653E-11 | 0.000E+00 |
| 42 | XYP | 0.000E+00 | 0.000E+00 | 1.372E+01 | 1.004E-02 | 0.000E+00 |

| | | X [m] | A [rad] | Y [m] | B [rad] | L [m] |
|----|-------|------------|------------|------------|------------|------------|
| 43 | XBB | -4.279E+02 | -2.905E+01 | 0.000E+00 | 0.000E+00 | 1.937E+02 |
| 44 | XBG | 0.000E+00 | 0.000E+00 | -1.861E-07 | 5.319E-08 | 0.000E+00 |
| 45 | XBP | 0.000E+00 | 0.000E+00 | -1.667E+02 | 4.734E+01 | 0.000E+00 |
| 46 | XGG | -4.050E-13 | 4.345E-10 | 0.000E+00 | 0.000E+00 | -6.729E-09 |
| 47 | XGP | 5.670E-07 | 2.327E-08 | 0.000E+00 | 0.000E+00 | -1.428E-07 |
| 48 | XPP | 2.523E+02 | 1.091E+01 | 0.000E+00 | 0.000E+00 | -6.954E+01 |
| 49 | AAA | 3.257E+04 | -4.588E+02 | 0.000E+00 | 0.000E+00 | -2.988E+03 |
| 50 | AA Y | 0.000E+00 | 0.000E+00 | -8.723E+02 | -5.836E+00 | 0.000E+00 |
| 51 | AAB | 0.000E+00 | 0.000E+00 | 5.197E+03 | -4.777E+02 | 0.000E+00 |
| 52 | AAG | 1.921E-09 | -4.045E-07 | 0.000E+00 | 0.000E+00 | 1.872E-06 |
| 53 | AAP | 3.157E+02 | -4.157E+02 | 0.000E+00 | 0.000E+00 | 1.698E+03 |
| 54 | AYY | 3.330E+01 | -4.449E+00 | 0.000E+00 | 0.000E+00 | 2.020E+01 |
| 55 | AYB | -2.518E+02 | 3.192E+00 | 0.000E+00 | 0.000E+00 | -1.401E+02 |
| 56 | AYG | 0.000E+00 | 0.000E+00 | 4.246E-07 | -1.221E-09 | 0.000E+00 |
| 57 | AYP | 0.000E+00 | 0.000E+00 | 3.975E+02 | -1.086E+00 | 0.000E+00 |
| 58 | ABB | 7.194E+03 | -1.001E+03 | 0.000E+00 | 0.000E+00 | -5.320E+02 |
| 59 | ABG | 0.000E+00 | 0.000E+00 | -9.462E-07 | -1.075E-07 | 0.000E+00 |
| 60 | ABP | 0.000E+00 | 0.000E+00 | -8.544E+02 | -1.085E+02 | 0.000E+00 |
| 61 | AGG | 4.666E-08 | -1.315E-13 | 0.000E+00 | 0.000E+00 | -3.580E-08 |
| 62 | AGP | 1.613E-06 | -3.621E-07 | 0.000E+00 | 0.000E+00 | -1.004E-06 |
| 63 | APP | 7.326E+02 | -1.611E+02 | 0.000E+00 | 0.000E+00 | -4.582E+02 |
| 64 | YYY | 0.000E+00 | 0.000E+00 | -5.441E+00 | -2.407E-01 | 0.000E+00 |
| 65 | Y Y B | 0.000E+00 | 0.000E+00 | 2.320E+01 | -4.811E+00 | 0.000E+00 |
| 66 | Y Y G | -1.374E-08 | 4.156E-09 | 0.000E+00 | 0.000E+00 | -7.348E-08 |
| 67 | Y Y P | -1.223E+01 | 3.600E+00 | 0.000E+00 | 0.000E+00 | -6.540E+01 |
| 68 | Y B B | 0.000E+00 | 0.000E+00 | -1.935E+02 | -1.037E+01 | 0.000E+00 |
| 69 | Y B G | 1.572E-08 | -1.980E-08 | 0.000E+00 | 0.000E+00 | 1.242E-07 |
| 70 | Y B P | 1.981E+01 | -1.762E+01 | 0.000E+00 | 0.000E+00 | 1.041E+02 |
| 71 | Y G G | 0.000E+00 | 0.000E+00 | 3.908E-13 | 8.090E-10 | 0.000E+00 |
| 72 | Y G P | 0.000E+00 | 0.000E+00 | -8.662E-07 | -4.085E-08 | 0.000E+00 |
| 73 | Y P P | 0.000E+00 | 0.000E+00 | -3.855E+02 | -1.713E+01 | 0.000E+00 |
| 74 | B B B | 0.000E+00 | 0.000E+00 | 7.247E+02 | -3.063E+02 | 0.000E+00 |
| 75 | B B G | 1.080E-06 | 8.956E-08 | 0.000E+00 | 0.000E+00 | -3.618E-06 |
| 76 | B B P | 1.100E+03 | 7.931E+01 | 0.000E+00 | 0.000E+00 | -3.203E+03 |
| 77 | B G G | 0.000E+00 | 0.000E+00 | 4.384E-08 | 1.421E-13 | 0.000E+00 |
| 78 | B G P | 0.000E+00 | 0.000E+00 | 3.515E-06 | -1.043E-06 | 0.000E+00 |
| 79 | B P P | 0.000E+00 | 0.000E+00 | 1.578E+03 | -4.641E+02 | 0.000E+00 |
| 80 | G G G | 1.652E-13 | -4.441E-15 | 0.000E+00 | 0.000E+00 | 4.134E-08 |
| 81 | G G P | -3.580E-08 | -6.729E-09 | 0.000E+00 | 0.000E+00 | 8.016E-08 |
| 82 | G P P | -7.185E-07 | -6.193E-08 | 0.000E+00 | 0.000E+00 | -8.526E-08 |
| 83 | P P P | -2.344E+02 | -2.365E+01 | 0.000E+00 | 0.000E+00 | 5.906E+01 |

Table A.4.: Matrix elements in 3rd order for the isochronous mode of the CR.

A.3. Additional Simulation Results

Additionally achieved simulation results from simulations performed with MOCADI, SIMION and COMSOL are attached below.

MOCADI simulations for absolute transmission efficiencies for different foil diameters are shown in figure A.1

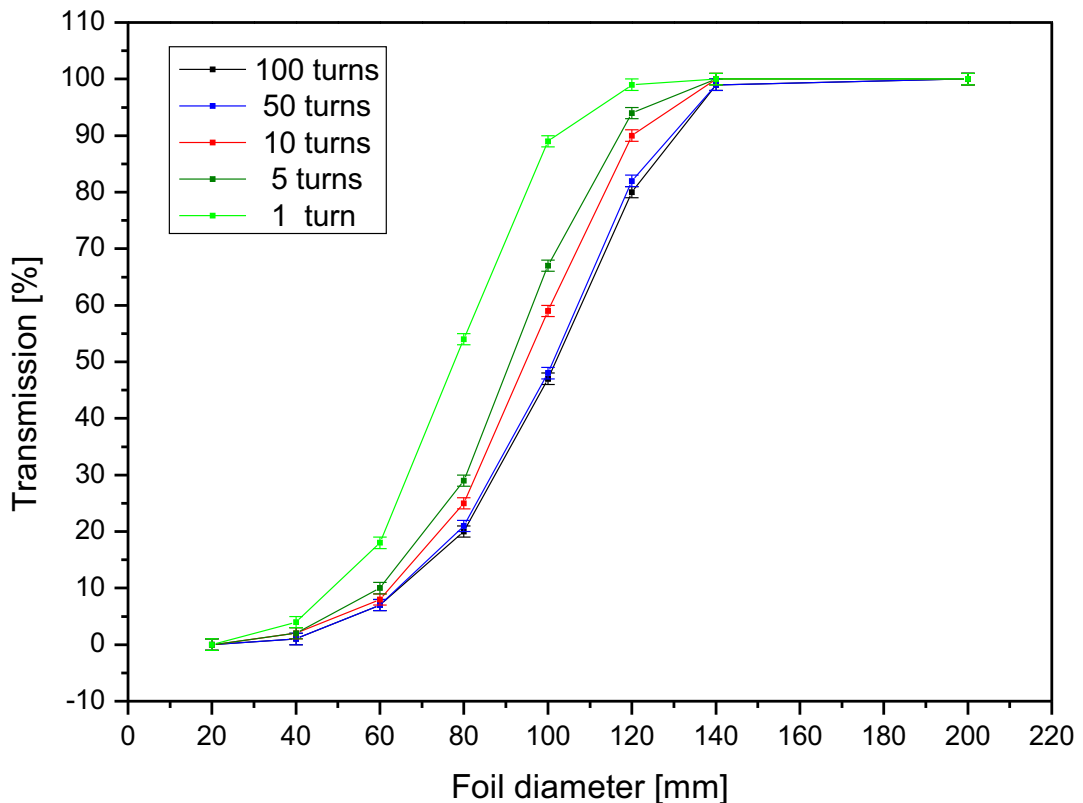


Figure A.1.: MOCADI simulations for different foil diameters and different turns in the CR.

As an example on how the timing uncertainties of the electron transport were achieved with SIMION the simulated ToF spectra for the forward and backward branches are shown in figure A.2. The simulated flight times were binned into 1 ps bins and plotted. A Gaussian distribution was fitted to the spectra and the corresponding σ of each fit was taken as the uncertainty for the specific branch and geometry. In order to find the coincidence uncertainty the simulated flight times for the forward and backward branch were subtracted from each other. For this it was considered that the starting positions on the foil (x, y and z-coordinates) have to be the same in forward and backward simulations in order to be able to find coincidences and to compare the flight times of individual electrons. The kinetic energy distribution for forward and backward simulations was different and randomly distributed.

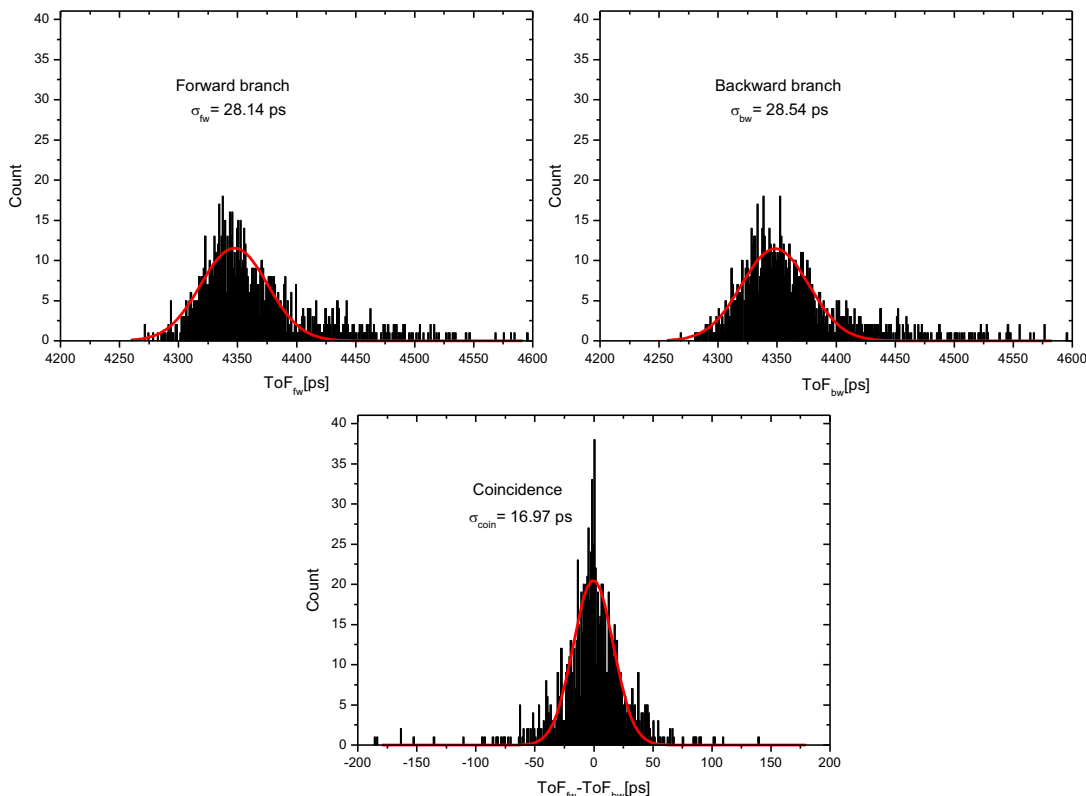


Figure A.2.: The graphs show the simulated ToF spectra for a displacement of 6 mm. In the upper left graph the spectrum of the forward branch including a Gaussian fit to the distribution is shown. The upper right graph shows the spectrum for the backward branch and the bottom graph shows the spectrum of the difference in ToF between forward and backward (coincidence). Each applied Gaussian fit yields a standard deviation σ that is stated in the according graph.

Systematic COMSOL simulations for different pole shoe diameter and the possibility of using so called Rose-shims [Ros38] to extend the homogeneity radius can be found in figure A.3. The Rose shims used for the simulations are simple iron rings placed on the edges of both pole shoes to increase the magnetic flux density at these positions. By doing so the total field strength is increased towards the center of the shoes, which leads to an increase of the homogeneity in case the shims are not too large and increase the field too much. The correlation between Rose-shim height h and width w for a given gap G_0 between the pole shoes is [Wol87a]

$$\frac{2h}{G_0} = 0.16 \exp\left(-2.7 \frac{2w}{G_0} + 0.42 \left(\frac{2w}{G_0}\right)^4\right) \quad (\text{A.1})$$

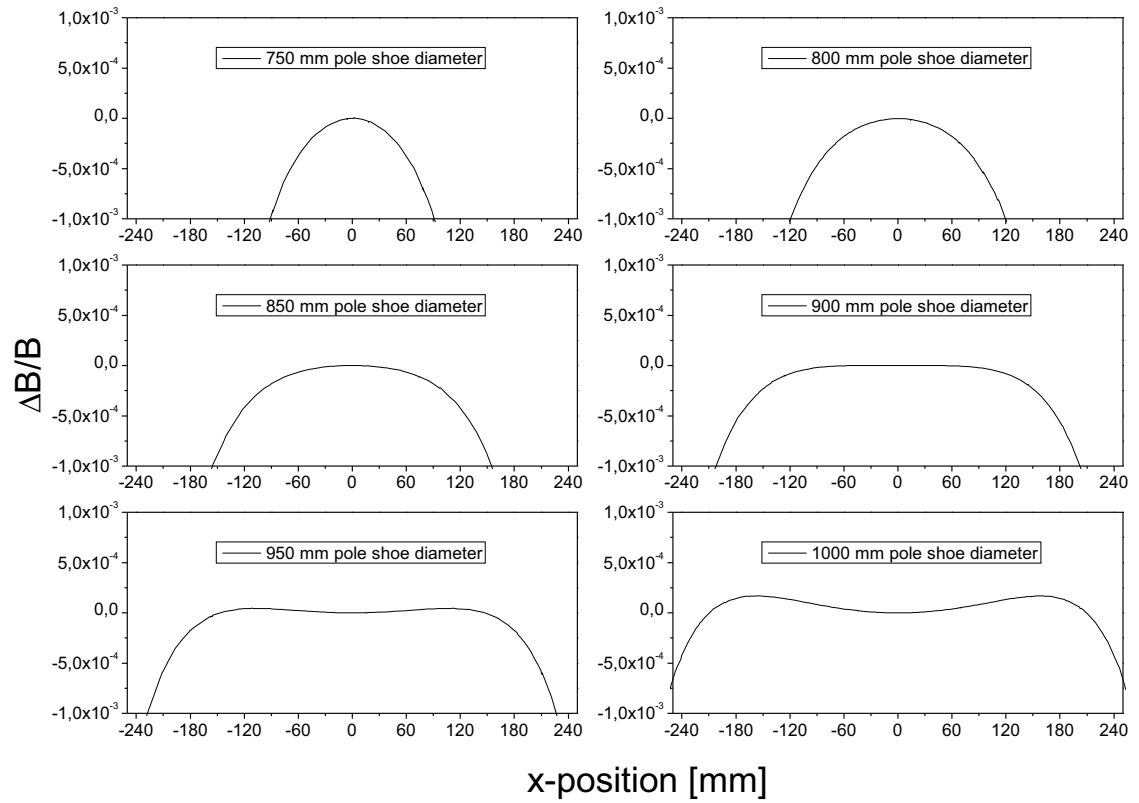


Figure A.3.: COMSOL simulations for different pole shoe diameters. For this simulations the gap width of the magnet was $G_0 = 258$ mm.

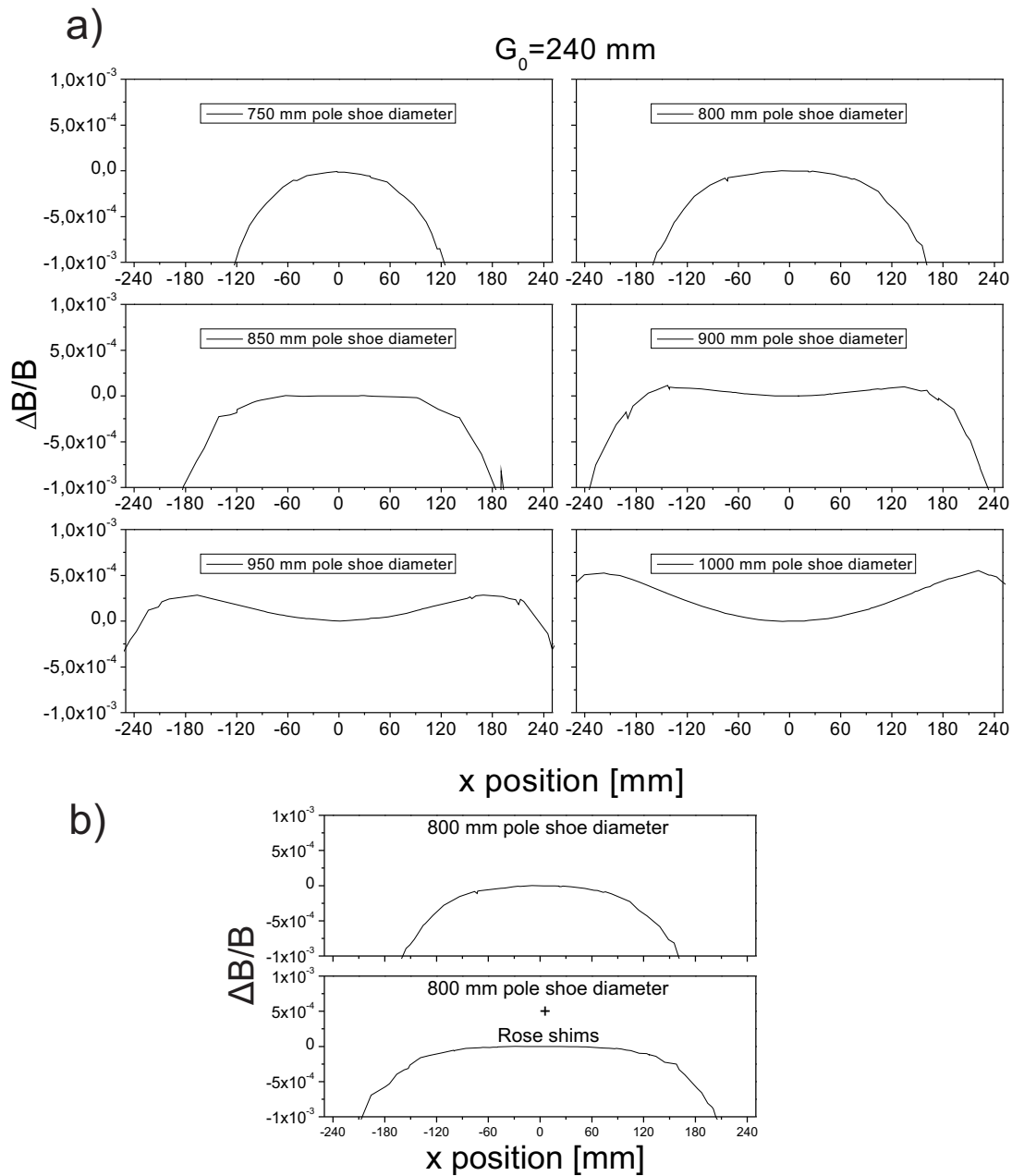


Figure A.4.: COMSOL simulations for different pole shoe diameters and additional application of Rose-shims. For these simulations the gap width of the magnet was $G_0 = 240 \text{ mm}$ to compare it with the larger gap width of the final magnet of 258 mm . For the simulated Rose-shims the combination of $w = 54 \text{ mm}$ and $h = 5 \text{ mm}$ was used and increased the homogeneity radius.

Bibliography

- [A⁺95] Y. Aboussir et al. Nuclear mass formula via an approximation to the Hartree-Fock method. *At. Data Nucl. Data Tables*, 61:127–176, 1995.
- [A⁺14] A. Aprahamian et al. Sensitivity studies for the main r process: nuclear masses. *AIP Advances*, 4, 2014.
- [Arc10] A. Arcones. Explosive nucleosynthesis: nuclear physics impact using neutrino-driven wind simulations. *arXiv*, 10112.3072v1, 2010.
- [AS69] N. Angert and C. Schmelzer. The UNILAC, a variable energy linear accelerator for atomic ions of any mass. *Kerntech.*, 11:690–695, 1969.
- [Ast19] F.W. Aston. A positive ray spectrograph. *Philosophical Magazine Series 6*, 38:707–714, 1919.
- [AWT03] G. Audi, A.H. Wapstra, and C. Thibault. The AME2003 atomic mass evaluation (II). Tables, graphs, and references. *Nucl. Phys*, A729:337, 2003.
- [B⁺63] W. H. Barkas et al. Resolution of the Σ^- -Mass Anomaly. *Phys. Rev. Lett.*, 11:26, 1963.
- [B⁺99] J.R.J. Bennett et al. Measurements of intense beams of ^{11}Li from tantalum foil target. *Nucl. Instr. and Meth. in Phys. Res.*, B155:515, 1999.
- [B⁺12] S. Brett et al. Sensitivity of the r-process to nuclear masses. *Eur. Phys. J. A*, 48:184, 2012.
- [BC79] C. Bouchard and J.D. Carette;. Secondary emission and ion feedback in a straight semiconducting channel. *J. Appl. Phys.*, 50(11):7168–7176, 1979.
- [Ber14] J. Bergmann. Systematische Untersuchung von MCP-Detektorsignalen zur Bestimmung der Zeitmarken mittels einer Software CFD-Methode. Vertiefungsmodul, Justus-Liebig-University Giessen, Germany, 2014.

- [Bet32] H.A. Bethe. Bremsformel für Elektronen relativistischer Geschwindigkeit. *Z. f. Phys.*, 76:293, 1932.
- [BF92] B. Blasche and B. Franczak. The Heavy Ion Synchrotron SIS. In *Proceedings of European Particle Accelerator Conference*, volume 9, page 37, 1992.
- [BH78] J. Bowman and R. Heffner. A novel zero time detector for heavyion spectroscopy. *Nucl. Instr. and Meth.*, 148:503, 1978.
- [BJ93] P. Bryant and K. Johnsen. *The principles of circular accelerator and storage rings*. Cambridge University Press, 1993.
- [Bla06] K. Blaum. High-accuracy mass spectrometry with stored ions. *Phys. Reports*, 425:1, 2006.
- [BND13] Y. Blumenfeld, T. Nilsson, and P. Van Duppen. Facilities and methods for radioactive ion beam production. *Physica Scripta*, 2013(T152):014023, 2013.
- [BR02] P.R. Bevington and D.K. Robinson. *Data Reduction and Error Analysis for Physical Sciences*. McGraw-Hill, 3rd edition, 2002.
- [Cha32] J. Chadwick. Possible Existence of a Neutron. *Nature*, 129:312, 1932.
- [COM08] COMSOL. *COMSOL Multiphysics User's Guide*. COMSOL AB, 2008.
- [COM15] COMSOL. Magnetic field of a helmholtz coil - solved with comsol multiphysics 3.5a, 2015.
- [CS80] M.V.K Chari and P.P. Silvester, editors. *Finite elements in electrical and magnetic field problems*. Wiley, 1980.
- [D⁺96] J. Dobaczewski et al. Mean-field description of ground-state properties of drip-line nuclei: Pairing and continuum effects. *Phys. Rev. C*, 53(6):2809–2840, 1996.
- [D⁺07] A. Dolinskii et al. Study of the mass resolving power in the CR storage ring operated as a TOF spectrometer. *Nucl. Instr. and Meth.*, A 574:207–212, 2007.
- [D⁺11] A. Dolinskii et al. Progress Report on the Collector Ring (CR) for the FAIR Project . *GSI Scientific Report 2010*, 1:305, 2011.
- [DD96] C. G. Drexler and R. D. DuBois. Energy- and angle-differential yields

- of electron emission from thin carbon foils after fast proton impact. *Phys. Rev. A*, 53(3):1630, 1996.
- [Dic06] T. Dickel. Aufbau und Charakterisierung eines Multi-Reflektions-Flugzeit-Massenspektrometers zur Isobarentrennung. Diploma thesis, Justus-Liebig-University Giessen, Germany, 2006.
- [Dic10] T. Dickel. *Design and Commissioning of an Ultra-High-Resolution Time-of-Flight Based Isobar Separator and Mass Spectrometer*. Phd thesis, Justus-Liebig-University Giessen, Germany, 2010.
- [Diw09] M. Diwisch. Untersuchung zur Steigerung der Ratenakzeptanz eines Flugzeitdetektors für isochrone Massenmessungen an FRS-ESR bei GSI. Bachelor thesis, Justus-Liebig-University Giessen, Germany, 2009.
- [Diw11] M. Diwisch. Untersuchung und Verbesserungen der Zeiteigenschaften eines Flugzeitdetektors für die Isochrone Massenspektrometrie an der FRS-ESR-Anlage bei der GSI. Master thesis, Justus-Liebig-University Giessen, Germany, 2011.
- [Dra08a] CR Technical Design Report Draft. http://www-win.gsi.de/fair-eoi/PDF/TDR_PDF/TDR_CR.pdf, 2008. [Online; accessed 01-May-2015].
- [Dra08b] Super-FRS Technical Design Report Draft. http://www-win.gsi.de/fair-eoi/PDF/TDR_PDF/TDR_Super-FRS_.pdf, 2008. [Online; accessed 01-May-2015].
- [DZ99] J. Duflo and A.P. Zuker. The nuclear monopole Hamiltonian. *Phys. Rev. C*, 59:R2347, 1999.
- [Edd20] A.S. Eddington. The internal constitution of the stars. *Nature*, 106:14–20, 1920.
- [Fab08] B. Fabian. *Characterization and Optimization of a Time-of-Flight Detector for Isochronous Mass Measurement at the ESR*. Phd thesis, Justus-Liebig-University Giessen, Germany, 2008.
- [Fer40] E. Fermi. The Ionization Loss of Energy in Gases and in Condensed Materials. *Phys. Rev.*, 57:485, 1940.
- [FGM87] B. Franzke, H. Geissel, and G. Münzenberg. Direct High Precision Mass Measurement in the ESR. Experiment - Proposal, 1987.
- [FGM08] B. Franzke, H. Geissel, and G. Münzenberg. Mass and lifetime mea-

- surements of exotic nuclei in storage rings. *Mass Spectrom. Rev.*, 27:428, 2008.
- [G⁺92a] H. Geissel et al. First storage and cooling of secondary heavy ion beams at relativistic energies. *Phys. Rev. Lett.*, 68:3412–3415, 1992.
- [G⁺92b] H. Geissel et al. The GSI projectile fragment separator (FRS): a versatile magnetic system for relativistic heavy ions. *Nucl. Instr. and Meth. in Phys. Res.*, B70:286–297, 1992.
- [G⁺03] H. Geissel et al. The Super-FRS project at GSI. *Nucl. Instr. and Meth. in Phys. Res.*, B204:71–85, 2003.
- [G⁺06] H. Geissel et al. A new experimental approach for isochronous mass measurements of short-lived exotic nuclei with the FRS-ESR facility. *Hyperfine Interactions.*, 173:55–60, 2006.
- [GCP13] S. Goriely, N. Chamel, and J.M. Pearson. Further explorations of Skyrme-Hartree-Fock-Bogoliubov mass formulas. XIII. The 2012 atomic mass evaluation and the symmetry coefficient. *Phys. Rev., C* 88, 2013.
- [Gei12] H. Geissel. Recent results from FRS experiments with exotic nuclei produced with uranium projectiles and perspectives with the Super-FRS. In *Proceedings of the International Symposium Vladivostok, Russia, 1-6 October 2012*, 2012.
- [GHMD14] H. Geissel, M. Huyse, G. Münzenberg, and P. Van Duppen. *Exotic Nuclear Beam Facilities*, volume 1. Wiley, 2014.
- [GIC] GICOSY. <http://web-docs.gsi.de/~weick/gicosy/>. [Online; accessed 04-May-2015].
- [GM09] H. Geiger and E. Marsden. On a diffuse reflection of the α -particles. In *Proceedings of the Royal Society*, A 82, pages 495–500, 1909.
- [GMR95] H. Geissel, G. Münzenberg, and K. Riisager. Secondary Exotic Nuclear Beams. *Annu. Rev. Nucl. Part. Sci.*, 45:163, 1995.
- [Gon14] M. L. Goncharov. *High-precision Penning-trap mass spectrometry at SHIPTRAP and PENTATRAP for neutrino physics research*. PhD thesis, Ruperto-Carola-University of Heidelberg, 2014.
- [GSI15] GSI. FAIR-Facility for Antiproton and Ion Research. https://www.gsi.de/de/forschung_beschleuniger/fair.htm?nr=%2527%2522, 2015. [Online; accessed 30-April-2015].

- [GSP07] S. Goriely, M. Samyn, and J. M. Pearson. Further explorations of Skyrme-Hartree-Fock-Bogoliubov mass formulas. VII. Simultaneous fits to masses and fission barriers. *Phys. Rev.*, C75:064312, 2007.
- [H⁺78] K. N. Huang et al. Neutral-Atom Electron Binding Energies from Relaxed-Orbital Relativistic Hartree-Fock-Slater Calculations $2 \leq Z \leq 106$. *At. Data Nucl. Data Tables*, 18:243–291, 1978.
- [H⁺79] S. Hofmann et al. Alpha decay studies of very neutron deficient isotopes of Hf, Ta, W, and Re. *Z. f. Phys.*, A291, 1979.
- [H⁺86] D. Hasselkamp et al. Ion-induced secondary electron spectra from clean metal surfaces. *Nucl. Instr. and Meth. in Phys. Res.*, B18:561–565, 1986.
- [H⁺06] U. Hager et al. First Precision Mass Measurements of Refractory Fission Fragments. *Phys. Rev. Lett.*, 96(042504), 2006.
- [H⁺07a] U. Hager et al. Precision mass measurements of neutron-rich Tc, Ru, Rh, and Pd isotopes. *Phys. Rev. C*, 75(064302), 2007.
- [H⁺07b] U. Hager et al. Precision mass measurements of neutron-rich yttrium and niobium isotopes. *Nucl. Phys. A* 793:20–39, 2007.
- [H⁺08] J. Hakala et al. Evolution of the N=50 Shell Gap Energy towards ⁷⁸Ni. *Phys. Rev. Lett.*, 101(052502), 2008.
- [H⁺11] J. Hakala et al. Precision mass measurements of neutron-rich Y, Nb, Mo, Tc, Ru, Rh, and Pd isotopes. *Eur. Phys. J. A*, 47:129, 2011.
- [H⁺12a] J. Hakala et al. Precision Mass Measurements beyond ¹³²Sn: Anomalous Behavior of Odd-Even Staggering of Binding Energies. *Phys. Rev. Lett.*, 109(032501), 2012.
- [H⁺12b] S. Hofmann et al. The reaction $^{48}\text{Ca} + ^{248}\text{Cm} \rightarrow ^{296}116^*$ studied at the GSI-SHIP. *Eur. Phys. J. A*, 48:62, 2012.
- [HAB⁺00] M. Hausmann, F. Attallah, K. Beckert, F. Bosch, A. Dolinskiy, H. Eickhoff, M. Falch, B. Franczak, B. Franzke, H. Geissel, Th. Kersch, O. Klepper, H.-J. Kluge, C. Kozhuharov, K. E. G. Löbner, G. Münzenberg, F. Nolden, Yu. N. Novikov, T. Radon, H. Schatz, C. Scheidenberger, J. Stadlmann, M. Steck, T. Winkler, and H. Wollnik. First isochronous mass spectrometry at the experimental storage ring ESR. *Nucl. Instrum. Meth. A*, 446:569–580, 2000.
- [Hau99] M. Hausmann. *Energieisochrone Massenmessungen am Experi-*

- mentierspeicherring der GSI*. Phd thesis, Justus-Liebig-University Giessen, Germany, 1999.
- [Hei12] S. Heinze. Kernreaktionen - Grundlagen, Experimente und Anwendungen. Lecture University Gießen, 2012.
- [HGK98] D. Hasselkamp, K.O. Groeneveld, and J. Kemmler. *Particle induced electron emission II*. Springer Verlag GmbH, 1998.
- [Hor13] C. Hornung. Investigations on the mcp-detector. Vertiefungsmodul, Justus-Liebig-University Giessen, Germany, 2013.
- [HS39] O. Hahn and F. Straßmann. Über den Nachweis und das Verhalten der bei der Bestrahlung des Urans mittels Neutronen entstehenden Erdalkalimetalle. *Naturwissenschaften*, 27:11–15, 1939.
- [I⁺97] N. Iwasa et al. "MOCADI" a Universal Code for the Transport of Ions through Matter within Ion-optical Systems. *Nucl. Instr. and Meth. in Phys. Res.*, B126:284, 1997.
- [Ich12] T. Ichikawa. Nuclear Fission Process, 2012.
- [ILI05] ILIMA. Technical Proposal for the ILIMA Project. http://www.fair-center.eu/fileadmin/fair/experiments/NUSTAR/Pdf/ILIMA_tp_20050120_2005. [Online; accessed 04-May-2015].
- [JS85] W.R. Johnson and G. Soff. The Lamb Shift in Hydrogen-Like Atoms $1 \leq Z \leq 110$. *At. Data Nucl. Data Tables*, 33:405–446, 1985.
- [JYF12] JYFLTRAP. http://research.jyu.fi/igisol/JYFLTRAP_masses/nrich.html, 2012. [Online; accessed 01-May-2015].
- [K⁺95] M. König et al. Quadrupole excitation of stored ion motion at the true cyclotron frequency. *Int. J. Mass Spectrom.*, 142:95, 1995.
- [K⁺03] T. Kubo et al. In-flight RI beam separator BigRIPS at RIKEN and elsewhere in Japan. *Nucl. Instr. and Meth. in Phys. Res.*, B 204(97), 2003.
- [KF⁺13] N. Kuzminchuk-Feuerstein et al. Design of the Dual TOF Detector System for Isochronous Mass Spectrometry in the CR at FAIR. *GSI Scientific Report 2012*, page 212, 2013.
- [KHN51] O. Kofoed-Hansen and K.O. Nielsen. Short-Lived Krypton Isotopes and Their Daughter Substances. *Phys. Rev.*, 82:96, 1951.
- [Knö08] R. Knöbel. *Neuartige Isochrone Massenmessung kurzlebiger neutro-*

- nenreicher, gespeicherter Kerne am FRS-ESR*. Phd thesis, Justus-Liebig-University Giessen, Germany, 2008.
- [Kuz11] N. Kuzminchuk. *Performance Studies and Improvements of a Time-of-Flight Detector for Isochronous Mass Measurements at the FRS-ESR Facility*. Phd thesis, Justus-Liebig-University Giessen, Germany, 2011.
- [L⁺13] S. Litvinov et al. Isochronicity correction in the CR storage ring. *Nucl. Instr. and Meth. in Phys. Res.*, A724:20–26, 2013.
- [Lip11] W. Lippert. Experimentelle Hadronen-, Kern- und Teilchenphysik. Vertiefungsmodul, Justus-Liebig-University Giessen, Germany, 2011.
- [LIS15] LISE++. <http://lise.nsl.msu.edu/lise.html>, 2015. [Online; accessed 01-May-2015].
- [Lit03] Y. Litvinov. *Basic Nuclear Properties of Neutron-Deficient Nuclei investigated via High Precision Mass Measurements in the Element Range of $36 \leq Z \leq 92$* . Phd thesis, Justus-Liebig-University Giessen, Germany, 2003.
- [Lit08] S. Litvinov. *Investigation of the Isochronous Mode of the Experimental Storage Ring (ESR) and the Collector Ring (CR). Decay Spectroscopy of Highly Charged Stored ^{140}Pr ions at the FRS-ESR facility*. Phd thesis, Justus-Liebig-University Giessen, Germany, 2008.
- [LPT03] D. Lunney, J. M. Pearson, and C. Thibault. Recent trends in the determination of nuclear masses. *Rev. Mod. Phys.*, 75:1021, 2003.
- [M⁺07] M. Mazzocco et al. Extension of the Monte-Carlo code MOCADI to fusion-evaporation reactions. *Eur. Phys. J. Special Topics*, 150:363–364, 2007.
- [Mat04] M. Matos. *Isochronous Mass Measurements of Short-Lived Neutron Rich Nuclides at the FRS-ESR Facilities*. Phd thesis, Justus-Liebig-University Giessen, Germany, 2004.
- [MD07] D.J. Manura and D.A. Dahl. *SIMION 8.0 User Manual*. Scientific Instrument Services, 2007.
- [MFH⁺79] G. Münzenberg, W. Faust, S. Hofmann, P. Armbruster, K. Güttner, and H. Ewald. The Velocity Filter SHIP, a Separator of Unslowed Heavy Ion Fusion Products. *Nucl. Instr. and Meth. in Phys. Res.*, 161:65–82, 1979.
- [MHJ98] A.G. Marshall, C.L. Hendrickson, and G.S. Jackson. Fourier trans-

- form ion cyclotron resonance mass spectrometry: a primer. *Mass Spectrom. Rev.*, 17:1–35, 1998.
- [MNMS95] P. Möller, J.R. Nix, W.D. Myers, and W.J. Swiatecki. Nuclear ground-state masses and deformations. *At. Data Nucl. Data Tables*, 59:185–381, 1995.
- [MOC15] MOCADI. <http://web-docs.gsi.de/~weick/mocadi/>, 2015.
- [MS66] W.D. Myers and W.J. Swiatecki. Nuclear masses and deformations. *Nucl. Phys.*, 81:1–60, 1966.
- [Nob14] Nobelprize.org. The Nobel Prize in Physics 1903. http://www.nobelprize.org/nobel_prizes/physics/laureates/1903/index.html, 2014. [Online; accessed 18-December-2014].
- [O⁺12] A Ozawa et al. The rare-RI ring. *Prog. Theor. Exp. Phys*, 03C009, 2012.
- [P⁺96] J.M. Pearson et al. Nuclear mass formula with Bogolyubov-enhanced shell-quenching: application to r-processnöllmöl. *Phys. Lett. B*, 387:455–459, 1996.
- [P⁺13] W.R. Plaß et al. Multiple-reflection time-of-flight mass spectrometry. *Int. J. Mass Spectrom.*, 349-350:134–144, 2013.
- [Pat15] Z. Patyk. Private Communication, Soltan Institute for Nuclear Studies, Warsaw, Poland, 2015.
- [Pea07] J.M. Pearson. Nuclear Mass Models, May 2007.
- [PHO14] PHOTONIS. Private Communication J. Harper, 2014.
- [PJS94] D.R. Plante, W.R. Johnson, and J. Sapirstein. Relativistic All-Order Many-Body Calculations of the $n = 1$ and $n = 2$ States of Heliumlike Ions. *Phys. Rev.*, A49(5):3519–3530, 1994.
- [R⁺90] H. Rothard et al. Secondary electron yields from thin foils: A possible probe for the electronic stopping power of heavy ions. *Phys. Rev. A*, 41(5):2521, 1990.
- [R⁺95] H. Rothard et al. Target-thickness-dependent electron emission from carbon foils bombarded with swiftt highly charged heavy ions. *Phys. Rev. A*, 51(4):3066, 1995.
- [R⁺97] T. Radon et al. Schottky mass measurement of cooled proton-

- rich nuclei at the GSI experimental storage ring. *Phys. Rev. Lett.*, 78(25):4701–4704, 1997.
- [R⁺00] T. Radon et al. Schottky mass measurements of stored and cooled neutron-deficient projectile fragments in the element range of $57 \leq Z \leq 84$. *Nucl. Phys.*, A677:75–99, 2000.
- [R⁺07] S Rahaman et al. Precise atomic masses of neutron-rich Br and Rb nuclei close to the r-process path. *Eur. Phys. J. A*, 32(1):87–96, 2007.
- [Ros38] M.E. Rose. Magnetic Field Corrections in the Cyclotron. *Phys. Rev.*, 53:715–719, 1938.
- [Rut19] E. Rutherford. Collision of α particles with light atoms, IV: An anomalous effect in nitrogen. *Philosophical Magazine*, 37:581–587, 1919.
- [Rut20] E. Rutherford. Nuclear constitution of atoms. In *Proceedings of the Royal Society*, A 97, pages 374–400, 1920.
- [S⁺94] C. Scheidenberger et al. Direct observation of systematic deviations from the Bethe stopping theory for relativistic heavy ions. *Phys. Rev. Lett.*, 73:50, 1994.
- [S⁺96] C. Scheidenberger et al. Energy-Loss-Straggling Experiments with Relativistic Heavy Ions in Solids. *Phys. Rev. Lett.*, 77:3987, 1996.
- [S⁺08] B. Sun et al. Nuclear Structure Studies of Short-Lived Neutron-Rich Nuclei with the Novel Large-Scale Isochronous Mass Spectrometry at the FRS-ESR Facility. *Nucl. Phys.*, 812(1-4):1–12, 2008.
- [S⁺10] B. Sun et al. Direct measurement of the 4.6 MeV isomer in stored bare ^{133}Sb ions. *Phys. Lett. B*, 688:294–297, 2010.
- [Sei13] D. Seiler. Private Communication, TU München, Germany, 2013.
- [Sen92] M. Sendor. Magnet-Konstruktion und Aufbau für einen Timing-Detektor. Diploma thesis, Justus-Liebig-University Giessen, Germany, 1992.
- [SG98] C. Scheidenberger and H. Geissel. Penetration of Relativistic Heavy Ions Through Matter. *Nucl. Instr. and Meth. in Phys. Res.*, B135:25–34, 1998.
- [SGP04] M. Samyn, S. Goriely, and J.M. Pearson. Further explorations of Skyrme-Hartree-Fock-Bogoliubov mass formulas. III. Role of particle-number projection. *Phys. Rev. C*, 70:044309, 2004.

- [Sta02] J. Stadlmann. *Erste isochrone Massenmessung kurzlebiger Nuklide am Experimentierspeicherring der GSI*. Phd thesis, Justus-Liebig-University Giessen, Germany, 2002.
- [Ste57] E.J. Sternglass. Theory of secondary electron emission by high speed ions. *The Phys. Rev., Second series*, 108:1–12, 1957.
- [Sun08] B. Sun. . Phd thesis, Beijing University, China, 2008.
- [T⁺92] J. Trötscher et al. Mass measurements of exotic nuclei at the ESR. *Nucl. Instr. and Meth. in Phys. Res.*, B70:455–458, 1992.
- [Tho12] J.J. Thomson. Further experiments on positive rays. *Philosophical Magazine Series 6*, 24:209–253, 1912.
- [Trö93] J. Trötscher. *Der Experimentierspeicherring der GSI als Flugzeit-massenspektrometer für exotische Nuklide*. Phd thesis, Justus-Liebig-University Giessen, Germany, 1993.
- [VAC] VACOM. Private Communication M. Roßburger.
- [vW35] C.F. von Weizsäcker. Zur Theorie der Kernmassen. *Z. f. Phys.*, 96:431–458, 1935.
- [W⁺97] H. Wollnik et al. TOF Mass Measurements of Exotic Nuclei at the ESR of the GSI. *Nucl. Phys.*, A626:327c, 1997.
- [W⁺06] G. Wu et al. Ion Trajectory Simulation for Electrode Configurations with Arbitrary Geometries. *J. Am. Soc. Mass. Spectrom.*, 17:1216–1228, 2006.
- [W⁺13a] P.M. Walker et al. The ILIMA project at FAIR. *Int. J. Mass Spectrom.*, 349-350:247–254, 2013.
- [W⁺13b] N. Wang et al. An improved nuclear mass formula: WS3. In *Journal of Physics: Conference Series*, volume 420, 2013.
- [Wag91] C. Wagemans. *The nuclear Fission Process*, volume 1. CRC Press, 1991.
- [WAW12] M. Wang, G. Audi, and A.H. Wapstra. The AME2012 atomic mass evaluation (II). Tables, graphs, and references. *Chin. Phys. C*, 36:1603–2014, 2012.
- [Wei15] H. Weick. Private Communication, GSI, Darmstadt, Germany, 2015.

- [Wiz79] J.L. Wiza. Micro channel plate detectors. *Nucl. Instr. and Meth.*, 162:587–601, 1979.
- [Wol87a] H. Wollnik. Laterally and longitudinally dispersive recoil mass separators. *Nucl. Instr. and Meth.*, B26:267–272, 1987.
- [Wol87b] H. Wollnik. Mass separators. *Nucl. Instr. and Meth. in Phys. Res.*, A258:289–296, 1987.
- [Wol87c] H. Wollnik. *Optics of Charged Particles*, volume 1. Academic Press, 1987.
- [WWV87] H. Wollnik, J. M. Wouters, and D. J. Vieira. An Isochronous Time-of-Flight Mass Spectrometer. *Nucl. Instr. and Meth. in Phys. Res.*, A258:331–334, 1987.
- [Y⁺08] Y. Yamaguchi et al. Rare-RI ring project at RIKEN RI beam factory. *Nucl. Instr. and Meth. in Phys. Res.*, B 266:4575–4578, 2008.

Acknowledgments

I would like to thank all the people who supported and helped me during my work. Many thanks to Prof. Dr. Christoph Scheidenberger and the IONAS group in Gießen for giving me the opportunity and means to work on such an interesting and important topic. I am very grateful for the fruitful discussions and ideas from Dr. Wolfgang R. Plaß. In particular my biggest thanks go to my Ph.D. supervisor Prof. Dr. Dr. h.c Hans Geissel for sharing his experience (not only in physics but also in life) and supporting me whenever possible. Without your help, encouragement and understanding this work would have not been possible.

Many many thanks to my team-mate Dr. Ronja Knöbel who introduced me to the IMS data analysis and supported me with countless figures, ideas and in the analysis process. I thank Prof. Dr. Zygmunt Patyk for his sustained help during the mass analysis process, Dr. Helmut Weick for supporting me during the MOCADI simulations, and Dr. Timo Dickel for discussions and valuable input during the SIMION simulations (I still like the CAD import feature).

I am grateful to Evelin Prinz for supporting me also in bad times and taking care of the bureaucracy. I also would like to thank all IONAS-group members (present and former) for the excellent working atmosphere and funny discussions, Dipl. Phys. Christian Jesch, and B.Sc. Florian Greiner (admins oh admins), M.Sc. Jens Ebert, my most important office partner M.Sc. Wayne Lippert, M.Sc. Moritz Pascal Reiter, M.Sc. Ann-Kathrin Rink, M.Sc. Christine Hornung, M.Sc. Julian Bergmann, Samuel Ayet San Andres (FCB ole!), Dr. Natalia Kuzminchuk-Feuerstein, Dipl. Phys. Johannes Lang, and last but not least B.Sc. Matti Werner.

A big thank to my best friends Sebastian Petry, Wayne Lippert, Christian Drucker, Johannes Krombach, and Sebastian Reimann for kidnapping me into the real world besides physics on a regular basis. I plan to return the favor to each one of you as good as I can.

Finally, I thank my wife-to-be Magdalena Schilling, my brother Renè Diwisch, my mother Birgit Diwisch, and my father Rainer Diwisch. Without your support and love all this would not be possible. This work is dedicated to my family.

